Fachbereich Mathematik und Naturwissenschaften
Fachgruppe Physik
Bergische Universität Wuppertal

Properties of confined and unconfined water

A computer simulation study at ambient and supercooled conditions

Dissertation
by
Christa Guse

2011
WU

Diese Dissertation kann wie folgt zitiert werden:

urn:nbn:de:hbz:468-20111125-120831-6
[http://nbn-resolving.de/urn/resolver.pl?urn=urn:nbn:de:hbz:468-20111125-120831-6]

Summary

The aim of this work is to add to the long lasting efforts to provide an unified picture of the properties of confined and unconfined water. Water is an ubiquitous substance with special importance for geological and biological as well as technical processes. There are 1.4 billion km^3 of water on earth, most of it in liquid form, 0.001% as vapor in the atmosphere and 1.8% as ice (mainly crystalline hexagonal ice I_h) frozen at the poles and in Greenland [1]. But water can also exist in an amorphous form, which is produced by rapidly cooling liquid water and constitutes the most common structure of H_2O in the universe.

In addition to its rich and complicated phase structure, water exhibits several interesting properties which differ from those of "normal liquids". These anomalies include for instance the heat capacity minimum, the compressibility minimum, the viscosity minimum and the density maximum [2]. Although most of water's anomalies were already well established at the beginning of the 20th century, to this day there neither exists an accepted theory explaining all the different anomalies nor is the phase diagram known in the full temperature and pressure regime.

Despite numerous proposals for a universal theory of water, progress has been slow. Mainly because the main distinctive features of the different models appear in the so-called "no man's land" of water's phase space, between the temperature of homogeneous nucleation and the crystallization temperature between 150 and 236 K at ambient pressure [3]. Bulk water crystallizes in this region making experimental investigations on liquid water impossible.

To circumvent this problem, a number of experiments have been performed on confined water, which can be supercooled below the homogeneous nucleation temperature without crystallization. But the question remains in how far results obtained under confined conditions are transferable to bulk water [4].

In contrast to experiments computer simulations are feasible in the "no man's land". In this case the limitations of simulation studies regarding system size and observation time are of advantage, because they prevent crystallization. Thus simulation studies can help to add pieces to the puzzle of water's anomalies by helping to interpret experimental results and to test the different proposed theoretical scenarios [5].

In this work simulations of rigid classical water models are used to investigate the properties of bulk water and water confined in single walled carbon nanotubes.

While today there exist a number of water models that perform exceptionally well in reproducing experimental results, the models themselves exhibit a complexity and diversity in phase behavior as well as in structure that makes it difficult, to draw conclusions for actual water from them.

It is therefore important to test different models and to gain knowledge of their characteristics and limitations in order to assess their relevance.

Regarding the bulk simulations our interest lay mainly in the connection between the structural features that result in the density maximum of water and their manifestation in the coherent x-ray scattering intensities as it is observed experimentally.

We therefore computed scattering intensities for a number of different water models and compared them to experimental ones. It turns out that the best results regarding density, diffusion and intensity curves can be achieved with the TIP4P/2005 model, which shows the least change in the hydrogen bond network with temperature, while most other models seem to overestimate structural development.

As there is a special interest in the small-angle scattering, which is clouded by some experimental controversy, we simulated large systems at small temperatures to gather additional information in this region. We find that our simulations can reproduce the experimentally observed enhancement of the intensity curves without showing any large scale density fluctuations.

For the observation of water in confinement, carbon nanotubes possess the advantage of a relatively week interaction with H_2O molecules, which may not influence the hydrogen bonding too much. In order to gain an overview of the general behavior of water in these geometries we investigated a vast range of temperatures, pressures and tube diameters. We put our emphasis on the structural and transport properties of water as well as on its phase behavior. We compute density profiles, pair correlation functions and energy by grand-canonical Monte Carlo and determine the diffusion constant parallel and perpendicular to the tube axis by molecular dynamics simulations.

Bibliography

[1] Häckel H. *Meteorologie.* UTB, Stuttgart, 6., corrected edition edition, 2008.

[2] Stanley H. Liquid water: A very complex fluid. *Pramana*, 53(1):53–83, 1999.

[3] Debenedetti P G. Supercooled and glassy water. *J. Phys.: Condens. Matter* , 15(45):R1669–R1726, 2003.

[4] Ricci M A, Bruni F, and Giuliani A. Similarities between confined and supercooled water. *Faraday Discuss.*, 141:347–58, 2009.

[5] Guillot B. A reappraisal of what we have learnt during three decades of computer simulations on water. *J. Mol. Liq.*, 101(1-3):219–60, 2002.

Contents

Appendices

1. Introduction

1.1. Development of this project

Our interest in water was initially stirred by the lack of an explanation for its density maximum at 4° C.

It is possible to envision the density anomaly as a superposition effect in a two-fluid model. One less dense fluid, characterized by an on average larger hydrogen bond density, mixing with a denser fluid, characterized by an on average smaller hydrogen bond density. Increasing temperature leads to a reduction of the hydrogen bond density and thus to an overall density increase. Simultaneously there is 'normal' thermal expansion, due to anharmonic interactions between water molecules, reducing the density. Both effects added may produce a density maximum. Our initial goal therefore was the study of the water structure as well as its dynamics on the nanometer scale to possibly obtain evidence for such a two fluid model [1].

In a first step we investigated the microscopic origin of water's structural anomaly. We selected a number of classical water models, polarizable and non-polarizable ones, which exhibit a density maximum similar to water. We then sought to identify a common and distinct change in the H-bond network structure on cooling. But although we could establish similar trends in the H-bond structure of all models, their structural change on cooling proved to be moderate and homogeneous without the development of clear-cut structures like clusters or chains.

To establish the relevance of this observation we decided to take a more thorough look at the comparability of our simulation studies with experimental scattering results. As an experimentally observed increase in the small angle region of the intensities on cooling was suspected to signal large scale heterogeneities it was interesting to see, that our simulations reproduce this enhancement without showing large obvious density fluctuations. The main differences in the simulated spectra of different models and temperatures lie in the intermediate q range of the intensity curves, where a distinct shoulder develops with decreasing temperature. Unfortunately there exist precious few experimental scattering results in the supercooled temperature region. Thus we are very thankful for the experimental results provided by Prof. Bomsdorf, that with others from literature allowed us to compare the simulated structures to the experimental ones and also heightened our awareness of the limitations and problems that are incurred by these kind of experiments.

We discovered that the performance of a water model regarding thermodynamic and transport properties does not seem to be directly correlated to their ability to reproduce experimentally observed intensity curves, thus hindering definite conclusions about the models overall qualities.

There are a number of attempts to connect the density maximum and other anomalies to different scenarios underlying the water phase diagram. These have their distinct features at very low temperatures below the homogeneous nucleation temperature, where bulk experiments are no longer feasible. Because water in confinement can be supercooled to lower temperatures without freezing, some experimental effort has been concentrated on this area. In the second part of this project we therefore investigated the behavior of water confined in carbon nanotubes using the water model, which performed best in our bulk simulations. The main features, which intrigued us immediately, are the varied

---

[1] Our first idea was to perhaps identify a reversible network of hydrogen-bonded chains, which may be modeled with for instance the Tlusty-Safran defect model [1].

phase structure that occurs in those systems: the adsorption and desorption transition and its characterization, which in itself is a long standing problem in experimental and simulation studies as well as different freezing transitions that can be observed in small tubes. While dramatic structural changes occur in small tubes, water confined in tubes with a diameter of 50 Å, is already behaving very similar to bulk water, e.g. exhibiting a density maximum, although at lower temperatures. This convergence to bulk behavior is of special interest in order to judge in how far experimental and simulation results obtained in confined systems are useful to explain bulk water behavior.

1.2. Known facts about water and proposals for its phase diagram

1.2.1. Experimental results about bulk water

As water is such an ubiquitous substance with an immense importance for geographical and biological as well as chemical processes, it moved into the focus of scientific interest early in history and because of its complex and anomalous behavior remained there to this day. The main anomalies of liquid water were already well established at the beginning of the 20th century including thermodynamic anomalies (heat capacity minimum in 1879 by Rowland, compressibility minimum in 1851 by Grassi), dynamical anomalies (viscosity minimum in 1884 by Röntgen and by Warburg and Sachs), and structural anomalies (density maximum (first observed in 1657 by Florentine scientists, final prove in 1805 by Hope)). For an overview of the historical development see [2].
Early attempts to explain these unusual results were based on two state mixture models. When Bernal and Fowler introduced the concept of a continuous three-dimensional tetrahedral network for liquid water in the early 1930s [3] it became the central problem to identify inhomogeneities in the network that could be treated as "microphases" in a two-state model.

Two new experimental results shed further light on the nature of water's mysterious behavior and inspired the development of new scenarios for the phase diagram of water. Mishima et al discovered that there are two forms of amorphous ice, namely a low-density (LDA) and a high-density form (HDA) and that there seems to be a first order phase transition between the two [4], while Angell et al found evidence for the existence of an apparent singularity of liquid water at about 228 K [5, 6].
Using these new findings three scenarios to explain the thermodynamic behavior of water were put forward: (i) Retracing spinodal scenario/ Stability-limit conjecture [7]; (ii) Singularity-free scenario [8, 9]; (iii) Critical-point scenario [10, 11]. Unfortunately it is very difficult to find experimental evidence to support either of these models, because their distinctive features appear in the so called "no man's land" of water's phase space, between the temperature of homogeneous nucleation, T_H and the crystallization temperature, T_X, between 150 K and 236 K at ambient pressure [12].

To circumvent this problem, a number of experiments have been performed on confined water which can be supercooled below T_H without crystallization. But the question remains in how far results obtained under confined conditions are transferable to bulk water [13]. Another way to gain insight into the "no man's land" is the investigation of different model systems, that can be solved analytically or by simulation. Here a number of new ideas and concepts were developed like the existence of multiple critical points [14] (getting some experimental backing by the discovery of very high density amorphous ice (VHDA) and its transitions to HDA and LDA [15]) or the importance of two different length scales for the anomalous behavior [16] as well as the significance of structural changes in the second neighbor shell signalized by the fifth neighbor distribution [17].

A combination of calculated clusters (e.g. [18]) and recent experiments yielded detailed information about structural and dynamic aspects of small clusters leading to the development of water models based on the assumption that calculated molecular clusters and structures may be constituents of the liquid phase [19].

A clear picture of the structure of water from simulations is shrouded by difficulties with the definition of hydrogen bonds and by the high connectivity of the hydrogen network, which complicates the search for correlations between dynamics, occupied space and hydrogen configuration of single water molecules or groups of molecules. In addition as for the experiments on confined water it is difficult to say if a simulated scenario is realized in actual liquid water.

It is therefore important to learn more about the microstructure of water from experiments to find the connection between the thermodynamic and structural properties of liquid water and to determine if models and confined water really share the characteristics of bulk water or just exhibit similar behavior based on a different microstructure.

Scattering experiments are the mean of choice to clarify structure. A number of elastic X-ray experiments were performed dating back to the 1930s, which although in general agreement differ slightly in peak positions and heights [20, 21, 22, 23, 24]. A qualitatively very good study with small experimental errors was performed in 2000 by Hura, et al [25, 26]. Relatively new papers investigating the supercooled regime were published in 2008 and 2010 [27, 28].
In order to gain more information on the expected heterogeneities and fluctuations in the supercooled region experiments were performed in the small q regime. In this area the first results were quite confusing, with Bosio, et al [29] finding an enhancement of the X-ray spectrum in the low q range and Michielsen finding none [30]. Here also a new study performed by Huang, et al in 2009 seems to have cleared the dispute in favor of an enhancement [31], which was confirmed by Clark et al [32].

A new chapter in the experimental studies investigating the structure of liquid water was opened by Wernet et al in 2004 by X-ray absorption experiments (XAS) [33]. They gave a different picture of water's structure suggesting the dominance of water molecules with just two hydrogen bonds forming chains and rings. But unlike elastic scattering spectra, absorption spectra are very difficult to interpret. Most studies referred to comparisons with bulk and surface ice spectra or to DFT calculations in order to suggest a structure based on the data. Smith et al for example arrived at a totally different picture claiming that only a relatively minor distortion from the ice structure in the H-bond network is required to produce the observed pre-edge intensity [34]. This controversy demonstrates as Holt et al pointed out [35] that the experimental picture of water depends to a large part on the time scale that is being probed.

Lately there have been a number of attempts to improve on the time resolution of experiments e.g. [36, 37]. Concerning the dynamical anomalies of water and the dynamic crossover observed in confined water there were a number of attempts to connect these to the proposed different scenarios for the phase diagram of water [38, 39]. The comparison of water with other similar liquids whose anomalous region is easier to investigate experimentally is also promising [40].

1.2.2. Phase diagram

Water can exist in a number of different phases: liquid, vapor, different forms of crystalline ice (I to XVI) and amorphous ices (LDA, HDA, VHDA).

Figure 1.1(a) is a simple and well-established representation of the phase diagram of water. Water can exist in at least 16 ice phases, of which 5 can coexist with liquid water. The corresponding melting lines of ice I, III, V, VI and VII are shown as well as the liquid-vapor phase transition line and the critical point, P_C. The data for this plot are taken from the IAPWS Formulation 1995 [41].

Figure 1.1(b) includes additional experimental results that will be helpful in demonstrating the three predominant scenarios, that were proposed to explain the thermodynamic anomalies of water.

F denotes the line of first-order phase transitions that separates the high-density and low-density amorphous ices HDA and LDA ([42] fig. 8). The curves denoted L and H are the limits of metastability of the HDA and LDA phases, respectively ([43] fig. 8). The parameter range, where liquid bulk water cannot be investigated experimentally, the so called "no man's land", is located between the crystallization line [42], T_X, and the limit of stability, T_S respectively [7] T_H. Two lines of thermodynamic anomalies, the line of density maxima and that of isothermal compressibility minima, are denoted by T_{MD} and T_{MC} respectively.

On the basis of these experimental findings three scenarios to explain the thermodynamic behavior of water were put forward: (i) Retracing spinodal scenario/ Stability-limit conjecture [5, 7]; (ii) Singularity-free scenario [8, 9]; (iii) Critical-point scenario [10, 11].

1.2.3. Retracing spinodal scenario/ Stability-limit conjecture

The retracing spinodal scenario or stability-limit conjecture was first proposed by Speedy and Angell in 1976 [5]. The spinodal line, or limit of stability, is the locus of points $P_S(T)$ or $T_S(P)$ in the P-T plane, where $(\partial P/\partial V)_T = 0$. In normal liquids, the liquid spinodal has positive slope, its zero-temperature limit yielding an upper bound for the liquid's tensile strength. According to Speedy's conjecture it would instead retrace towards positive pressures. In this theory the stability limits for superheating and supercooling of water are the observed branches of a continuous line of stability limits which passes through the negative pressure region of the P-T plane and also defines the limit of stability for stretched water. In figure 1.2(a) estimates gained from experimental data for the stability limits of superheated, stretched and supercooled water are plotted together with the proposed course of the spinodal, all taken from [7]. To gain estimates for T_S from experimental data an extrapolation is needed that is especially difficult for stretched water, where it depends on the input of a reliable equation of state. But if one takes the estimates at face value it is very intuitive to connect the different lines of instability as demonstrated in figure 1.2(a). This assumption in combination with some thermodynamic relations is sufficient to explain most of the anomalous behavior of the thermodynamic response functions. The main conclusions can be drawn by looking at the line of stability limit P_S. Following [7] we start from the differential of the volume, V,

$$dV = (\partial V/\partial T)_P \, dT + (\partial V/\partial P)_T \, dP \tag{1.1}$$

we look at the derivative with respect to temperature, T, along the stability limit $P_S(T)$, where $(\partial V/\partial T)_{P_S(T)} = dV_S/dT$ and $(\partial P/\partial T)_{P_S(T)} = dP_S/dT$

$$\begin{aligned} (\partial V/\partial T)_{P_S(T)} &= (\partial V/\partial T)_P + (\partial V/\partial P)_T \, (\partial P/\partial T)_{P_S(T)} \text{ and thus} && (1.2) \\ \alpha &= (dV_S/dT)/V_S + (dP_S/dT)\,\kappa_T \quad \text{at } P_S. && (1.3) \end{aligned}$$

As the variables P, T, V, S, and U are finite along the line $P_S(T)$ it follows that their differentials must be finite except for isolated singular points (like the gas-liquid critical point, the minimum in $P_S(T)$ and the minimum in $T_S(P)$). The subsequent results are not necessarily valid at these points. Expressing the isobaric heat capacity, C_P, similar to α one arrives at

$$C_P = T\,(dS_S/dT) + TV_S\,(dP_S/dT)^2\,\kappa_T \quad \text{at } P_S. \tag{1.4}$$

And for the isochoric heat capacity one gets

$$C_V = T\,(dS_S/dT) - T\,(dV_S/dT)\,\alpha/\kappa_T \quad \text{at } P_S. \tag{1.5}$$

The adiabatic compressibility, κ_S, and the thermal pressure coefficient, β, are given by

$$\begin{aligned} \kappa_S &= \kappa_T C_V/C_P && (1.6) \\ \beta &= (\partial P/\partial T)_V = \alpha/\kappa_T. && (1.7) \end{aligned}$$

Equation 1.3 and 1.4 imply that in leading order the divergences of α, C_P, and κ_T are the same except for a constant. It can also be shown [45] that C_P/κ_T and α/κ_T tend to a finite limit as $P \to P_S(T)$ so that C_V, κ_S and β remain finite.

Now that we have explained the experimentally observed apparent divergences we will have a look at the locus of density maximum. Therefore we will investigate the sign of α along the limit of stability line. Since $\kappa_T \to \infty$ at the line P_S and $(dV_S/dT)/V_S$ is finite (except at singular points), it follows from eq. 1.3

$$\alpha/(dP_S/dT) \to +\infty \quad \text{as} \quad P \to P_S. \tag{1.8}$$

Thus near P_S the expansivity and (dP_S/dT) share the same sign. For small temperatures ($\approx$ 160 to 300 K) P_S decreases with increasing temperature (see fig 1.2(a)), the expansivity is therefore negative, but elsewhere dP_S/dT is positive and so is the expansivity. It follows that there exists a line $\alpha(P,T) = 0$, the locus of a density extremum. It follows that α must change from $+\infty$ to $-\infty$ at the meeting point of the two lines $\alpha(P,T) = 0$ and P_S. It can also be shown [8] that if one assumes that the temperature of maximum density remains negatively sloped at negative pressures, the inevitable intersection of this line with the liquid-gas spinodal results in a retracing of the spinodal as a consequence of thermodynamic consistency alone. Independent of any proposed scenario, the increase of the isothermal compressibility κ_T on cooling below a negatively sloped TMD line is a requirement of thermodynamics.

Although the stability-limit conjecture seems to offer a plausible unification of the thermodynamic anomalies in superheated, stretched, supercooled and ordinary water, it does not account for the existence of amorphous solid water, as a re-entrant spinodal represents a continuous limit of stability bounding the entire liquid state, preventing any continuity between amorphous ice and liquid water.

But a more serious problem with this thermodynamic interpretation was pointed out by Debenedetti in 2003 [12]. He argues, that a retracing spinodal must intersect the metastable continuation of the vapor-liquid equilibrium curve. As any point in the (P, T) plane along a phase coexistence locus corresponds to two different densities, here liquid and vapor, and as the spinodal is a locus of liquid state points, the intersection of the two lines must correspond to the same liquid state. This can only be possible if the spinodal and the binodal coincide, which implies a critical point. There is no experimental evidence that such a point exists, although a metastable lower critical point for water's vapor-liquid transition cannot be ruled out completely.

This problem does in fact only arise, if the spinodal retraces to positive pressures. A number of water models exist, in which the spinodal is retracing but does not extend to positive pressure and is superseded by a locus of limits of stability of the supercooled liquid with respect to the solid phase.

Singularity-free scenario

Sastry et al [8] considered the thermodynamic constraints imposed by the existence of a negatively-sloped TMD in the absence of a retracing liquid-gas spinodal and thus developed the singularity-free scenario, for the proposed phase diagram see figure 1.2(b). They derived a relation between the temperature dependence on κ_T and the slope of the TMD

$$\left(\frac{\partial \kappa_T}{\partial T}\right)_{P,TMD} = \frac{1}{V}\frac{\partial^2 V/\partial T^2}{(\partial P/\partial T)_{TMD}}. \tag{1.9}$$

Thus it follows that where the TMD has negative slope in the (P, T) plane, κ_T increases on cooling. Sastry et al show that given the assumption that the TMD locus does not extend beyond T_C and that there is no retracing behavior of the spinodal, it is inevitable that the TMD locus and the locus of κ_T extrema meet. Following from eq. 1.9 the slope of the TMD locus is infinite at this point and the TMD changes slope. In addition to the κ_T minimum at higher temperatures there develops a κ_T maximum at low temperatures. The singularity-free scenario demonstrates that broad thermodynamic features of anomalous behavior can neither be used to support singular behavior nor to distinguish between scenarios involving singularities and those that do not. X-ray data at small angles could be used to differentiate between a singular and singularity-free scenario, as a singular interpretation requires a divergence at $q = 0$ as $T \rightarrow T_S$. This is because the structure factor $S(q = 0)$ depends directly on κ_T

$$S(q = 0) = k_B T N \rho \kappa_T \tag{1.10}$$

Critical-point scenario The idea of the Critical-point scenario was developed by Poole et al [10] in 1992 motivated by computer simulations of ST2 water, where instead of a retracing spinodal they found evidence for a second critical point. The proposed phase diagram is pictured in figure 1.2(c). The line of first-order phase transitions between HDA and LDA, F, extends into the experimentally inaccessible region, where it ends in a second critical point, T_{C_2}. Here the phase transition locus has a negative slope, as the high-density phase is also the one with the largest entropy. This idea was further investigated in [11]. They found that in the simulations of ST2, SPC/E and TIP4P water the density maximum line changes slope in the region of $P < 0$ and the spinodal is not re-entrant. On further investigation they observed inflections in the isotherms that become stronger at lower T and end in an apparent critical isotherm that for real water should be located at $T = 185$ K and $P = 120$ Pa. If this critical point exists then there should be two phases with the same symmetry and a coexistence line between them. In order to characterize these two phases they study the structure of the liquid at a temperature close to but lower than T_{C_2} at two densities far from the critical density. They find, that the two structures resemble the two amorphous ices, HDA and LDA. They are also able to perform both the forward and reverse transformations from LDA to HDA in their simulations. The fragile to strong liquid transformation occurring during hyperquenching of liquid water can be explained as the passage from the equilibrium liquid (fragile) through the neighborhood of the critical point to the region dominated by LDA ice (strong). There is some experimental support for the critical-point scenario [46]. In their experiments Mishima and Stanley observed a sharp change in the slope of the melting curve of metastable ice IV in the region where it would intersect the presumed line of first-order liquid-liquid phase transition. Since the solid phase does not undergo an abrupt change along its melting line, the sudden change in slope corresponds to a change in the nature of the liquid phase into which the solid melts. As it is impossible to distinguish a sharp change from a discontinuous one this experimental evidence is also in agreement with the singularity-free scenario. Thus although there is no definitive experimental prove of the critical-point scenario, it has the advantage, that it does not only explain the anomalous behavior of liquid water, but also the occurrence of multiple amorphous ices and the fragile to strong transition.

Brovchenko and Oleinikova [2] point out, that there are two qualitatively different scenarios possible, where the liquid-liquid critical point is either at positive or at negative pressure. The first scenario is the same as imagined by Poole et al and described above. Here the anomalous behavior of liquid water along the liquid-vapor coexistence line is attributed to the crossing of the Widom line. The second scenario is somewhat different and does not involve the Widom line. The liquid-liquid and the liquid-vapor transitions cross at a triple point and vapor coexists with two different liquid phases. At this temperature, liquid water undergoes a first-order phase transition to strongly tetrahedral water upon cooling along the liquid-vapor coexistence curve. As this strongly tetrahedral liquid water is very similar to hexagonal ice it is assumably much less stable with respect to freezing and leads to immediate nucleation. Thus the temperature of homogeneous nucleation can be attributed to the liquid-liquid-vapor triple point and the line $T_H(P)$ to the line of the liquid-liquid phase transition. The apparent singularity at ambient pressure can then be attributed to the spinodal of the liquid-liquid transition. In a second step this scenario can be combined with the retracing spinodal picture as shown in figure 1.2(d). If the second critical point is located at strongly negative pressures, where the liquid is unstable with respect to evaporation, the liquid-vapor spinodal continuously crosses over to the liquid-liquid spinodal upon cooling. (With regards to the MD simulations in Brovchenko's and Oleinikova's paper, it is also interesting to note, that the inclusion of long-range electrostatics seems to be enough, to shift the critical point from negative to positive pressures.)

Critical-point free scenario

The critical-point free scenario was first introduced by Angell in 2008 [47]. He hypothesizes an order-disorder transition with a possible weak first-order transition character, separating two liquid phases and extending to $P < 0$ down to the superheated limit of stability of liquid water. This scenario predicts a continuous line of stability limit spanning the superheated, stretched and supercooled state, similar to the retracing spinodal scenario. But here the spinodal associated with the first-order transition will intersect the liquid-gas spinodal at negative pressure. There is no critical point present in this scenario, see figure 1.3. It does however explain the weakness of the glass transition observed in water, as well as the fragile-to-strong transition of supercooled water.

Connection between the different scenarios

Two papers were published showing, that it is possible to go from one scenario to another by continuous change of the parameters in model systems. Poole et al [48] investigate an extension of the van der Waals equation which incorporates the effects of the network of hydrogen bonds. By changing the energy of the H-bonds it is possible to change from the critical-point scenario to the retracing spinodal one. Stokely et al [49] are able to connect three different scenarios by varying the strength of the directional component of the hydrogen bond and the strength of the cooperative component of the hydrogen bond of their microscopic cell model. They can thus move between the singularity free scenario, the critical point free scenario with retracing spinodal and the critical-point scenario with the critical point at positive and negative pressure.

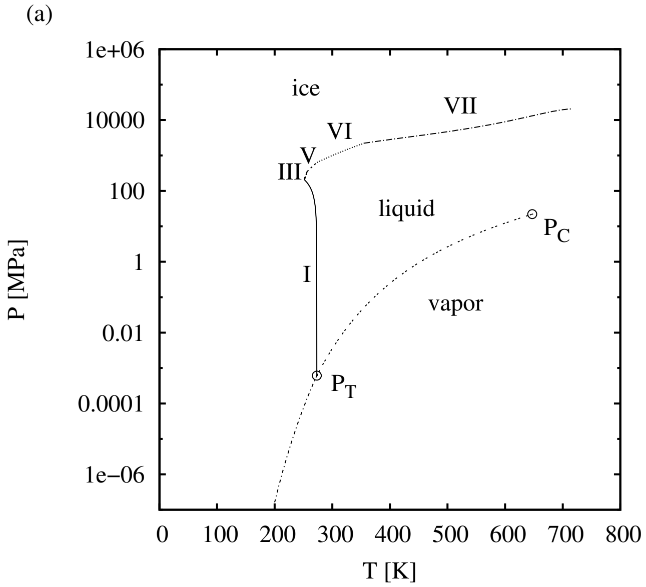

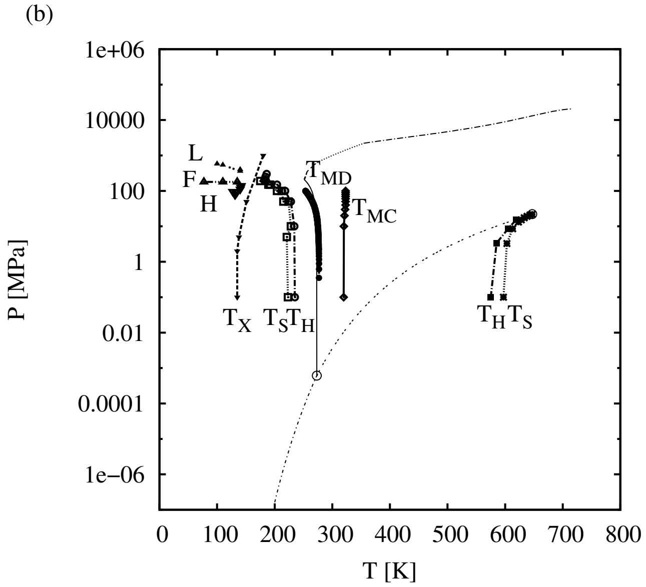

Figure 1.1.: Different aspects of the experimental phase diagram of water (a) Simple phase diagram of water, showing the melting curves of the different ice forms that coexist with liquid water (I,III,V,VI,VII), the triple point, P_T, and the liquid-vapor critical point, P_C, ([41] p.398-401). (b) Additionally shown are the line of maximum density, T_{MD}, and of minimal isothermal compressibility, T_{MC}, [44], the spinodal (limit of stability), T_S, and the homogeneous nucleation line (kinetic limit of stability), T_H, [7] as well as the crystallization temperature, T_X, [42]. F denotes the line of first-order phase transitions that separates the high-density and low-density amorphous ices HDA and LDA ([42] fig. 8). The curves denoted L and H are the limits of metastability of the HDA and LDA phases, respectively ([43] fig. 8).

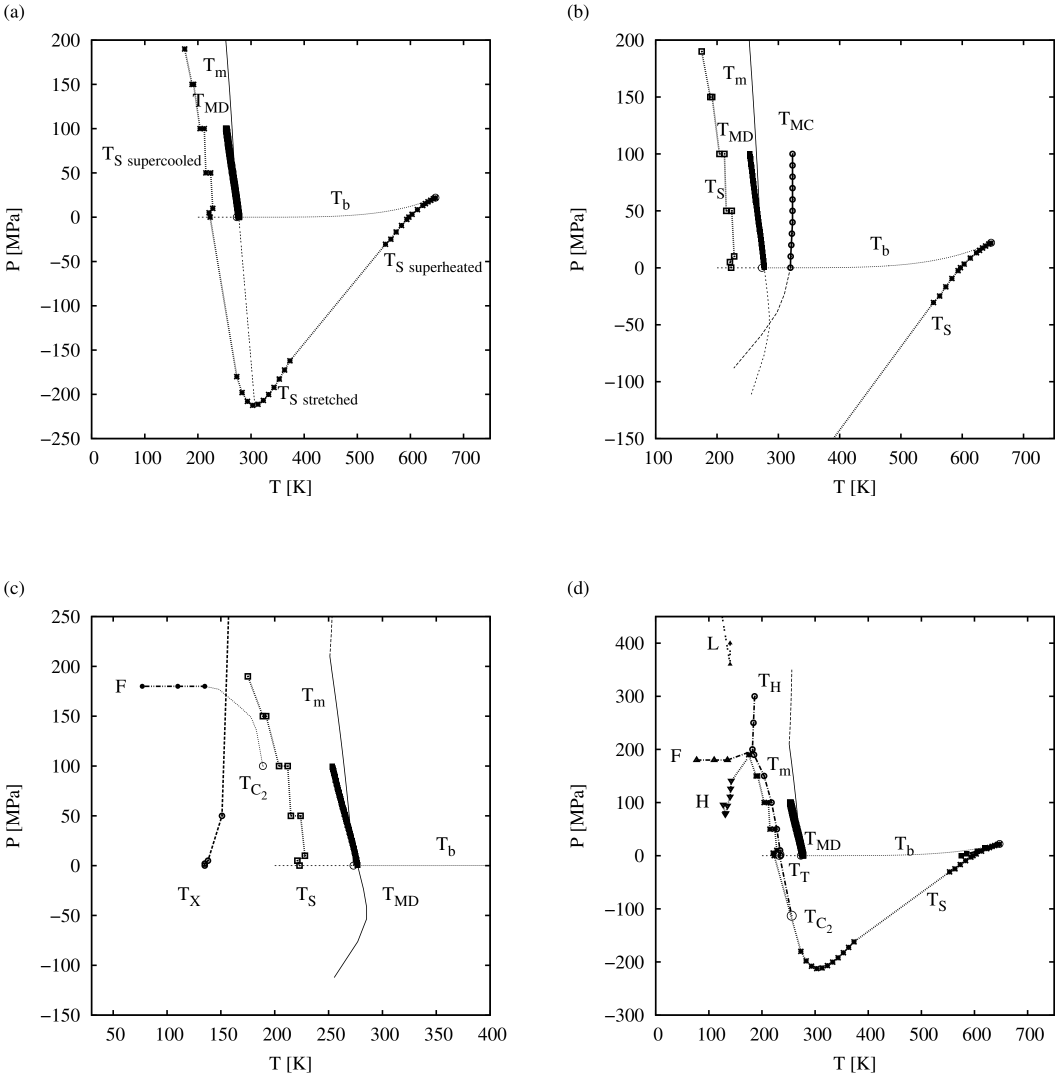

Figure 1.2.: Different scenarios for the phase diagram of water: (a) Stability-limit conjecture: The estimated limits of stability, T_S, for supercooled, stretched and superheated water are conjunct (T_m =melting line, T_b =boiling line). Additionally shown is the line of maximum density, T_{MD}. (b) Singularity-free scenario: The line of maximum density, T_{MD}, retraces on meeting the line of minimal isothermal compressibility, T_{MC}. (c) Critical-point scenario: The line of first-order phase transitions between HDA and LDA, F, extends into the "no man's land" and ends in a second critical point, T_{C_2}. (d) Critical-point scenario with T_{C_2} at strongly negative pressures: The line of first-order phase transitions between HDA and LDA, F, crosses over to the homogeneous nucleation line, T_H, while the spinodal of the HDA → LDA transition, H, is connected to the retracing spinodal, T_S.

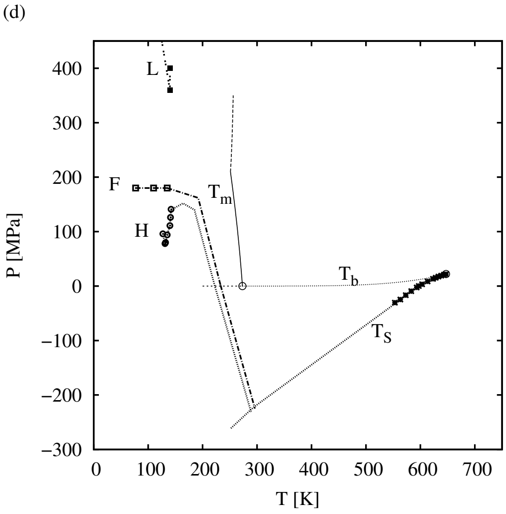

Figure 1.3.: Critical-point free scenario: The HDL-LDL coexistence line, F, extends to the superheated liquid region at $P < 0$. The superheated liquid-to-gas spinodal, T_S, and the supercooled HDL-to-LDL spinodal, H, join and give a re-entrant behavior similar to that in the retracing spinodal scenario.

Bibliography

[1] Tlusty T and Safran S A. Defect-induced phase separation in dipolar fluids. *Science*, 290(5495):1328–31, 2000.

[2] Brovchenko I and Oleinikova A. Multiple phases of liquid water. *ChemPhysChem*, 9(18):2660–75, 2008.

[3] Bernal J D and Fowler R H. A theory of water and ionic solution, with particular reference to hydrogen and hydroxyl ions. *J. Chem. Phys.* , 1(8):515–48, 1933.

[4] Mishima O, Calvert L D, and Whalley E. An apparently first-order transition between two amorphous phases of ice induced by pressure. *Nature*, 314:76–8, 1985.

[5] Speedy R J and Angell C A. Isothermal compressibility of supercooled water and evidence for a thermodynamic singularity at -45°C. *J. Chem. Phys.* , 65(3):851–8, 1976.

[6] Angell C A, Sichina W J, and Oguni M. Heat capacity of water at extremes of supercooling and superheating. *J. Phys. Chem.* , 86(6):998–1002, 1982.

[7] Speedy R J. Stability-limit conjecture. an interpretation of the properties of water. *J. Phys. Chem.* , 86(6):982–91, 1982.

[8] Sastry S, Debenedetti P G, Sciortino F, and Stanley H E. Singularity-free interpretation of the thermodynamics of supercooled water. *Phys. Rev. E*, 53(6):6144–54, 1996.

[9] Rebelo L P N, Debenedetti P G, and Sastry S. Singularity-free interpretation of the thermodynamics of supercooled water. II. thermal and volumetric behavior. *J. Chem. Phys.* , 109(2):626–33, 1998.

[10] Poole P H, Sciortino F, Essmann U, and Stanley H E. Phase behaviour of metastable water. *Nature*, 360(6402):324–8, 1992.

[11] Stanley H E, Angell C, Essman U, Hemmati P, and Poole P. Is there a second critical point in liquid water. *Physica A*, 205:122–39, 1994.

[12] Debenedetti P G. Supercooled and glassy water. *J. Phys.: Condens. Matter* , 15(45):R1669–R1726, 2003.

[13] Ricci M A, Bruni F, and Giuliani A. Similarities between confined and supercooled water. *Faraday Discuss.*, 141:347–58, 2009.

[14] Brovchenko I, Geiger A, and Oleinikova A. Liquid-liquid phase transitions in supercooled water studied by computer simulations of various water models. *J. Chem. Phys.* , 123(4):44515–31, 2005.

[15] Winkel K, Elsaesser M S, Mayer E, and Loerting T. Water polyamorphism: Reversibility and (dis)continuity. *J. Chem. Phys.* , 128(4):044510–6, 2008.

[16] Yan Z, Buldyrev S V, Kumar P, Giovambattista N, and Stanley H E. Correspondence between phase diagrams of the TIP5P water model and a spherically symmetric repulsive ramp potential with two characteristic length scales. *Phys. Rev. E*, 77(4):042201–4, 2008.

[17] Yan Z, Buldyrev S V, Kumar P, Giovambattista N, Debenedetti P G, and Stanley H E. Structure of the first- and second-neighbor shells of simulated water: Quantitative relation to translational and orientational order. *Phys. Rev. E*, 76(5):051201–5, 2007.

[18] Hartke B. Morphing lennard–jones clusters to tip4p water clusters: Why do water clusters look like they do? *Chemical Physics*, 346(1-3):286–94, 2008.

[19] Ludwig R. Water: From clusters to the bulk. *Angew. Chem. Int. Ed.*, 40(10):1808–27, 2001.

[20] Stewart G W. X-Ray diffraction in water: The nature of molecular association. *Phys. Rev.* , 37(1):9–16, 1931.

[21] Morgan J and Warren B E. X-Ray analysis of the structure of water. *J. Chem. Phys.* , 6(11):666–73, 1938.

[22] Narten A H, Danford M D, and Levy H A. X-ray diffraction study of liquid water in the temperature range 4-200°C. *Discuss. Faraday Soc.*, 43:97–107, 1967.

[23] Nishikawa K and Kitagawa N. X-Ray diffraction study of liquid water. *Bull. Chem. Soc. Jpn.*, 53(10):2804–8, 1980.

[24] Corban R and Zeidler M D. X-ray investigation of supercooled water. *Ber. Bunsenges. Phys. Chem.*, 96(10):1463–7, 1992.

[25] Hura G, Sorenson J M, Glaeser R M, and Head-Gordon T. A high-quality x-ray scattering experiment on liquid water at ambient conditions. *J. Chem. Phys.* , 113(20):9140–8, 2000.

[26] Hura G, Russo D, Glaeser R M, Head-Gordon T, Krack M, and Parrinello M. Water structure as a function of temperature from x-ray scattering experiments and ab initio molecular dynamics. *Phys. Chem. Chem. Phys.*, 5(10):1981–91, 2003.

[27] Yokoyama H, Kannami M, and Kanno H. Existence of clathrate-like structures in supercooled water: X-ray diffraction evidence. *Chem. Phys. Lett.*, 463(1-3):99–102, 2008.

[28] Guse C, Simionescu A, Schünemann B, Hentschke R, and Bomsdorf H. Temperature-dependent structure of liquid water investigated by means of energy-dispersive x-ray diffraction and molecular dynamics simulations. *Journal of Physics: Condensed Matter*, 22:325105–14, 2010.

[29] Bosio L, Teixeira J, and Eugene Stanley H. Enhanced density fluctuations in supercooled H2O, D2O, and Ethanol-Water solutions: Evidence from Small-Angle X-Ray scattering. *Phys. Rev. Lett.* , 46(9):597–600, 1981.

[30] Michielsen J C F, Bot A, and van der Elsken J. Small-angle x-ray scattering from supercooled water. *Phys. Rev. A*, 38(12):6439–41, 1988.

[31] Huang C, Wikfeldt K T, Tokushima T, Nordlund D, Harada Y, Bergmann U, Niebuhr M, Weiss T M, Horikawa Y, Leetmaa M, Ljungberg M P, Takahashi O,

Lenz A, Ojamae L, Lyubartsev A P, Shin S, Pettersson L G M, and Nilsson A. The inhomogeneous structure of water at ambient conditions. *Proc. Natl. Acad. Sci. U.S.A.*, 106(36):15214–8, 2009.

[32] Clark G N I, Hura G L, Teixeira J, Soper A K, and Head-Gordon T. Small-angle scattering and the structure of ambient liquid water. *Proc. Natl. Acad. Sci. USA*, 107(32):14003–8, 2010.

[33] Wernet P, Nordlund D, Bergmann U, Cavalleri M, Odelius M, Ogasawara H, Naslund L A, Hirsch T K, Ojamae L, and Glatzel P. The structure of the first coordination shell in liquid water. *Science*, 304(5673):995–9, 2004.

[34] Smith J D, Cappa C D, Messer B M, Drisdell W S, Cohen R C, and Saykally R J. Probing the local structure of liquid water by x-ray absorption spectroscopy. *J. Phys. Chem. B*, 110(40):20038–45, 2006.

[35] Holt J K. Methods for probing water at the nanoscale. *Microfluidics and Nanofluidics*, 5(4):425–42, 2008.

[36] Ashihara S, Huse N, Espagne A, Nibbering E T J, and Elsaesser T. Ultrafast structural dynamics of water induced by dissipation of vibrational energy. *J. Phys. Chem. A*, 111(5):743–6, 2007.

[37] Wernet Ph, Gavrila G, Godehusen K, Weniger C, Nibbering E, Elsaesser T, and Eberhardt W. Ultrafast temperature jump in liquid water studied by a novel infrared pump-x-ray probe technique. *Appl. Phys. A*, 92(3):511–16, 2008.

[38] Cavagna A. Fragile vs. strong liquids: A saddles-ruled scenario. *Europhys. Lett.*, 53(4):490–6, 2001.

[39] Kumar P, Buldyrev S V, and Stanley H E. Dynamic crossover and Liquid-Liquid critical point in the TIP5P model of water. *Soft Matter Under Exogenic Impacts*, pages 23–33, 2007.

[40] Angell C A, Bressel R D, Hemmati M, Sare E J, and Tucker J C. Water and its anomalies in perspective: tetrahedral liquids with and without liquid-liquid phase transitions. invited lecture. *Phys. Chem. Chem. Phys*, 2(8):1559–66, 2000.

[41] Wagner W and Pruß A. The IAPWS formulation 1995 for the thermodynamic properties of ordinary water substance for general and scientific use. *J. Phys. Chem. Ref. Data*, 31:387–535, 2002.

[42] Loerting T and Giovambattista N. Amorphous ices: experiments and numerical simulations. *J. Phys.: Condens. Matter* , 18:R919–R977, 2006.

[43] Gromnitskaya E L, Stal'gorova O V, Brazhkin V V, and Lyapin A G. Ultrasonic study of the nonequilibrium pressure-temperature diagram of H2O ice. *Phys. Rev. B*, 64(9):094205–16, 2001.

[44] Fine R A and Millero F J. Compressibility of water as a function of temperature and pressure. *J. Chem. Phys.* , 59(10):5529–37, 1973.

[45] Ahlers G. *The Physics of liquid and solid Helium*, chapter 2. Part I (edited by KH Bennemann and JB Ketterson) New York: John Wiley and Sons, 1976.

[46] Mishima O and Stanley H E. Decompression-induced melting of ice IV and the liquid-liquid transition in water. *Nature*, 392(6672):164–8, 1998.

[47] Angell A C. Insights into Phases of Liquid Water from Study of Its Unusual Glass-Forming Properties. *Science*, 319(5863):582–7, 2008.

[48] Poole P H, Sciortino F, Grande T, Stanley H E, and Angell C A. Effect of hydrogen bonds on the thermodynamic behavior of liquid water. *Phys. Rev. Lett.* , 73(12):1632–1635, 1994.

[49] Stokely K, Mazza M G, Stanley H E, and Franzese G. Effect of hydrogen bond cooperativity on the behavior of water. *Proc. Natl. Acad. Sci. USA*, 107(4):1301–6, 2010.

2. Methods

In this chapter we want to explain the theoretical and computational methods that where instrumental to perform our simulations. First we will describe the different geometries of the classical water models that are used and introduce the coordinate system to describe the position and orientation of the molecules. Subsequently the different simulation algorithms and the computation of energies, forces and pressure will be described, including the way polarizability was implemented. Then finally we can discuss the limitations of classical water models and explain which models we chose and why. Therefore first simulation results will be presented in order to test our implementation and to characterize the models according to their thermodynamic and transport properties.

Finally the computation of the chemical potential and the characteristics of the carbon nanotubes will be explained, which we need for the water simulations in confinement.

2.1. Water models

In this thesis we only consider rigid classical water models. The limitations that are associated with this choice will be discussed in section 2.6. For now we just want to introduce the different geometries.

We will only use water models of the TIPnP (transferable intermolecular potential n point) type. The n stands for the number of interaction sites. The geometry is close to actual water with a bond length of 0.9572 Å and a bond angle of 104.52°. Usually there is a LJ interaction site on the oxygen and two positive charges on the hydrogen atoms. The main difference between the different models is the location of the negative charge or charges. As a TIP3P water model only has 3 interaction sites the negative charge is placed on the oxygen atom.

The TIP4P geometry is planar with an additional massless interaction site located on the symmetry axis between the hydrogen atoms close to the oxygen. A negative charge is placed on this dummy site balancing the positive charges on the hydrogens.

In case of TIP5P water the negative charge is distributed on two massless dummy sites, that are arranged in a near tetrahedral geometry with the hydrogen atoms. The TIP4P and TIP5P geometry are pictured in figure 2.1.

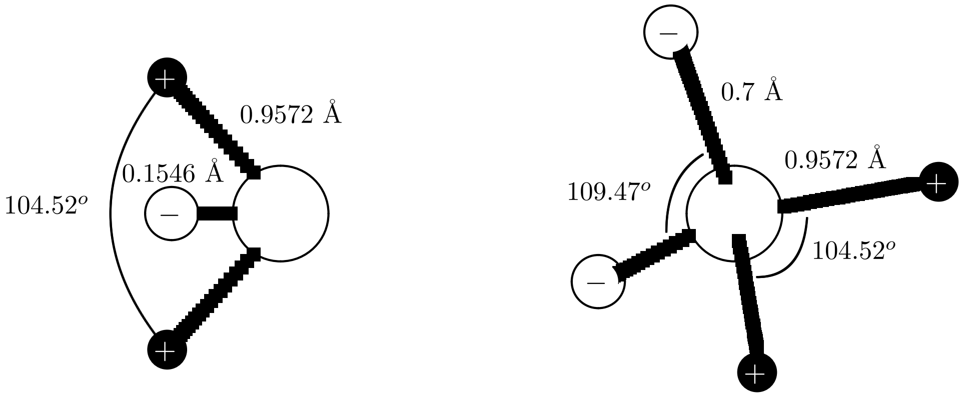

Figure 2.1.: The TIP4P (left) and the TIP5P (right) geometry.

2.1.1. Orientation representation by quaternions

As we want to simulate the dynamics of rigid bodies the first intuitive approach would be to represent the orientation of the molecules by Euler angles. We start with a body fixed frame, chosen thus that the molecule lies in the x-y plane and the origin is on the O-atom .The atom positions are given by:

$$\vec{x}_O = \begin{pmatrix} 0 \\ 0 \\ 0 \end{pmatrix} \qquad \vec{x}_{H_1} = l \cdot \begin{pmatrix} \cos(\beta) \\ \sin(\beta) \\ 0 \end{pmatrix} \qquad \vec{x}_{H_2} = l \cdot \begin{pmatrix} -\cos(\beta) \\ \sin(\beta) \\ 0 \end{pmatrix} . \tag{2.1}$$

Here $\beta = \pi - \alpha/2$ and α is the angle enclosed by the three atoms of the molecule. The center of gravity can now be calculated easily

$$\frac{2lm_H \sin(\alpha/2)}{m_O + 2m_H} \begin{pmatrix} 0 \\ 1 \\ 0 \end{pmatrix} \tag{2.2}$$

and we can shift our body fixed frame so that the center of gravity lies in the origin.

$$\begin{aligned} \vec{x}_O &= -2l \sin(\alpha/2) \frac{m_H}{m_O + 2m_H} \begin{pmatrix} 0 \\ 1 \\ 0 \end{pmatrix} && (2.3) \\ \vec{x}_{H_1} &= l \cdot \begin{pmatrix} -\cos(\alpha/2) \\ m_O/(m_O + 2m_H) \sin(\alpha/2) \\ 0 \end{pmatrix} && (2.4) \\ \vec{x}_{H_2} &= l \cdot \begin{pmatrix} \cos(\alpha/2) \\ m_O/(m_O + 2m_H) \sin(\alpha/2) \\ 0 \end{pmatrix} && (2.5) \end{aligned}$$

Thus the moment of inertia is given by:

$$I^{(b)} = 2l^2 M \begin{pmatrix} \delta_O \delta_H \sin^2(\gamma) & 0 & 0 \\ 0 & \delta_H \cos^2(\gamma) & 0 \\ 0 & 0 & \delta_O \delta_H \sin^2(\gamma) + \delta_H \cos^2(\gamma) \end{pmatrix} , \tag{2.6}$$

where $M = m_O + 2m_H$, $\delta_O = m_O/M$, $\delta_H = m_H/M$ and $\gamma = \alpha/2$. Now the principal axes of the molecule are in agreement with those of the body fixed frame. All quantities in the space fixed frame will be denoted by an (s) and the ones in the body fixed frame by a (b).

We now want to describe the rotation of a molecule by the angular velocity $\vec{\omega}^{(b)}$ in the body fixed frame, which expressed by Euler angles is given by

$$\vec{\omega}^{(b)} = \begin{pmatrix} \cos(\psi) & \sin(\theta)\sin(\psi) & 0 \\ -\sin(\psi) & \sin(\theta)\cos(\psi) & 0 \\ 0 & \cos(\theta) & 1 \end{pmatrix} \begin{pmatrix} \dot{\theta} \\ \dot{\phi} \\ \dot{\psi} \end{pmatrix} . \tag{2.7}$$

The determinant of this matrix becomes zero for $\theta = 0, \pi$, which leads to singularities and makes numerical integration inefficient. Evans noticed that one needs a parameter space of at least 4 dimensions in order to remove the singularities and recommanded a quaternion formulation that also simplifies the equation of motion [1].

The quaternion parameters $\mathbf{q} = (\chi, \eta, \xi, \zeta)$ can be defined in terms of the Euler angles by

$$\left.\begin{aligned} \chi &= \cos(\theta/2)\cos((\phi+\psi)/2) \\ \eta &= \sin(\theta/2)\cos((\phi-\psi)/2) \\ \xi &= \sin(\theta/2)\sin((\phi-\psi)/2) \\ \zeta &= \cos(\theta/2)\sin((\phi+\psi)/2) \end{aligned}\right\} \tag{2.8}$$

From equation 2.8 it can be seen that the quaternions are not independent but satisfy the relation

$$\chi^2 + \eta^2 + \xi^2 + \zeta^2 = 1\,. \tag{2.9}$$

One can now describe the orientation of a molecule in the space fixed frame by multiplying $\vec{x}_O$, $\vec{x}_{H_1}$ and $\vec{x}_{H_2}$ by the inverse of the transformation matrix A.

$$\vec{x}^{(s)} = A^{-1}\vec{x}^{(b)} \tag{2.10}$$

with

$$A = \begin{pmatrix} \chi^2+\eta^2-\xi^2-\zeta^2 & 2(\eta\xi+\chi\zeta) & 2(\eta\zeta-\chi\xi) \\ 2(\eta\xi-\chi\zeta) & \chi^2-\eta^2+\xi^2-\zeta^2 & 2(\xi\zeta+\chi\eta) \\ 2(\eta\zeta+\chi\xi) & 2(\xi\zeta-\chi\eta) & \chi^2-\eta^2-\xi^2+\zeta^2 \end{pmatrix} \tag{2.11}$$

A can be computed much faster from the quaternions than from the Euler angles as the equation does not involve any trigonometric functions. The angular velocity $\vec{\omega}$ is related to the quaternions by the matrix equation

$$\dot{\mathbf{q}} = \begin{pmatrix} \dot{\chi} \\ \dot{\eta} \\ \dot{\xi} \\ \dot{\zeta} \end{pmatrix} = \frac{1}{2}S(q)\boldsymbol{\omega} \tag{2.12}$$

with

$$S(q) = \begin{pmatrix} \chi & -\eta & -\xi & -\zeta \\ \eta & \chi & -\zeta & \xi \\ \xi & \zeta & \chi & -\eta \\ \zeta & -\xi & \eta & \chi \end{pmatrix} \quad \text{and} \quad \boldsymbol{\omega} = \begin{pmatrix} 0 \\ \omega_x \\ \omega_y \\ \omega_z \end{pmatrix}. \tag{2.13}$$

The equations of motion are now free of singularities as the 4x4 matrix is orthonogal and its inverse easy to find. Another relation follows directly from equation 2.9.

$$\mathbf{q}\cdot\dot{\mathbf{q}} = \chi\dot{\chi} + \eta\dot{\eta} + \xi\dot{\xi} + \zeta\dot{\zeta} = 0 \tag{2.14}$$

For the second time derivative of the quaternions one finds

$$\ddot{\mathbf{q}} = \frac{1}{2}S(q)\dot{\boldsymbol{\omega}} - s\mathbf{q} \quad \Leftrightarrow \tag{2.15}$$

$$\begin{pmatrix} \ddot{\chi} \\ \ddot{\eta} \\ \ddot{\xi} \\ \ddot{\zeta} \end{pmatrix} = \begin{pmatrix} \frac{1}{2}(-\eta\dot{\omega}_x - \xi\dot{\omega}_y - \zeta\dot{\omega}_z) - \chi s \\ \frac{1}{2}(\chi\dot{\omega}_x - \zeta\dot{\omega}_y + \xi\dot{\omega}_z) - \eta s \\ \frac{1}{2}(\zeta\dot{\omega}_x + \chi\dot{\omega}_y - \eta\dot{\omega}_z) - \xi s \\ \frac{1}{2}(-\xi\dot{\omega}_x + \eta\dot{\omega}_y + \chi\dot{\omega}_z) - \zeta s \end{pmatrix} \tag{2.16}$$

(2.17)

with $s = \dot{\chi}^2 + \dot{\eta}^2 + \dot{\xi}^2 + \dot{\zeta}^2$. Now that we have found a way to represent the orientation of each molecule by $\mathbf{q}$ in addition to its position that is defined by the coordinates of its center of mass $\vec{r}$, we can look at the different algorithms used in this work.

2.2. MD and MC algorithms

There are two big classes of algorithms MD (Molecular Dynamics) and MC (Monte Carlo) algorithms, which are suitable for different setups. While the MD method is based on the integration of the discretized equations of motion, the MC method statistically generates configurations according to the distribution that is required by the investigated ensemble. The MD method has the advantage, that it provides dynamic information about the system, but has the drawback that the finite time step in the integration renders it not exact. The MC method provides an exact algorithm which can describe ensembles with varying particle number but does not contain dynamic information about the system. Hybrid algorithms that combine MD and MC algorithms are capable to eliminate most of the drawbacks each individual method possesses.

2.2.1. MD algorithm

In a MD simulation the equations of motion are integrated numerically for small time steps Δt and a fixed number of particles N, thus leading to a deterministic algorithm. In this work we will use the velocity-verlet algorithm.

$$\vec{r}(t+\Delta t) = \vec{r}(t) + \Delta t \vec{v}(t) + \frac{1}{2}\Delta t^2 \vec{a}(t) + O(\Delta t^4) \tag{2.18}$$

$$\vec{v}(t+\Delta t) = \vec{v}(t) + \frac{1}{2}\Delta t \left(\vec{a}(t) + \vec{a}(t+\Delta t)\right) + O(\Delta t^3) \tag{2.19}$$

Here $\vec{v}(t) = d\vec{r}(t)/dt$ and $\vec{a}(t) = d\vec{v}(t)/dt$. This integration scheme is reversible in time and symplectic i. e. it does preserve the phase space exactly which is why it is so popular. It's memory demand is also low.

In order to integrate the equation of motion for the rotational degrees of freedom Omelyan [2] introduced a version of the quaternion approach within the Verlet algorithm in velocity form based on a formulation of the quaternion dynamics with constraints.

We start with the integration scheme for $\mathbf{q}$.

$$q_\alpha(t+\Delta t) = q_\alpha(t) + \dot{q}_\alpha(t)\Delta t + \frac{1}{2}\ddot{q}_\alpha \Delta t^2 - \lambda q_\alpha \Delta t^2 + O(\Delta t^3) \tag{2.20}$$

with $\lambda \Delta t^2 = 1 - 1/2 s_1 \Delta t^2 - \sqrt{1 - s_1 \Delta t^2 - s_2 \Delta t^3 - (s_3 - s_1^2)\Delta t^4/4}$, where $s_1 = \dot{q}_\alpha(t)\dot{q}_\alpha(t)$, $s_2 = \dot{q}_\alpha(t)\ddot{q}_\alpha(t)$ and $s_3 = \ddot{q}_\alpha(t)\ddot{q}_\alpha(t)$. Here $-2q_\alpha\lambda$ is an additional force introduced to constrain the orientational matrices to orthonormal form and thus to guarantee exact rigidity. The Lagrange parameter λ is defined from the constraint relation $q_\alpha^2(t+\Delta t) - 1 = 0$.

To construct the integration scheme for ω, we start with the Euler equation of motions.

$$I_\alpha \frac{\omega_\alpha}{dt} = N_\alpha(t) + (I_\beta - I_\gamma)\omega_\beta(t)\omega_\gamma(t) \tag{2.21}$$

Here $(a, b, \gamma) = (1, 2, 3)$, $(2, 3, 1)$, and $(3, 1, 2)$ and I_x, I_y and I_z are the moments of inertia along the principal axes of the molecule (see equation 2.6) and $\vec{N}$ is the torque exerted on the molecule with respect to its center of mass due to the interactions with the other molecules. Inserting equation 2.21 into the expansion

$$\omega_\alpha\left(t+\frac{\Delta t}{2}\right) = \omega_\alpha\left(t-\frac{\Delta t}{2}\right) + \frac{\Delta t}{2}\left[\dot{\omega}_\alpha\left(t-\frac{\Delta t}{2}\right) + \dot{\omega}_\alpha\left(t+\frac{\Delta t}{2}\right)\right] + O(\Delta t^3)$$

leads to

$$\begin{aligned}\omega_\alpha\left(t+\frac{\Delta t}{2}\right) &= \omega_\alpha\left(t-\frac{\Delta t}{2}\right) + \frac{\Delta t}{I_\alpha}\left[N_\alpha(t) + (I_\beta - I_\gamma)\frac{1}{2}\cdot\right. \\ &\left.\left[\omega_\beta\left(t-\frac{\Delta t}{2}\right)\omega_\gamma\left(t-\frac{\Delta t}{2}\right) + \omega_\beta\left(t+\frac{\Delta t}{2}\right)\omega_\gamma\left(t+\frac{\Delta t}{2}\right)\right]\right]. \end{aligned} \tag{2.22}$$

The equation is simple and can be solved by iteration, starting with $\omega_\alpha(t + \Delta t/2) = \omega_\alpha(t - \Delta t/2)$.

In this form the MD algorithm generates configurations according the NVE ensemble, although there is a slight drift in energy due to its lack of exactness. As we want to perform the simulations of the unconfined system in the NPT ensemble in order to be close to the experiment, we have to control the temperature and the pressure during the simulation. This can be achieved by applying a thermostat and a barostat during the simulation.

Thermostat and barostat We will only control the translational temperature by adding an additional friction term as proposed by Berendsen [3] into the equation of motion

$$\ddot{\vec{r}} = \frac{1}{m}\vec{F} - \zeta\dot{\vec{r}} \quad \text{with} \tag{2.23}$$

$$\zeta = \frac{1}{2\tau_T}\left(1 - \frac{T_B}{T}\right) \tag{2.24}$$

The momentary temperature T is adjusted exponentially with relaxation time τ_T towards the target temperature T_B. As the Berendsen thermostat does not actually reproduce the canonical ensemble it is customary to choose the coupling as small as possible to avoid a too strong disturbance of the system.

For the pressure control we also choose the method proposed by Berendson, where the pressure adjustment happens exponentially with relaxation time $\tau_P = \kappa_T/\alpha_T$, where κ_T is the isothermal compressibility. The boxlength as well as the particle positions are scaled by a factor of $\mu = \Delta t\eta + 1$, while the equation of motion are changed in the following way.

$$\ddot{\vec{r}} = \frac{1}{m}\vec{F} - \eta\dot{\vec{r}} \quad \text{with} \tag{2.25}$$

$$\eta = -\frac{1}{3}\alpha_P(P_B - P) \tag{2.26}$$

We will use the MD algorithm for the simulations of the unconfined water systems and to gain information about the dynamics, e.g. diffusion, in the confined systems.

2.2.2. MC algorithm

The MC scheme shares with the MD algorithm the basic feature that a new configuration is generated from an existing configuration by an update step, but now the update is no longer deterministic but stochastic. This means that the transition from one state $[\psi]$ to the next one $[\psi']$ happens with the transition probability $\mathcal{P}([\psi'] \leftarrow [\psi])$. In order for the chain of generated configurations (Markov chain) to converge to the desired ensemble, the algorithm must posses several properties. On the one hand the update process must be ergodic, which means that all possible states of the system must be reached with a final probability $\mathcal{P}([\psi'] \leftarrow [\psi]) > 0$. On the other hand it must satisfy the condition of detailed balance, so that the desired ensemble with probability density W_c is an actual fixpoint of the transition probability.

$$\mathcal{P}([\psi'] \leftarrow [\psi])\, W_c[\psi] = \mathcal{P}([\psi] \leftarrow [\psi'])\, W_c[\psi'] \tag{2.27}$$

By accepting a new configuration with probability $\min\left(1, W_c[\psi']/W_c[\psi]\right)$ the MC algorithm does satisfy all these conditions. We will generate a new configuration by either the random insertion or removal of a molecule or by its random translational or rotational motion. Then we will accept the new configuration with the afore mentioned probability.

In order to apply the MC algorithm we have to generate random orientations for the insertion of a new molecule. We use the formalism developed by Marsaglia [4].

A schematic prescription of the procedure is shown below.

1. generate pairs of random numbers ξ_1, ξ_2 independent and uniform on (-1,1) until $S_1 = \xi_1^2 + \xi_2^2 < 1$;
2. do the same for pairs ξ_3, ξ_4 until $S_2 = \xi_3^2 + \xi_4^2 < 1$;
3. now the new orientation is given by the quaternion

$$\mathbf{q} = (\xi_1, \xi_2, \xi_3\sqrt{(1-S_1)/S_2}, \xi_4\sqrt{(1-S_1)/S_1})\,. \tag{2.28}$$

To compute the Metropolis criteria for insertion, removal and motion of water molecules we first look at the partition function in the grand-canonical ensemble, which is given by

$$Q = \sum_{N=0}^{\infty} \frac{1}{N!} \int \frac{d^{3N}r\, d^{3N}p\, d^{3N}n\, d^{3N}p_n}{h^{3N}h^{3N}} e^{-\beta(H-\mu N)}\,. \tag{2.29}$$

Changing to volume scaled coordinates ρ.

$$Q = \sum_{N=0}^{\infty} \frac{V^N}{N!} \int \frac{d^{3N}\rho\, d^{3N}p\, d^{3N}n\, d^{3N}p_n}{h^{3N}h^{3N}} e^{-\beta(E_{rot}+E_{trans}+U-\mu N)}\,. \tag{2.30}$$

The integration over the translational momentum variables can be performed easily

$$\frac{1}{h^{3N}} \int d^{3N}p\, \exp\left(-\beta \sum_{i=1}^{3N} p_i^2/(2m)\right) = \left(\frac{1}{\lambda_T}\right)^{3N}\,, \tag{2.31}$$

with $\lambda_T = \sqrt{(h^2\beta)/(2\pi m)}$ the thermal wave length. For the rotational part we evaluate

$$q_{rot} = \frac{1}{\sigma h^3} \int dp_\psi d\psi dp_\theta d\theta dp_\phi d\phi e^{-\beta E_{rot,i}} , \tag{2.32}$$

which with symmetry factor $\sigma = 2$ and $E_{rot,i} = \sum_{i=1}^{3N} 1/2 I_i \omega_i^2$ and $dn^3 = dp_\psi dp_\theta dp_\phi = I_1 I_2 I_3 sin\theta \, d\omega_1 d\omega_2 d\omega_3$ leads to

$$q_{rot} = \frac{4\pi^2}{h^3} \sqrt{I_1 I_2 I_3} \sqrt{\frac{2\pi}{\beta}}^3 = e^{-\beta\mu_{rot}} \tag{2.33}$$

Thus we can rewrite equation 2.30.

$$Q = \sum_{N=0}^{\infty} \frac{V^N}{N!} \left(\frac{1}{\lambda_T}\right)^{3N} \int d^{3N}\rho \, d^N\psi d^N\theta d^N\phi \left(\prod_{i=1}^{N} \frac{\sin\theta_i}{8\pi^2}\right) e^{-\beta(U-(\mu-\mu_{rot})N)} \tag{2.34}$$

Now we want to obtain the probability p of a certain configuration with random positions and random orientations, which will be computed according to procedure (2.28). As a random distribution of Euler angles does not generate an uniformly distributed set of orientations we have to correct with a factor $\sin\theta$ cancelling out the $\sin\theta$ from the integration over the rotational part. Thus we arrive at

$$p = \frac{V^N}{N!} \left(\frac{1}{\lambda_T}\right)^{3N} e^{-\beta(U-(\mu-\mu_{rot})N)} \tag{2.35}$$

Finally we can write down the Monte Carlo criteria for the insertion and removal as well as for a move or rotation of a molecule.

$$\min\left(1, \frac{p^{\text{new}}}{p^{\text{old}}}\right) \geq \xi \in (0,1) \tag{2.36}$$

$$\left(\frac{p^{\text{new}}}{p^{\text{old}}}\right)_{\text{ins}} = \frac{V}{(N+1)\lambda_T^3} e^{-\beta(U_{N+1}-U_N-(\mu-\mu_{rot})N)} \tag{2.37}$$

$$\left(\frac{p^{\text{new}}}{p^{\text{old}}}\right)_{\text{rem}} = \frac{N\lambda_T^3}{V} e^{-\beta(U_N-U_{N-1}+(\mu-\mu_{rot})N)} \tag{2.38}$$

$$\left(\frac{p^{\text{new}}}{p^{\text{old}}}\right)_{\text{mov}} = e^{-\beta(U_{new}-U_{old})} \tag{2.39}$$

2.2.3. Periodic boundary conditions and minimum image convention

As our simulated systems are quite small in comparison to their surface, we use periodic boundary conditions to mimic a large system and to reduce surface effects. For the pure water systems periodic boundary conditions are used for all three directions, for slits we use them in two for the tube in one direction. In order to compute the distance between particles the minimum image convention illustrated in figure 2.2 is applied, where always the nearest periodic image of the particle is used. Thus the new particle-particle distance in a rectangular box can be computed by

$$r_{\alpha,ij}^{\text{min}} = |r_{\alpha,ij} - L_\alpha \, \text{ANINT}\,(r_{\alpha,ij}/L_\alpha)| \ . \tag{2.40}$$

Thus the range of the potential is limited to half the box length. To reduce the computing time we cutoff the potential at a cutoff radius $r_{cut} < L/2$.

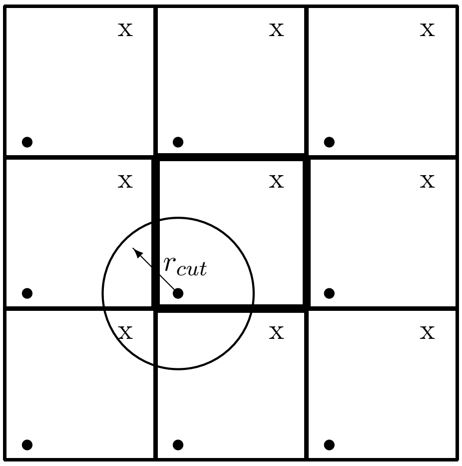

Figure 2.2.: Illustration of the minimum image convention.

2.3. Calculation of energies, forces and pressure

The potential energy U of all models used in this work consists of two parts. A short-ranged Lennard-Jones part which will be indicated by U^{LJ} and a long-ranged Coulomb part U^{c}. For the MC and MD simulations we need to compute energy, force, torque, temperature and pressure at each simulation step.

Temperature The temperature can be computed by applying the equipartition theorem. As there are 6 degrees of freedom in our case, 3 translational ones and 3 rotational ones, the temperature is given by the average kinetic energy $\langle K \rangle$ according to

$$\langle K \rangle = 3Nk_BT \,, \tag{2.41}$$

or if one wants to differentiate between the rotational and the translational temperatures

$$\begin{aligned}
\langle K_{rot} \rangle = \frac{1}{MN}\sum_{m=1}^{M}\sum_{n=1}^{N}\frac{1}{2}\omega_n^t I_n \omega_n &= 3/2Nk_BT_{rot} \\
\langle K_{trans} \rangle = \frac{1}{MN}\sum_{m=1}^{M}\sum_{n=1}^{N}\frac{1}{2}m_n v_n^2 &= 3/2Nk_BT_{trans} \,.
\end{aligned}$$

Here the sum over n and m signify the sum over molecules and over the configurations respectively. As we only control the translational temperature by the thermostat, it is a good test to check, that $T_{rot} = T_{trans}$ during the simulation.

Pressure The thermodynamic pressure is defined as

$$P = -\left(\frac{\partial F}{\partial V}\right)_{T,N} \quad \text{with} \tag{2.42}$$

$$Q_N(V,T) = e^{-\beta F} = \alpha \int\int d\Gamma\, e^{-\beta H} \tag{2.43}$$

$$= \alpha \int\int e^{-\beta H(\vec{r}^N,\vec{p}^N,\vec{n}^N,\vec{p}_n^N)}\, d\vec{r}^N\, d\vec{p}^N\, d\vec{n}^N\, d\vec{p}_n^N \tag{2.44}$$

Where N stands for the number of molecules, $\vec{r}$ and $\vec{p}$ for the center of mass and its momentum and $\vec{n}$ and $\vec{p_n}$ are the positions of the atoms relative to the center of mass and their impulses. α is a proportionality factor that won't be relevant.

If the potential is not explicitly volume dependent it is easy to compute the pressure with the help of the Anderson scaling relation for cubic systems $\vec{r}_{i\alpha,j\beta} = V^{1/3}\vec{\rho}_{ij} + \vec{n}_{i\alpha} - \vec{n}_{j\beta}$, where $\vec{\rho}_{ij}$ is a scaled and volume independent centre-of-mass–centre-of-mass vector between molecules i and j [5].

Thus one can rewrite the partition function as

$$\begin{aligned} Q_N(V,T) &= \alpha\, V^N \int\!\!\int e^{-\beta H(\vec{\rho}^N,\vec{p}^N,\vec{n}^N,\vec{p_n}^N)}\, d\vec{\rho}^N\, d\vec{p}^N\, d\vec{n}^N\, d\vec{p_n}^N && (2.45)\\ &= \alpha\, V^N \int\!\!\int d\Gamma'\, e^{-\beta H} && (2.46) \end{aligned}$$

Therefore the pressure is given by

$$\begin{aligned} P &= \beta^{-1} \left.\frac{\partial}{\partial V}\right|_{T,N} \ln\left[V^N \int\!\!\int d\Gamma'\, e^{-\beta(K+U)}\right] \\ &= \frac{N}{\beta V} + \beta^{-1} \left.\frac{\partial}{\partial V}\right|_{T,N} \ln\left[\int\!\!\int d\Gamma'\, e^{-\beta(K+U)}\right] \\ &= \frac{N}{\beta V} + \beta^{-1} \frac{\int\!\int d\Gamma'\,(-\beta)\left(\frac{\partial}{\partial V}U\right)\, e^{-\beta(K+U)}}{\int\!\int d\Gamma'\, e^{-\beta(K+U)}} \\ &= \frac{N}{\beta V} - \frac{\int\!\int d\Gamma\,\left(\frac{\partial}{\partial V}U\right)\, e^{-\beta(K+U)}}{\int\!\int d\Gamma\, e^{-\beta(K+U)}} \\ P &= \frac{N}{\beta V} - \left\langle \frac{\partial U}{\partial V} \right\rangle = \frac{N}{\beta V} - \mathcal{V}/(3V)\,, && (2.47) \\ & && (2.48) \end{aligned}$$

with the virial $\mathcal{V}$

$$\begin{aligned} \mathcal{V} &= 3V \left\langle \frac{\partial U}{\partial V} \right\rangle = 3V \left\langle \frac{1}{2} \sum_{i,j}^{N} \sum_{\alpha,\beta}^{M} \frac{\partial \vec{r}_{i\alpha,j\beta}}{\partial V} \cdot \vec{\nabla}_{\vec{r}_{i\alpha,j\beta}} U \right\rangle && (2.49) \\ &= 3V \left\langle \frac{1}{2} \sum_{i,j}^{N} \sum_{\alpha,\beta}^{M} \frac{1}{3V^{2/3}} \vec{\rho}_{ij} \cdot \vec{\nabla}_{\vec{r}_{i\alpha,j\beta}} U \right\rangle && (2.50) \\ &= -\left\langle \frac{1}{2} \sum_{i,j}^{N} \vec{r}_{ij} \cdot \vec{\mathcal{F}}_{ij} \right\rangle && (2.51) \end{aligned}$$

If the potential is explicitly volume dependent as is the case for the Ewald sum, additional terms will arise.

For non-homogeneous systems like water confined in slits and tubes we will compute the pressure tensor, as first derived from hydrodynamics by Irving and Kirkwood [6], to gain information about the pressure in different directions.

$$P_{\alpha\beta} = \frac{1}{V}\left(\sum_i m_i \dot{r}_{i,\alpha} \dot{r}_{i,\beta} + \sum_{i<j} r_{ij,\alpha} F_{ij,\beta} \right) \qquad (2.52)$$

Here α and β signal the x, y or z coordinate of r, $\dot{r}$ and F.

$$P = \frac{1}{3}\,\mathrm{Tr}(P) = \frac{1}{3}(P_{xx} + P_{yy} + P_{zz}) \tag{2.53}$$

2.3.1. Lennard Jones interaction

To mimic the repulsive as well as the van der Waals attraction between the molecules, the oxygen atom in the TIPnP water models carries a LJ interaction, which is widely used in simulations and is a realistic potential for neutral atoms like rare gases. The LJ potential is a pair potential.

$$U^{\mathrm{LJ}} = \frac{1}{2}\sum_{i,j}^{N}\sum_{\alpha,\beta}^{M} 4\varepsilon \left[\left(\frac{\sigma}{r_{i\alpha,j\beta}}\right)^{12} - \left(\frac{\sigma}{r_{i\alpha,j\beta}}\right)^{6}\right], \tag{2.54}$$

where N is the number of molecules in the system and M is the number of atoms per molecule. σ and ϵ are two parameters giving the zero-crossing and the depth of the potential respectively, see figure 2.3.

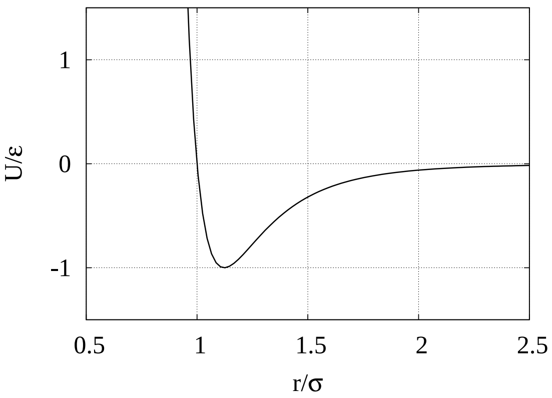

Figure 2.3.: The LJ potential.

As described in [7] the dominant contribution at large separations to the potential comes from the multipolar dispersion interactions between the instantaneous electric moments on one atom, created by spontaneous fluctuations in the electronic charge distribution, and moments it induces in the other. In the LJ potential only the leading r^{-6} term of the multipole series is taken into account. But the higher order terms, dipole-quadrupole (r^{-8}) and quadrupole (r^{-10}) are generally small in comparison. Although the short-range repulsion can be adequately expressed by an exponential function of the form $\exp(-r/r_0)$, where r_0 is a range parameter, it is represented by a r^{-n} term out of convenience.

The associated force can be computed by

$$\vec{\mathcal{F}}_{i\alpha,j\beta} = -\vec{\nabla}_{\vec{r}_{i\alpha,j\beta}} U \quad \Rightarrow \tag{2.55}$$

$$\vec{\mathcal{F}}^{\mathrm{LJ}}_{i\alpha,j\beta} = 24\varepsilon \left[2\left(\frac{\sigma}{r_{i\alpha,j\beta}}\right)^{12} - \left(\frac{\sigma}{r_{i\alpha,j\beta}}\right)^{6}\right] \cdot \frac{\vec{r}_{i\alpha,j\beta}}{r^2_{i\alpha,j\beta}}\,. \tag{2.56}$$

Long Range Correction for the LJ potential

In order to correct for the error, that is introduced by neglecting the interaction outside of the cutoff sphere, we add an additional term. As the LJ interaction is short ranged and radial symmetric the correction can be computed by assuming that outside the cuttoff sphere the structure vanishes and the pair correlation function equals one.

$$\begin{aligned} U^{\mathrm{LJ}}_{corr} &= \frac{1}{V}\frac{N(N-1)}{2}\int_{r>r_{cut}} d^3r\, U^{\mathrm{LJ}}(r)g(r) \\ &= \frac{1}{V}\frac{N(N-1)}{2}\int_{r>r_{cut}} d^3r\, U^{\mathrm{LJ}}(r) \\ &\approx -\frac{8}{3}\pi N\rho\epsilon\sigma^3\left[-\frac{1}{3}\left(\frac{\sigma}{r_{cut}}\right)^9+\left(\frac{\sigma}{r_{cut}}\right)^3\right] \qquad (2.57) \\ P^{\mathrm{LJ}}_{corr} &= -\frac{16}{9}\pi\rho^2\epsilon\sigma^3\left[-2\left(\frac{\sigma}{r_{cut}}\right)^9+3\left(\frac{\sigma}{r_{cut}}\right)^3\right]. \qquad (2.58) \end{aligned}$$

Properties of the simple LJ fluid

At this point we want to discuss some properties of a simple LJ fluid. One very interesting aspect is that as was pointed out to me by Prof. Hentschke even a simple LJ fluid exhibits an enhancement in the small q regime of its intensity curve. Figure 2.4 depicts the structure factor, $h(q)$, of a LJ fluid at $T^* = 1.3$, $\rho^* = 0.6$ and $N = 16000$. In addition the structure factor that results from using just the repulsive part of the potential is shown. Here $h(q)$ was computed from the pair correlation function $g(r)$ by

$$h(q) = 4\pi\rho\int r^2\left[g(r)-1\right]\frac{\sin(qr)}{qr}dr$$

It was already noted in [8] that the small q regime is very sensitive to the attractive part of the potential [9]. It was shown by Evans et al [10] that this behavior persists although weak far away from the critical point.

This 'simple feature' has the following special significance. Because the structure factor $h(q)$ is proportional to the isothermal compressibility, κ_T, at $q = 0$ and $\kappa_T \approx |T - T_c|^{-\gamma}$ diverges on approach to T_c (or to criticality in general), an increase of $h(q)$ at small q may be mistaken as approach to criticality. This caveat applies in particular to computer simulation, where the finite size cutoff of the fluctuation-correlation-length does not permit a true divergence even if there is one in the infinite system.

Still another possibility is that an increase of the structure factor at small q may be interpreted in terms of a 'structural feature' on a lengthscale $2\pi/q$. The LJ liquid, even though devoid of such a 'structural feature' at small q, does show an increase of the structure factor. Thus, any structur factor increase at small q (not showing a clear maximum) should be treated with caution.

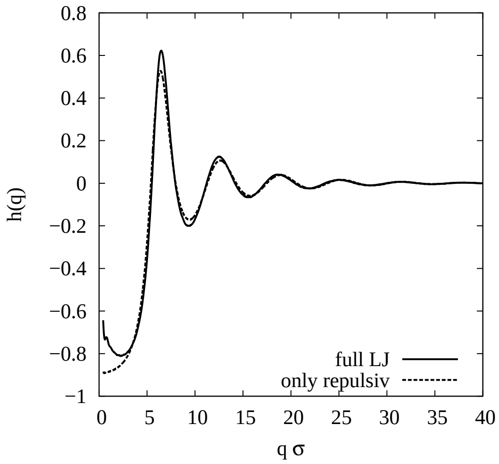

Figure 2.4.: Depicted is the structure factor of a LJ fluid at $T^* = 1.3$, $\rho^* = 0.6$ and $N = 16000$ as well as the structure factor that results from using just the repulsive part of the potential.

2.3.2. Coulomb interaction

The Coulomb interaction is given as usual by

$$U^c = \frac{1}{2} \sum_{i,j}^{N} \sum_{\alpha,\beta}^{M} \frac{q_\alpha q_\beta}{4\pi\varepsilon_0} \sum_{\substack{\vec{a} \\ (i \neq j \text{ for } \vec{a} = \vec{0})}} \frac{1}{|\vec{r}_{i\alpha,j\beta} + \vec{a}|} \tag{2.59}$$

and the corresponding force by

$$\vec{\mathcal{F}}^{c}_{i\alpha} = \sum_{j}^{N} \sum_{\beta}^{M} \frac{q_\alpha q_\beta}{4\pi\varepsilon_0} \sum_{\substack{\vec{a} \\ (i \neq j \text{ for } \vec{a} = \vec{0})}} \frac{\vec{r}_{i\alpha,j\beta} + \vec{a}}{|\vec{r}_{i\alpha,j\beta} + \vec{a}|^3} \,. \tag{2.60}$$

2.3.3. Polarization correction

As was first noticed by Berendsen et al in 1987 [11] a self-energy correction should be included into all effective pair potentials that include the average effects of polarization. In water there exists a considerable average polarization, which causes effective pair potentials to exhibit larger dipole moments than the isolated molecules. The self-energy due to this polarization has to be included into the total of the Coulomb interaction. The correction term is given by

$$E_{pol} = \frac{1}{2} \sum_{i} \left(\mu - \mu^0\right)^2 / \alpha_i \tag{2.61}$$

where μ is the dipole moment of the effective pair model and μ^0 is the dipole moment of the isolated molecule, while α denotes the polarizability, which for water is around 0.001445 nm^3. For SCP/E water one arrives at $E_{pol} = 5.22$ kJ/mol and for TIP4P/2005 water at $E_{pol} = 4.21$ kJ/mol.

2.3.4. Long Range Corrections for the Coulomb Potential

The Coulomb Potential is different from the Lennard-Jones potential, in that it describes a long range interaction rather than a short ranged one. A potential term of the form r^{-n} is short ranged if the following integral converges and long ranged otherwise.

$$\int_{r_{cut}}^{\infty} dr\, r^{d-1} \frac{1}{r^n} = \begin{cases} \frac{1}{d-n} r^{d-n} |_{r_{cut}}^{\infty} & n \neq d \\ \ln\left[r\right] |_{r_{cut}}^{\infty} & n = d \end{cases}$$

The Coulomb interaction is thus an example of a long range interaction and cannot be treated by a simple cutoff as in the Lennard-Jones case.

3D

Ewald Summation There are two common kinds of methods to compute the correction for a system with 3D periodic boundary conditions.

In the reaction field method [12] the electric field that effects a molecule is devided into two parts. The contribution that comes from the other particles within the cutoff sphere and the part that originates from the molecules outside the sphere which are assumed to form a continuum with dielectric constant ϵ. We will not discuss this method further as it will not be applied in this work.

Apart from this continuum scheme there exist a number of Fourier methods of which we will use the Ewald sum and the PPPM (particle particle particle mesh) in our simulations. The Ewald method [13] was introduced by Ewald as early as 1921 in order to compute the potentials of lattices. The same procedure can be used to sum up the potential of the periodic images of the box. The algorithm in its original form is of order N^2. Fast Fourier methods as implemented in the PPPM scheme improve the order to $N \ln(N)$.

If one tries to compute

$$\mathcal{U} = \frac{1}{2} \sum_{i,j}^{N} \frac{q_i q_j}{4\pi\varepsilon_0} \sum_{\substack{\vec{a} \\ (i \neq j \text{ for } \vec{a} = \vec{0})}} \frac{1}{|\vec{r}_{ij} + \vec{a}|} \tag{2.62}$$

explicitly the result will depend on the order of summation as the sum is only conditionally convergent. Normally one sums in spherical shells but the convergence is very slow. Ewald rearranges the sum into parts.

$$\mathcal{U}^{\text{ewald}} = \mathcal{U}^{\text{real}} + \mathcal{U}^{\text{rec}} + \mathcal{U}^{\text{self}} \tag{2.63}$$

Each charge is screened by a Gaussian charge distribution $\rho_i = -q_i \kappa^3 \exp(-\kappa^2 r^2)/\sqrt{\pi}$ and then summed up in real space, while the screening charges form a smooth charge density and can be summed in reciprocal space see figure 2.5.

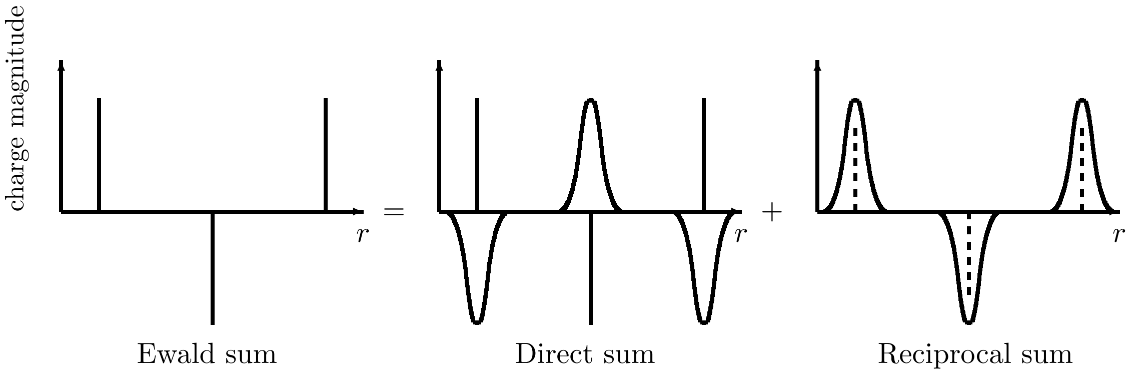

Figure 2.5.: Principal of the Ewald summation.

$$
\begin{aligned}
\mathcal{U}^{\text{real}} &= \frac{1}{2}\sum_{i,j}^{N} \frac{q_i q_j}{4\pi\varepsilon_0} \sum_{\substack{\vec{a} \\ (i \neq j \text{ for } \vec{a}=\vec{0})}} \frac{\operatorname{erfc}\left[\kappa \left|\vec{r}_{ij}+\vec{a}\right|\right]}{\left|\vec{r}_{ij}+\vec{a}\right|} - \sum_{i}^{N} \frac{q_i^2}{4\pi\varepsilon_0} \frac{\kappa}{\sqrt{\pi}} \\
\mathcal{U}^{\text{rec}} &= \frac{1}{2}\sum_{i,j}^{N} \frac{q_i q_j}{4\pi\varepsilon_0} \frac{4\pi}{V} \sum_{\vec{g}\neq\vec{0}} g^{-2} \exp\left[-\frac{g^2}{4\kappa^2}\right] \exp\left[i\vec{g}\cdot\vec{r}_{ij}\right] \\
\mathcal{U}^{\text{self}} &= -\sum_{i}^{N} \frac{q_i^2}{4\pi\varepsilon_0} \frac{\kappa}{\sqrt{\pi}}
\end{aligned}
$$

$$
\text{where} \qquad \operatorname{erfc}(x) = 1 - \operatorname{erf}(x) = 1 - (2/\sqrt{\pi}) \int_0^x e^{-u^2}\, du \tag{2.64}
$$

For a derivation of these forumlas see appendix B.4.

Figure 2.6 shows that the energy conservation is improved massively by introducing the Ewald summation.

PPPM To improve on the performance of the Ewald method a number of Fast Fourier Methods were introduced (e.g. PPPM, PME (Particle Mesh Ewald), smooth PME) in which the sum in reciprocal space is computed more efficiently. The PPPM method as investigated in [14, 15] is very effective and allows to control the accuracy of the computation.

The PPPM method was introduced by Hockney and Eastwood in 1988 [16]. The principle steps are similar in all FFT (Fast Fourier Transformation) methods:

1. discretize the charge density on a mesh
2. solve the Poisson equation on the mesh by FFT
3. differentiate the potential to compute the forces on the mesh
4. assign the forces to the individual molecules

If we can compute the reciprocal

$$
\mathcal{U}^{\text{rec}} = \frac{1}{2}\sum_{i,j}^{N} \frac{q_i q_j}{4\pi\varepsilon_0} \frac{4\pi}{V} \sum_{\vec{g}\neq\vec{0}} g^{-2} \exp\left[-\frac{g^2}{4\kappa^2}\right] \exp\left[i\vec{g}\cdot\vec{r}_{ij}\right] \tag{2.65}
$$

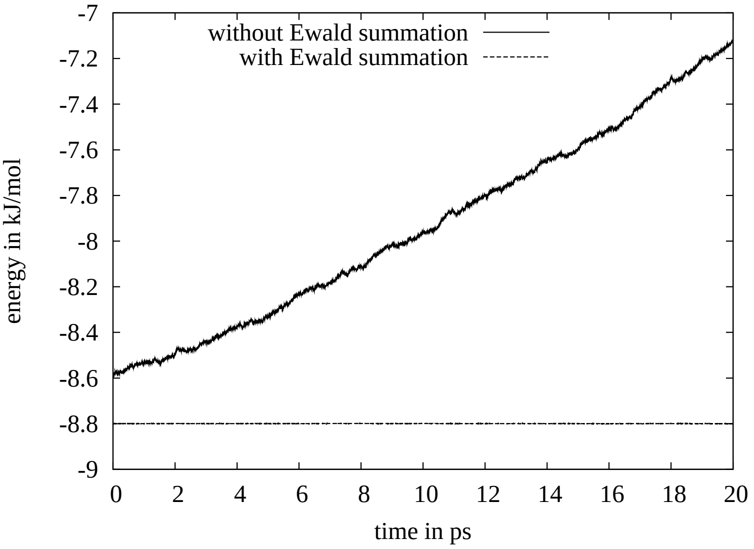

Figure 2.6.: The difference in energy conservation with and without Ewald summation for a cutoff of 9 Å.

more efficiently with a $N \ln(N)$ scaling instead of N^2 by FFT, we are able to choose the largest Ewald parameter κ consistent with the required accuracy and thus minimize r_{cut}. Then the scaling of the whole algorithm can be improved to $N \ln(N)$.

Further explanations can be found in the appendix B.5.

2D

Following the discussion in [17] we use the ELC (electrostatic layer correction) method in the case of 2D periodic boundary conditions. Here a linearly scaling correction term is combined with a 3D standard method like PPPM. Thus the whole method will scale like the underlying standard summation method. In addition reliable error estimates exist, so the precision can be tuned as desired. Starting with a system with dimension $L \times L \times h$ which is only periodic in the first two dimensions and where h is the maximal z-distance of two particles one places this box into a larger box with dimensions $L \times L \times L_z$ with $L_z \gg h$. Then this box is replicated periodically in all three dimensions. The gab size $L_z - h$ is denoted by δ.

The trick is now to use slab-wise summation instead of the spherical one used usually as demonstrated in figure 2.7. Now we consider the nth image layer which has an offset of nL_z to the original layer. If nL_z is large enough, each particle of charge q_j at position $(x_j, y_j, z + nL_z)$ and its images in the x-y-plane can be viewed as constituting a homogeneous charged sheet of charge density $\sigma_j = q_j/L^2$. The resulting potential for a sheet at distance z is $2\pi\sigma_j|z|$. If one now considers the contribution of a pair of sheets located at $\pm nL_z$, it vanishes by charge neutrality:

$$\begin{aligned}
2\pi q_i \sum_{j=1}^{N} \sigma_j (|z_j - z_i + nL_z| + |z_j - z_i - nL_z|) &= 2\pi q_i \sum_{j=1}^{N} \sigma_j (nL_z + z_j - z_i nL_z - z_j + z_i) \\
&= 4piq_i nL_z \sum_{j=1}^{N} \sigma_j = 0 \,. \qquad (2.66)
\end{aligned}$$

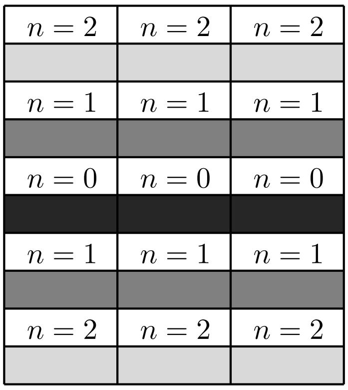

Figure 2.7.: Schematic view of the slab-wise summation order.

Smith [18] has shown that by adding to the Coulomb energy the term

$$E_c = 2\pi M_z^2 - \frac{2\pi \vec{M}^2}{3} \,, \qquad (2.67)$$

where $\vec{M} = \sum q_i \vec{r}_i$ is the total dipole moment, the slab-wise summation result can be obtained instead of the spherical limit. Applying this slab-wise summation order, Yeh and Berkowitz showed that a gap size of at least h is normally sufficient to obtain an moderately accurate result [19]. The ELC method does improve an this simple slab-wise method by explicitly correcting for the interlayer interactions, giving accurate results for any $L_z > h$. For details see appendix B.6.

1D

In order to compute the electrostatic interaction in the one dimensional periodic geometry, we decided on the MMM1D method (MMM is not an abbreviation but just the name of the method) of Arnold and Holm as described in [20, 21].

The algorithm scales with N^2, like the 2D Ewald method but does allow for error estimation. Here the Coulomb sum is transformed into a series of fast decaying functions via a convergence factor. Then two different formulas the near formula for close distances and the far formula for large distances are derived. For particle pairs at large distances the Lekner approach is used. As this is not numerically stable at short distances a rapidly convergent series is applied for particles at close distances.

For details see the appendix B.7.

Bibliography

[1] Evans D J. On the representatation of orientation space. *Mol. Phys.*, 34(2):317–27, 1977.

[2] Omelyan I P. On the numerical integration of motion for rigid polyatomics: The modified quaternion approach. *Computers in Physics*, 12(1):97–103, 1998.

[3] Berendsen H J C, Postma J P M, van Gunsteren W F, DiNola A, and Haak JR. Molecular dynamics with coupling to an external bath. *J. Chem. Phys.* , 81:3684, 1984.

[4] Marsaglia G. Choosing a point from the surface of a sphere. *The Ann. Math. Stat.*, 43(2):645–6, 1972.

[5] Nymand T M and Linse P. Ewald summation and reaction field methods for potentials with atomic charges, dipoles, and polarizabilities. *J. Chem. Phys.* , 112:6152–60, 2000.

[6] Irving J H and Kirkwood J G. The statistical mechanical theory of transport processes. iv. the equations of hydrodynamics. *J. Chem. Phys.* , 18:817–29, 1950.

[7] Hansen J-P and McDonald I R. *Theory of Simple Liquids, Third Edition.* Academic Press, 3 edition, 2006.

[8] Verlet L. Computer "Experiments" on classical fluids. II. equilibrium correlation functions. *Phys. Rev.*, 165(1):201–15, 1968.

[9] Andersen H C, Chandler D, and Weeks J D. Roles of repulsive and attractive forces in liquids: the equilibrium theory of classical fluids. *Adv. Chem. Phys*, 105, 1976.

[10] Evans R and Sluckin T J. The role of attractive forces in the structure of simple liquids: a theory for small-angle scattering. *Journal of Physics C: Solid State Physics*, 14(19):2569–79, 1981.

[11] Berendsen H J C, Grigera J R, and Straatsma T P. The missing term in effective pair potentials. *J. Phys. Chem.* , 91(24):6269–71, 1987.

[12] Onsager L. Electric moments of molecules in liquids. *J. Am. Chem. Soc.*, 58(8):1486–93, 1936.

[13] Ewald P P. Die berechnung optischer und elektrostatischer gitterpotentiale. *Annalen der Physik*, 369(3).

[14] Deserno M and Holm C. How to mesh up ewald sums. I. a theoretical and numerical comparison of various particle mesh routines. *J. Chem. Phys.* , 109:7678–93, 1998.

[15] Deserno M and Holm C. How to mesh up ewald sums. II. an accurate error estimate for the particle-particle-particle-mesh algorithm. *J. Chem. Phys.* , 109:7694–702, 1998.

[16] Hockney R W and Eastwood J W. *Computer simulation using particles.* Taylor & Francis, 1988.

[17] Holm C. Efficient methods for long range interactions in periodic geometries plus one application. *Computational Soft Matter: From Synthetic Polymers to Proteins*, 23:195–236, 2004.

[18] Smith E R. Electrostatic energy in ionic crystals. *Proc. R. Soc. A, Mathematical and Physical Sciences*, 375(1763):475–505, 1981.

[19] Yeh I C and Berkowitz M L. Ewald summation for systems with slab geometry. *J. Chem. Phys.* , 111:3155–62, 1999.

[20] Arnold A and Holm C. MMM1D: A method for calculating electrostatic interactions in one-dimensional periodic geometries. *J. Chem. Phys.* , 123:144103–8, 2005.

[21] Bródka A. Comment on MMM1D: A method for calculating electrostatic interactions in one-dimensional periodic geometries[J. Chem. Phys.[bold 123], 144103 (2005)]. *J. Chem. Phys.* , 125:107103–2, 2006.

2.4. Fluctuating Charges

We want to investigate the influence of polarizability on the structure of bulk water. The section describes the method of fluctuating charges used to implement polarizability in the models we used following [1].

The principle of electronegativity equalization (EE) was first proposed by Sanderson in 1951 [2] and it was used to construct a polarizable version of the TIP4P model with great success by Rick and Berne [1]. The basic idea is that in a many-atom system the electron gas will distribute itself so that its electrochemical potential is equal at every nuclear site. It was shown by Parr [3] that the electrochemical potential is the negative of the Mulliken electronegativity, which for an isolated atom i is given by:

$$\chi_i = e\frac{\partial E}{\partial Q_i} = -\frac{\partial E}{\partial N} = -\mu_i \tag{2.68}$$

Here E is the ground state energy and N the number of electrons in the atom. In the isolated atom, the energy of creating a partial charge Q_A can be expanded to second order as

$$E(Q_A) = E_A(0) + \tilde{\chi}_A^0 Q_A + \frac{1}{2} J_{AA}^0 Q_A^2, \tag{2.69}$$

where $\tilde{\chi}_A^0$ and J_{AA}^0 are parameters dependent on the atom type. $\tilde{\chi}_A^0$ is the Mulliken electronegativity (per electronic charge e) and J_{AA}^0 is twice the hardness of the electronegativity of the isolated atom. The energy of a system of N_m molecules each with N_a atoms is

$$\begin{aligned} U\left[(Q),(r)\right] = \quad & \textstyle\sum_{i=1}^{N_m}\sum_{\alpha=1}^{N_a} && \left[E_\alpha(0) + \tilde{\chi}_\alpha^0 Q_{i\alpha} + \frac{1}{2} J_{\alpha\alpha}^0 Q_{i\alpha}^2\right] \\ & + \textstyle\sum_{i\alpha<j\beta} && J_{\alpha\beta}(r_{i\alpha j\beta}) Q_{i\alpha} Q_{j\beta} \\ & + \textstyle\sum_{i\alpha<j\beta} && V(r_{i\alpha j\beta}) \, , \end{aligned} \tag{2.70}$$

where $E_\alpha(0)$ is the ground state energy of atom α, $r_{i\alpha j\beta}$ is the distance, $J_{\alpha\beta}(r_{i\alpha j\beta})$ is the Coulomb interaction and $V(r_{i\alpha j\beta})$ is the Lennard-Jones interaction. The electronegativity per unit charge of atom A is given by

$$\tilde{\chi}_A = \left(\frac{\partial U}{\partial Q_A}\right) \tag{2.71}$$

We constrain the molecule to stay neutral, so there is no intermolecular charge transfer.

$$\sum_{\alpha=1}^{N_a} Q_{i\alpha} = 0 \tag{2.72}$$

Using Lagrange multipliers one arrives at

$$L = \sum_{i=1}^{N_m}\sum_{\alpha=1}^{N_a} \frac{1}{2} m_\alpha \dot{r}_{i\alpha}^2 + \sum_{i=1}^{N_m}\sum_{\alpha=1}^{N_a} \frac{1}{2} M_Q \dot{Q}_{i\alpha}^2 - U\left[(Q),(r)\right] - \sum_{i=1}^{N_m} \lambda_i \sum_{\alpha=1}^{N_a} Q_{i\alpha} \, , \tag{2.73}$$

where m_α is the mass of atom α and M_Q is a fictitious charge mass which has units of energy time^2/charge^2 and the λ_i are Lagrange multipliers. The nuclear degrees of freedom evolve according to Newton's equation

$$m_\alpha \ddot{r}_{i\alpha} = -\frac{\partial U\left[(Q),(r)\right]}{\partial r_{i\alpha}} \tag{2.74}$$

and the set of charges evolve in time according to

$$M_Q \ddot{Q}_{i\alpha} = -\frac{\partial U\left[(Q),(r)\right]}{\partial Q_{i\alpha}} - \lambda_i = -\widetilde{\chi}_{i\alpha} - \lambda_i \tag{2.75}$$

After the elimination of λ one arrives at

$$M_Q \ddot{Q}_{i\alpha} = -\frac{1}{N_a}\sum_{\beta=1}^{N_a}(\widetilde{\chi}_{i\alpha} - \widetilde{\chi}_{j\beta}) \tag{2.76}$$

The charge mass M_Q should be chosen to be small enough to guarantee that the charges re-adjust very rapidly to changes in the nuclear degrees of freedom. If M_Q is sufficiently small, there will be essentially no thermal coupling between the nuclear and electronic degrees of freedom (see figure 2.8 (a)).

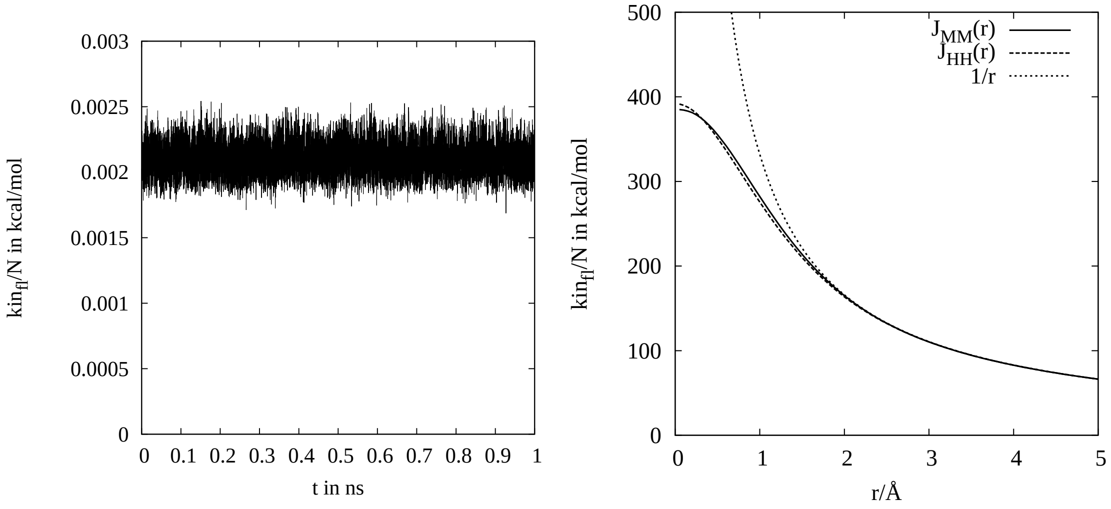

(a)

(b)

Figure 2.8.: (a) Kinetic energy of the charge fluctuation over a simulation trajectory of 1 ns at $T = 280$ K for TIP4P-FQ water ($M_Q = 298$ kJ/mol (fs/e)^2). The kinetic energy stays at a small level because of the low coupling between the nuclear and electronic degrees of freedom. (b) Screened potential for H-H and M-M pairs of TIP5P-FQ water, in comparison with the pure Coulomb $1/r$ interaction in kcal/mol/e^2.

The potential energy contains the Lennard-Jones part and the electrostatic part and since we are defining the energies relative to the isolated gas-phase energy the gas-phase energy E_{gp} needs to be subtracted. For the SPC and the TIP4P model one gets

$$\begin{aligned} Q_H^{gp} &= \frac{(\widetilde{\chi}_O^0 - \widetilde{\chi}_H^0)}{2J_{OO}^0 + J_{HH}^0 - 4J_{OH}(r_{MH}) + J_{HH}(r_{HH})} && (2.77) \\ E_{gp} &= -\frac{(\widetilde{\chi}_O^0 - \widetilde{\chi}_H^0)}{2J_{OO}^0 + J_{HH}^0 - 4J_{OH}(r_{MH}) + J_{HH}(r_{HH})} && (2.78) \end{aligned}$$

where M stands for the O-atom in the SPC and for the M site in the TIP4P model. For the TIP5P model Q_H^{gp} and E_{gp} are given by

$$\begin{aligned} Q_H^{gp} &= -Q_M = \frac{\widetilde{\chi}_M^0 - \widetilde{\chi}_H^0}{J_{HH}^0 + J_{MM}^0 + J_{HH}(r_{HH}) + J_{MM}(r_{MM}) - 4J_{MH}(r_{MH})} \\ E_{gp} &= -\frac{(\widetilde{\chi}_M^0 - \widetilde{\chi}_H^0)^2}{J_{HH}^0 + J_{MM}^0 + J_{HH}(r_{HH}) + J_{MM}(r_{MM}) - 4J_{MH}(r_{MH})}\,. && (2.79) \end{aligned}$$

For a more detailed derivation see appendix B.1.

The total energy for N_m molecules is then

$$\begin{aligned} E &= \sum_{i=1}^{N_m}\sum_{j<i}\left\{4\epsilon\left[\left(\frac{\sigma}{r_{iOjO}}\right)^1 2 - \left(\frac{\sigma}{r_{iOjO}}\right)^6\right] + \sum_{\alpha=1}^{N_a}\sum_{\beta=1}^{N_a}\frac{Q_{i\alpha}Q_{j\beta}}{r_{i\alpha j\beta}}\right\} \\ &\quad + \sum_{i=1}^{N_m}\sum_{\alpha=1}^{N_a}\left[\widetilde{\chi}_\alpha^0 Q_{i\alpha} + \frac{1}{2}\sum_{\beta=1}^{N_a} Q_{i\alpha}Q_{i\beta}J_{\alpha\beta}(r_{i\alpha j\beta})\right] - N_m E_{gp}\,. && (2.80) \end{aligned}$$

Following Rappe and Goddard [4], the Coulomb interaction $J_{ij}(r)$ for intramolecular pairs is taken to be the Coulomb overlap integral between Slater orbitals centered on each atomic site

$$J_{ij}(r) = \int dr_i dr_j \, |\phi_{n_i}(r_i)|^2 \, \frac{1}{|r_i - r_j - r|} \, |\phi_{n_j}(r_j)|^2$$

The Slater orbitals are given by

$$\phi_{n_i}(r) = A_i r^{n_i - 1} e^{-\zeta_i r}$$

and are characterized by a principal quantum number n_i and an exponent ζ_i. A_i is a normalization factor. The value of $J_{ii}(r)$ for $r = 0$ is J_{ii}^0 and therefore the value of ζ_i uniquely determines J_{ii}^0. For hydrogen, $n_H = 1$ and $J_{HH}^0 = \frac{5}{8}\zeta_H$ and for oxygen, $n_O = 2$ and $J_{OO}^0 = (93/256)\zeta_O$. For an example see figure 2.8 (b).

Most of the polarizable models only screen the charges for the intramolecular interaction and use the unscreened coulomb interaction between atoms from different molecules. This works fine if one only looks at water model geometries like in SPC and TIP4P where the charged sites don't stick out too much from the LJ-center. And even there as was observed by Stöckelmann et al [5] one runs into convergence problems if the interaction of ions with water is simulated.

Parametrization of the TIP5P-FQ model

In addition to the TIP4P-FQ model designed by Rick and Berne [1] whose parameters are given in the appendix A.2.1, we want to design our own polarizable version of TIP5P water.

If one uses an unscreened intermolecular potential for the TIP5P model, a stable simulation can only be achieved by choosing unnatural values for σ_{LJ} and ϵ_{LJ} in order to prevent a polarization catastrophe. In addition the convergence is not stable against slight changes in the screening parameter, so that a stability analysis is necessary to find possible screening parameters. Thus we screen the charges if the distance between the interaction sites is smaller than 5 Å. In this case there is a greater freedom to choose the Lennard-Jones parameters. If one uses the screening parameters from [5] for the simulation, using the oxygen screening function for the M-sites the program runs stable for different parameters of σ_{LJ} and ϵ_{LJ}. The electronegativity difference is set to yield a gas phase dipole moment of 1.855 D. The LJ parameters, $\sigma = 3.18$ Å and $\epsilon = 0.2436$ kcal/mol, are chosen to give the best agreement with experimental data for the diffusion coefficient and the density in the temperature range between 250 K to 310 K.

In figure 2.9 the dipole moments of two typical configurations for TIP4P-FQ and TIP5P-FQ water for $T = 240$ K and $T = 320$ K. The dipole moment of TIP5P-FQ water is on average higher than that of TIP4P-FQ water and shows a larger spreading. The temperature dependence on the average dipole moment μ for the two models is shown in figure 2.10.

Unfortunately as shown in figure 2.12 our TIP5P-FQ parametrization is inferior to the non-polarizable TIP5P-E, showing only a shallow density maximum at a too low density as well as a too small self-diffusion coefficient. The main reason is that only the LJ parameters were adjusted while the geometry and the screening functions were left unaltered. Thus there may still be room for improvement, although a combination with polarizable dipole models like in the POL5 model was found to be necessary in Ref. [6] to get superior results to the non-polarizable model. Thus it seems rather difficult to improve on the non-polarizable TIP5P model.

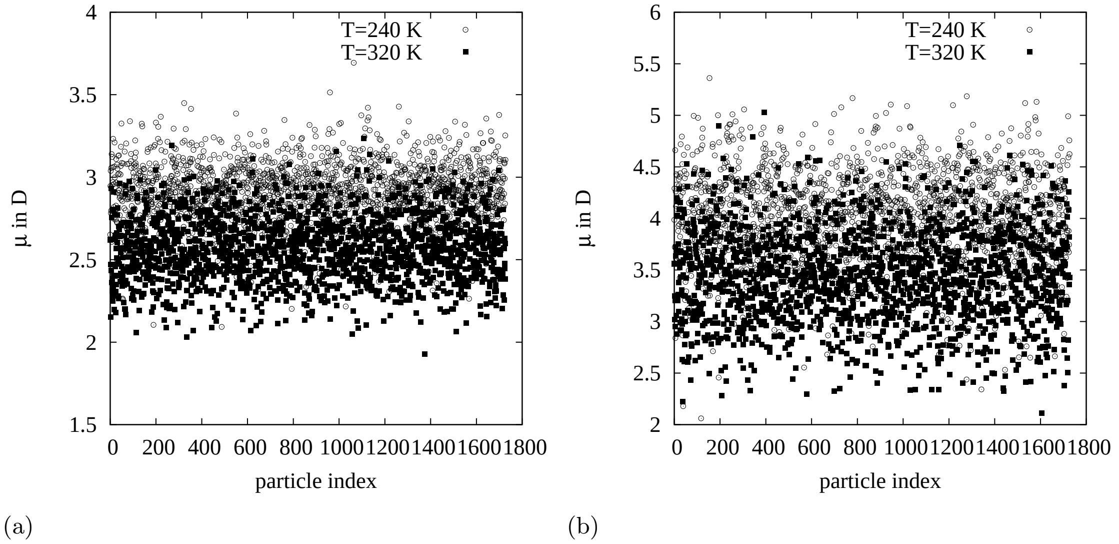

Figure 2.9.: Dipole moments for two typical configurations of TIP4P-FQ (a) and TIP5P-FQ (b) water for $T = 240$ K and $T = 320$ K.

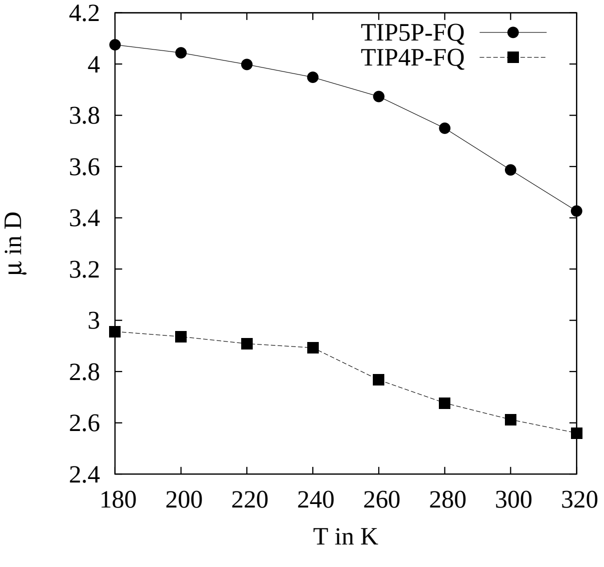

Figure 2.10.: Temperature dependence of the average dipole moment μ of TIP4P-FQ and TIP5P-FQ water

Bibliography

[1] Rick S W, Stuart S J, and Berne B J. Dynamical fluctuating charge force fields: Application to liquid water. *J. Chem. Phys.* , 101(7):6141–56, 1994.

[2] Sanderson R T. An interpretation of bond lengths and a classification of bonds. *Science*, 114(2973):670, 1951.

[3] Parr R G and Yang W. *Density-functional theory of atoms and molecules.* Oxford University Press, USA, 1994.

[4] Rappe A K and Goddard W A. Charge equilibration for molecular dynamics simulations. *J. Phys. Chem.* , 95(8):3358–63, 1991.

[5] Stöckelmann E and Hentschke R. A molecular-dynamics simulation study of water on NaCl(100) using a polarizable water model. *J. Chem. Phys.* , 110(24):12097–107, 1999.

[6] Stern H A, Rittner F, Berne B J, and Friesner R A. Combined fluctuating charge and polarizable dipole models: Application to a five-site water potential function. *J. Chem. Phys.* , 115:2237–51, 2001.

2.5. Characteristics of different water models

We want to simulate liquid water on a microscopic scale to understand the changes in its structure depending on pressure and temperature. Thus we need a model that is sophisticated enough to display the molecular properties of water and that is simple enough to simulate relative big samples in the bulk system and a large number of different geometries for the confined system.

The number of water models documented in the literature is impressive. Counting only the most frequent ones yields around 50 models [1, 2]. Thus some thought has to go into making a reasonable selection.

Therefore we only use rigid classical models for simplicity and look for models that exhibit a density maximum quantitatively similar to that of real water.

There are two non-polarizable models that perform exceptionally well in this regard. The thetrahedral TIP5P-E model introduced by Rick [3] in 2004 based on the TIP5P model [4] and the planar TIP4P/2005 model [5]. Both force fields have been parametrized including long-range corrections in form of the Ewald sum using tin-foil boundary conditions, which makes them more appealing than for instance the original TIP5P model. The TIP5P-E model is parameterized to reproduce the density curve in the temperature range from 236 to 373 K. The TIP4P/2005 model is parameterized targeting the temperature of maximum density, the enthalpy of vaporization, the densities of liquid water at ambient conditions, of ice II at 123 K and 0 MPa, and of ice V at 223 K and 530 MPa as well as the stability of several ice polymorphs.

In order to judge the importance of dynamic polarization we also include the TIP4P-FQ model, which was introduced in 1994 [6] and which shows an equally good agreement with the experimental density data. In addition we parametrize our own dynamically polarizable model, TIP5P-FQ, based on the TIP5P geometry combined with the fluctuating charge algorithm.

Another polarizable model, the TIP4P-Pol2 model, which shows good agreement with experimental intensity curves [7], was developed by Chen and Siepmann in Ref. [8]. It is parametrized to give good agreement with experimental saturated liquid and vapor densities, vapor pressures, and heats of vaporizations. We do not include this model in our investigations, because the included TIP4P/2005 model also shows very good coexistence densities of the vapor-liquid equilibria, admittedly without reproducing the experimental vapor pressures correctly, as discussed in Ref. [9]. In addition it is superior to the TIP4P-Pol2 model with regards to the density maximum, which is of special interest to us. Furthermore, the intensity curves calculated for TIP4P/2005 and TIP4P-Pol2 water are very close (see figure 2.11), so that in the present context no additional insight is gained by including both models.

Thermodynamic and dynamic properties of the selected models

Now we want to take a look at the performance of the different models in comparison to experimental data. The temperature dependence on the self-diffusion coefficient, D, computed using the Einstein relation, and of the density, ρ, in comparison to experimental data are displayed in figure 2.12. The first three models mentioned above all perform in reasonable agreement in the temperature range, where experimental data are

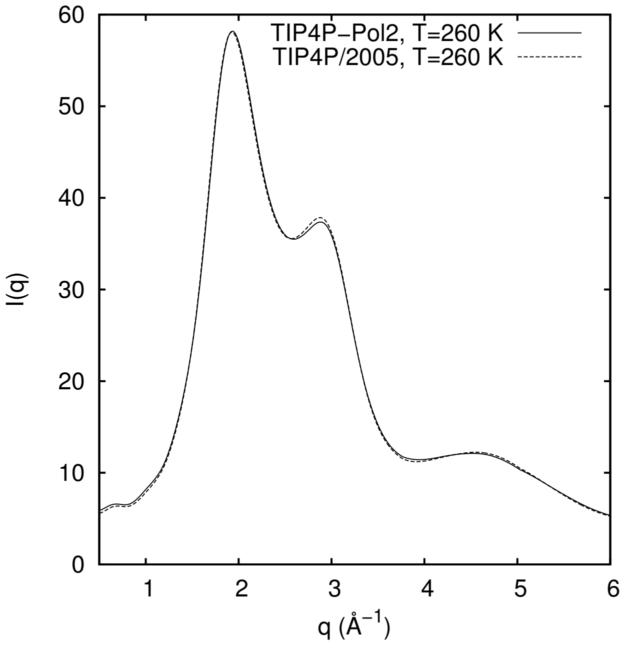

Figure 2.11.: The computed intensity curves at $T = 260$ K for TIP4P-Pol2 and TIP4P/2005 water. They are remarkable similar although the TIP4P-Pol2 model is much more complex being polarizable with an additional coupling between the Lennard-Jones interaction parameters for a pair of oxygen sites and their partial charges.

available. Our TIP5P-FQ parametrization apparently is inferior, showing only a shallow density maximum at a too low density as well as a too small self-diffusion coefficient. The main reason is that only the LJ parameters were adjusted while the geometry was left unaltered. Nevertheless inferior performance in the present case may serve as a marker possibly allowing to trace the relation between microscopic structure and the macroscopic density anomaly, which may for instance be viewed in terms of a binary mixture of "chain"-, "network"- or "cluster"- water with ordinary liquid water.

We also tested how well the models reproduce the pressure dependence of the density by computing the compressibility $\kappa_T = -\frac{1}{V}\left(\frac{\partial V}{\partial P}\right)_T$. Therefore we measured the density at two different pressures 1 atm and 1000 atm to estimate κ_T at about 500 atm and compared our results with experimental data at 1 and 1000 atm taken from [12]. While the simple SPC-E model does neither exhibit its density maximum nor its compressibility minimum near the experimentally expected temperatures (see figure 2.13) all models considered by us reproduce the experimentally observed anomalies (see figure 2.14,2.15,2.16 and 2.18). But only the TIP4P/2005 model reproduces the data quantitatively.

Evidence for a density minimum

A density minimum was first observed in vitreous silica [13] and later by Liu et al [14] in heavy water confined in 1D cylindrical pores of mesoporous silica at 210 K. We see

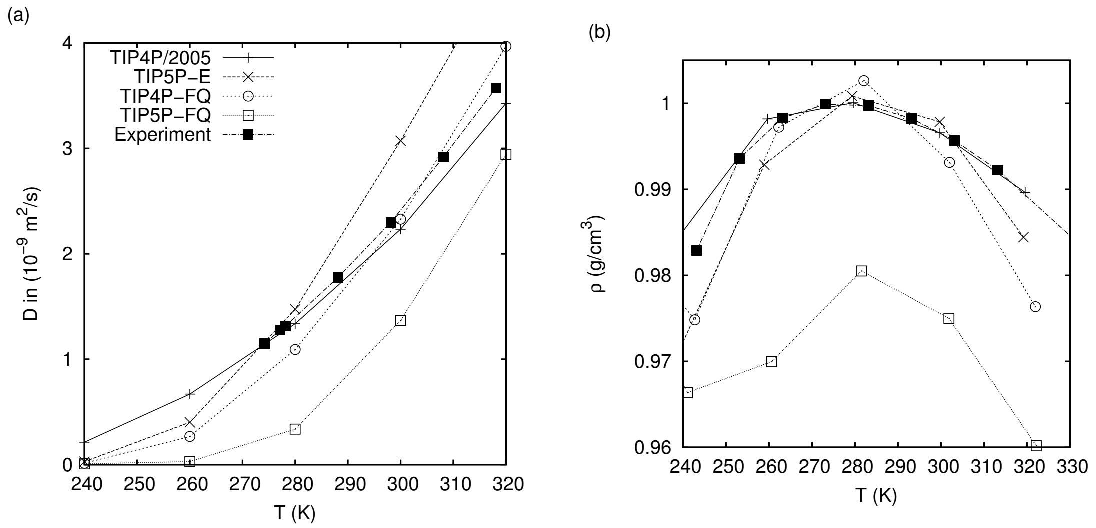

Figure 2.12.: (a) Temperature dependence on the diffusion coefficient, D, and (b) density, ρ, for the different models in comparison to experimental data (a) [10] ,(b) [11].

evidence for a density minimum in TIP5P-E water at about 220 K in agreement with a study by Paschek [15], in TIP4P-FQ water at about 200 K and in TIP5P-FQ water between 200 and 240 K depending on pressure. Poole et al [16] argue that the density minimum arises due to the approach of the liquid structure to a defect-free random tetrahedral network of hydrogen bonds.

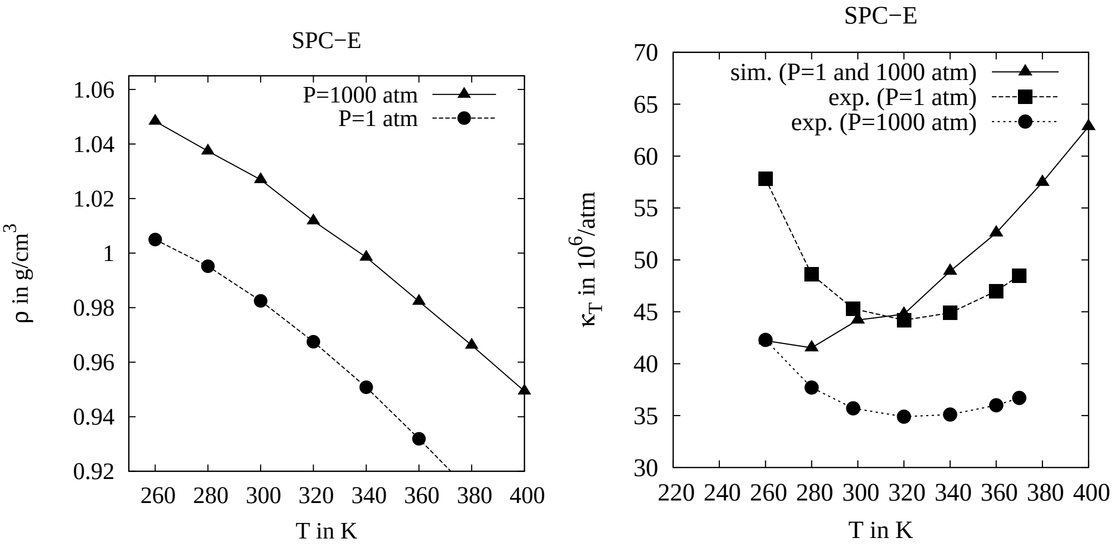

(a) (b)

Figure 2.13.: (a) Density at 1 and 1000 atm for SPC-E water. No density maximum is visible in the considered temperature range. (b) Estimated compressibility for SPC-E water at about 500 atm in comparison to experimental data at 1 and 1000 atm. The compressibility minima is just visible at about 270 K.

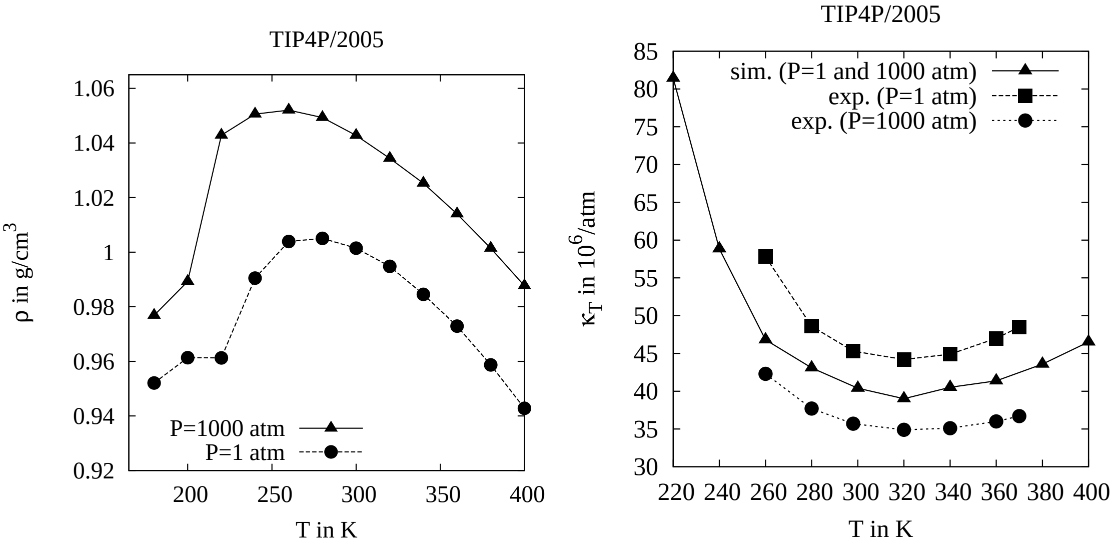

(a) (b)

Figure 2.14.: (a) Density at 1 and 1000 atm for TIP4P/2005 water. (b) Estimated compressibility for TIP4P/2005 water at about 500 atm in comparison to experimental data at 1 and 1000 atm. The experimental compressibility is even reproduced quantitatively in the considered temperature range.

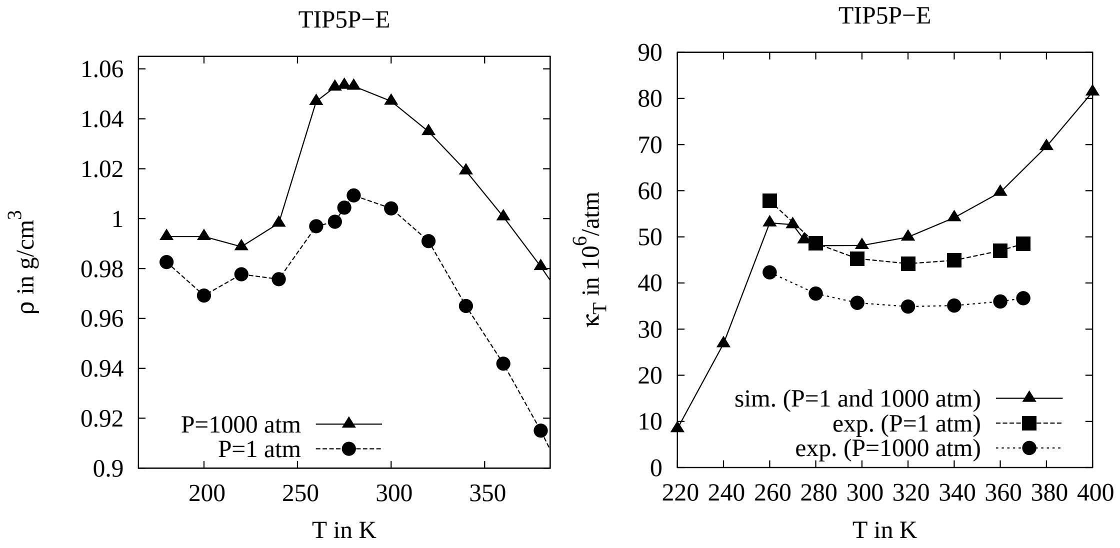

(a) (b)

Figure 2.15.: (a) Density at 1 and 1000 atm for TIP5P-E water. (b) Estimated compressibility for TIP5P-E water at about 500 atm in comparison to experimental data at 1 and 1000 atm. A compressibility minima is visible.

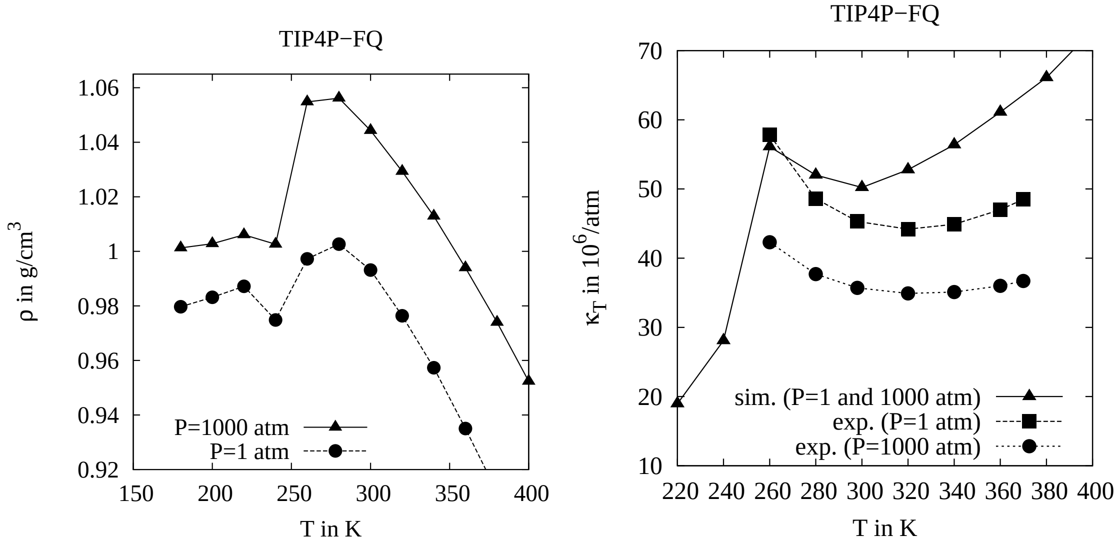

(a) (b)

Figure 2.16.: (a) Density at 1 and 1000 atm for TIP4P-FQ water. (b) Estimated compressibility for TIP4P-FQ water at about 500 atm in comparison to experimental data at 1 and 1000 atm. A compressibility minima is visible.

Phase behavior of the different water models

Brovchenko et al [17, 18] find two liquid-liquid phase transitions for TIP4P and TIP5P water (TIP4P: $T_{c_1} = 180$ K, $P_{c_1} = -1000$ kbar and $\rho_{c_1} = 0.99$ g cm^{-3}; $T_{c_2} = 210$

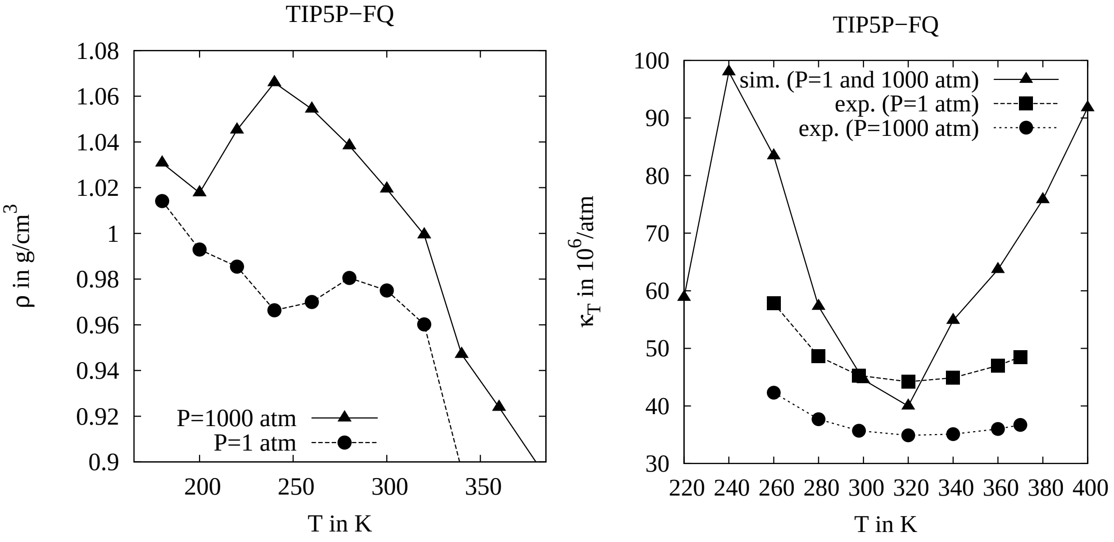

(a)

(b)

Figure 2.17.: (a) Density at 1 and 1000 atm for TIP5P-FQ water. (b) Estimated compressibility for TIP5P-FQ water at about 500 atm in comparison to experimental data at 1 and 1000 atm. The compressibility minima is too pronounced in comparison to the experimental data.

K, $P_{c_2} = 0.5$ kbar and $\rho_{c_2} = 1.07$ g cm^{-3}, TIP5P: $T_{c_1} = 200$ K, $P_{c_1} = 0$ kbar and $\rho_{c_1} = -0.99$ g cm^{-3}; $T_{c_2} = 240$ K, $P_{c_2} = 0.5$ kbar and $\rho_{c_2} = 1.07$ g cm^{-3}). Because of the similarities of the models we can assume that TIP4P/2005 water also exihibits liquid-liquid critical points.

In case of TIP5P-E water we calculated the maxima of the heat capacity $c_P = \left(\frac{\partial H}{\partial T}\right)_P$ in order to trace the Widom line. Our results are in agreement with those of [19].

2.6. Limits of the classical models

While classical rigid models are computationally very fast and thus allow simulations of big systems (like 32000 molecules in our study or more) for long simulation times, ab initio computations are only feasible for systems of about 100 molecules. Because of our interest in large scale structures, we had to turn towards classical water models. But the question remains what aspects of the hydrogen bond structure are neglected by this choice.

In their comprehensive study Mantz et al [20] compare rigid non-polarizable, polarizable, flexible water models and an ab inito water model in order to expose the different influence of charge distribution, molecular flexibility and polarizability as well as nuclear quantum effects on hydrogen bonding.

They compare the first solvation shell, the distribution of the donating molecules orientation to the H-bond (angle $H_D - O_D \cdots O_A$) and the distribution of the torsional angle $H - O_D - H_D \cdots O_A$ of liquid water at 300 K and 353 K. They find, that the first shell structure is dramatically affected by the charge placement and polarizability,

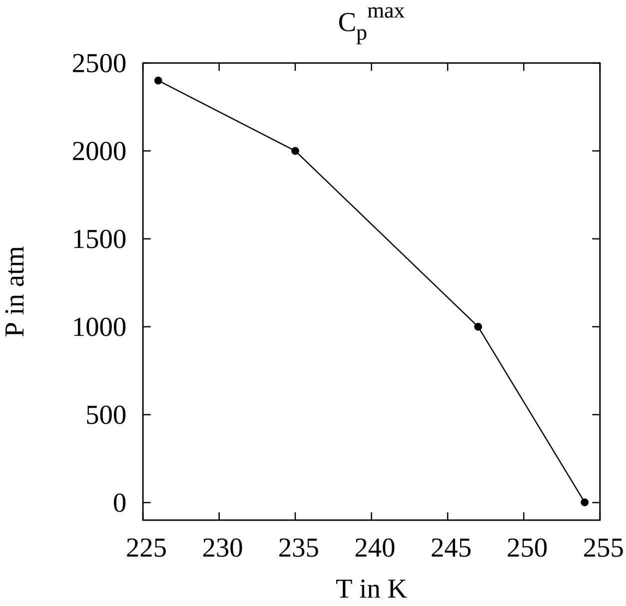

Figure 2.18.: The Widom line of TIP5P-E water is located by computation of the heat capacity maxima.

while quantum delocalization of the donating hydrogen atoms and flexibility are less important. Concerning the angular distribution the picture is not so clear. While the ab initio and the TIP4P model computations are in agreement with experimental values refered from experimental X-ray absorption and Raman spectra at 300 K and the TIP5P and TIP3P models show some deviations, all effective models and the ab initio results differ from the experimental values at 353 K. In addition all simulations predict a greater percentage of water molecules accepting two hydrogen bonds and a weaker temperature dependence of the hydrogen bond angle than experimental reports suggest. This leads Mantz et al to cast doubt on the reliability of the way the data were extracted from the experimental results (Empirical Potential Structure Refinement (EPSR) and Reverse Monte Carlo (RMC)).

Thus we can conclude that classical rigid water models that are parametrized to reproduce the thermodynamic properties of liquid water are also able to give reasonable liquid water structure compared to ab initio computations. Although models of the TIP4P type seem to perform slightly better than others in this respect.

A more recent paper by Møgelhøj et al [21] discusses different AIMD (ab initio MD) results based on different exchange-correlation functionals. They trace the discrepancy between AIMD and experimental results back to the relatively small simulation that can only give a picture of the local structure of water not observing fluctuations between two different water structures coexisting in nanoscale patches and propose a 70:30 mixture between the vdWDF2 HDL pair correlation function and the experimentally derived LDL pair correlation function. This shows that there are still fundamental problems with AIMD computations, which diminish their advantage in accuracy against classical water models.

2.7. Computation of the intensity curves

Results of scattering experiments are usually expressed by giving the intensity distribution in q-space, $I(q)$. Here q is the momentum transfer which is related to the scattering angle θ and the incident beam wavelength λ by $q = 4\pi \sin(\theta/2)/\lambda$. Two different functions can be used to represent scattering data in reduced form. The first one, denoted $\Sigma(q)$, is the differential scattering cross-section per unit volume of the sample

$$\Sigma(q) := \frac{1}{V}\frac{d\sigma}{d\Omega} = \frac{1}{V}\frac{I(q)A^2}{I_0},$$

where I_0 is the incident beam intensity. In light scattering experiments this function is usually called the Rayleigh-ratio. While the effect of the volume is removed, $\Sigma(q)$ remains dependent on the scattering power of the particles in the sample, which varies with the applied radiation. For x-rays, the scattering power is related to the electron densities, for light scattering to the associated refractive indices and for neutron scattering to the scattering length densities. This dependence on the applied radiation is eliminated in the second function which, however, can only be employed if the scattering can be treated as being due to just one class of particles. In water the water molecules. For equal particles the scattering properties can be described by the interference function S(q), also called scattering function or scattering law, which is defined as

$$S(q) := \frac{I(q)}{I_m N_m},$$

where N_m represents the total number of molecules in the sample, and I_m is the scattering intensity produced by one molecule, if placed in the same incident beam. The interference function expresses the ratio between the actual intensity and the intensity which would be measured, if all particles in the sample were to scatter incoherently, thus describing the structure of the molecules in the liquid. $\Sigma(q)$ and $S(q)$ are related by the equation

$$\Sigma(q) = \rho_0 \left(\frac{d\sigma}{d\Omega}\right)_m S(q)$$

Here $(d\sigma/d\Omega)_m$ denotes the scattering cross section per molecule and ρ_0 stands for their mean density

$$\rho_0 = \frac{N_m}{V}$$

On the other hand the density distribution is connected to the scattering amplitude $C(q)$ by

$$I(q) \sim \left\langle |C(q)|^2 \right\rangle$$

As the normalization of the amplitudes of the single scattered waves is already implied in the definition of the interference function one arrives at

$$S(q) = \frac{1}{N_m}\left\langle |C(q)|^2 \right\rangle$$

Using the relation between the scattering amplitude of a single microstate and the associated density distribution

$$C(q) = \int_V \exp(i\mathbf{q}\mathbf{r}) \cdot (\rho(\mathbf{r}) - \rho_0)\ d^3r$$

Thus leading to

$$S(q) = \frac{1}{\rho_0} \int_V \exp(i\mathbf{qr}) \cdot \rho_0^2 \left(g(\mathbf{r}) - 1\right) \, d^3\mathbf{r},$$

where

$$g(\mathbf{r}) = \frac{\langle \rho(\mathbf{r}) \rho(\mathbf{0}) \rangle}{\rho_0^2}$$

and for liquids, where only the radial dependence can be measured

$$S(q) = \int_{r=0}^{\infty} \frac{\sin(qr)}{qr} 4\pi\rho_0 r^2 \left(g(r) - 1\right) \, dr$$

$S(0)$ is connected to the compressibility by $S(0) = \rho k_B T \kappa_T$.

We can thus compute the scattering intensity, $I(q)$, from our simulations by

$$I(q) \;=\; \sum_{ij} x_i x_j f_i(q) f_j(q) \frac{\sin(q r_{ij})}{q r_{ij}} + \sum_{i \leq j} x_i x_j f_i(q) f_j(q) h_{ij}(q). \tag{2.81}$$

Here the sums are over the different atom types i and j, x_i and x_j are the atomic fractions, and $f_i(q)$ and $f_j(q)$ are the atomic scattering factors. The first term is the contribution coming from the individual molecules and the second term that arising from intermolecular correlations defined by the structure factor

$$h_{ij}(q) = 4\pi\rho \int_0^{\infty} r_{ij}^2 \, \left[g_{ij}(r_{ij}) - 1\right] \, \frac{\sin(q r_{ij})}{q r_{ij}} \, dr_{ij}. \tag{2.82}$$

Here ρ is the atom number density, r_{ij} is the intramolecular distance between atom centres, and $g_{ij}(r_{ij})$ is the radial distribution function describing intermolecular correlations between atom types i and j. Inherent in these equations is the assumption, that the electron density can be represented by a superposition of spherical electron density distributions. For water this is not the case. In Ref. [7] rescaled atomic scattering factors are used to represent the polarization in the liquid phase. It is demonstrated that the use of these modified atomic form factors gives similar spectra as those calculated from the same classical configurations by DFT-LDA.

Effects of polarizability

If one uses a polarizable model the polarization of a molecule should be included into the computed x-ray intensity spectra. In our case we want to use the charge distribution inherent in our models to rescale the atomic scattering factors, which were taken from Ref. [22]. Therefore we use the hydrogen atomic form factor for the virtual M sites and reweight the different atomic form factors locally for each site according to their partial charge.

$$\begin{aligned} \tilde{f}_H &= f_H \cdot (2Q_H^{gp} - Q_H)/Q_H^{gp} \\ \tilde{f}_M &= f_H \cdot (Q_M^{gp} - Q_M)/Q_M^{gp} \\ \tilde{f}_O &= f_O \end{aligned} \tag{2.83}$$

As shown in figure 2.19 this leads to a very similar effect as in Ref. [7] for the TIP4P-like models, whereas in the case of the TIP5P model the effect is very small. The reason for this difference lies in the near tetraedric geometry of the TIP5P-like models, which leads to an approximate addition of the charges on the M and H sites that results in a positive charge near unity.

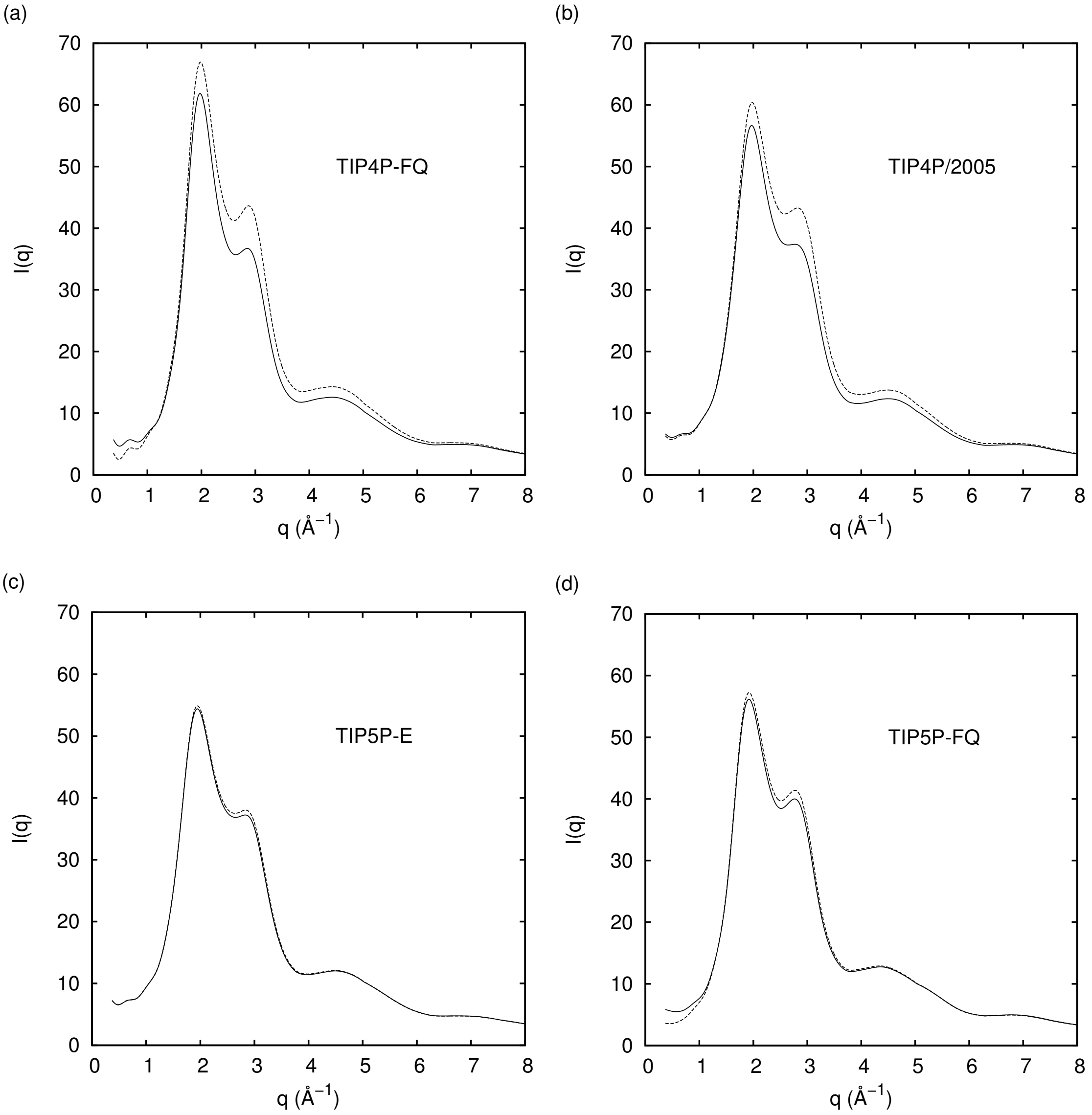

Figure 2.19.: Effect of the use of rescaled scattering factors for the different models at 280 K. The spectra computed using simple atomic form factors are represented by the solid lines, whereas the intensity curves using the rescaled form factors are given by the dashed lines.

2.7.1. X-ray Diffraction Corrections and Normalization

Usually the scattered intensity observed in x-ray experiments has an arbitrary relative scale. It is desirable to obtain the intensities on an absolute scale in order to compare the results of different experiments and to prepare the data for the extraction of the pair correlation function. In the early days this was done by assuming that the observed intensity converges at large scattering angles to the sum of the squares of the atomic form factors and incoherent scattering thus also allowing to fit and substract the Compton part of the spectrum. This procedure was generally found unsatisfactory, as it requires accurate measurements of the low intensity scattered at large angles and will show ambiguity if there are still appreciable undulations in this region. There are two papers describing a better method to normalize the x-ray diffraction intensity curves [23, 24] which was first utilized by Norman in 1954.

It is easy to see, that the normalized experimentally observed intensity $\alpha N_m I_e(q)$ corrected by the incoherent scattering intensity $N_m I_i(q)$ is equal to the normalized total coherent scattering intensity $I_t(q)$.

$$N_m \cdot I(q) = I_t(q) = N_m(\alpha I_e(q) - I_i(q))$$

First the scattering which arises from distances within the same molecule will be subtracted. This scattering is given by

$$N_m f_m^2(q) = N_m V \int_0^\infty \langle \rho_e^m(r) \rho_e^m(0) \rangle \frac{\sin(qr)}{qr}\, dr = N_m \int_0^\infty \sigma_m(r) \frac{\sin(qr)}{qr}\, dr,$$

where f_m is the molecular form factor and $\sigma_m(r)$ is the pair distribution function involving only distances within the same molecule. Thus one arrives at

$$\begin{aligned} I_t(q) - N_m f_m^2(q) &= \alpha N_m I_e(q) - N_m(f_m^2 + I_i(q)) \\ &= \int_0^\infty \left[4\pi r^2 V(\rho_0)_e^2 (g_e(r) - 1) - \sigma_m(r)\right] \frac{\sin(sr)}{sr}\, dr \end{aligned}$$

Here $g_e(r)$ and $(\rho_0)_e$ means that the pair correlation function and the density are referring to the electron densities not to the molecular densities as do ρ_0 and $g(r)$. A Fourier transform gives:

$$\begin{aligned} 4\pi V(\rho_0)_e^2 r^2 (g_e(r) - 1) - \sigma_m(r) &= 4\pi V(\rho_0)_e^2 r^2 g_e(r) - \sigma_m(r) - 4\pi V(\rho_0)_e^2 r^2 \\ = 4\pi V \rho_0^2 r^2 g(r) - 4\pi V(\rho_0)_e^2 r^2 &= \frac{2rN_m}{\pi} \int_0^\infty \left[\alpha I_e(q) - f_m^2 - I_i(q)\right] q \sin(qr)\, dq \end{aligned}$$

As $g(r)$ is zero for small r especially for $r = 0$ one arrives at

$$-2\pi^2 (\rho_0)_e^2 \frac{V}{N_m} = \int_0^\infty \left[\alpha I_e(q) - f_m^2 - I_i(q)\right] q^2\, dq$$

This equation can in principle be used for finding α since the left-hand side of the equation can be determined separately from the density of the sample. The infinity in the upper integration limit must be substituted by the highest experimentally accessible value, q_{max}. Therefore the usefulness of the equation depends upon how fast the difference of the integrals on the left-hand side converges. Now it is easy to extract $I(q)$ as:

$$I(q) = \alpha \cdot I_e(q) - I_i(q)$$

We use this technique whenever we want to compare our data to experimental curves that are not normalized or compton corrected like in the case of [25].

2.7.2. Formfactors and incoherent scattering intensity

So we need the molecular structure factor f_m^2 and the incoherent scattering intensity pro molecule $I_i(q)$ in order to normalize the measured intensity and to compute it from our simulations. There exist a number of calculations and measurements concerning these values. The atomic formfactor was determined in works of Cromer [26] and Hubbell [22]. They are in nearly absolute agreement, as Hubbell also provides values for the H atom, these values will be used to calculate the molecular formfactor from the spherical atomic form factors and to compute the scattering intensities from our simulations. Here the assumption is made that the scattering can be represented as arising from independent neutral atoms, each with a spherical electron density distribution. The molecular formfactor is then given by

$$f_m^2 = \sum_{ij} x_i x_j f_i(q) f_j(q) \frac{\sin(qr_{ij})}{qr_{ij}},$$

where the sums are over the atom types present in the sample, x_i is the atomic fraction of atom type i, $f_i(q)$ is the atomic scattering factor for atom type i and r_{ij} are the intramolecular distances between atom centers. It is only an approximation of the molecular formfactor as the electron density in a molecule is changed by the covalent bonds and the environment of the molecule. Thus it is better to directly use the molecular form factor for the normalization of the experimental scattering curves. The total coherent + incoherent form factor is provided by Hubbell (calculated out of the spherical atomic formfactors), Wang (self-consistent-field (SCF) approximation to the Hartree-Fock wave funtion calculation with configuration interaction method (SCFCI) to account for correlations) [27] and Takeuchi (experimentally) [28]. There is a pronounced difference between the molecular formfactor calculated from the sperical atomic form factors and the experimental molecular form factor (see fig:2.20). The molecular formfactor calculated by Wang also shows a deviation to the experimental values although the agreement is better than for the approximation computed from Hubbell's results. I will use the formfactor computed by Wang as his work is the only one of the two giving the coherent as well as the incoherent molecular formfactor.

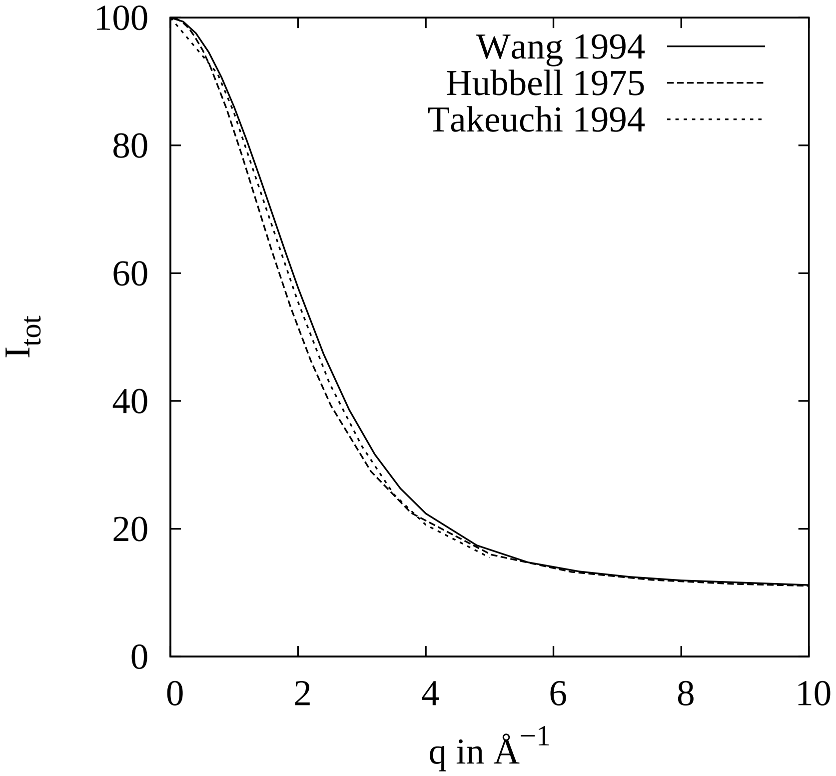

Figure 2.20.: Total molecular formfactor extracted from Wang [27], Takeuchi [28], and Hubbell [22].

Bibliography

[1] Guillot B. A reappraisal of what we have learnt during three decades of computer simulations on water. *J. Mol. Liq.*, 101(1-3):219–60, 2002.

[2] Vega C, Abascal J L F, Conde M M, and Aragones J L. What ice can teach us about water interactions: a critical comparison of the performance of different water models. *Faraday Discuss.*, 141:251–276, 2009.

[3] Rick S W. A reoptimization of the five-site water potential (TIP5P) for use with ewald sums. *J. Chem. Phys.* , 120(13):6085–93, 2004.

[4] Mahoney M W and Jorgensen W L. A five-site model for liquid water and the reproduction of the density anomaly by rigid, nonpolarizable potential functions. *J. Chem. Phys.* , 112(20):8910–22, 2000.

[5] Abascal J L F and Vega C. A general purpose model for the condensed phases of water: TIP4P/2005. *J. Chem. Phys.* , 123:4505–17, 2005.

[6] Rick S W, Stuart S J, and Berne B J. Dynamical fluctuating charge force fields: Application to liquid water. *J. Chem. Phys.* , 101(7):6141–56, 1994.

[7] Hura G, Russo D, Glaeser R M, Head-Gordon T, Krack M, and Parrinello M. Water structure as a function of temperature from x-ray scattering experiments and ab initio molecular dynamics. *Phys. Chem. Chem. Phys.*, 5(10):1981–91, 2003.

[8] Chen B, Xing J, and Siepmann J I. Development of polarizable water force fields for phase equilibrium calculations. *J. Phys. Chem. B*, 104:2391–2401, 2000.

[9] Vega C, Abascal J L F, and Nezbeda I. Vapor-liquid equilibria from the triple point up to the critical point for the new generation of tip4p-like models: Tip4p/ew, tip4p/2005, and tip4p/ice. *J. Chem. Phys.* , 125(3):034503–0312, 2006.

[10] Mills R. Self-diffusion in normal and heavy water in the range 1-45°C. *J. Phys. Chem.* , 77(5):685–8, 1973.

[11] Kell G S and Whalley E. Reanalysis of the density of liquid water in the range 0–150 °C and 0–1 kbar. *J. Chem. Phys.* , 62(9):3496–503, 1975.

[12] Fine R A and Millero F J. Compressibility of water as a function of temperature and pressure. *J. Chem. Phys.* , 59(10):5529–37, 1973.

[13] Sen S, Andrus R L, Baker D E, and Murtagh M T. Observation of an anomalous density minimum in vitreous silica. *Phys. Rev. Lett.*, 93(12):125902–6, 2004.

[14] Liu D, Zhang Y, Chen C-C, Mou C-Y, Poole P H, and Chen S-H. Observation of the density minimum in deeply supercooled confined water. *Proc. Natl. Acad. Sci. USA*, 104(23):9570 –4, 2007.

[15] Paschek D. How the Liquid-Liquid transition affects hydrophobic hydration in deeply supercooled water. *Phys. Rev. Lett.*, 94(21):217802–6, 2005.

[16] Poole P H, Saika-Voivod I, and Sciortino F. Density minimum and liquid–liquid phase transition. *Journal of Physics: Condensed Matter*, 17(43):L431–7, 2005.

[17] Brovchenko I, Geiger A, and Oleinikova A. Liquid-liquid phase transitions in supercooled water studied by computer simulations of various water models. *J. Chem. Phys.* , 123(4):44515–31, 2005.

[18] Brovchenko I, Geiger A, and Oleinikova A. Multiple liquid–liquid transitions in supercooled water. *J. Chem. Phys.* , 118(21):9473–6, 2003.

[19] Xu L, Kumar P, Buldyrev S V, Chen S H, Poole P H, Sciortino F, and Stanley H E. Relation between the widom line and the dynamic crossover in systems with a liquid–liquid phase transition. *Proc. Natl. Acad. Sci. USA*, 102(46):16558–62, 2005.

[20] Mantz Y A, Chen B, and Martyna G J. Temperature-dependent water structure: Ab initio and empirical model predictions. *Chem. Phys. Lett.*, 405(4-6):294–9, 2005.

[21] Møgelhøj A, Kelkkanen A, Wikfeldt K T, Schiøtz J, Mortensen J J, Pettersson L G M, Lundqvist B I, Jacobsen K W, Nilsson A, and Nørskov J K. Ab initio van der waals interactions in simulations of water alter structure from mainly tetrahedral to high-density-like. *Submitted to J. Phys. Chem. B*, 2011.

[22] Hubbell J H, Veigele W J, Briggs E A, Brown R T, Cromer D T, and Howerton R J. Atomic form factors, incoherent scattering functions, and photon scattering cross sections. *J. Phys. Chem. Ref. Data*, 4(3):471–538, 1975.

[23] Krogh-Moe J. A method for converting experimental x-ray intensities to an absolute scale. *Acta Crystallogr.* , 9(11):951–3, 1956.

[24] Norman N. The fourier transform method for normalizing intensities. *Acta Crystallogr.* , 10(5):370–3, 1957.

[25] Corban R and Zeidler M D. X-ray investigation of supercooled water. *Ber. Bunsenges. Phys. Chem.*, 96(10):1463–7, 1992.

[26] Cromer D T. Compton scattering factors for aspherical free atoms. *J. Chem. Phys.* , 50(11):4857–9, 1969.

[27] Wang J, Tripathi A N, and Smith Jr. Chemical binding and electron correlation effects in x-ray and high energy electron scattering. *J. Chem. Phys.* , 101(6):4842–54, 1994.

[28] Takeuchi H, Nakagawa M, Saito T, Egawa T, Tanaka K, Konaka S, and Mitsuhashi T. X-ray scattering by water molecules studied by using synchrotron radiation. *Int. J. Quant. Chem.*, 52(6):1339–48, 1994.

2.8. Computation of the chemical potential

In order to perform a Monte-Carlo simulation in the Grand-Canonical ensemble, we need to determine the chemical potential of liquid water at all thermodynamic conditions of interest. There are different methods to calculate the chemical potential, whose efficiency depends on the structure and density of the investigated fluid.

Widom's test particle insertion method

The standard approach to determine the chemical potential directly from MD or MC simulations was introduced by Widom and independently by Jackson and Klein [1, 2].

In our previous MD computations of liquid water we have generated our configurations in the NPT ensemble whose partition function is given by

$$Q_{NPT} = \frac{1}{N!}\frac{1}{(2\pi\hbar)^{6N}}\frac{1}{2^N}\int dV\, \exp(-\beta PV)\int d\Gamma \exp(-\beta E(\Gamma)) \tag{2.84}$$

Here Γ specifies a point in phase space, which in case of our rigid water models can be described by

$$\Gamma = (\vec{\mathbf{r}}, \vec{\mathbf{s}}, \vec{\mathbf{p}}_r, \vec{\mathbf{p}}_s) = (\vec{r}_1, \ldots, \vec{r}_N, \vec{s}_1, \ldots, \vec{s}_N, \vec{p}_{r1}, \ldots, \vec{p}_{rN}, \vec{p}_{s1}, \ldots, \vec{p}_{sN}) \tag{2.85}$$

r stands for the translational degrees of freedom and s for the rotational ones.

The Gibbs free energy can then be expressed by $G = -k_B T \ln Q_{NPT}$. Based on the definition of the chemical potential in the NPT ensemble

$$\mu = \left.\frac{\partial G}{\partial N}\right|_{T,P} \tag{2.86}$$

one can approximate it by

$$\mu \approx G(N+1, P, T) - G(N, P, T)\,. \tag{2.87}$$

Expressing the Gibbs free energy by the logarithm of the partition function one arrives at

$$\begin{aligned}\mu &= -k_B T \ln Q_{(N+1),P,T} + k_B T \ln Q_{N,P,T} = -k_B T \ln \frac{Q_{(N+1),P,T}}{Q_{N,P,T}} \qquad (2.88)\\ &= -k_B T \ln\left[\frac{1}{N+1}\frac{1}{(2\pi\hbar)^6}\frac{\int\cdots\int d^{3(N+1)}r\, d^{3(N+1)}s\, d^{3(N+1)}p_r\, d^{3(N+1)}p_s\, \exp(-\beta E)}{\int\cdots\int d^{3N}r\, d^{3N}s\, d^{3N}p_r\, d^{3N}p_s\, \exp(-\beta E)}\right].\end{aligned}$$

With the internal energy E given by

$$E = \sum_{i=1}^{N}\frac{\vec{p}_{ri}^{\,2}}{2m} + \sum_{i=1}^{N}\sum_{j=x,y,z}\frac{p_{sij}}{2I_j} + U(\mathbf{r}, \mathbf{s}) \tag{2.89}$$

the chemical potential can be splitted in an ideal (kinetic) and an excess part $\mu = \mu_{id} + \mu_{ex}$. Assuming that the potential energy of $N+1$ particles can be written as the energy of N particles plus some $\Delta U = U_{N+1} - U_N$ one arrives at

$$\begin{aligned}
\mu_{ex} &= -k_B T \ln \left[\frac{1}{\langle V \rangle_N} \frac{1}{8\pi^2} \frac{\int \cdots \int d^{3(N+1)}r \, d^{3(N+1)}s \exp(-\beta U_{N+1}(\mathbf{r},\mathbf{s}))}{\int \cdots \int d^{3N}r \, d^{3N}s \, \exp(-\beta U_N(\mathbf{r},\mathbf{s}))} \right] && (2.90) \\
&= -k_B T \ln \left[\frac{1}{\langle V \rangle_N} \langle V \exp(-\beta \Delta U) \rangle_N \right] . && (2.91)
\end{aligned}$$

Here the average $\langle V \exp(-\beta\Delta U)\rangle_N$ is practically computed by randomly inserting a "ghost molecule" into the N molecule configurations and determining its interaction energy ΔU and then averaging over all insertions and all configurations.

The ideal part decomposes into $6(N+1)$ Gaussian integrals in the numerator and $6N$ ones in the denominator which then cancel to just 6 integrals that can be computed analytically.

$$\begin{aligned}
\mu_{id} &= -k_B T \ln \left[\frac{\langle V \rangle}{N+1} \frac{1}{(2\pi\hbar)^3} \int dp_r^3 \exp\left(-\beta \vec{p}_r/(2m)\right) \right] \\
&\quad -k_B T \ln \left[\frac{8\pi^2}{(2\pi\hbar)^3} \int dp_s^3 \exp\left(-\beta \sum_{j=x,y,z} \frac{p_{sj}}{2I_j} \right) \right] && (2.92) \\
&= -k_B T \ln \left[\frac{\langle V \rangle}{N+1} \left(\frac{m k_B T}{2\pi\hbar^2} \right)^{3/2} \right] - k_B T \ln \left[\frac{(2k_B T)^{3/2} (\pi I_1 I_2 I_3)^{1/2}}{2\hbar^3} \right] \\
&= k_B T \ln \left[\frac{N+1}{V} \Lambda_T^3 \right] - k_B T \ln q^{(rot)} && (2.93) \\
&= \mu_{id}^{(trans)} + \mu_{id}^{(rot)} && (2.94)
\end{aligned}$$

Thus the Widom method in principle allows an easy determination of the chemical potential using simple MD or MC configurations. But the problems start if the investigated system is dense or otherwise badly conditioned, then convergence of the method becomes poor and the quality of convergence difficult to determine. This is because insertions with a negative ΔU that would contribute to the average $\langle V \exp(-\beta\Delta U)\rangle_N$ with exponential weight become seldom. A negative ΔU implies a hole in the configuration were the inserted "ghost molecule" can fit in without overlapping with other molecules. This in case of a dense liquid like water is very rare.

One can improve the performance of the Widom method by introducing grid search methods that concentrate the insertions on holes in the configurations but the problem remains, that configurations with holes occur only infrequently but dominate the average, thus resulting in bad convergence. As an example for the problems that arise for the Widom method for water figure 2.21 shows two typical running averages against the number of configurations. For each configuration 1000000 insertions were made. One observes that a single configuration can lead to a big jump in the chemical potential and that a convergence is not apparent. In addition the corresponding results for the overlapping distribution method of Shing and Gubbins are shown, which is much better behaved and will be explained in the next section.

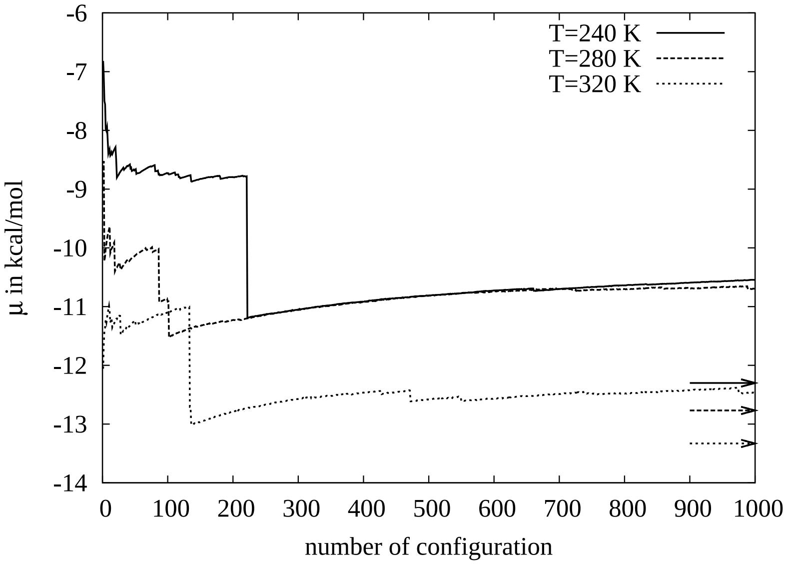

Figure 2.21.: Results of the chemical potential calculation for TIP4P/2005 water with the Widom insertion method. The results for the overlapping distribution method of Shing and Gubbins are shown as arrows.

Overlapping distribution method of Shing and Gubbins

The overlapping distribution method of Shing and Gubbins [3] improves on the Widom insertion method because it combines insertion and deletion of molecules to gain more information about the system. Shing and Gubbins ansatz in the NVT ensemble is based on the following equation.

$$\begin{aligned}\langle\exp(-\beta\Delta U)\rangle_{N-1} &= \frac{\int\exp(-\beta\Delta U)\exp(-\beta U_{N-1})dx^{N-1}}{\int\exp(-\beta U_{N-1})dx^{N-1}}\\ &= \frac{\int\exp(-\beta U_N)dx^{N-1}}{\int\exp(-\beta U_N)\exp(\beta\Delta U)dx^{N-1}}\\ &= \frac{\int\exp(-\beta U_N)dx^{N}}{\int\exp(-\beta U_N)\exp(\beta\Delta U)dx^{N}}\\ &= \langle\exp(\beta\Delta U)\rangle_N^{-1} \qquad (2.95)\end{aligned}$$

It implies that the chemical potential can be calculated by averaging over the deletion of molecules, but as with the Widom insertion method there is a problem concerning sampling that is even more severe in this case. There are no configurations with overlapping molecules in the reference sample that was generated by MD or MC simulations. Thus there will always be a hole in the $N-1$ configurations after molecule deletion introducing a bias in the calculation. There are some methods to circumvent this problem [4].

But Shing and Gubbins found an easier and much more practical method by combining insertion and deletion. Therefore they introduced two distribution functions f and g

which are defined so that

$$\begin{aligned}\langle \exp(-\beta\Delta U)\rangle_{N-1} &= \int f_{N-1}(\Delta U)\exp(-\beta\Delta U)d(\Delta U) && (2.96)\\ \langle \exp(\beta\Delta U)\rangle_{N} &= \int g_{N}(\Delta U)\exp(\beta\Delta U)d(\Delta U) && (2.97)\end{aligned}$$

with

$$f_{N-1}(\Delta U)\,d(\Delta U) = \frac{\int_c \exp(-\beta U_{N-1})\,dx_2\cdots dx_N}{\int \exp(-\beta U_{N-1})\,dx_2\cdots dx_N} \qquad (2.98)$$

$$g_{N}(\Delta U)\,d(\Delta U) = \frac{\int_c \exp(-\beta U_{N})\,dx_2\cdots dx_N}{\int \exp(-\beta U_{N})\,dx_2\cdots dx_N}\,, \qquad (2.99)$$

where c constrains the integration to values of ΔU between ΔU and $\Delta U + d(\Delta U)$.

f_{N-1} is the energy distribution of the particle insertion and g_N is the energy distribution of the particle deletion.

To see that the f and g distribution functions are related by the chemical potential we first look at g_N.

$$\begin{aligned} g_N(\Delta U)d(\Delta U) &= \frac{\exp(-\beta\Delta U)\int_c \exp(-\beta U_{N-1})dx_2\ldots dx_N}{\int \exp(-\beta U_N)dx_2\ldots dx_N}\\ &= \frac{\exp(-\beta\Delta U)f_{N-1}(\Delta U)d(\Delta U)\ \int \exp(-\beta U_{N-1})dx_2\ldots dx_N}{\int \exp(-\beta U_N)dx_2\ldots dx_N}\\ &= \frac{\exp(-\beta\Delta U)f_{N-1}(\Delta U)d(\Delta U)}{\langle \exp(-\beta\Delta U)\rangle_{N-1}}\,. && (2.100)\end{aligned}$$

Thus we find

$$g_N(\Delta U) = \exp(\beta\mu_e x)f_{N-1}(\Delta U)\exp(-\beta\Delta U) \qquad (2.101)$$

μ_{ex} can be directly computed from f and g if the distributions overlap sufficiently namely are known at the same ΔU region to an adequate accuracy. This procedure eliminates any sampling problems as the fitting will exclude the regions of ΔU that suffered from sampling problems or poor statistics namely the small ΔU region for the f_{N-1} distribution and the large ΔU one for the g_N distribution.

For large N the difference between g_N and g_{N-1} is very small and it is sufficient to use MD simulations performed at $N-1$ thus giving g_{N-1} instead of g_N. The main error originates from the size and the quality of the overlap region.

As a first test in a relatively dense system that is still accessible for the Widom insertion method, we computed the chemical potential of a LJ fluid at $T = 1$ and $\rho = 0.8$. In figure 2.22 (a) μ_{ex} is plotted in dependence on ΔU showing a clear and large plateau. This is due to the strong overlap of the two distributions $f(N-1)$ and $g(N-1)$, which is visible in figure 2.22 (b). Here one can also see, that each distribution alone is enough to give in impression of the whole distribution, so that it is possible to compute μ_{ex} by the Widom insertion method. A comparison of the results of both methods is given in figure 2.22 (c).

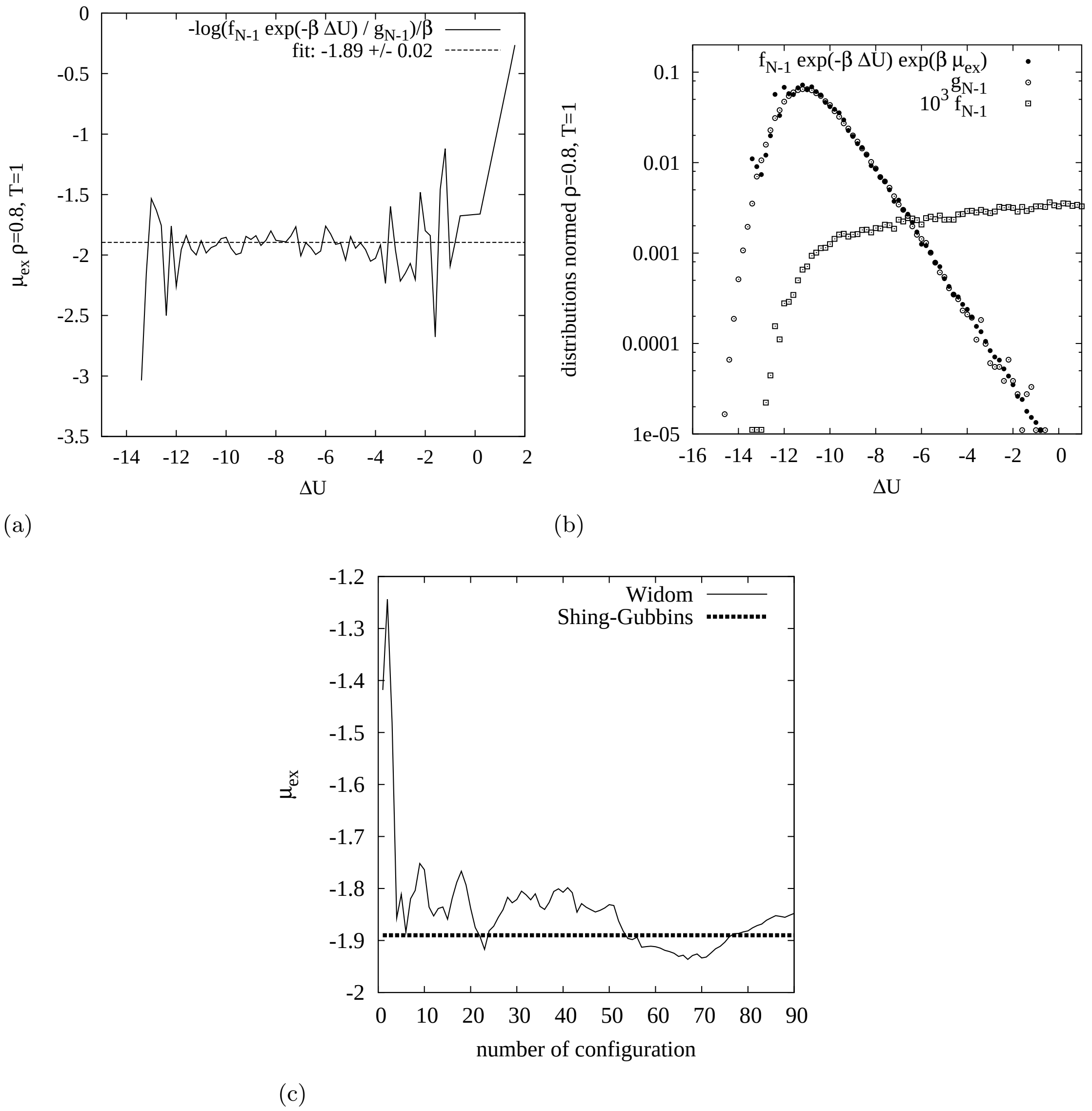

Figure 2.22.: (a) μ_{ex} in dependence on ΔU as it is calculated from 2.101 for a LJ fluid at $T = 1$ and $\rho = 0.8$. (b) The f and g distributions together with $f_{N-1}\exp(-\beta\Delta U)\exp(\beta\mu_{ex})$ which as expected matches g_{N-1}. (c) Comparison between the results of the Widom insertion method and of Shing-Gubbins' method.

Figure 2.23 shows the f and g distributions for the TIP4P/2005 model at two different temperatures as well as $f_{N-1}\exp(-\beta\Delta U)$ which should be proportional to g_{N-1} according to equation 2.101. Here one can see, that the overlap region is big and smooth for high temperatures but small and noisy for small ones, thus increasing the error in the μ_{ex} determination with decreasing temperature. One can also identify why the Widom insertion method performs so poorly for water in comparison to the LJ fluid. This is because $f_{N-1}exp(-\beta\Delta U)$ while giving a good overlap with g_{N-1} is not enough to reproduce the general form especially the maximum of g_{N-1}.

Figure 2.24 shows the excess chemical potential μ_{ex} in dependence on ΔU as it is calcu-

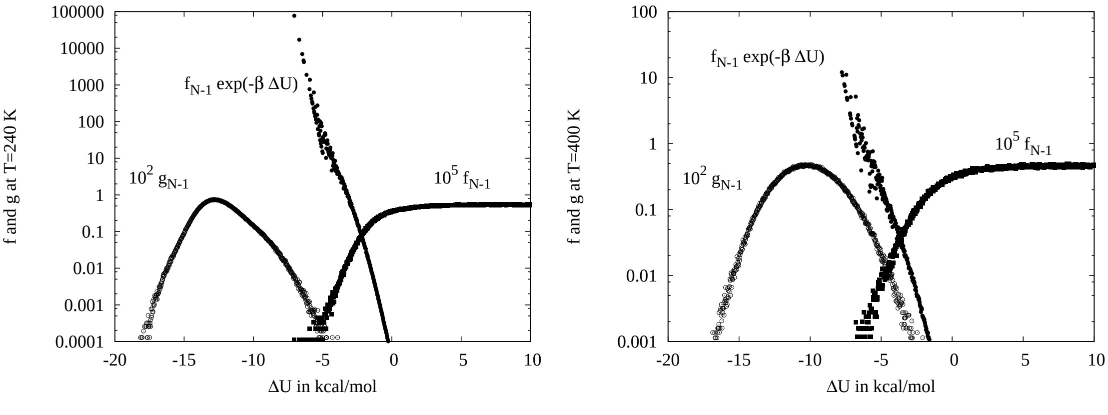

(a) (b)

Figure 2.23.: The f_{N-1} and g_{N-1} distributions of the TIP4P/2005 model for $T = 240$ K (a) and for $T = 400$ K (b) as well as $f_{N-1} \exp(-\beta\Delta U)$ which should be proportional to g_{N-1} according to equation 2.101.

lated from 2.101 for $T = 240$ K and $T = 400$ K. In agreement with figure 2.23 there is a big overlap region in the high temperature case leading to a clear plateau, which can be used to fit the exact value of μ_{ex}. In the low temperature case the plateau is much smaller but the determination of the chemical potential is still possible.

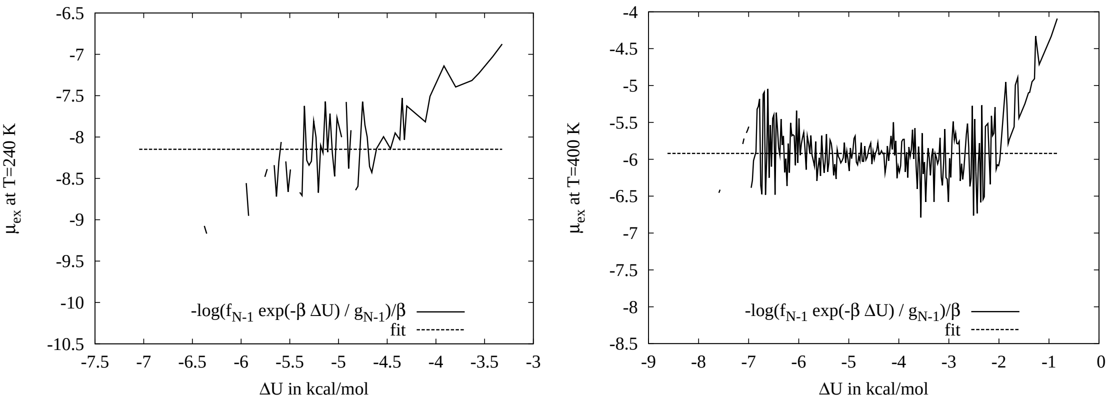

(a) (b)

Figure 2.24.: μ_{ex} in dependence on ΔU as it is calculated from 2.101 for $T = 240$ (a) K and $T = 400$ K (b).

Replotting the g distribution determined directly together with that computed from equation 2.101 one observes that they match very well confirming our values for μ_{ex}.

Thermodynamic integration

In order to test if our results for the chemical potential are self-consistent, we use thermodynamic integration. If one knows the chemical potential at one state point it is possible to get further values by integration in the T, P plane. We use the Gibbs-Helmholtz

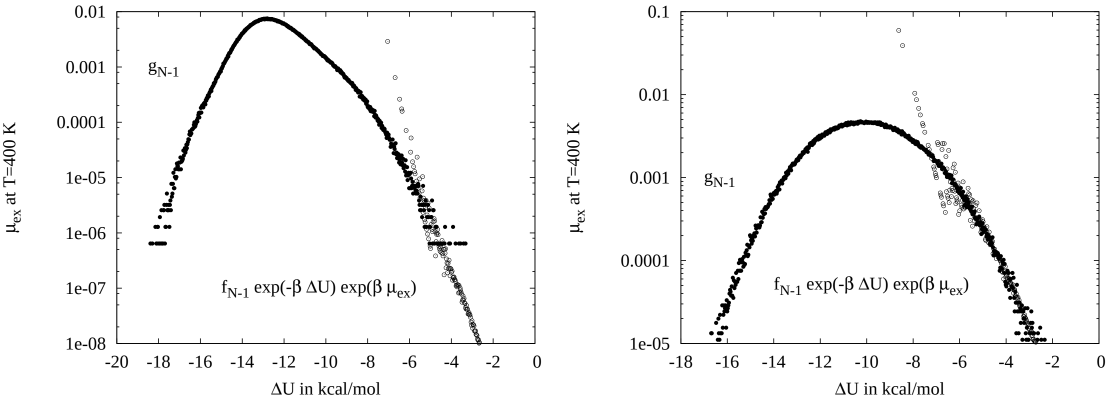

(a) (b)

Figure 2.25.: g computed directly from the MD configurations ($T = 240$ K (a) and $T = 400$ K (b)) together with g computed from equation 2.101

equation to move along a line of constant pressure P

$$\frac{\partial \mu / T}{\partial T} = -\frac{h}{T^2} \to \frac{\mu(T,P)}{T} = \frac{\mu(T_0,P)}{T_0} - \int_{T_0}^{T} \frac{h}{T^2} dT \tag{2.102}$$

and the following equation from thermodynamics to move along a line of constant temperature T

$$dG|_T = Nd\mu|_T = VdP \to \mu(T,P) = \mu(T,P_0) + \int_{P_0}^{P} \frac{dP}{\rho}. \tag{2.103}$$

Here h is the enthalpy per molecule and ρ is the density, which were taken from our own MD simulations of the TIP4P/2005 water and from [5].

First we compute the chemical potential on the coexistence line at $T = 550$ K and $\rho = 0.0213$ g/cm^3 and $P = 38$ bar [6] by Widom's insertion method. This is easily possible because the density is so low. Thus we arrive at $\mu = -18.38$ kcal/mol which is near the ideal gas value of $\mu = -18.72$ kcal/mol as would be expected. As we know that the chemical potential is the same on both sides of the coexistence line, we can now compute the chemical potential at a different state point by equation 2.102 and 2.103.

2.8.1. Results

Figure 2.26 shows the final result for the chemical potential as it was computed with the Shing-Gubbins method and with thermodynamic integration for several pressures and temperatures. The agreement is excellent giving us confidence that we now have reliable values for the chemical potential of TIP4P/2005 water in the temperature range of 240 K to 400 K which we can use for our Grand-Canonical ensemble simulations.

We also want to perform Grand-Canonical ensemble simulations in the low temperature range, where the chemical potential cannot be determined precisely enough by the Shing-Gubbins method because of a large gap between the g and f distributions (see figure 2.29). We therefore use the values obtained by thermodynamic integration in this

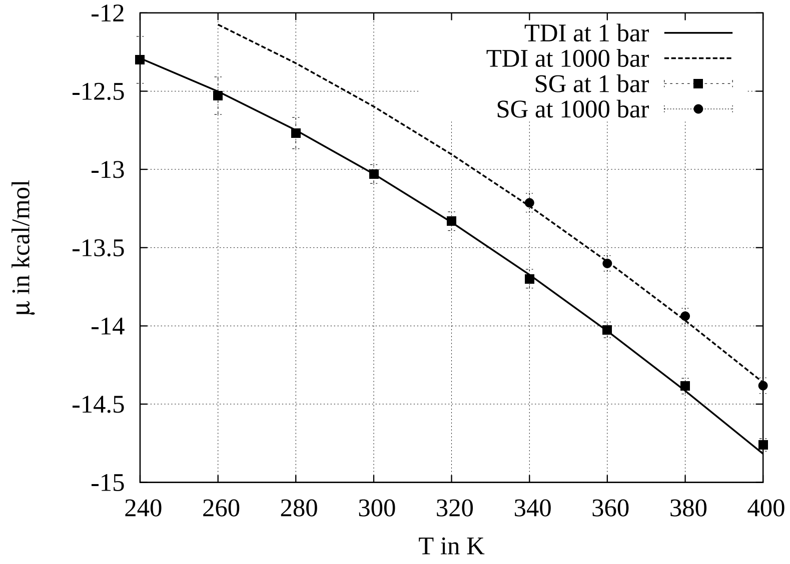

Figure 2.26.: Results of the chemical potential calculation for TIP4P/2005 water. The thermodynamic integration (TDI) results are in excellent agreement with the results from the Shing-Gubbins (SG) computations.

temperature region without a direct check. the results are presented in figure 2.28. Here we also include results obtained by Vlot et al using the Shing-Gubbins method on TIP4P water [7], which are quite close to our results because the TIP4P and the TIP4P/2005 model are very similar. The TIP4P/2005 water reproduces the experimental data for the chemical potential, taken from [8], very well demonstrating the good quality of the potential.

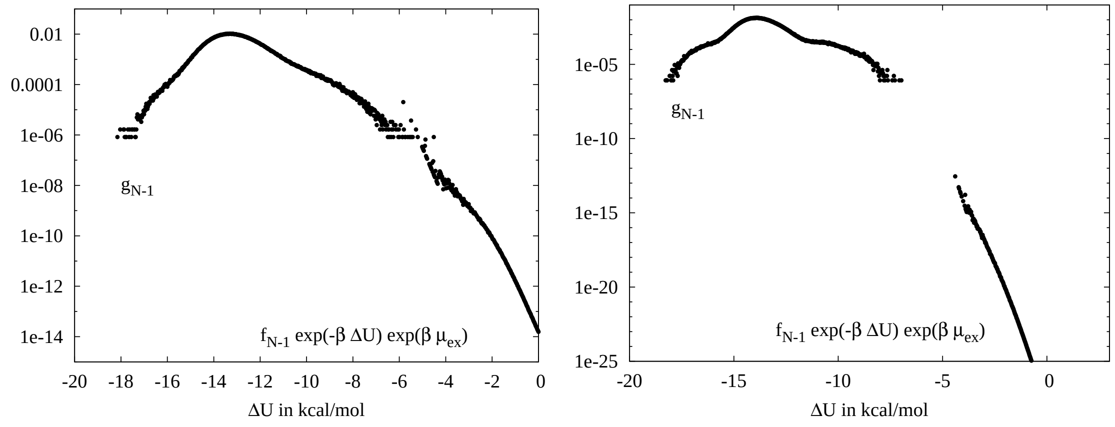

(a) (b)

Figure 2.27.: g computed directly from the MD configurations ($T = 200$ K (a) and $T = 100$ K (b)) together with g computed from equation 2.101

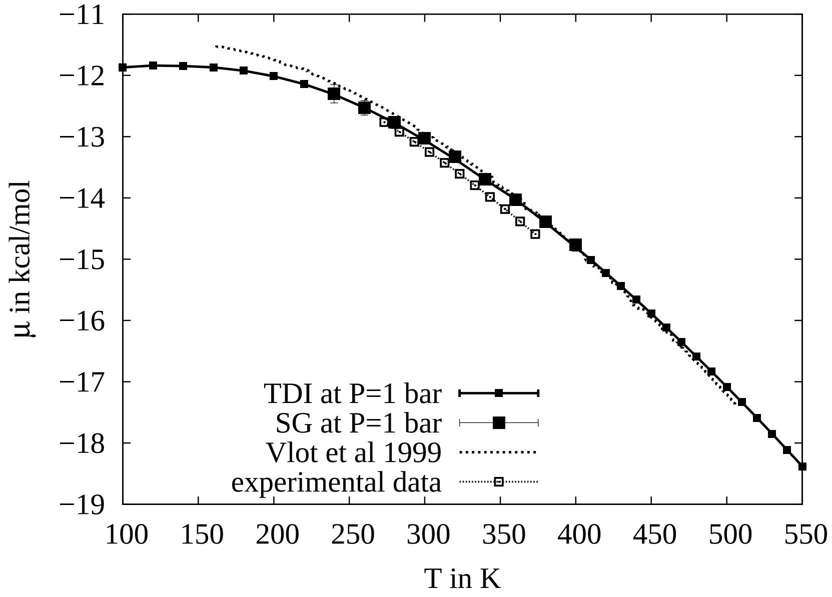

Figure 2.28.: Results of the chemical potential calculation for TIP4P/2005 water. The thermodynamic integration (TDI) results are extended to the low temperature regime, where the Shing-Gubbins (SG) method is no longer applicable. The results of Vlot et al for the very similar TIP4P model are plotted in comparison [7] together with experimental values from [8].

Final consistency check

As a final consistency check we perform a MC simulation at $T = 320$ K with $\mu = -13.33$ kcal/mol and check if the density converges to the MD value of $\rho = 0.9896$ g/cm^3. As a start configuration for the MC run we take a MD configuration generated at $T = 280$ K and a density of $\rho = 1.0001$ g/cm^3. The result is displayed in figure 2.29. The converence is very slow because the probability of insertion is small in the dense fluid. The average density of the MC simulation is 0.9899 g/cm^3 which is very close to the expected density indicated by an arrow. A table of the chemical potential values including the polarization correction of 4.21 kJ/mol is included in the appendix A.2.2

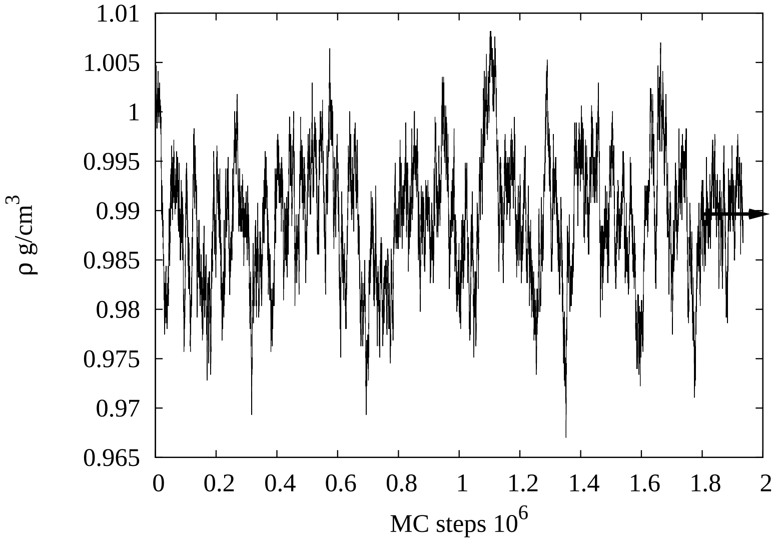

Figure 2.29.: The development of the density and its convergence to the expected value, which is indicated by an arrow.

Bibliography

[1] Widom B. Some topics in the theory of fluids. *J. Chem. Phys.* , 39:2808–12, 1963.

[2] Jackson J L and Klein L S. Potential distribution method in equilibrium statistical mechanics. *Phys. Fluids*, 7:228–32, 1964.

[3] Shing K S and Gubbins K E. The chemical potential in dense fluids and fluid mixtures via computer simulation. *Molecular Physics*, 46(5):1109–28, 1982.

[4] Parsonage N G. Chemical-potential paradox in molecular simulation. explanation and monte carlo results for a Lennard-Jones fluid. *J. Chem. Soc., Faraday Trans.*, 92(7):1129–1134, 1996.

[5] Pi H L, Aragones J L, Vega C, Noya E G, Abascal J L F, Gonzalez M A, and McBride C. Anomalies in water as obtained from computer simulations of the TIP4P/2005 model: density maxima, and density, isothermal compressibility and heat capacity minima. *Mol. Phys.*, 107:365–74, 2009.

[6] Vega C, Abascal J L F, and Nezbeda I. Vapor-liquid equilibria from the triple point up to the critical point for the new generation of TIP4P-like models: TIP4P/Ew, TIP4P/2005, and TIP4P/ice. *J. Chem. Phys.* , 125:034503–9, 2006.

[7] Vlot M J, Huinink J, and van der Eerden J P. Free energy calculations on systems of rigid molecules: An application to the TIP4P model of h[sub 2]O. *J. Chem. Phys.* , 110(1):55, 1999.

[8] Domotor G and Hentschke R. Atomistically modeling the chemical potential of small molecules in dense systems. *J. Phys. Chem. B*, 108(7):2413–7, 2004.

2.9. Characteristics of carbon nanotubes

2.9.1. Why are carbon nanotubes interesting for water studies

The carbon nanotube (CNT) provides a confining geometry without a strong interaction with H_2O molecules, which may influence the hydrogen bonding. It is thus an ideal medium to study the hydrogen bond network under extreme conditions. While confinement suppresses the melting temperature of water by about 100 K and thus allows to investigate liquid water at deep temperatures, it is questionable if any insights into confined water are constructive to understand bulk water. We will investigate the comparability of confined and bulk water in the results section.

Another motivation to study the vicinal phases of water in CNTs stems from its unusually enhanced transport properties, which make CNTs similar to biological water channels and open up possible applications as novel drug delivery agents or water filters.

We will investigate thermodynamic, structural and dynamic properties by Grand Canonical Monte Carlo and molecular dynamics simulations in order to characterize the properties of confined water systematically in dependence on tube diameter, temperature and pressure.

2.9.2. Carbon nanotubes - general characteristics

As detailed in [1] one can start with a perfect graphene sheet in order to imagine the structure of a carbon nanotube. Graphene is a polyaromatic monoatomic layer consisting of sp^2-hybridized carbon atoms arranged in hexagons. Genuine graphite consists of layers of this graphene.

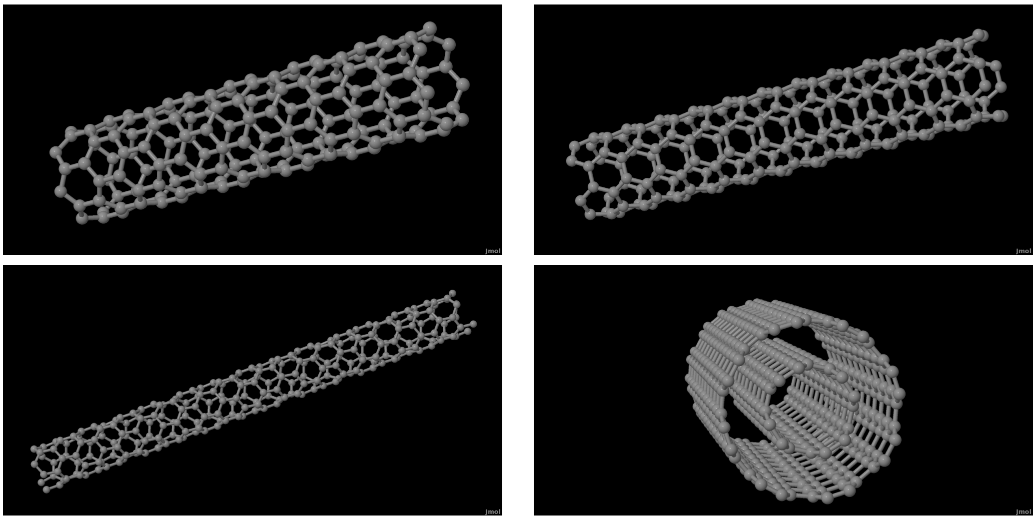

Figure 2.30.: Different structures of carbon nanotubes: zig-zag (upper left), armchair (upper right), helical or chiral (lower left) and double walled tube (lower right)

In order to create a nanotube one can now roll up the graphene sheet in the direction of any lattice vector thus allowing for a smooth closure because of the periodicity of the lattice. Thus the different kinds of single walled carbon nanotubes can be characterized by the lattice vector of the roll direction. Figure 2.30 shows some examples. One can differentiate between tubes with a zig-zag structure (upper left) with lattice vector (n,0), where the hexagonal rings on the surface seem to alternate in a zig-zag course, tubes with an armchair structure (upper right) with lattice vector (n,n), where the hexagonal rings are on a parallel line to the tube axis, and the chiral or helical structure (lower left) with lattice vector (n,m), which looks irregular. In addition the tubes can be double walled or more (lower right). In multi walled carbon nanotubes the intergraphene distance varies between 3.4 Å for the inner walls and approaches the value of genuine graphite (3.35 Å) for the outer ones, where the shift in the relative positions of carbon atoms from superimposed graphenes is small with respect to that in graphite.

A direct consequence of this construction is that the tube diameter and length cannot be choosen continuously but are limited by the discrete lattice vectors (n,m). The tube diameter is given by

$$D = \frac{a_{CC}\sqrt{3(n^2+m^2+nm)}}{\pi}\,, \tag{2.104}$$

where a_{CC} is the C-C bond length, which lies somewhere between 1.41 Å, which is the bond length in graphite, and 1.44, which is the bond length in C_{60}. For our computations we choose a bond length of 1.44 Å for tubes and 1.421 Å for sheets.

As we use a smeared potential for the carbon-water interaction, the explicit geometry of the carbon nanotube does only enter our computations through the constraints on its possible diameter.

The smallest SWNTs (single wall nanotubes) successfully synthesized had a diameter of 4 Å [2], while the most frequent diameter encountered for most high yield synthesis techniques is $\approx$ 14 Å. Calculations have shown that collapsing the single wall tube into a flattened two-layer ribbon is energetically more favorable than maintaining the tubular morphology beyond a diameter value of $\approx$ 25 Å [3]. This results in a flattening of the tubes against each other, so that they form a honeycomb structure.

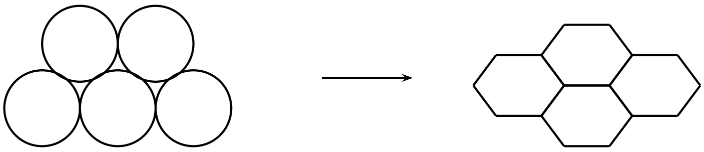

Experimental data seem to confirm this statement as diameters wider than 25 Å are only rarely reported. We therefore limit our investigation to tubes of diameters from 11 Å to a maximum of 26 Å. We only use armchair structures and two chiral ones whose diameters are given in table B.3. In order to make contact to bulk water we also study a 49.50 Å diameter tube. Carbon nanotubes can have lengths in the micrometer or millimeter range depending on the preparation method. We will try to choose the length long against the tube diameter which for the widest tubes gives a diameter-length ratio of about 1/3.

Note that despite the use of periodic boundaries along the tube axis and the inclusion of long range interactions this is important when longitudinally ordered water structures are observed. In this case incommensurability of the ordering along the tube axis in relation to the tube length may induce artificial effects.

Considering the geometric construction of carbon nanotubes it is important to note that while one can imagine them to be formed out of rolled up graphene sheets their hybridization is not pure sp^2 as the $C = C$ bond angles are not planar but deformed because of the tube curvature. Thus depending on the tube diameter there is a degree of sp^3 hybridization, which results in a more reactive SWNT surface and by inducing variable overlapping of energy bands results in an unique and versatile electronic behavior [1].

The graphenes in graphite have π electrons which allow for van der Waals forces to develop between the sheets. Similar reasons cause the SWNTs to spontaneously arrange into hexagonal arrays.

2.9.3. Modelling the water-carbon interaction

There exists a broad range of water-carbon interaction potentials in the literature. As far as we could establish all of them are based on a pairwise additive Lennard-Jones potential between the oxygen atoms of the water and the carbon atoms $U(r) = 4\epsilon_{CO}((\sigma_{CO}/r)^{12} - (\sigma_{CO}/r)^6)$. Some models also include a carbon-hydrogen LJ interaction and an electrostatic interaction between the partially charged sites on the water molecules and point quadrupole moments on the carbons. An overview is given in [4].

One of the most common potentials was published by Bojan and Steele in 1987 [5]. They used experimental low-coverage isotherm data of O_2 on exfoliated graphite to obtain the first two virial coefficients for this absorbate over a range of temperature. The results were then compared with the virial expression of the LJ potential yielding $\epsilon_{CO} = 0.3135$ kJ/mol and $\sigma_{CO} = 3.19$ Å.

In their studies from 1999 and 2001 Markovic et al. [6, 7] performed scattering experiments of water monomers and water clusters on graphite. They increased ϵ_{CO} to 0.3908 kJ/mol with $\sigma_{CO} = 3.19$ Å and introduced a C-H Lennard-Jones interaction $\epsilon_{CH} = 0.2528$ kJ/mol and $\sigma_{CH} = 2.82$ Å. They also added an electrostatic interaction between point quadrupole moments on the carbon and the charges on the oxygen and hydrogen sites.

In order to determine the parameters for the water-carbon interaction Werder et al [4] determined the contact angle of water droplets on graphite as a function of the water-carbon interaction and found that the macroscopic contact angle of 86° is recovered for $\epsilon_{CO} = 0.392$ kJ/mol and $\sigma_{CO} = 3.19$ Å.

Other parametrizations are based on the Lorentz-Berthelot mixing rules

$$\epsilon_{CI} = \sqrt{\epsilon_{CC}\epsilon_{II}} \quad \sigma_{CI} = \frac{1}{2}(\sigma_{CC} + \sigma_{II}) \quad I = O, H \tag{2.105}$$

giving parameters of $\epsilon_{CO} = 0.389$ kJ/mol, $\sigma_{CO} = 3.28$ Å, $\epsilon_{CH} = 0.129$ kJ/mol and $\sigma_{CH} = 2.81$ Å [8] and $\epsilon_{CO} = 0.3876$ kJ/mol and $\sigma_{CO} = 3.262$ Å [9].

Totally different parameters result from an estimation of the water/single-layer graphite interaction by Feller and Jordan [10], who used second-order Møller-Plesset perturbation theory to calculate the interaction energy between a water molecule and acenes as large as $C_{96}H_{24}$. They obtain a binding energy of -5.8 kcal/mol which would correspond to $\epsilon_{CO} = 1.2970$ kJ/mol and $\sigma_{CO} = 3.2473$ Å [4].

As it is difficult to judge which parametrization is superior to others, we put the emphasis on simlicity and comparability and use the potential of Bojan and Steele because it is very common and consists just of a LJ potential between the oxygen and the carbon.

But it is important to note at this point that the condensation transition and thus the filling of the tubes is sensitive to the choice of the water-carbon interaction parameter as pointed out by Hummer et al [11]. They conducted MD simulations of a 8.1 Å tube at $\sigma_{CO} = 3.2751$ Å and $\epsilon_{CO} = 0.114333$ kcal/mol, as well as for a weakened water-nanotube van der Waals attraction with parameters $\sigma_{CO} = 3.4138$ Å and $\epsilon_{CO} = 0.06461$ kcal/mol, observing, that this change leads to a transition from a filled tube to one fluctuating between a full and empty state on a nanosecond timescale.
As our potential is relatively weak we observe a filling of the SCNTs only for diameters larger than 11 Å at atmospheric pressure in contrast to other studies, which find single-file filling for smaller tubes. We will investigate the influence of ϵ on the condensation transition in the following section.

Potential of the carbon sheet

Instead of considering the interaction of the water molecules with each carbon atom explicitly we use a smeared potential, which can be computed by integrating over a carbon sheet of surface density θ.

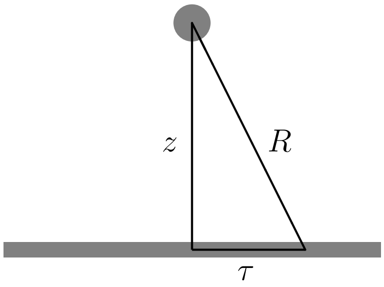

Figure 2.31.: We integrate over the carbon sheet with carbon atom number density θ.

$$U(z) = 2\pi\theta \int_0^\infty U_{LJ}(R;\epsilon,\sigma)\tau d\tau \,, \tag{2.106}$$

where $R = \sqrt{z^2+\tau^2}$ see figure 2.31. Thus the potential at a distance z from the carbon sheet is given by

$$U(z) = 2\pi\theta\epsilon\sigma^2 \left[\frac{2}{5}\left(\frac{\sigma}{z}\right)^{10} - \left(\frac{\sigma}{z}\right)^4\right] . \tag{2.107}$$

For a derivation see appendix B.2.

To judge the quality of the smearing approximation we also compute the explicit potential by generating coordinates for a large sheet of carbon 60×60 Å^2 and determining

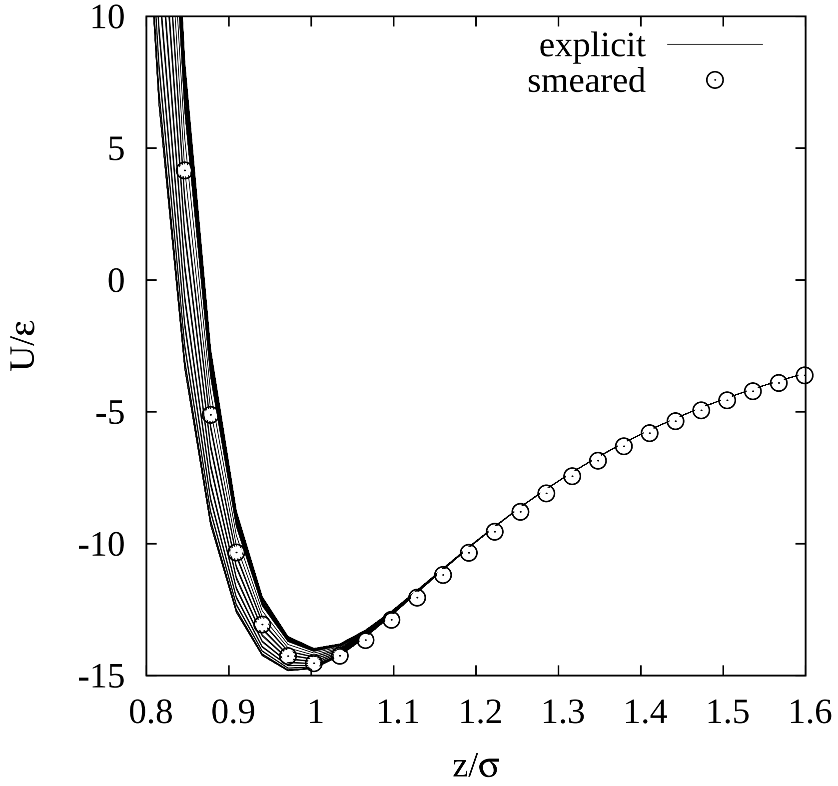

Figure 2.32.: The potential U of carbon sheet against the distance z to the wall. The smeared potential (points) is shown in comparison to the explicit potential (lines) calculated using the actual carbon atom positions. The spread in the explicit potential lines is due to the different local carbon environment near the surface.

the potential of a water molecule that is near the middle of the sheet. Figure 2.32 shows the spread in the explicit potential that originates from the different local environment, depending on the exact position of the water molecule with regards to the carbon sheet.

Potential of the carbon nanotube

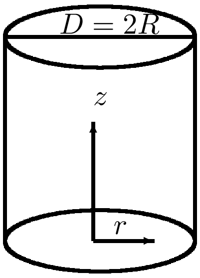

Figure 2.33.: The sketch demonstrates our notation.

We also use a smeared potential for the carbon nanotubes. The potential at distance

$r = Rx$ from the axis of a single wall nanotube is given by [12]

$$U(r;R) = 3\pi\theta\epsilon\sigma^2 \left[\frac{21}{32}\left(\frac{\sigma}{R}\right)^{10} M_{11}(x) - \left(\frac{\sigma}{R}\right)^4 M_5(x)\right] \tag{2.108}$$

where θ is the surface density of C atoms and R is the radius of the cylinder. Here we use the integrals

$$M_n(x) = \int_0^\pi d\phi \frac{1}{(1 + x^2 - 2x\cos\phi)^{n/2}} \tag{2.109}$$

where n is a positive integer. For a derivation see appendix B.2.

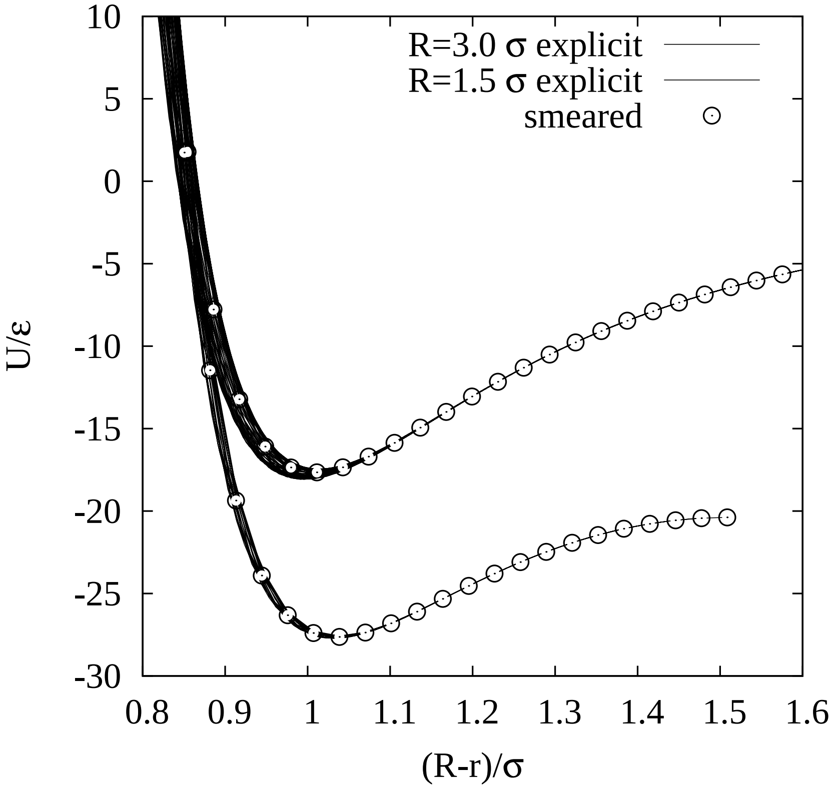

Figure 2.34.: The potential U of carbon nanotubes of radius $1.5\sigma_{CO}$ and $3.0\sigma_{CO}$ against the distance r to the tube wall. The smeared potential (points) is shown in comparison to the explicit potential (lines) calculated using the actual carbon atom positions in an armchair configuration. The spread in the explicit potential lines is due to the different local carbon environment near the surface, which is more pronounced for a larger tube diameter.

As for the carbon sheets we also compute the exact potential of a water molecule in a long 60 Å tube far away from the edges to see the spread in the potential due to the local carbon environment. The results are shown in figure 2.34. The spread increases with the diameter of the tube and is largest for the carbon sheet as demonstrated in figure 2.32. This is due to the screening ability of the carbon atoms on the other side of the tube that level out the potential ripples near the surface.

Our assumption that a smeared potential suffices to describe the behavior of water in CNTs is further strengthened by a study of Wang et al [13] that found only a very small helicity effect for the tube diameters investigated in this work.

We limit our investigation to single walled carbon nanotubes as it was shown by Rana and Chandra [14] that the thickness of the nanotube wall has only minor effects on the density profiles, hydrogen bond network and the wetting characteristics.

2.9.4. Water model for confined water

As was pointed out by Alexiadis and Kassinos [15] the water models proposed for bulk water are generally not correct for confined water [1]. But they show by investigating 6 different flexible and non-flexible water models in rigid and flexible tubes that the general trend of density, hydrogen bond number, and diffusion does not depend on the specific water or tube model. We thus limit our investigation to rigid carbon nanotubes filled by TIP4P/2005 water, as we found this water model to perform best in the bulk simulations.

---

[1] This, by the way, is a basic problem which plagues phenomenological force fields quite generally. A phenomenological force field is always parameterized to fit certain physical / thermodynamical data measured for small subsets ('training sets') of targetted systems. All interactions which are not or insufficiently present in the training sets are therefore not reliably parameterized and must be treated with caution or entirely avoided.

Bibliography

[1] Monthioux M, Serp P, Flahaut E, Razafinimanana M, Laurent C, Peigney A, Bacsa W, and Broto J-M. *Springer handbook of nanotechnology*, chapter 3. edited by Bharat Bhushan (Springer), 2006.

[2] Wang N, Tang Z K, Li G D, and Chen J S. Materials science: Single-walled 4 å carbon nanotube arrays. *Nature*, 408:50–1, 2000.

[3] Tersoff J and Ruoff R S. Structural properties of a carbon-nanotube crystal. *Phys. Rev. Lett.* , 73(5):676–9, 1994.

[4] Werder T, Walther J H, Jaffe R L, Halicioglu T, and Koumoutsakos P. On the water- carbon interaction for use in molecular dynamics simulations of graphite and carbon nanotubes. *J. Phys. Chem. B*, 107(6):1345–52, 2003.

[5] Bojan M J and Steele W A. Interactions of diatomic molecules with graphite. *Langmuir*, 3(6):1123–7, 1987.

[6] Markovi N, Andersson P U, Någård M B, and Pettersson J B C. Scattering of water from graphite: simulations and experiments. *Chem. Phys.*, 247(3):413–30, 1999.

[7] Tomsic A, Andersson P U, Markovic N, Piskorz W, Svanberg M, and Pettersson J B C. Molecular-dynamics simulations of clustersurface collisions: Emission of large fragments. *J. Chem. Phys.* , 115(22):10509–18, 2001.

[8] Gordillo M C and Marti J. Hydrogen bond structure of liquid water confined in nanotubes. *Chem. Phys. Lett.*, 329(5-6):341–5, 2000.

[9] Koga K, Gao G T, Tanaka H, and Zeng X C. Formation of ordered ice nanotubes inside carbon nanotubes. *Nature*, 412(6849):802–5, 2001.

[10] Feller D and Jordan K D. Estimating the strength of the water/single-layer graphite interaction. *J. Phys. Chem. A*, 104(44):9971–5, 2000.

[11] Hummer G, Rasaiah J C, and Noworyta J P. Water conduction through the hydrophobic channel of a carbon nanotube. *Nature*, 414(6860):188–90, 2001.

[12] Stan G and Cole M W. Low coverage adsorption in cylindrical pores. *Surface Science*, 395(2-3):280–91, 1998.

[13] Wang J, Zhu Y, Zhou J, and Lu X-H. Diameter and helicity effects on static properties of water molecules confined in carbon nanotubes. *Phys. Chem. Chem. Phys.*, 6(4):829–35, 2004.

[14] Rana M and Chandra A. Filled and empty states of carbon nanotubes in water: Dependence on nanotube diameter, wall thickness and dispersion interactions. *J. Chem. Sciences*, 119(5):367–76, 2007.

[15] Alexiadis A and Kassinos S. Self-diffusivity, hydrogen bonding and density of different water models in carbon nanotubes. *Molecular Simulation*, 34(7):671–84, 2008.

2.10. Adsorption

There exist two very good reviews about adsorption in general [1] and of water on porous carbons in particular [2] on which we rely for the following discussion.

Types of adsorption isotherms

First we want to present the classification of adsorption isotherms according to Brunauer. Pictures 2.35, 2.36, 2.37, 2.38 and 2.39 show typical adsorption isotherms and schematic descriptions of the underlying adsorption processes for the five different classification types. Here P_0 denotes the saturation pressure.

The first adsorption type is characterized by a single monolayer that is adsorbed onto the substrate. The adsorption isotherm does increase rapidly till the first layer is filled at V_m.

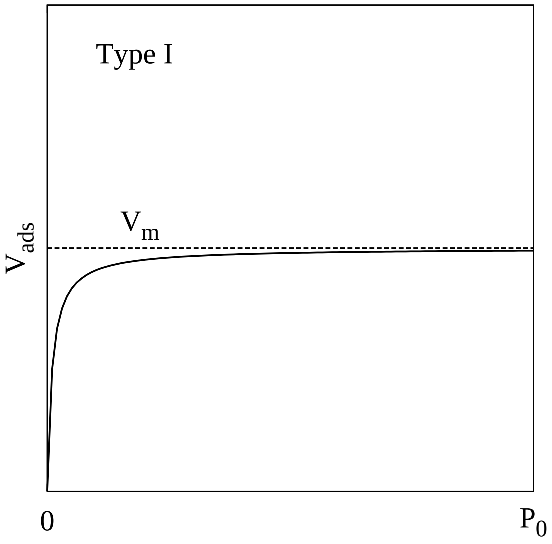

(a) Typical monolayer adsorption isotherm

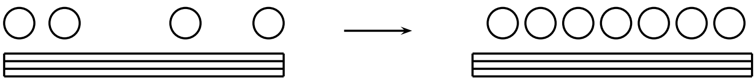

(b) Schematic picture of monolayer adsorption

Figure 2.35.: The adsorption isotherm of type I is typical for monolayer adsorption e.g. NH_3 on charcoal.

Type II is determined by multilayer absorption after filling of the first layer. It is still possible to estimate V_m and thus the surface area of the substrate that is accessible by the adsorbate.

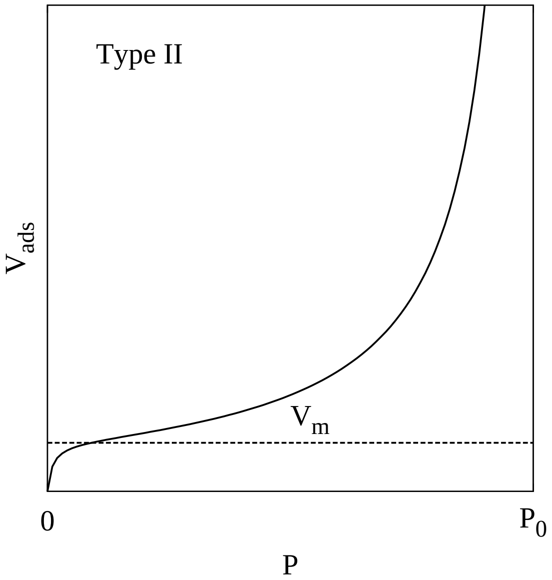

(a) Typical multilayer adsorption isotherm

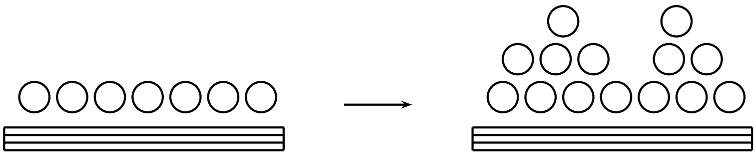

(b) Schematic picture of multilayer adsorption

Figure 2.36.: The adsorption isotherm of type II is typical for multilayer adsorption without cluster formation e.g. N_2 on silica.

Type III isotherms are characterized by their convexity in relation to the pressure axis. This indicates a cooperative behavior, where the adsorption becomes easier with increasing adsorbate. This suggests that the attraction of the adsorbate molecules for each other exceeds their attraction for the adsorbent. A typical example for this behavior is Br_2 on silica or H_2O on clean graphite.

The type IV isotherms are related to the type II ones as they also have a point of inflection at the low pressure end. They occur in porous solids, where a capillary condensation transition leads to pore filling and thus to the observed plateau in figure 2.38. Hysteresis is regularly observed in type IV isotherms. It sets in after the first monolayer is filled. There exist a number of explanation attempts but no single answer to the cause of the hysteresis.

Type V isotherms are the equivalent of type III isotherms for porous solids, where instead of approaching the saturated vapor pressure line asymptotically the curve reaches a plateau when capillary condensation is completed. As with type III isotherms the adsorbate-adsorbate interaction is much stronger than the adsorbate-adsorbent interaction. Here as in type IV isotherms hysteresis is common.

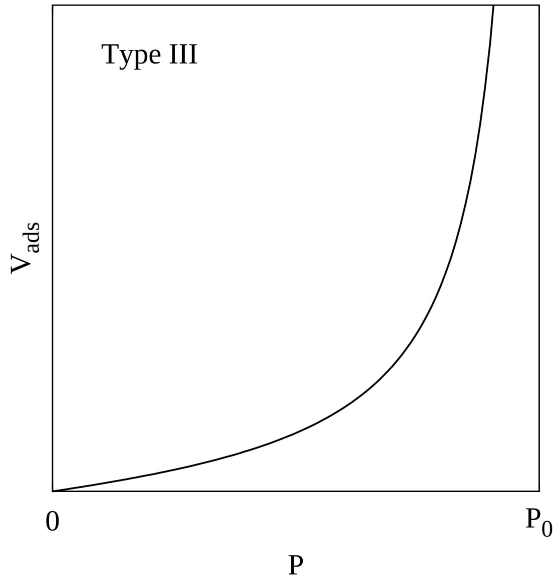

(a) Typical multilayer adsorption isotherm

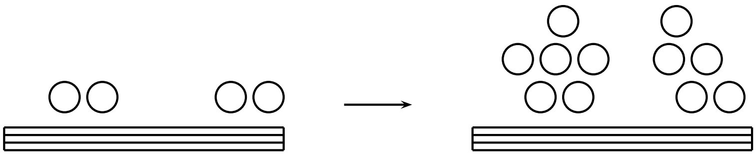

(b) Schematic picture of multilayer adsorption with cluster building

Figure 2.37.: The adsorption isotherm of type III is typical for multilayer adsorption with cluster formation e.g. Br_2 on silica.

Adsorption behavior of water

The first hint that water does not adsorb in simple layers was given by Young et al in 1954 [3]. They observed, that the monolayer capacity for water on graphitized carbon black amounts to only 1/1500 of that expected from the nitrogen surface area, which suggests that the formation of second and higher layers of adsorbed water molecules commences whilst the first layer is still incomplete. This is also confirmed by water showing type III or weak type II behavior. As demonstrated in [1] water adsorption on graphitized carbon black is essentially zero for $P/P_0 < 0.7$ and remains very small up to the saturation pressure $P/P_0 = 1.0$ as the ratio of the fluid-wall attractive interaction to the fluid-fluid attractive interaction is very small.

The general view on the process of water absorption in porous carbons [4] distinguishes three different stages. It is believed that the first water molecules are adsorbed on oxygen containing functional groups on the carbon surface. This view is supported by the proportionality between the number density of active sites and water adsorption [5]. Figure 2.44 (a) presents adsorption isotherms of water vapor on oxygenated carbon [6]. The substrate was heat treated at different temperatures reducing the amount of active sites. One can easily see that the adsorption decreases by nearly a factor of ten. A similar effect can be observed on porous carbon [2] (see figure 2.44 (b)) where the reduction in primary centers leads to a shift of adsorption and desorption to higher pressures and to a slight broadening of the hysteresis. It is therefore not implausible that on a substrate without oxygenated sites, as assumed in our simulations, adsorption might be suppressed even stronger leading to a noticeable uptake of water only above the saturation pressure. This point was also investigated in a simulation study by Birkett et al. [7]. They performed MD simulations for water adsorption on several model graphitized carbon blacks. They used a Steele-type water-carbon interaction varying the interaction parameter from $\epsilon = 0.389$ kJ/mol to $\epsilon = 0.83145$ kJ/mol. They found that they could not reproduce experimental data for water on highly graphitized carbon black without including active sites into their simulations. Even with the strongest carbon-water interaction tested the adsorption was less than 1 % of the experimentally observed one at 302.15 K. Including active sites they were able to gain isotherms similar to the experimental ones but only for $\epsilon > 0.6$ kJ/mol, which is much bigger than in any of the commonly used potential models.

At intermediate loading, where the inflection point of the isotherm is situated, adsorption seems to be governed by cluster formation which is based on the cooperative behavior in water. Our simulation data indicate that the pore size and the carbon-water potential parameters are of special importance for the exact position of the inflection and the width of the hysteresis loop. Finally the adsorption volume becomes crowded with molecules and the adsorption isotherm levels-off to a plateau region. The hight of the plateau does also depend on the pore size distribution as it is experimentally confirmed that water does not fill all the micropore volume determined by nitrogen adsorption.

We simulated TIP4P/2005 water adsorption on carbon slits ranging in width from 7 to 100 Å by GCMC applying periodic boundary conditions in the directions parallel to the slit and treating the long range Coulomb interaction by the ELC method as described. We carried out at least 500 Million MC steps. We observed capillary condensation in all cases, indicating that a direct comparison with experiment is only possible regarding activated carbons with a known pore distribution.

As described in [2] the isosteric heat of adsorption, q_{st}, calculated from isotherms for which the first measured point is at $P/P_0 \approx 0.1$, where P_0 is the is saturation pressure, is very close to the latent heat of bulk water condensation, indicating that the formation of water clusters around primary sites must occur at very low relative-pressure.

This observation of early cluster formation is in agreement with our simulation results. Figure 2.41(a) shows the typical course of pore filling during a MC simulation. First a small cluster builds near the carbon wall, which then grows till the whole slit is filled. The typical development of desorption is presented in figure 2.41(b). Usually water begins to retreat from one or both walls of the slit until the whole pore is empty. We can thus note, that while the creation of an initial cluster is required for adsorption, the desorption mechanism is simpler. This is of special importance regarding our simulations, as we do not include any active sites, which enhance cluster formation. Our results for the desorption are thus more suitable for comparison with experiment, although the evaporation is also influenced by the presence of primary adsorption centers.

Figure 2.42 shows our simulation results for different geometries and water-carbon interactions. (a) presents the adsorption and desorption isotherms at 300 K for two different values of the carbon-water interaction parameter ϵ depending on P/P_0, where P_0 is the saturation pressure. We used the ideal value of the chemical potential for our simulations, having established, that the chemical potential at the saturation pressure at 300 K of TIP4P/2005 water is given by its ideal value within our computational error. While capillary condensation during adsorption occurs at very high pressure in comparison to experiment for both potentials, which may be connected to the lack of active sites, evaporation happens at a more reasonable value. An increase in ϵ from 0.3135 kJ/mol to 0.47869 kJ/mol, decreases the width of the hysteresis and shifts the capillary condensation and evaporation transitions to lower pressures.

Experimentally the adsorption is determined by the pore size distribution of the substrate as well as by its purity. The condensation of water on Charcoal S84 for example occurs at 0.8 P_0 while evaporation happens at 0.67 P_0 [1]. Also according to [1] condensation happens on graphitized charcoal at about 0.8 P_0 and evaporation at 0.6 P_0. Adding 4.6 % of oxygenated surface groups [2] shifts condensation to 0.65 P_0 and evaporation to 0.5 P_0 reducing the hysteresis.

For a comparison to experiment the results of Kaneko are quite interesting [8] as they investigate the adsorption of water in dependence on the micropore structure, determined gravimetrically by N_2 adsorption at 77 K, and the number of active sites. The comparison between PIT-5 (pore width 0.75 nm) and PIT-20 (pore width 1.13 nm) samples shows reduction of hysteresis with decreasing pore size and a shift of condensation from 0.7 to 0.42 P_0 and of evaporation from 0.5 to 0.4 P_0.

This is not in total agreement with our simulation results, see figure 2.42 (b) as the evaporation in small slits is shifted to considerably higher pressures, while condensation occurs at a smaller pressure for $D = 10$ Å but at increasing pressure for $D = 8$ and $D = 7$ Å. The dependence of pore evaporation and condensation on the slit size is weak for slits larger than 20 Å, while the hysteresis is much reduced for slit diameters of 7 Å and 10 Å in agreement with experiment.

The observed difference is in agreement with simulation studies of Stiolo et al [9]. They observe a similar pattern, where the hysteresis narrows with decreasing slit size before being shifted to higher pressures for slit sizes of about 7 Å. The reason for this is that the tetrahedral hydrogen bond network is frustrated in very small pores, thus requiring higher pressures for pore filling. While our results are in qualitative agreement, Stiolo et al observe adsorption and desorption at pressures which are smaller by about a factor of ten shifting them below the saturation pressure. This difference cannot be explained solely by our smaller interaction as demonstrated in figure 2.42 (a). Although this sounds like an irreconcilable difference, it may be rooted in the conversion from chemical potential to relative pressure, which because of its exponential functional relationship can lead to large errors. While we have computed the coexistence pressure very thoroughly as described earlier, Strolio et al might have overestimated P_0 by computing the coexistence chemical potential from GCMC simulations, which may produce metastable states near the vapor-liquid phase transition. This is also criticized in a study by Liu and Monson [10], who use Gibbs ensemble Monte Carlo to find the bulk vapor-liquid equilibrium and discover that condensation does not occur in larger slits for pressures below the bulk saturation pressure, P_0. They attribute this behavior to the lack of hydrogen bonding with the graphite surface that destabilizes dense water phases relative to the bulk water. Depending on the used water model and the exact slit width they observe adsorption below the saturation pressure, P_0, in smaller tubes, which they ascribe to a stabilization by the strong dispersion interactions with both carbon surfaces. In agreement with our data they find desorption at pressures below P_0 for all but very small slits.

Their adsorption and desorption pressure values can be brought into approximate quantitative agreement with our results anticipating a small shift to lower pressures resulting from the difference in the interaction potential.

Thus it seems, that the discrepancy between the simulated adsorption pressures and those observed in experiment is solely based on the lack of active sites in the simulations.

Figures 2.42 (c) and (d) show the water-water potential energy for different simulation setups. While the change in water-carbon interaction does not seem to change the internal structure of the adsorbed water giving a similar potential energy, the slit geometry has a strong effect on the water-water potential energy. The reason for this can easily be deduced by looking at the water density distribution in figure 2.43 (a). While in a 7 Å slit only one layer of water can form allowing only for lateral water-water interaction, two and more layers exist in the larger slits. Thus we see a rapid decrease in potential enery with growing slit width converging to its bulk value. The effect of the slit width is also clearly apparent in the carbon-water interaction of one Å^2 of the carbon surface in figure 2.43 (b). It seems that with growing slit width water is more flexible structured and thus able to arrange in a way to minimize its interaction potential with the wall. Figures 2.43 (c) and (d) present the whole potential energy including the carbon-water interaction. For a fixed geometry and different ϵ the evaporation seems to happen at the same potential energy, while condensation occurs at similar pressure but different energy. For different geometries (see figure (d)) the water-carbon interaction reduces the potential energy strongly for small slits, as here most molecules are situated on the surface and weakly for large slits. Thus the potential energies move closer together.

Unfortunately we have to conclude that because of the strong impact active sites have on the experimental adsorption curves, a comparison with simulation in order to set limits on the water-carbon interaction parameters becomes near impossible.

In addition we compute the isosteric heat of adsorption by the fluctuation formula taken from [11].

$$q_{st} = -\frac{<UN> - <U><N>}{<N^2> - <N>^2 - \tilde{N}^G} + kT \tag{2.110}$$

Here U is the potential energy, N the adsorbed molecule number and $\tilde{N}^G$ the number of molecules that would be in the adsorption volume if it were filled homogeneously by the gas phase. $\tilde{N}^G$ thus depends on slit volume, that is accessible to the water molecules. For a derivation see the appendix B.8.

In figure 2.44 (a) we report q_{st} for different slit geometries. As the results are quite noisy, lines are added to guide the eye. The closed symbols indicate the adsorption and the open ones the desorption branch. As indicated by the horizontal line values for q_{st} after filling of the slit exceed the value expected from the enthalpy of condensation for TIP4P/2005 water. As q_{st} gets closer to its expected value with increasing slit width, this is probably due to the narrowness of the tubes. The limit of zero coverage for q_{st} lies at around 8 to 9 kJ/mol, which is close to the value found in a simulation study by Striolo [9]. In the pressure range close to pore filling on the adsorption branches one can observe a rising of q_{st} to a value of $\approx$ 26 kJ/mol. This is due to the formation of small clusters of about 4-8 water molecules during the simulation. We do not include the polarization correction, which is required by all effective pair potentials that include the average effects of polarization [14], in the full pressure regime. We only apply it at

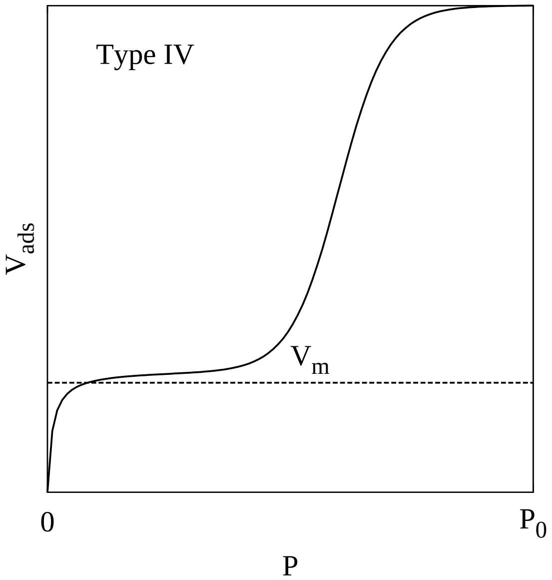

(a) Typical condensation adsorption isotherm

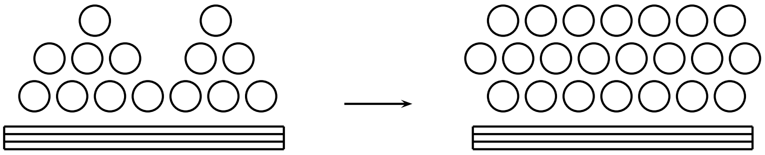

(b) Schematic picture of condensation adsorption

Figure 2.38.: The adsorption isotherm of type IV is typical for the condensation in pores without cluster formation e.g. Benzene on Fe_2O_2.

higher coverage, where cluster formation is visible, as isolated water molecules in the slit are only interacting by the wall-water LJ potential and are thus similar to molecules in the gas phase.

Figure 2.44 (b) shows the isosteric heat of adsorption for three different temperatures. The hysteresis decreases with growing temperature, while the temperature dependence of the limiting values of q_{st} for low and high coverage is only small.

Figure 2.45 shows two experimental studies ((a) and (b)) in comparison to our simulation results. Figure (a) presents results of Salame and Bandosz taken from [2]. They find a similar trend for various activated carbons. The isosteric heat rises steeply from about 20 kJ/mol reaching the heat of condensation of bulk water at a low surface coverage of about 0.6 molecules/nm^2.

Figure (b) presents the results of an adsorption study by Naono et al [13] on AC-1 and AC-2 activated carbons. The substrates were characterized by nitrogen adsorption giving a pore size of 0.9 nm and a total surface area of 2500 and 2030 m^2 g^{-1} for AC-1 and AC-2 respectively. They compute the differential adsorption enthalpies at low coverage from the Clausius-Clapyron equation and find a steep rise from 17 to 32 kJ/mol depending on the type of carbon with growing coverage. So for AC-1 carbon their values are not to far from our simulation results shown in figure (c), where a rise from 10 to 30 kJ/mol is

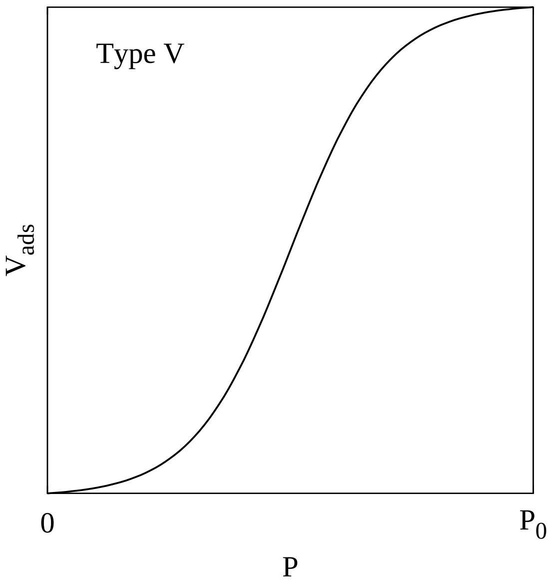

(a) Typical multilayer adsorption isotherm

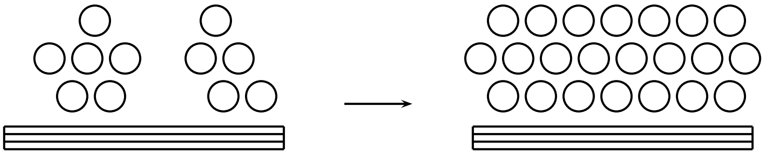

(b) Schematic picture of condensation adsorption with cluster building

Figure 2.39.: The adsorption isotherm of type V is typical for the condensation in pores with cluster formation e.g. H_2O on charcoal.

observed in this coverage regime. Overall our simulations show a similar picture to the experimental one, although less continuous. At very low coverage where we find only one or two molecules in a configuration q_{st} is very low at about 8-9 kJ/mol. It grows to about 30 kJ/mol on the formation of small clusters built from about 4 to 8 molecules. When the clusters grow further the pore is always filled completely leading to a isosteric heat close to the condensation heat of bulk water and resulting in a jump in coverage that is determined by the slit size.

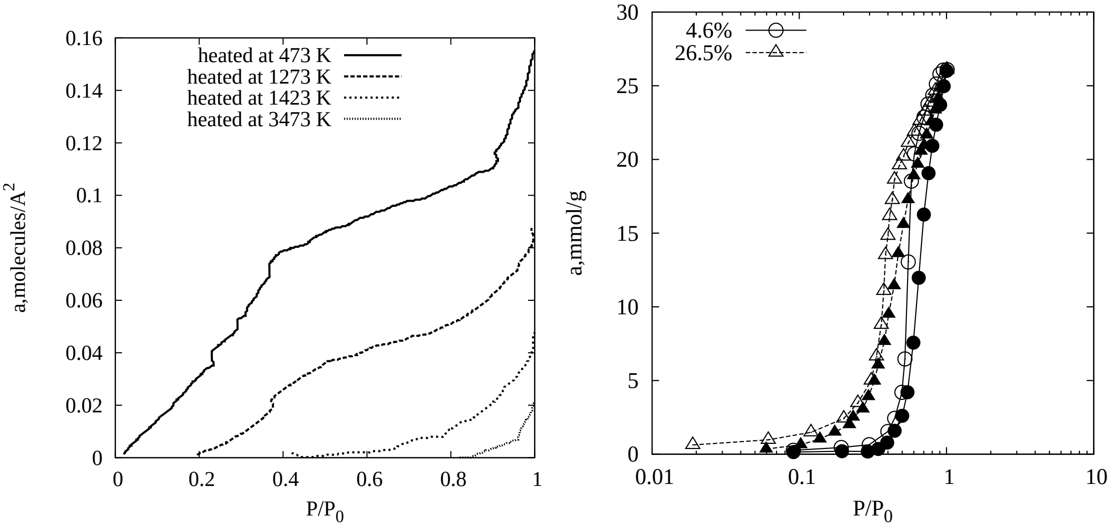

(a) (b)

Figure 2.40.: (a) Adsorption of water vapor on oxygenated carbon [6]. The substrates were heat treated at increasing temperatures in order to reduce the density of active sites. (b) Adsorption (filled symbols) and desorption (open symbols) of water at 293 K containing 4.6 % and 26.5 % of primary adsorption centers [2].

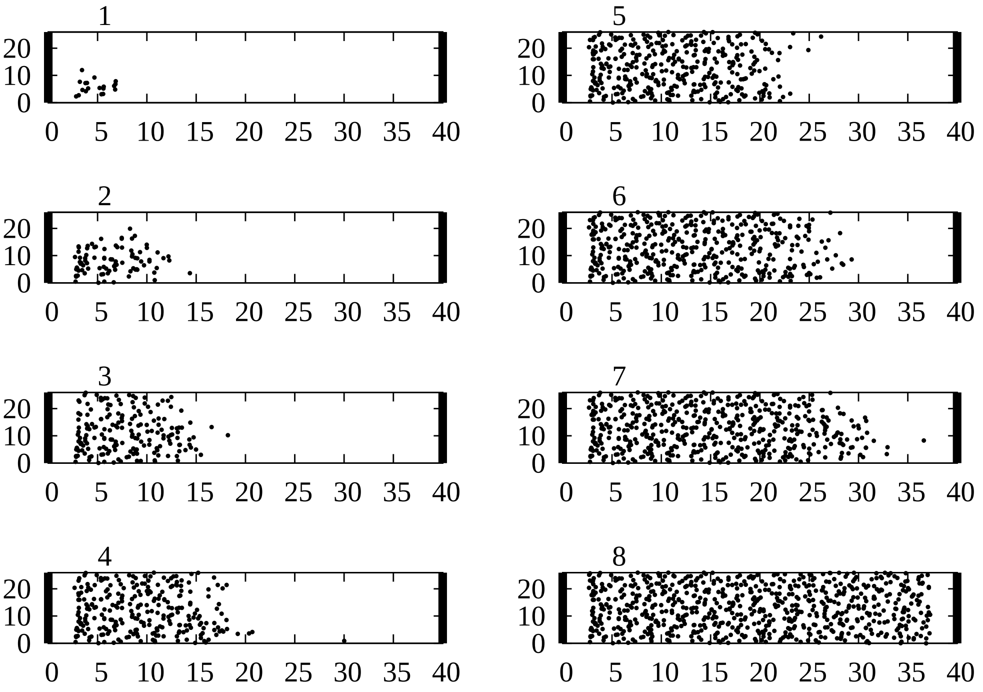

(a) Typical development of water adsorption in our MC simulations. After cluster formation near the wall, the whole pore is filled progressively.

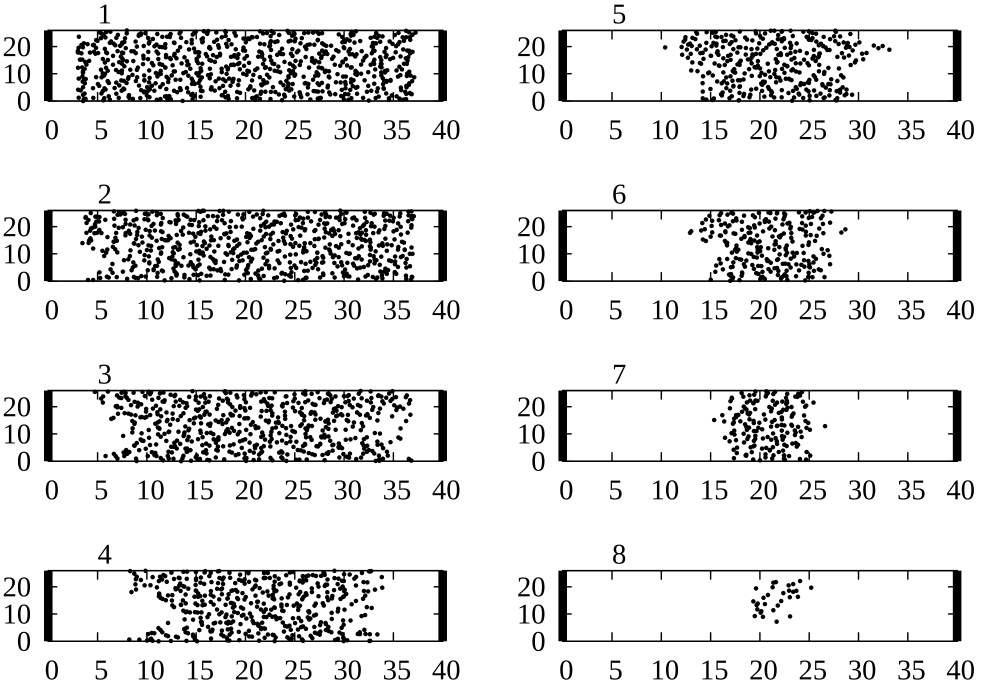

(b) Typical development of water desorption. Water desorbs first from the walls and retreats till the whole pore is empty.

Figure 2.41.: Simulation progression of the adsorption (a) at $T = 300$ K and $\mu = -48$ kJ/mol and desorption (b) at $T = 300$ K and $\mu = -62$ kJ/mol. The carbon water interaction parameters are $\sigma = 3.19$ Å and $\epsilon = 0.3135$ kJ/mol. The configurations are taken in intervalls of 0.2 million MC steps (a) and 0.6 million MC steps (b).

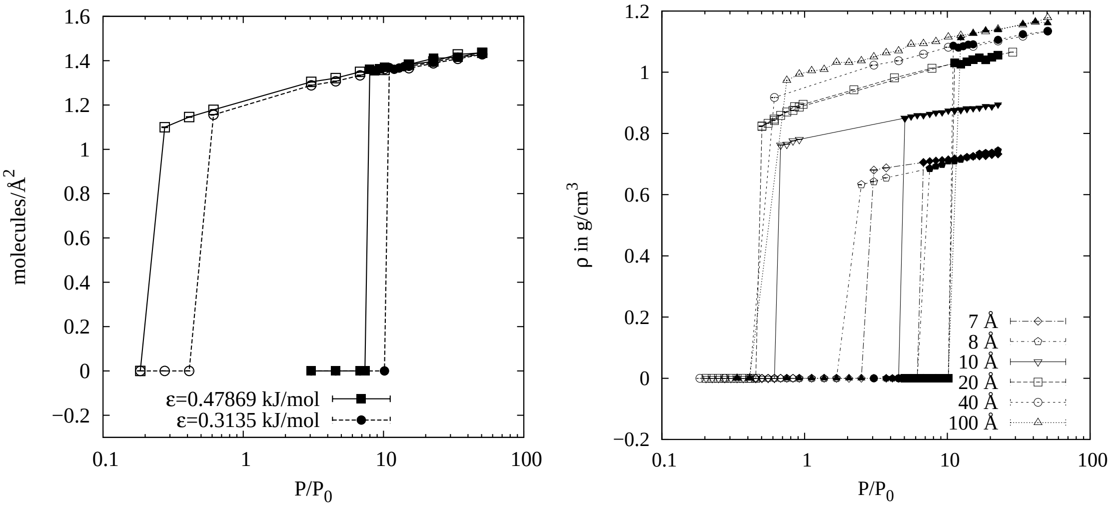

(a) 40 Å, 25.92×25.92 Å^2 slit (b) $\epsilon = 0.3135$ kJ/mol

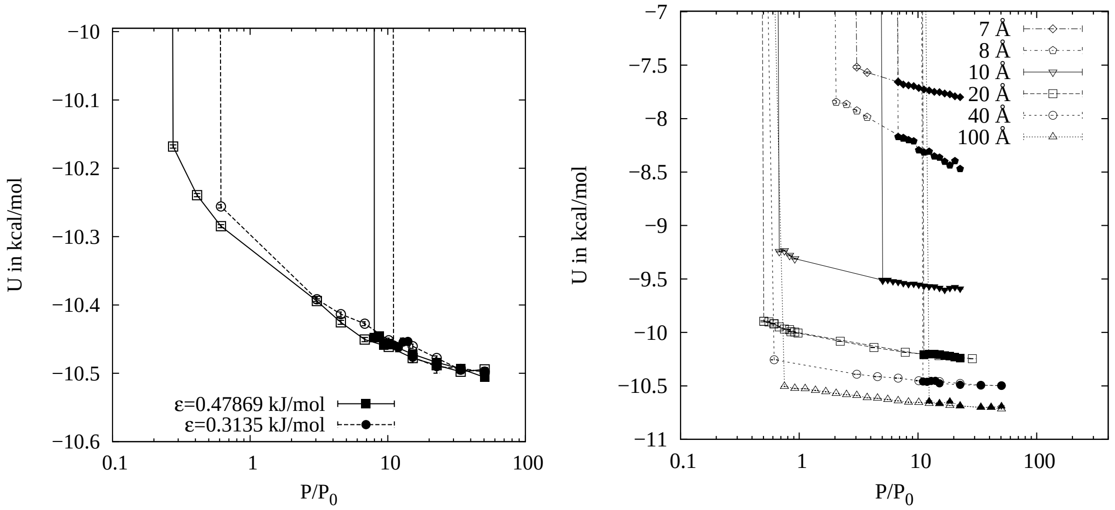

(c) 40 Å, 25.92×25.92 Å^2 slit (d) $\epsilon = 0.3135$ kJ/mol

Figure 2.42.: Adsorption (filled symbols) and desorption (open symbols) isotherms at 300 K against relative pressure (P_0 saturation pressure). (a) Adsorption and desorption in molecules per Å^2 with $\epsilon = 0.47869$ kJ/mol and $\epsilon = 0.3135$ kJ/mol at fixed geometry in a 40 Å, 25.92×25.92 Å^2 slit. (b) Density for different geometries at $\epsilon = 0.3135$ kJ/mol. (c) The potential energy (only water-water) corresponding to the adsorption isotherms in (a). (d) The potential energy (only water-water) corresponding to the adsorption isotherms in (b).

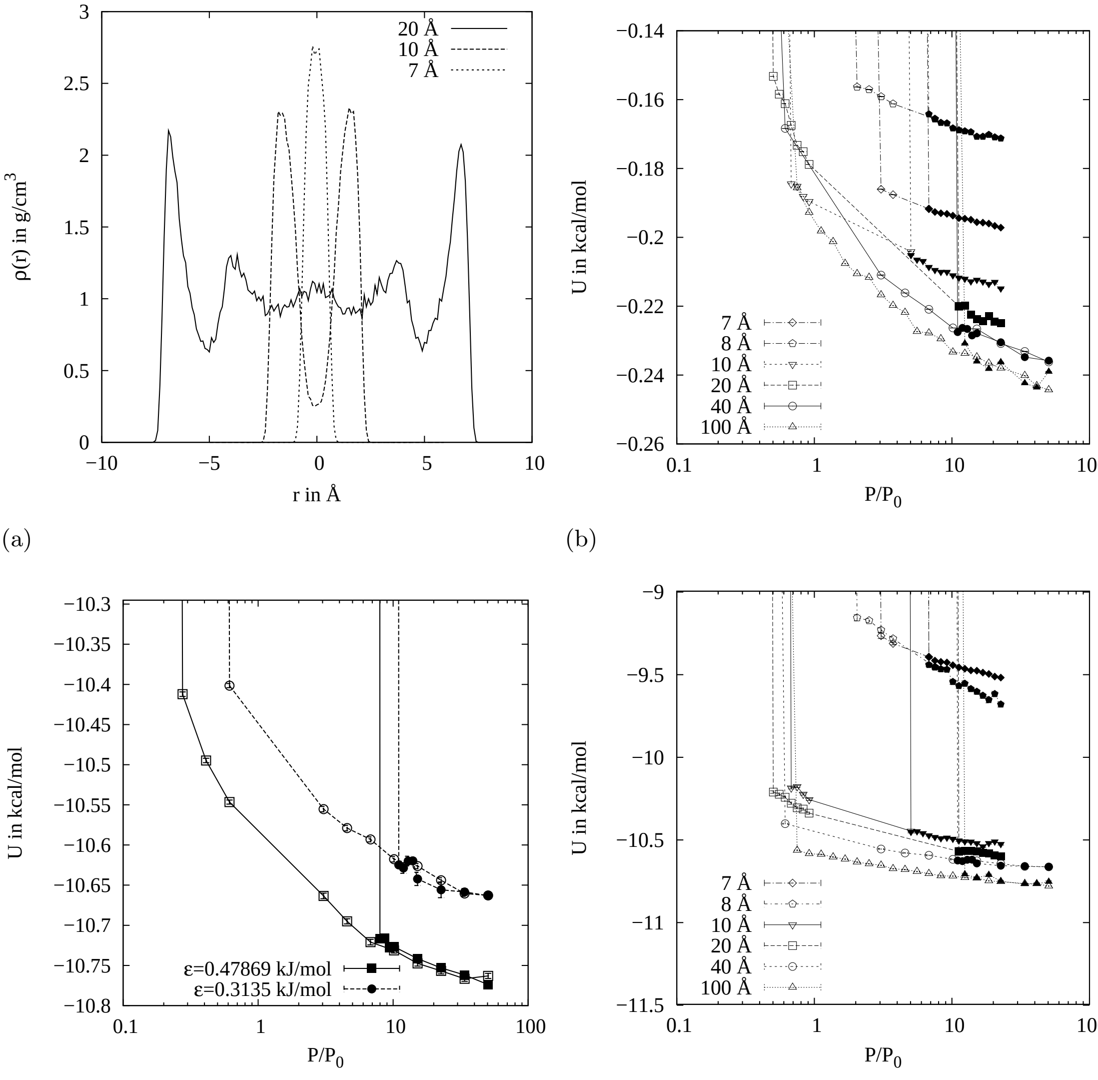

(a) (b)

(c) (d)

Figure 2.43.: (a) Density profile of different slit geometries. (b) Carbon-water potential energy for different geometries at $\epsilon = 0.3135$ kJ/mol. (c) Same as figure 2.42 (c) but including carbon-water interaction. (d) Same as figure 2.42 (d) but including carbon-water interaction.

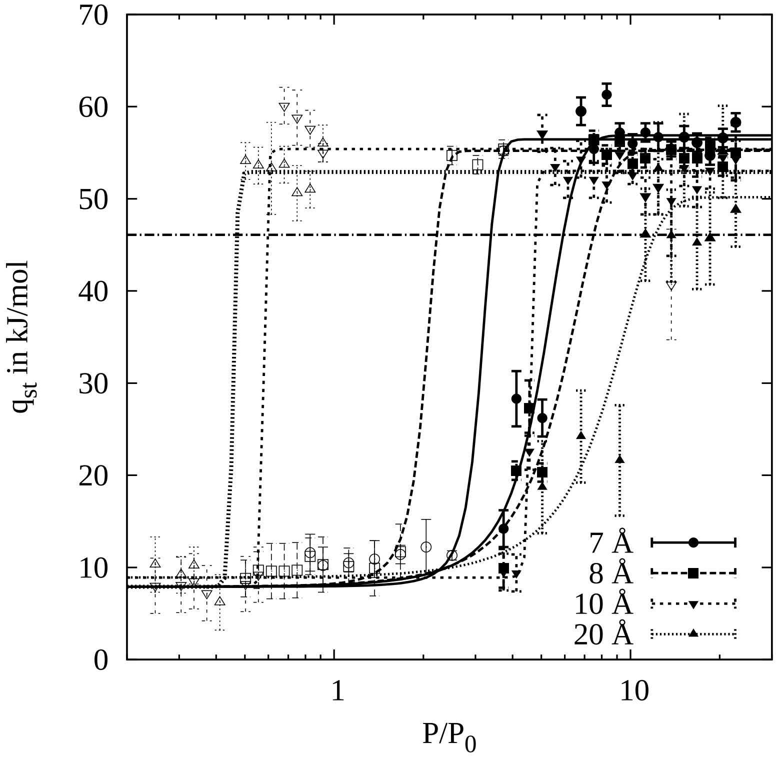

(a)

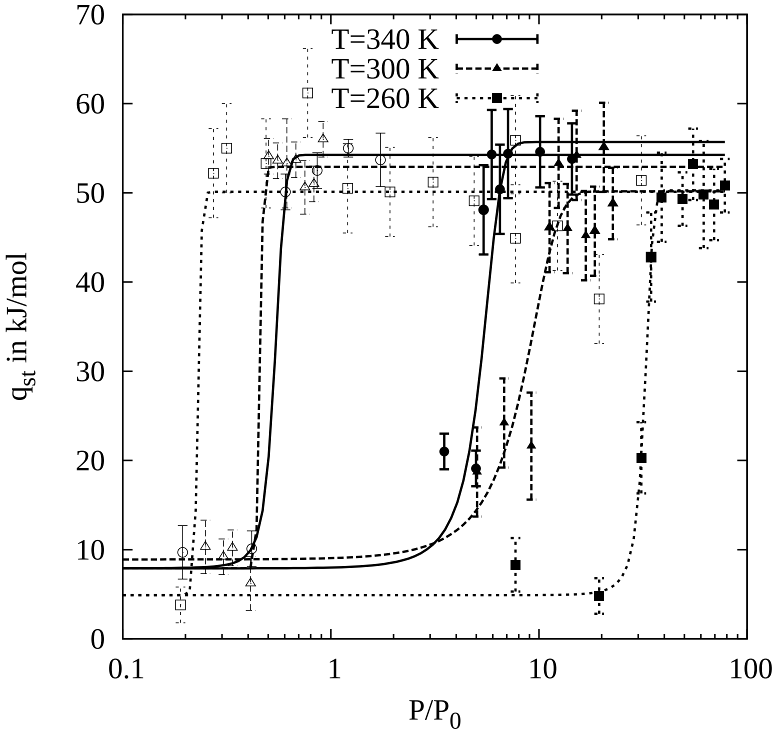

(b)

Figure 2.44.: (a) Isosteric heat of adsorption for different slit geometries at 300 K. The horizontal line denotes the heat of vaporization of TIP4P/2005 water (polarization correction not included) taken from [12]. The other lines are there to guide the eye. (b) Isosteric heat of adsorption for temperatures for a 20 Å slit. The lines are there to guide the eye.

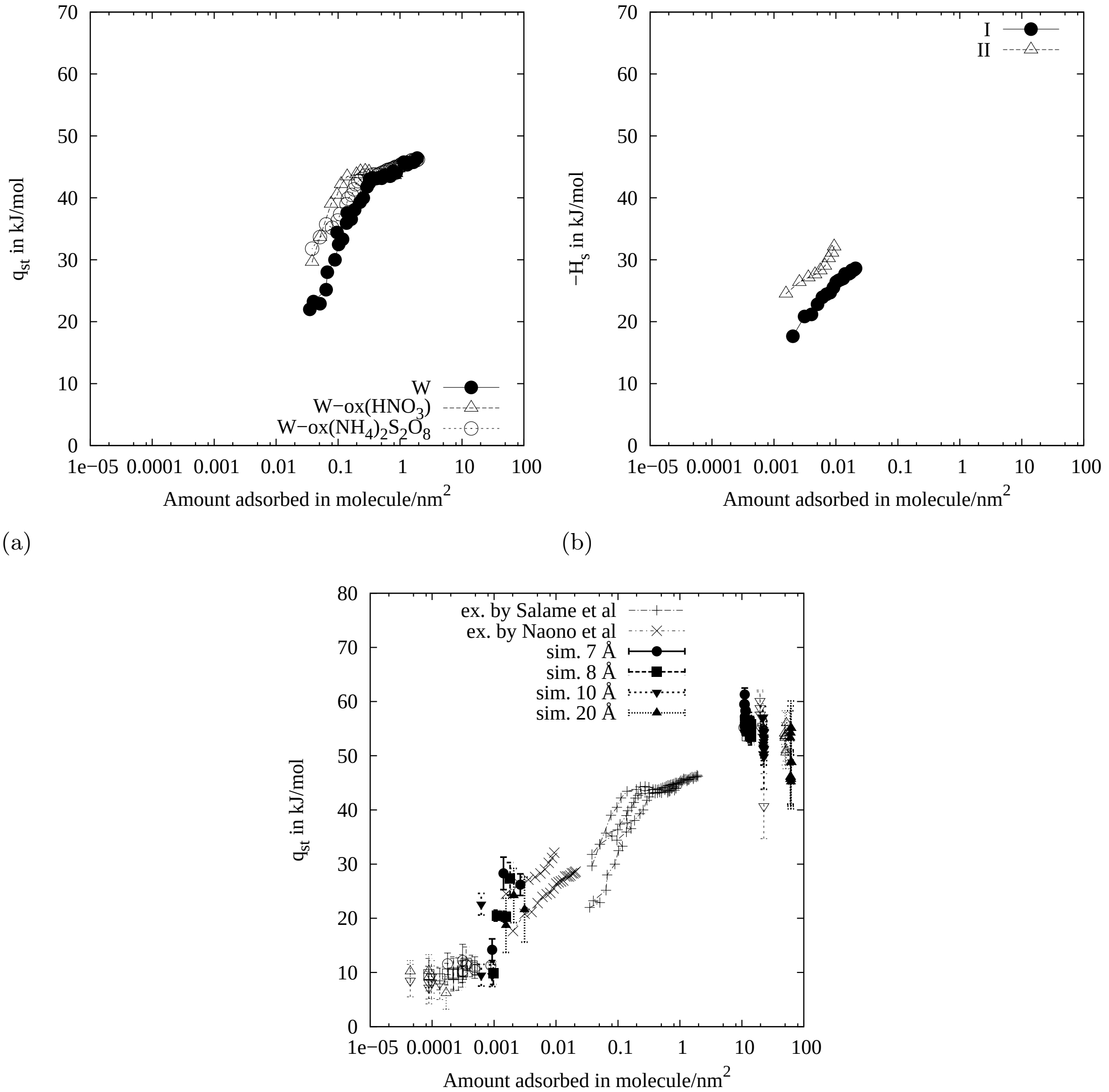

(a) (b)

(c)

Figure 2.45.: (a) Isosteric heats of water adsorption on initial and oxidized carbons, taken from [2] (b) Differential enthalpy of adsorption ($-H_s$) of water vapor for active carbons (AC-1 (I), AC-2 (II)), taken from [13] (c) Simulated q_{st} against coverage for different slit widths at 300 K.

Bibliography

[1] Gregg S J and Sing K S W. *Adsorption, surface area, and porosity.* Academic Press, 1991.

[2] Brennan J K, Bandosz T J, Thomson K T, and Gubbins K E. Water in porous carbons. *Colloids and Surfaces A: Physicochemical and Engineering Aspects*, 187-188:539–68, 2001.

[3] Young G J, Chessick J J, Healey F H, and Zettlemoyer A C. Thermodynamics of the adsorption of water on graphon from heats of immersion and adsorption data. *J. Phys. Chem.* , 58(4):313–5, 1954.

[4] Orhan Talu and Francis Meunier. Adsorption of associating molecules in micropores and application to water on carbon. *AIChE Journal*, 42(3):809–19, 1996.

[5] Pierce C, Smith R N, Wiley J W, and Cordes H. Adsorption of water by carbon. *J. Am. Chem. Soc.*, 73(10):4551–7, 1951.

[6] Müller E A, Rull L F, Vega L F, and Gubbins K E. Adsorption of water on activated carbons: a molecular simulation study. *J. Phys. Chem.* , 100(4):1189–96, 1996.

[7] Birkett G R and Do D D. Simulation study of water adsorption on carbon black: The effect of graphite water interaction strength. *J. Phys. Chem. C*, 111(15):5735–42, 2007.

[8] Kaneko K, Hanzawa Y, Iiyama T, Kanda T, and Suzuki T. Cluster-mediated water adsorption on carbon nanopores. *Adsorption*, 5(1):7–13, 1999.

[9] Striolo A, Chialvo A A, Cummings P T, and Gubbins K E. Water adsorption in carbon-slit nanopores. *Langmuir*, 19(20):8583–91, 2003.

[10] Liu J C and Monson P A. Does water condense in carbon pores? *Langmuir*, 21(22):10219–25, 2005.

[11] David Nicholson and Neville George Parsonage. *Computer simulation and the statistical mechanics of adsorption.* Academic Press, December 1982.

[12] Abascal J L F and Vega C. A general purpose model for the condensed phases of water: TIP4P/2005. *J. Chem. Phys.* , 123:4505–17, 2005.

[13] Naono H, Hakuman M, Shimoda M, Nakai K, and Kondo S. Separation of water and ethanol by the adsorption technique: Selective desorption of water from micropores of active carbon. *Journal of colloid and interface science*, 182(1):230–8, 1996.

[14] Berendsen H J C, Grigera J R, and Straatsma T P. The missing term in effective pair potentials. *J. Phys. Chem.* , 91(24):6269–71, 1987.

3. Results

3.1. Simulations of bulk water

3.1.1. Computation of the intensity curves

In order to calculate the intensity curves $I(q)$, we generate 1-ns-long MD trajectories for each of the chosen classical water models. We use systems of $N = 1728$ rigid water molecules in a simple cubic box with periodic boundary conditions and treat the long range electrostatics with the Ewald sum employing tin-foil boundary conditions. The cutoff for the electrostatic (real space) and for the LJ interaction is set to 9 Å using standard LJ corrections to the energy and pressure, except for the TIP5P-E model. In this case we use a LJ cutoff of 12 Å and no tail corrections according to the parametrization of the model. In order to estimate finite size effects and to take a closer look at the small angle regime of the spectrum we also simulate systems with 4096 and 32768 molecules for the TIP5P-E model. We find no significant difference in the simulated intensities for $q > 1$ [1/Å] (see figure 3.1).

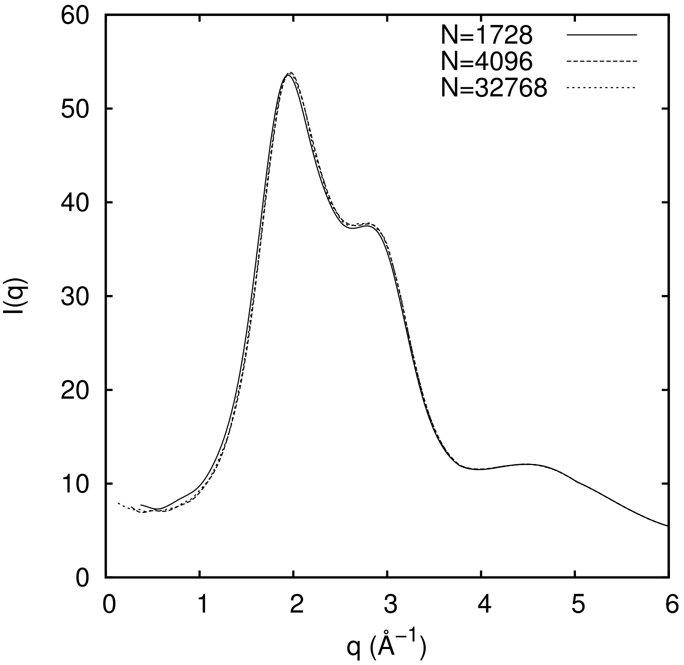

Figure 3.1.: Three intensity curves for the TIP5P-E model at $T = 286$ K for different system sizes.

We use the Berendsen thermostat and barostat [1] to adjust the temperature, ranging from 180 K to 320 K, and set the pressure equal to 1 bar. The MD trajectories are integrated via the velocity verlet algorithm, which is also used to compute the charge dynamics in the fluctuating charge models. The rigid water molecules are treated by the quaternion approach [2]. An optimized PPPM technique, as described in Ref. [3], is used to calculate the Fourier component of the Ewald sum. The force field parameters for the TIP4P/2005, the TIP5P-E and the TIP4P-FQ models are taken from the literature [4, 5, 6]. A summary of the parameters is given in the appendix A.2.1.

Finally we want to compare the simulated curves with experimental results. There exist a number of experimental intensity curves of water but only two studies were carried out in the supercooled regime. Figure 3.2 presents a collection of the experimental results close to our simulation temperatures. While the data sets of Bomsdorf et al [7], Head-Gordon et al [8], Narten et al [9] and Nishikawa et al [10] could all be compared directly, we needed to Compton correct and normalize the data of Corban et al [11]. There is a wide spread in the experimental results, especially between the older studies of Narten et al, Nishikawa et al and Corban et al to the newer ones of Bomsdorf et al and Head-Gordon et al. But generally one can see that the shoulder that is just visible at about T=320 K is increasing with decreasing temperature.

As the experiment of Head-Gordon et al at the ALS (Advanced Light Source at Berkeley) is especially sophisticated and comprehensive and the results of Bomsdorf et al are in very good agreements with them and include the supercooled regime, we will use these results for the comparison with our simulation data.

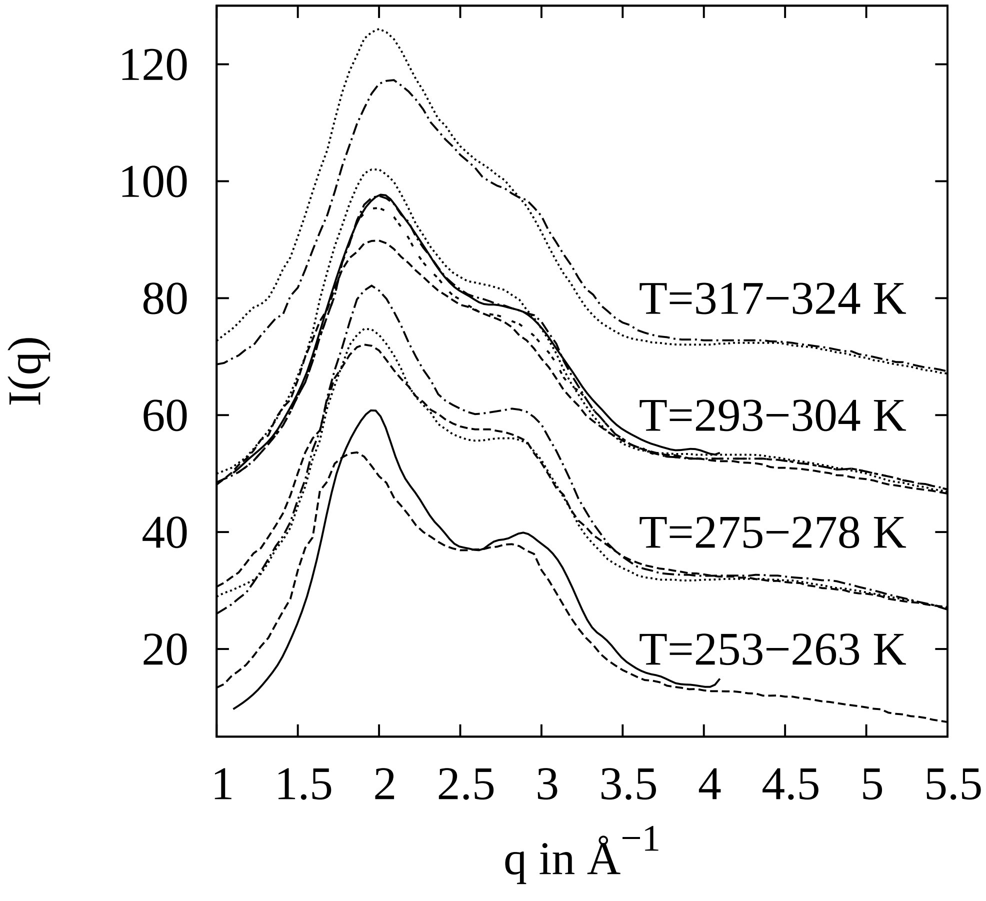

Figure 3.2.: The experimental intensity curves at similar temperatures are grouped together and an offset of 20 is introduced between the different curves belonging to a termperature margin. The data is taken from the following sources: ——— Bomsdorf et al [7] T=263, 293 K; – – – – Corban et al [11] T=253.15, 277.15, 303.15; – · – · – Head-Gordon et al [8] T=275.15, 298.15, 323.15 K; · · · · · · Narten et al [9] T=277.15, 298.15, 323.15 K; · · · · ·· Nishikawa et al [10] T=298.15 K

Figure 3.3 depicts the results using the simple atomic form factor in comparison with those obtained using the rescaled form factors. It can be seen that the TIP5P-FQ model although performing the worst with regards to ρ and D is able to reproduce the intensity data very well. The TIP4P-FQ model yields a too high intensity in the area of the main peaks, which is amplified using the rescaled form factors. The first peak in the intensity curve of the TIP4P/2005 model is improved by including the distribution of the partial charges into the form factors while the shoulder following the first peak is amplified too much. The TIP5P-E model exhibits a slightly too low intensity which is not corrected by the very small change due to the rescaling.

Although the rescaling of the atomic form factors improves the intensity curves slightly for the TIP5P-like models it has the converse effect on the TIP4P-FQ model. Although intuitively appealing the rescaling does not improve the intensity curves systematically. For all simulation data the shoulder next to the first peak is more pronounced than in the experimental data, signaling an exaggerated temperature dependence in the supercooled region.

We also want to compare our data to those of Yokoyama et al [12], who present pair correlation functions extracted from X-ray diffraction at supercooled temperatures. They observe a peak at ≈ 10.8 Å, which grows with decreasing temperature and according to their analysis indicates the existence of clathrate-like structures. Figure 3.4(a) shows Yokoyama's data in comparison with our results for TIP5P-E water. Although the first peak in the pair correlation data does not match, the increase of the peak at 10.8 Å is clearly visible and is a general characteristic of all water models studied by us (see figure 3.4(b)). Although we can reproduced the experimental pair correlation functions quite well, we are not able to find the clathrate-like structures postulated. This must not necessarily signify a contradiction as Yokoyama mentions that fracmental and deformed clathrate structures should be considered the main local structures and thus may be difficult to observe.

By Fourier transforms of the pair correlation functions truncated after different neighbor shells (see figure 3.5) we can determine that for all considered models the first two shells are responsible for the development of the shoulder. On further examination of the position distribution of the different neighbors we find that by far the largest change in position with temperature occurs for the fifth neighbor (see figure 3.6). The latter migrates nearer to the first neighbor shell with increasing temperature. Thus we assume that the development of the pronounced shoulder in the spectrum is due to extrusion of the fifth neighbor from the first neighbor shell. This finding is in agreement with Ref. [13] (see figure 4(f) in Ref. [13]). Possible consequences of this broad position distribution of the fifth neighbor that at moderate temperatures allows it to be part either of the first or second shell were discussed in [14]. They argue that the defects in the tetrahedral bond network, caused by the intrusion of the fifth neighbor into the first neighbor shell leads to a bifurcated bond which offers paths with low energy barriers between different network configurations and thus a fast restructuring of the network.

The average number of hydrogen bonds per molecule, <Hbonds> $/N$, is computed according to the following geometric criteria. The first shell of each water molecule is searched for molecules, whose oxygen atom lies within a cone of angle α around the OH bond of the central water molecule. The first neighbor shell is determined using the pair correlation functions computed earlier. In a second step we observe the decay of these hydrogen bonds allowing for different excursion times. The excursion time , t_E, is

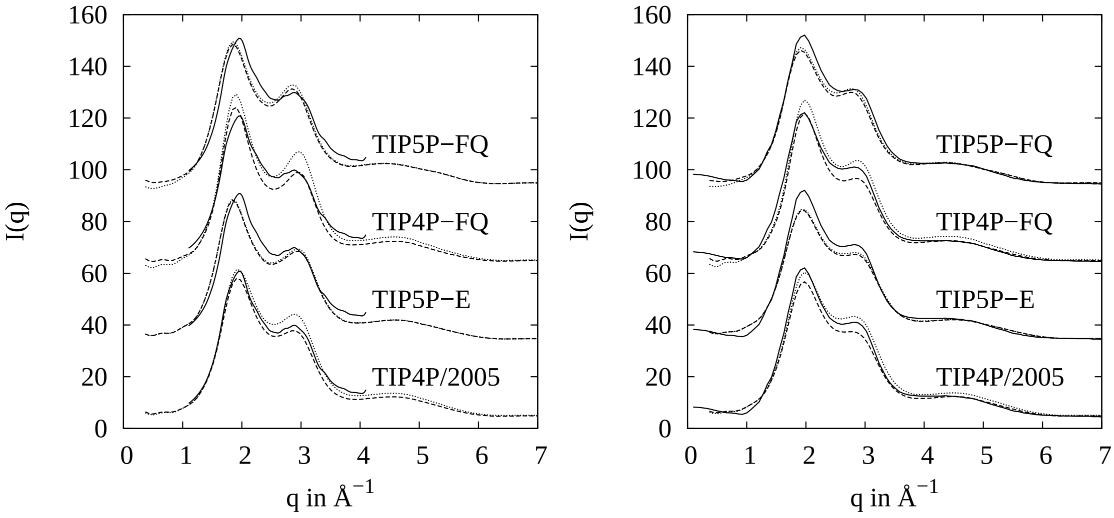

(a) T=260 K (b) T=280 K

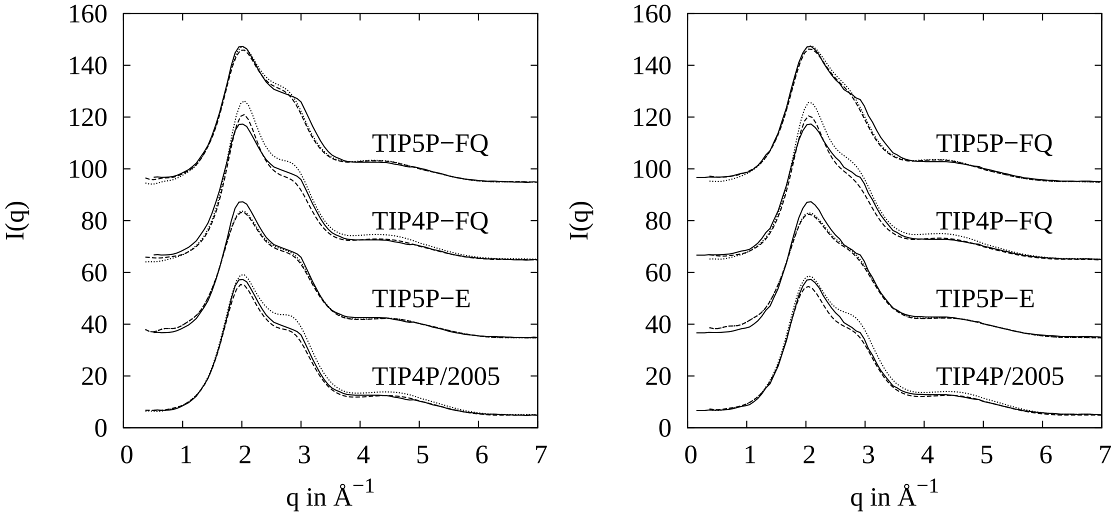

(c) T=300 K (d) T=320 K

Figure 3.3.: Simulation results using the simple (— — ——) and the rescaled (······) atomic form factors compared to experimental intensity curves (———). (a) Experimental results at 263 K [8] are shown together with simulation results for 260 K. (b) Experimental results at 275.15 K [8] and simulation results at 280 K. (c) Experimental results at 298.15 K [8] and simulation results at 300 K. (d) Experimental results at [8] 323.15 K and simulation results at 300 K. The different intensity curve sets are displaced vertically for better distinguishability.

the maximum time a water molecule is allowed to violate the above geometric criterion without being discarded. In figure 3.7 three different decay curves for the TIP4P/2005 model at $T = 280$ K are shown. The excursion times range from 0.0 ps to 0.4 ps. In this logarithmic plot two decay times are visible: a short one, which we identify with passing water molecules that form no real hydrogen bonds, and a long one, which we identify with the actual H-bonds. Thus we perform a fit of the decay curves using a function of

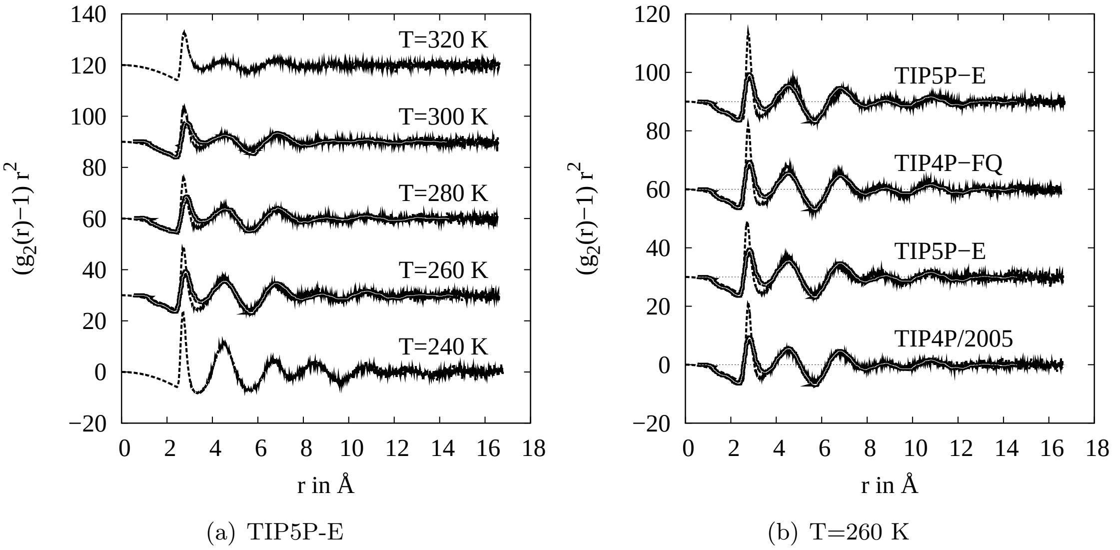

(a) TIP5P-E (b) T=260 K

Figure 3.4.: (a) Pair correlation functions of TIP5P-E water for different temperatures (− − − −) in comparison with experimental data [12] (white line) at 258.15 K, 268.15 K, 298.15 K. (b) Pair correlation functions of different water models at 260 K in comparison to experimental data [12] at 258.15 K.

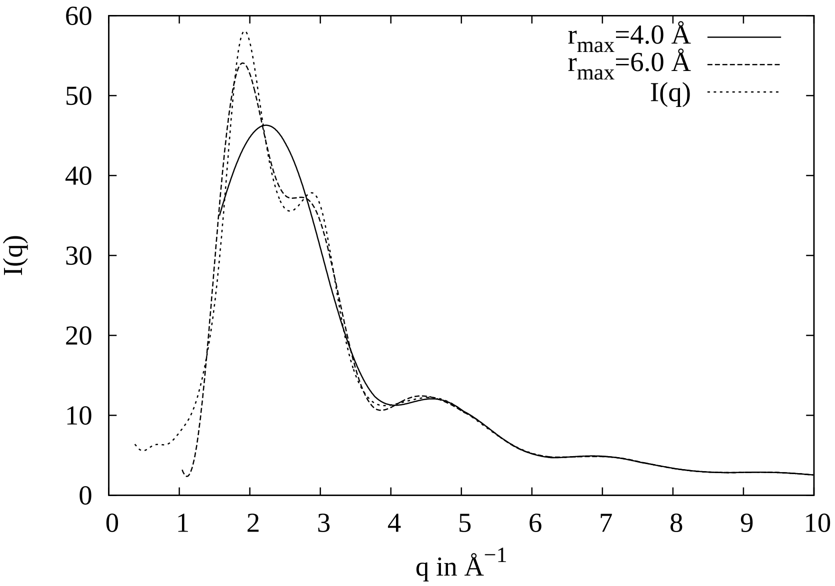

Figure 3.5.: The Fourier transforms of the pair correlation functions of TIP4P/2005 water at 260 K were truncated after 4 Å and 6 Å , which corresponds roughly to a truncation after the first and second neighbor shell. While the first shell is not enough to reproduce the intensity curves, its main features seem to be already present by the inclusion of the first two shells. This feature is consistent for all investigated water models.

the form: $f(x) = a_1 exp(-x/\tau_1) + a_2 exp(-x/\tau_2)$. In figure 3.7 the extrapolation of the H bond count for bonds with a long lifetime to $t = 0.0$ ps is depicted showing convergence for increasing t_E. Now we look more closely at the dependence on t_E. The real number of hydrogen bonds increases with the excursion time before reaching a kink between 0.2 and 1.5 ps depending on the temperature and then increasing further, because the unnatural long excursion time leads to an artificial extension of the lifetime of the hydrogen bonds. We use this kink, which is only visible at very low temperatures up to 260 K to determine the optimal excursion time, see figure 3.9. Although this procedure may seem somewhat arbitrary, it does not influence the final count of the H-bonds, which is only weakly dependent on t_E for low temperatures. With increasing temperature the kink becomes smaller until it disappears completely. As the lifetime of the hydrogen bonds drops below 10.0 ps in this temperature range, we use a small excursion time of about 10 % of the H-bond lifetime.

Thus we arrive at the temperature dependence depicted in figure 3.7. Here the average H-bond number per molecule is depicted for all four models using an angle of $\alpha = 30$ degrees. The error increases with temperature, because of a stronger dependence of the H-bond number on the excursion time. Increasing the angle α leads to a moderate increase in $<\text{Hbond}> /N$ for higher temperatures weakening its temperature dependence. The lifetimes depend only weakly on α. We choose $\alpha = 30$ degrees, because a larger angle seems to loosen the geometric constraints unnecessarily, washing out our signal, while a too small α leads to a considerable change even in the low temperature range, indicating a too constrictive setup. An angle of 30 degrees is also a sensible choice, as it has been estimated in Ref. [15] from the Debye-Waller factors that this is the amplitude of librations breaking the hydrogen bonds.

For all four models we can observe a decrease in the average hydrogen bond count with temperature, which seems to be stronger for the models with a TIP5P geometry than for the ones with a TIP4P geometry. Polarizability does not have a considerable effect on the bond count.

In the q-range considered here the signature of structure change upon cooling is the development of a pronounced shoulder around $q \simeq 3$ [1/Å]. In the simulated scattering curves the same shoulder is strongly affected by the handling of the electronic density distribution, which is rather uncertain even for the models producing very nice agreement in the case of the temperature dependence of experimental self-diffusion coefficients and the density anomaly (as well as other anomalous behavior not discussed here). Thus even rather bad models may perform well with respect to the scattering curves they produce. This in turn means that it is difficult to determine the microscopic cause of anomalous behavior on the basis of scattering curves produced by phenomenological force field models.

The model performing best with respect to the density anomaly shows the least change of <Hbonds> in the temperature range considered here. According to this it appears unlikely that chain-like structures play a significant role for anomalous behavior in this temperature range.

Small q limit

Another interest arising from the three most popular thermodynamic theories of water (stability-limit conjecture, liquid-liquid transition hypothesis, singularity-free scenario), led to further investigation in the small q regime, because of the connection between the compressibility and $S(q = 0) = k_BTN\rho\kappa_T$.

Bosio, Teixeira and Stanley were the first to investigate the small q limit in x-ray scattering. They studied q from 0.15 $Å^{-1}$ to 1.0 $Å^{-1}$ with temperatures ranging from 253 K to 348 K. Their main result was a surprising increase of $I(q)$ with decreasing q corresponding to density fluctuations with a length scale that increases to about 8 Å as T is decreased to 253 K [16]. In 1988 Michielsen, Bot and van der Elsken published results for 0.50 $\mathrm{nm}^{-1} < q < 5.0\ \mathrm{nm}^{-1}$ and for 247 K $< T <$ 274 K [17]. Their results contradict those of Bosio et al giving a maximum of 4 nm for the length scale of the density fluctuations. Bosio et al confirmed their previous results in 1989 by neutron scattering experiments [18], which showed an increase of the structure factor with decreasing momentum transfer, below 0.5 $Å^{-1}$. In 1991 Dings, Michielsen and van der Elsken then report that no enhanced intensity could be measured in the q range $0.4 - 1.8\ \mathrm{nm}^{-1}$ and the temperature range $273 - 253$ K [19]. Another measurement of the small q regime was performed by Ludwig et al in 1993, who measured the absolute structure factor of liquid water over the wave-number range $0.05 < q < 0.30\ Å^{-1}$ and the temperture range $-34 < T < 25°$ C finding that the correlation lengths of the density fluctuations are small and change very little with temperature, suggesting that supercooled water may not be approaching a proposed spinodal point. They conclude that the increasing density fluctuations with supercooling in water appear to be due to an increasing fraction of water molecules participation in clusters not an increasing range of correlations [20]. A new study performed by Huang, et al in 2009 seems to have cleared the dispute in favor of an enhancement [21].

Figure 3.10 shows our simulation results for the small q regime of TIP5P-E water. As the pair correlation function can only be computed to a maximal distance r_{max} depending on the system size, the scattering intensity is limited to a minimal q_{min}. The abrupt edge at the end of the pair correlation function entails the creation of ripples in the small q regime of the intensity curves. But despite of the ripples visible in figure 3.10 a clear minimum is visible even in the data extracted from the $N = 4096$ simulations. This is in general agreement with [22] Additional smooth line fits are added to guide the eye. But the fits are unfortunately not reliable enough to compute the compressibility. While our measurements confirm recent experimental results we do not see any clear heterogeneities in the liquid structure as postulated by Huang et al [21].

While the historical dispute seems to have been resolved in favor of a small q enhanced on the experimental and on the simulation side, the enhancement is not pronounced enough to infer strong heterogeneities and thus signals for singular behavior [22].

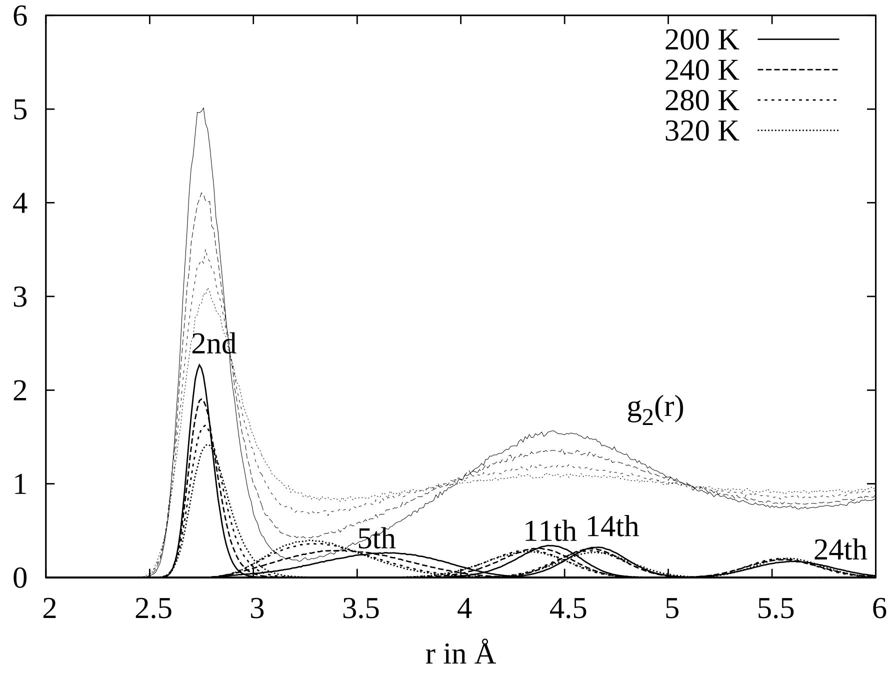

(a)

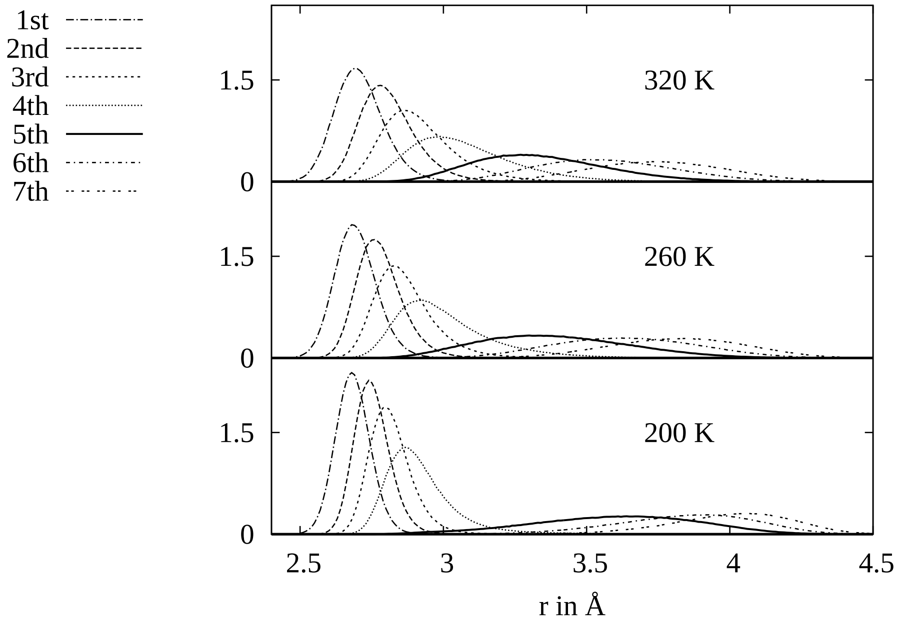

(b)

Figure 3.6.: (a) The pair correlation functions $g_2(r)$ of TIP4P/2005 water at different temperatures are shown together with position distributions of different neighbors. One can see, that the 5th neighbor shows the largest movement, migrating nearer to the first neighbor shell with increasing temperature. This picture is very similar for all of the investigated water models. (b) The position distributions for the first seven neighbors are shown for different temperatures.

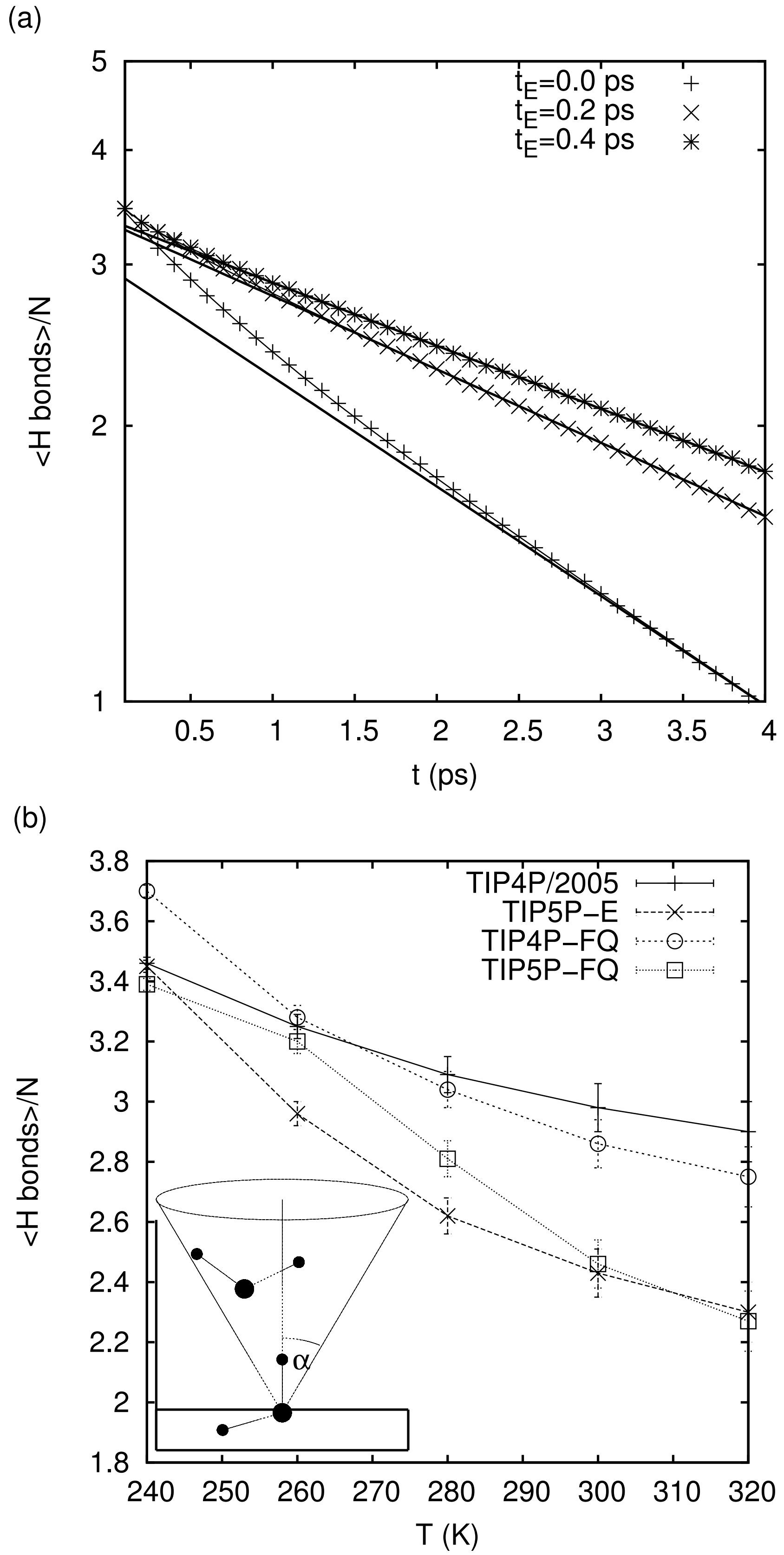

Figure 3.7.: (a) Typical results for the H-bond decay curves here shown for the TIP4P/2005 model at T=280 K. (b) Temperature dependence of the average H-bond number per molecule for all four models using an angle of $\alpha = 30$ degrees for the initial H-bond search. The inset illustrates the geometric search criteria for the hydrogen bonds.

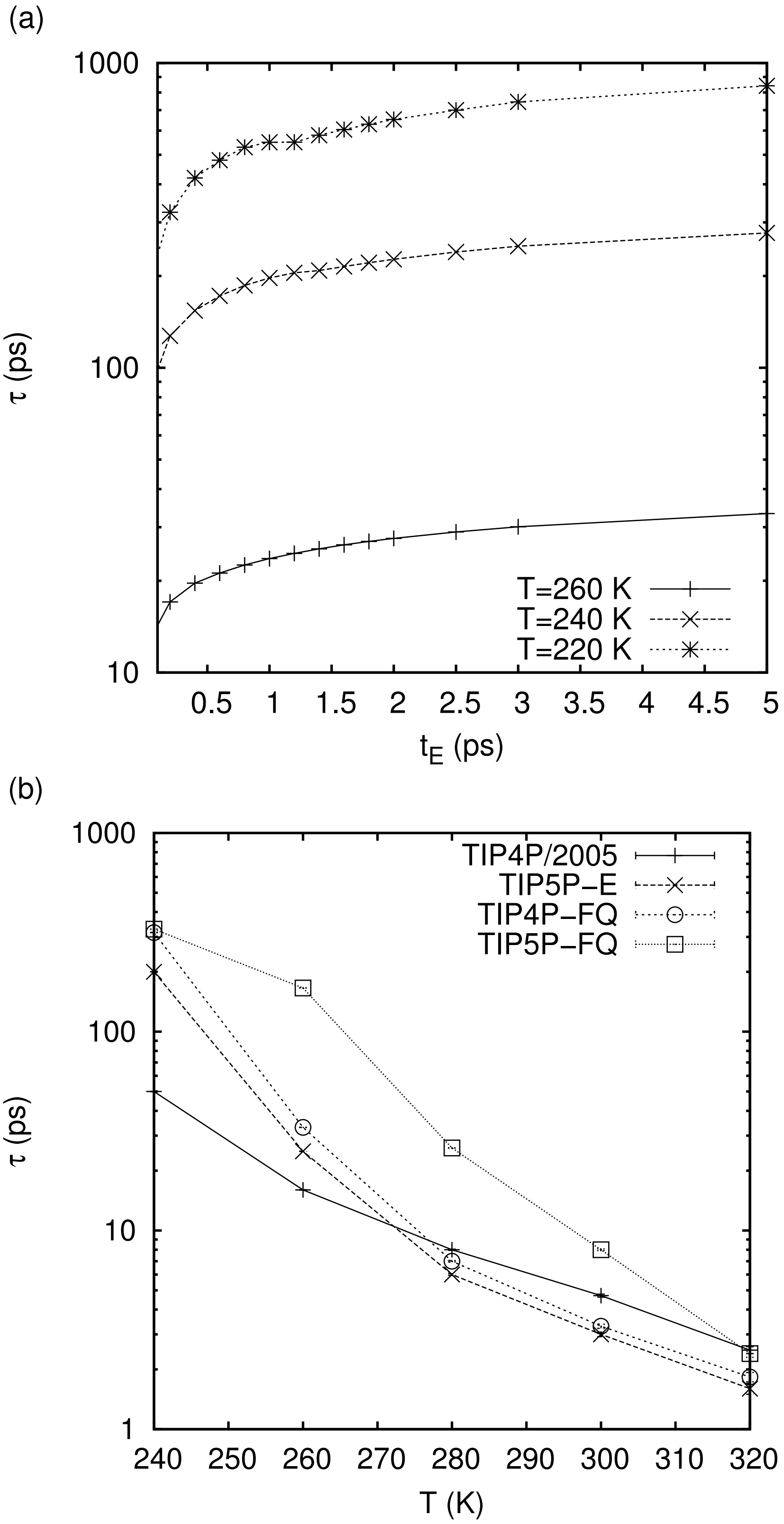

Figure 3.8.: (a) Dependence of the fitted H-bond lifetime, τ, on the excursion time, t_E, for three low temperatures. A small kink is visible. (b) Resulting H-bond lifetimes for the four different models.

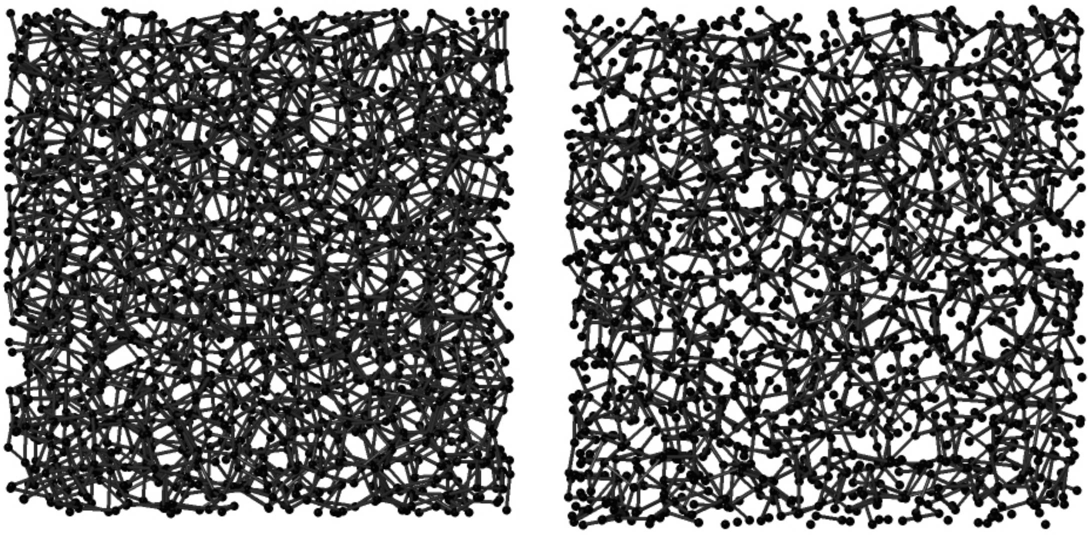

(a) (b)

Figure 3.9.: The change in hydrogen bonds is clearly visible between two configurations of TIP4P/2005 water at 240 K (a) and 320 K (b). It is also notable, that the H-bond distribution is very homogeneous without bigger holes in the network.

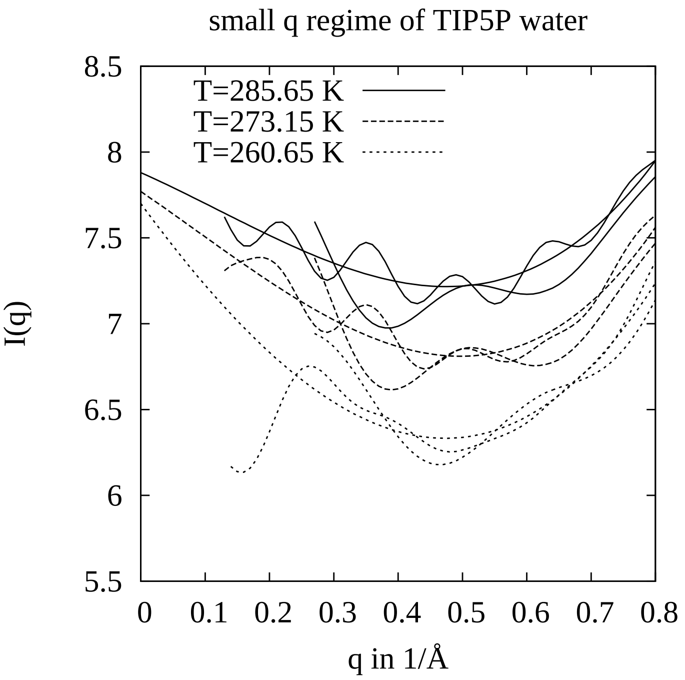

Figure 3.10.: Shown is the small q range of TIP5P water for three different temperatures. While the rippled lines are the simulation data, the ones stopping at about 0.3 $\AA^{-1}$ are from the 4096 molecule simulations and the ones stopping at about 0.12 $\AA^{-1}$ are from the 32768 molecule simulations, the smooth lines are polynomial fits to guide the eye.

Bibliography

[1] Berendsen H J C, Postma J P M, Van Gunsteren W F, DiNola A, and Haak J R. Molecular dynamics with coupling to an external bath. *J. Chem. Phys.* , 81:3684–90, 1984.

[2] Omelyan I P. On the numerical integration of motion for rigid polyatomics: The modified quaternion approach. *Computers in Physics*, 12(1):97–103, 1998.

[3] Deserno M and Holm C. How to mesh up ewald sums. I. a theoretical and numerical comparison of various particle mesh routines. *J. Chem. Phys.* , 109:7678–93, 1998.

[4] Abascal J L F and Vega C. A general purpose model for the condensed phases of water: TIP4P/2005. *J. Chem. Phys.* , 123:4505–17, 2005.

[5] Rick S W. A reoptimization of the five-site water potential (TIP5P) for use with ewald sums. *J. Chem. Phys.* , 120(13):6085–93, 2004.

[6] Rick S W, Stuart S J, and Berne B J. Dynamical fluctuating charge force fields: Application to liquid water. *J. Chem. Phys.* , 101(7):6141–56, 1994.

[7] Guse C, Simionescu A, Schünemann B, Hentschke R, and Bomsdorf H. Temperature-dependent structure of liquid water investigated by means of energy-dispersive x-ray diffraction and molecular dynamics simulations. *Journal of Physics: Condensed Matter*, 22:325105–14, 2010.

[8] Head-Gordon T and Hura G. Water structure from scattering experiments and simulation. *Chem. Rev.*, 102(8):2651–70, 2002.

[9] Narten A H, Danford M D, and Levy H A. X-ray diffraction study of liquid water in the temperature range 4-200°C. *Discuss. Faraday Soc.*, 43:97–107, 1967.

[10] Nishikawa K and Kitagawa N. X-Ray diffraction study of liquid water. *Bull. Chem. Soc. Jpn.*, 53(10):2804–8, 1980.

[11] Corban R and Zeidler M D. X-ray investigation of supercooled water. *Ber. Bunsenges. Phys. Chem.*, 96(10):1463–7, 1992.

[12] Yokoyama H, Kannami M, and Kanno H. Existence of clathrate-like structures in supercooled water: X-ray diffraction evidence. *Chem. Phys. Lett.*, 463(1-3):99–102, 2008.

[13] Yan Z, Buldyrev S V, Kumar P, Giovambattista N, Debenedetti P G, and Stanley H E. Structure of the first- and second-neighbor shells of simulated water: Quantitative relation to translational and orientational order. *Phys. Rev. E*, 76(5):051201–5, 2007.

[14] Sciortino F, Geiger A, and Stanley H E. Isochoric differential scattering functions in liquid water: The fifth neighbor as a network defect. *Phys. Rev. Lett.*, 65(27):3452–55, 1990.

[15] Teixeira J, Bellissent-Funelt M C, and Chen S H. Dynamics of water studied by neutron scattering. *J. Phys.: Condens. Matter* , 2:105–8, 1990.

[16] Bosio L, Teixeira J, and Eugene Stanley H. Enhanced density fluctuations in supercooled H2O, D2O, and Ethanol-Water solutions: Evidence from Small-Angle X-Ray scattering. *Phys. Rev. Lett.* , 46(9):597–600, 1981.

[17] Michielsen J C F, Bot A, and van der Elsken J. Small-angle x-ray scattering from supercooled water. *Phys. Rev. A*, 38(12):6439–41, 1988.

[18] Bosio L, Teixeira J, and Bellissent-Funel M C. Enhanced density fluctuations in water analyzed by neutron scattering. *Phys. Rev. A*, 39(12):6612, 1989.

[19] Dings J, Michielsen J C F, and van der Elsken J. Equilibrium and nonequilibrium contributions to X-Ray scattering from supercooled water. *Phys. Rev. A*, 45(8):5731, 1992.

[20] Xie Y, Ludwig K F, Morales G, Hare D E, and Sorensen C M. Noncritical behavior of density fluctuations in supercooled water. *Phys. Rev. Lett.* , 71(13):2050, 1993.

[21] Huang C, Wikfeldt K T, Tokushima T, Nordlund D, Harada Y, Bergmann U, Niebuhr M, Weiss T M, Horikawa Y, Leetmaa M, Ljungberg M P, Takahashi O, Lenz A, Ojamae L, Lyubartsev A P, Shin S, Pettersson L G M, and Nilsson A. The inhomogeneous structure of water at ambient conditions. *Proc. Natl. Acad. Sci. U.S.A.*, 106(36):15214–8, 2009.

[22] Clark G N I, Hura G L, Teixeira J, Soper A K, and Head-Gordon T. Small-angle scattering and the structure of ambient liquid water. *Proc. Natl. Acad. Sci. USA*, 107(32):14003–8, 2010.

3.2. Simulations of confined water

3.2.1. Capillary condensation

In order to fill the tubes we first perform simulations with a chemical potential high enough to allow for easy entry of water into the tube. Then we decrease the chemical potential to its correct value and equalize it before performing the actual simulation.

In order to check for convergence we try to approach the equilibrium molecule number from above as well as from below (see figure 3.11).

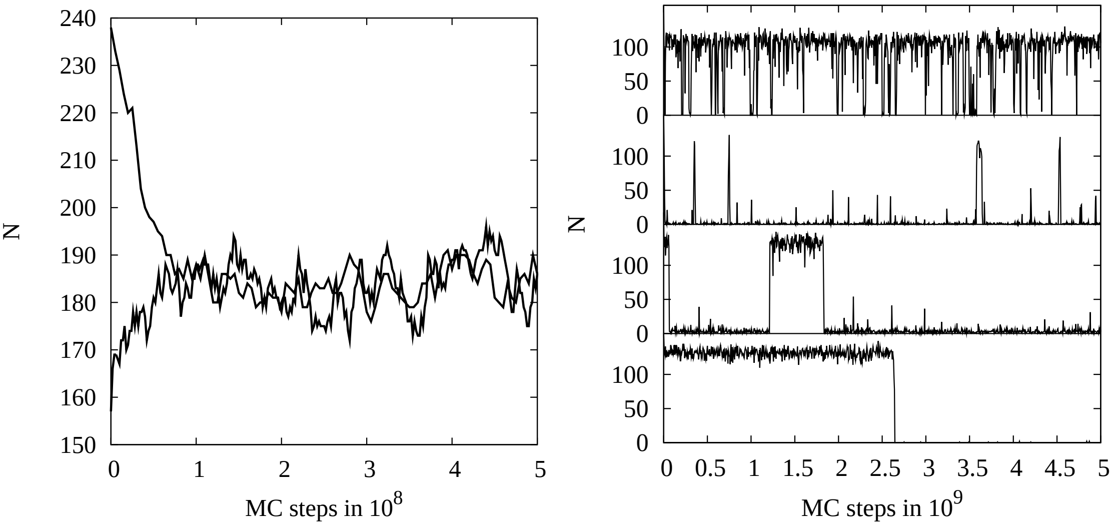

(a) Convergence of the MC simulation

(b) Time evolution

Figure 3.11.: (a) The convergence of the MC simulation can be judged by starting from two different configurations one above and one below the equilibrium. (b) Examples for the evolution of the molecule number, N, with simulation time after convergence.

With this procedure we observe only one part of the hysteresis curve which we investigated for the carbon slits and that was observed in numerous previous works like [1, 2]. We do not observe partially filling of the tubes. In some cases the tubes stay filled for relatively long periods (several million MC steps) before rapidly emptying indicating the existence of metastable states. At higher temperatures small tubes oscillate between filled and empty states.

This behavior seems similar to that observed by Hummer et al [3].
They conducted MD simulations of a 8.1 Å tube at $\sigma_{CO} = 3.2751$ Å and $\epsilon_{CO} = 0.114333$ kcal/mol, as well as for a weakened water-nanotube van der Waals attraction with parameters $\sigma_{CO} = 3.4138$ Å and $\epsilon_{CO} = 0.06461$ kcal/mol, observing, that this change leads to a transition from a filled tube to one fluctuating between a full and empty state on a nanosecond timescale.

In contrast to comparable studies [3, 4], where single-file filling is observed for smaller tubes, we see no filling of tubes smaller than 11 Å. This behavior can be traced back to our choice of a weaker water-carbon potential, which influences the desorption behavior.

We performed GCMC simulations of at least 500 Million MC steps after convergence applying periodic boundary conditions in the direction of the tube axis and treating the long range Coulomb interaction by the MMM1D method as described.

Figure 3.12 shows the information we gathered from our simulations regarding the evaporation transition in the tubes. As we did not try to locate the transition point exactly we just present estimates for it, by plotting the area between the filled and empty or oscillating tubes at 1 atm and 1000 atm. The problem remains, that we cannot be sure if the filled tubes would not empty themselves if we increased the simulation time, although we performed at least 500 Million MC steps for each set-up. An additional problem originates from the closeness of the chemical potential at $P = 1$ atm and at the bulk coexistence pressure P_{coex}, which for the TIP4P/2005 model are nearly indistinguishable even for temperatures up to 600 K. This is partly due to the moderate pressure dependence of the chemical potential and to the coexistence pressure of the TIP4P/2005 model, which is low compared to experimental values. Thus it is not astonishing, that we observe stable filled states for large tubes even at 560 K, although the bulk transition should be expected at about 400 K.

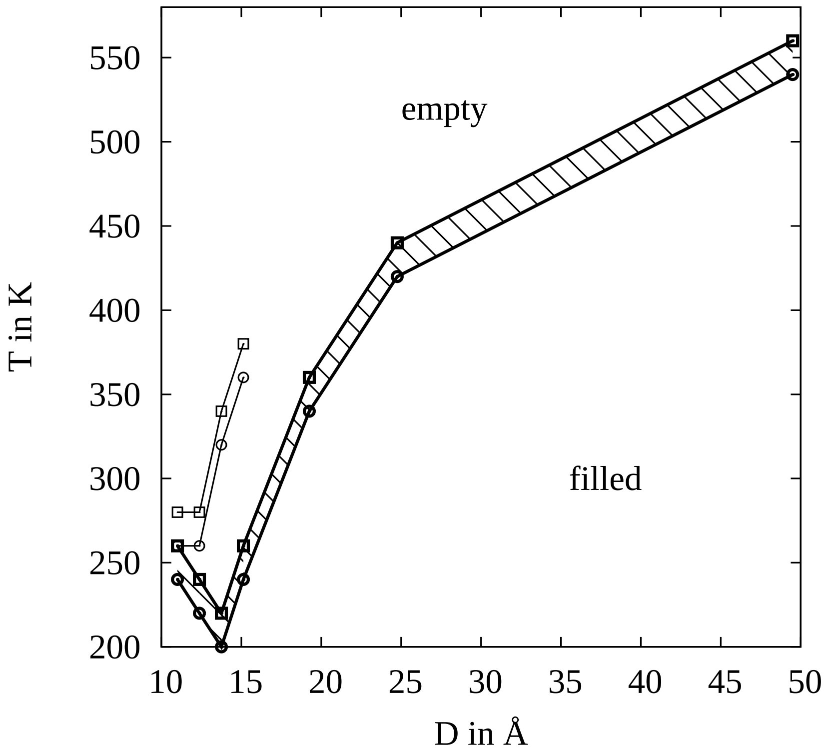

Figure 3.12.: The picture shows the evaporation transition for different nanotube diameters D and temperatures T for pressures of 1 atm (lower filled curves) and 1000 atm (upper curves). The areas between the curves indicate the domain between tubes that stayed filled during the whole simulation (lower boundary) and those that emptied themselves or oscillated (upper boundary).

3.2.2. Density and the excess adsorption Γ

In order to define the density of water in a carbon nanotube it is necessary to determine the internal tube diameter accessible to the fluid D_{eff}, which may vary with external factors like temperature and pressure. A simple commonly used relationship is $D_{eff} = D - \Delta$, where $\Delta = 3.4$ Å is the separation between two adjacent graphitic layers. Here one assumes that the adsorbate cannot penetrate beyond the graphite hard sphere contact. This approximation does not take the properties of the adsorbate into account and is thus mostly useful for heteronuclear adsorbates or mixtures. A more precise expression proposed by Kaneko et al [5] for carbon slit pores can be extended to nanotubes [6]

$$D_{eff} = D - (2z_0 - \sigma_{ff}) \tag{3.1}$$

where σ_{ff} is a measure of the fluid particle size and z_0 is the distance of closest approach between the fluid and the wall, which can be estimated by the zero-crossing of the fluid-wall potential (see figure 3.13). As demonstrated in the table below z_0 depends only weakly on the tube radius R for the tube sizes considered in this work and converges fast to the value for a carbon sheet. We will use the sheet value $z_0 = 0.85837\sigma_{fs}$ to compute D_{eff}. Thus $D_{eff} = D - 2.3175$ Å. The effective volume is given accordingly by $V_{eff} = \pi L D_{eff}^2/4$.

geometry	z_0
tube ($R = 3\sigma_{fs}$)	$0.85754\sigma_{fs}$
tube ($R = 5\sigma_{fs}$)	$0.85813\sigma_{fs}$
tube ($R = 7\sigma_{fs}$)	$0.85826\sigma_{fs}$
tube ($R = 10\sigma_{fs}$)	$0.85831\sigma_{fs}$
tube ($R = 20\sigma_{fs}$)	$0.85836\sigma_{fs}$
tube ($R = 30\sigma_{fs}$)	$0.85837\sigma_{fs}$
sheet	$0.85837\sigma_{fs}$

Table 3.1.: Zero-crossing of the fluid-wall potential for different geometries.

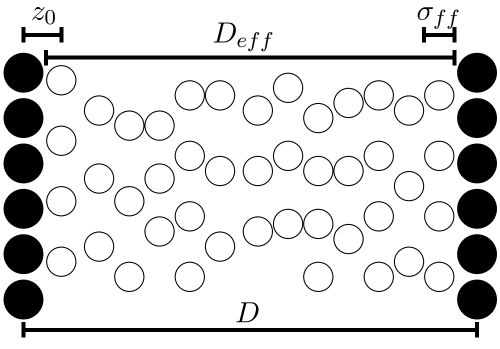

Figure 3.13.: Computation of the effective diameter $D_{eff} = D - (2z_0 - \sigma_{ff})$.

The excess adsorption Γ can now be defined as:

$$\Gamma = \int_0^{D_{eff}/2} \left[\frac{\langle N(r) \rangle}{V_{eff}} - \rho_{bulk} \right] dr\,. \tag{3.2}$$

Figure 3.14 shows the density for different temperatures in dependence on the tube diameter D for $P = 1$ atm and $P = 1000$ atm. From diameters 13 Å to 25 Å, where the water in the tube is liquid, the density decreases by about 20 %. This observation is in qualitative agreement with that of Alexiadis and Kassinos [7], who have computed the density of water inside a carbon nanotube surrounded by a water bath at $T = 300$ K and $P = 1$ atm by MD simulation. The arrows in figure 3.14 indicate the corresponding bulk densities. We observe that the density at $D = 25.0$ Å is still about 15 % off its bulk value.
As will be demonstrated later by a structural analysis water freezes in the two narrowest tubes, thus explaining the observed density jump. It can also be seen that for $D = 11$ Å there exist two stable ice structures one with a higher and one with a lower density.

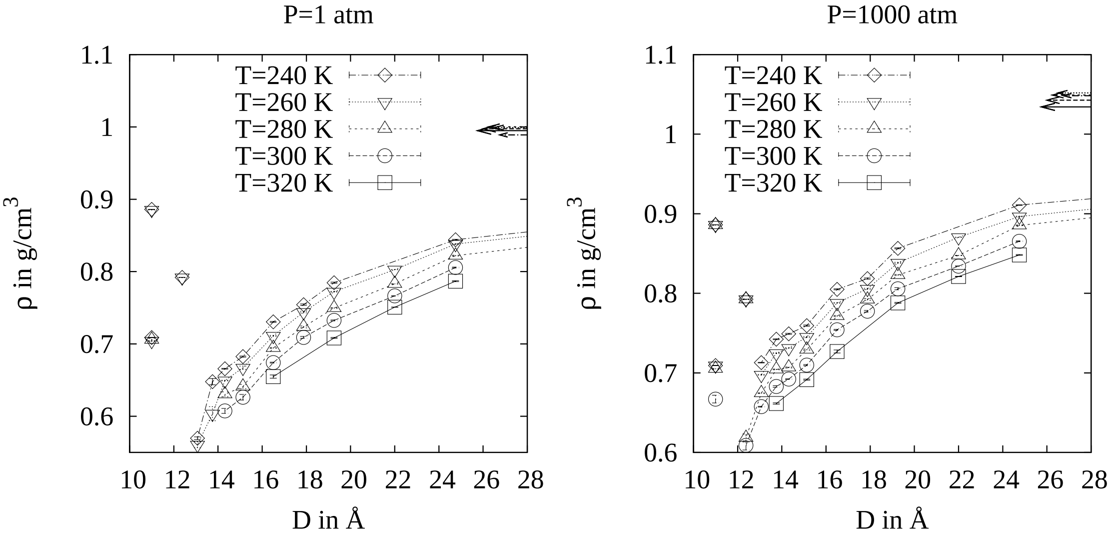

(a) (b)

Figure 3.14.: Depicted is the density against the tube diameter D for different temperatures at 1 atm (a) and 1000 atm (b). The arrows indicate the bulk values.

The excess adsorption Γ is depicted in figure 3.15 expressing the same information as the density plots.

The changes in density with temperature are plotted in figure 3.16. For narrow tubes at deep temperatures the density curve is flat, as here the ice structure is fully occupied by water molecules. A jump in density is observed on melting, visible at $P = 1000$ atm and $D = 12.38$ Å between 280 and 300 K. A change in density on melting can also be observed for the low density ice form in the 11.00 Å tube at $P = 1000$ atm at about 280 K. For larger tube diameters and higher temperatures the density seems to decrease monotonically with growing temperature.

We also simulated a larger tube with diameter 49.5 Å and a length of 59 Å to demonstrate the convergence to the bulk values. For the two largest tubes at $P = 1000$ atm we extended our investigation down to 180 K in order to establish if a density maximum similar to the bulk case exists. For the 49.5 Å tube we observe a shallow maximum at about 220 K which is not apparent in the smaller tube. Thus it seems, that the structural anomaly of water survives confinement in tubes larger than about 50 Å , even

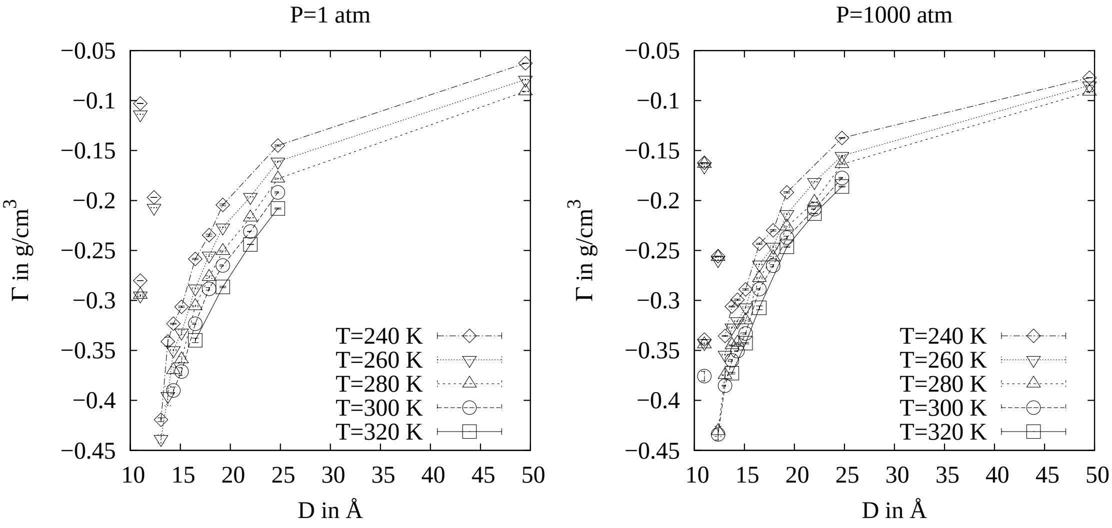

(a)

(b)

Figure 3.15.: The excess adsorption Γ against tube diameter D for two pressures 1 atm (a) and 1000 atm (b).

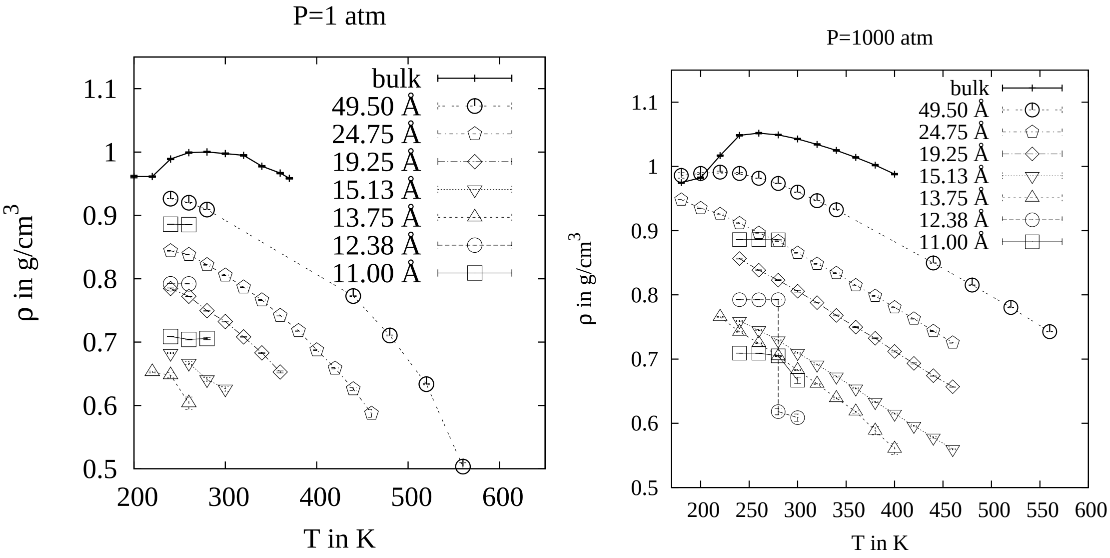

(a)

(b)

Figure 3.16.: The density is plotted against the temperature for several temperatures at 1 atm (a) and 1000 atm (b).

though it is shifted to lower temperatures by about 40 K. This means that if one tries to gain insight into the anomalous behavior of bulk water by experiments in confinement, one has to use rather big pores, where the hydrogen bond network can develop rather undisturbed and search at deeper temperatures.

We also investigated the density at the coexistence pressure of the bulk system (see figure 3.17) by starting from filled and empty tubes. The coexistence pressures and densities

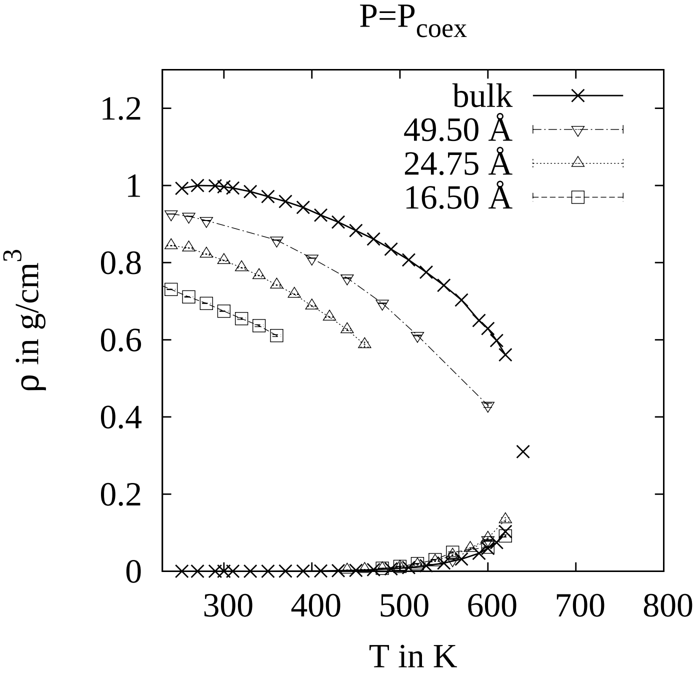

Figure 3.17.: Depicted is the density against the temperature for several temperatures along the coexistence line of the bulk system. The bulk data are taken from [8].

for bulk TIP4P/2005 water were taken from [8]. Unfortunately evaporation occurs early for small tubes, so that the high density branch cannot be traced to the bulk critical point. This indicates that the bulk coexistence pressure is not a good approximation for the confined one in smaller tubes. But from looking at the coexistence region at smaller temperatures, one gets the impression that the critical point for the largest investigated tube is already pretty close to the bulk one, while it might be shifted to deeper temperatures in smaller tubes. To determine the coexistence curves for confined water extensive Gibbs ensemble simulations would be necessary. Brovchenko et al [9] computed the coexistence curves of TIP4P water in hydrophobic cylindrical pores of sizes 12 Å to 20 Å, finding similar shapes to ours. They locate the pore critical temperatures at 530-540 K, with the pore size only having a weak effect.

3.2.3. Self-diffusion

As stated in [10] it is not a trivial problem to compute the self-diffusion in confined geometries. For the time being we will assume that the self-diffusion obeys Fick's law

$$\frac{\partial c(\vec{r},t)}{\partial t} = \nabla \cdot \mathbf{D} \cdot \nabla c(\vec{r},t)\,, \tag{3.3}$$

where $c(\vec{r},t)$ is the particle density at $\vec{r}$ and t and $\mathbf{D}$ denotes the diffusion tensor. Although $\mathbf{D}$ is in general time and position dependent it can be assumed to be constant in the hydrodynamic limit approximation. As we only investigate slit and pore geometries and all observed crystals have axis along the principal directions, we can assume that **D** is diagonal. For the slit (s) and the tube (t) we thus define

$$\begin{aligned} D_{\parallel}^{s} &= \frac{1}{2}(D_{xx}+D_{yy}) \\ D_{\perp}^{s} &= D_{zz} \\ D_{\parallel}^{t} &= D_{zz} \\ D_{\perp}^{t} &= \frac{1}{2}(D_{xx}+D_{yy})\,. \end{aligned} \tag{3.4}$$

For homogeneous, isotropic bulk phases there exist two simple formulas linking the macroscopically defined diffusion tensor with microscopic quantities.

$$D_{\alpha\alpha} = \int_0^\infty \langle \dot{\alpha}(0)\dot{\alpha}(t)\rangle \, dt \tag{3.5}$$

$$2D_{\alpha\alpha}t = = \lim_{t\to\infty} \left\langle [\alpha(0)-\alpha(t)]^2 \right\rangle \tag{3.6}$$

Unfortunately these equations do not hold for the diffusion in the confined directions, where the solution of equation 3.3 must match different boundary conditions. In case of the slit geometry Hall and Ross [11] provided altered expressions accounting for confinement. The boundary and initial conditions are given as

$$c(z,0) = \delta(z-z_0) \tag{3.7}$$

$$\left.\frac{\partial c(z,t)}{\partial z}\right|_{z=0,L_z} = 0\,,\, t>0 \tag{3.8}$$

describing a particle that at $t=0$ is at position $z=z_0$ between two rigid impermeable boundaries at $z=0$ and $z=L_z$. The solution of equation 3.3 in the hydrodynamic limit is then given by

$$c(z,t) = \frac{1}{L_z} + \frac{2}{L_z}\sum_{n=1}^{\infty} \exp(-n^2\pi^2 D_{\perp}^{s} t/L_z^2)\cos\left(\frac{n\pi z}{L_z}\right)\cos\left(\frac{n\pi z_0}{L_z}\right)\,. \tag{3.9}$$

The self-correlation function $G_s(z,t)$ can be derived by averaging $c(z,t)$ over all possible initial source positions.

$$G_s(z,t) = \frac{L_z - z}{L_z^2} + \sum_{n=1}^{\infty} \exp(-n^2\pi^2 D_{\perp}^{s} t/L_z^2)\left[\frac{L_z - z}{L_z^2}\cos\left(\frac{n\pi z}{L_z}\right) - \frac{1}{n\pi L_z}\sin\left(\frac{n\pi z}{L_z}\right)\right] \tag{3.10}$$

The diffusion constant can now be computed by

$$\begin{aligned} \left\langle [z(0)-z(t)]^2 \right\rangle &= \int_{-L_z}^{L_z} z'^2 G_s(z',t)dz' \\ &= \frac{L_z^2}{6} - \frac{16L_z^2}{\pi^4}\sum_{n=1}^{\infty}(2n-1)^{-4}\exp\left[-(2n-1)^2\pi^2 D_{\perp}^{s} t/L_z^2\right]\,. \end{aligned} \tag{3.11}$$

A similar expression for cylindric geometries was derived by Bródka [12]. He solved the diffusion equation for a particle in an infinite cylinder of radius R, assuming reflective cylindric walls and an uniform initial particle distribution

$$\left\langle [x(0)-x(t)]^2 + [y(0)-y(t)]^2 \right\rangle /2 = R^2 \left[\frac{1}{2} - 4\sum_{n=1}^{\infty} \frac{1}{\xi_{1n}^2(\xi_{1n}^2-1)} \exp\left(-\frac{\xi_{1n}^2}{R^2} D_{\perp}^t t\right)\right]. \tag{3.12}$$

Here ξ_{1n} is the nth root of the equation $[dJ_1(x)]/dx = 0$, $J_1(x)$ is the Bessel function of order 1.

There are three caveats when using equations 3.11 and 3.12 with our data for $\left\langle [\alpha(0)-\alpha(t)]^2 \right\rangle$. Firstly they only apply to uniform initial particle distributions, which may only be assumed for large slits and tubes, where the layering near the surface is not important. Secondly, as we do not use impermeable boundaries but soft ones, there is the addition difficulty of fixing L_z and R. We decide to fit R and L_z as well as $D_{\perp}$. The results are quite reasonable as one gets values that lie between the zero crossing of the potential and the soft wall and describe a straight line with a zero crossing of 4.843 Å, which is only 10 % smaller than our estimate of $2z_0$ (see figure 3.18).

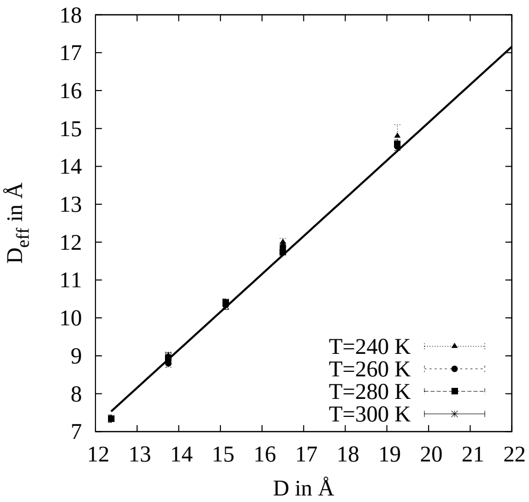

Figure 3.18.: Effective tube diameter D_{eff} originating from the diffusion fits 3.12 against the tube diameter D. Fitting a straight line $x-b$ results in an intercept of $b = 4.843$ Å.

Thirdly as noted by Stiolo [13] water does only diffuse according to a Fickian-type diffusion mechanism for large times. By investigating infinitely long carbon nanotubes of diameter 10.8 Å Stiolo finds that water molecules diffuse through a fast ballistic motion mechanism for up to 500 ps at room temperature, which changes then to Fickian. This is confirmed by Mukherjee et al [14] who search for single file-diffusion in open carbon nanotubes of diameter 8 Å. They observe an initial phase of ballistic diffusion followed by a Fickian one in the long run. For the very small tubes investigated they argue that the hydrogen bonds lead to a strong correlated motion similar to the ballistic mode ($|z(t)-z(0)|^2 \propto t^2$), but at the same time the quasi one-dimensional structure gives rise

to single-file diffusion ($|z(t) - z(0)|^2 \propto t^{1/2}$), resulting in an apparent Fickian diffusivity. Thus bulk and confined water share the same macroscopic diffusion mode.
Alexiadis and Kassinos [7] do not find a distinct, long period of ballistic diffusion, which they ascribe to using a higher density than Stiolo, where clusters have no space to perform coordinated ballistic motion. The show that the diffusion mechanism is mainly Fickian with α in $D \propto \frac{|z(t)-z(0)|^2}{t^\alpha}$ varying between 1 and 0.8.
In our case we observe no long period of non Fickian motion mechanism, but we nevertheless carried out MD runs of at least 500 ps to fit equations 3.5 and 3.12 to the long time behavior.

A good review of past results regarding the self-diffusion of water in carbon nanotubes has been given by Alexiadis and Kassinos in 2008 [15]. Most studies have focused on small carbon nanotubes at room temperature at 1 atm, with the most comprehensive one by Alexiadis and Kassinos themselves [7]. As we compute the self-diffusion for different temperatures and pressures in a wide range of tube radii, our investigation should broaden our knowledge of the dynamic behavior of water in confinement.

Regardless of all the uncertainties involved, the fit functions apply very well to our data for the larger slits and tubes see figure 3.19.

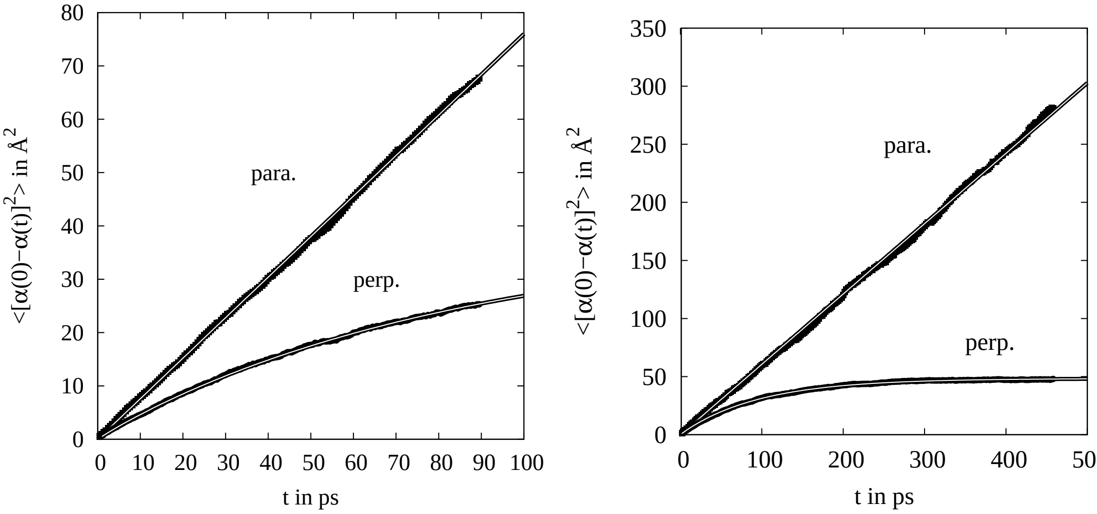

(a) (b)

Figure 3.19.: Simulation data for $\left\langle [\alpha(0) - \alpha(t)]^2 \right\rangle$ for a 20 Å slit at 320 K (a) and for a $D = 24.75$ Å tube at 300 K (b). Shown is the mean-square displacement parallel and perpendicular to the slit or tube respectively together with the fits from equations 3.5, 3.11 and 3.12.

Problems arise for the perpendicular diffusion in smaller tubes at higher temperatures, because here the diffusion is relatively large so that equation 3.12 reaches its plateau very quickly and a fit becomes difficult.

Our final results for the perpendicular diffusion are therefore afflicted with relatively large errors and we could not determine it for all simulated tube diameters and temperatures.

Our results for the parallel diffusion are depicted in figure 3.20, where the arrows indicate the bulk values. As for the density the diffusion values are still somewhat away from the bulk values.

Generally the diffusion along the tube axis lies somewhat above the unconfined one. This behavior might seem extraordinary as one would expect a decrease in the self-diffusion constant in confinement as the movement of the molecules is restricted. But it has already been shown experimentally that a fast molecular transport takes place in carbon nanotubes e. g. [16]. This is in agreement with results presented by Alexiadis and Kassinos [7] for $T = 300$ K, although the enhancement in the self-diffusion is less pronounced in their case. Results for the enhancement of the self-diffusion coefficient of TIP4P water in hydrophobic cylindrical pores at 300 K at the coexistence pressure by Brovchenko et al [17] are comparable to the ones observed in our simulations.

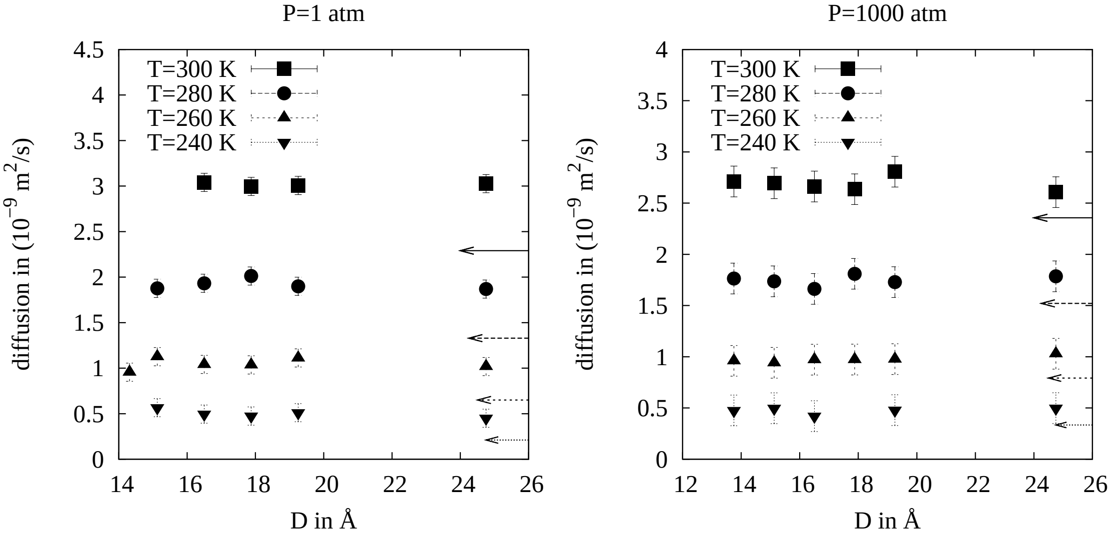

(a) (b)

Figure 3.20.: The diffusion along the tube axis $D_{\|}^{t}$ in dependence on the tube diameter D for different temperatures at 1 atm (a) and at 1000 atm (b).

Figure 3.21 demonstrates that the diffusion perpendicular to the tube axis is of the same size as the axial one and does not seem to change too much with the tube diameter, although we can only draw conclusions about relatively moderate tube radii.

Structure and potential energy

A number of papers discussing the structural behavior of water enclosed in carbon nanotubes of different radii were published in the last few years. It is difficult to analyse the data for a precise comparison as the used water models, carbon potentials and simulation setups differ widely between different studies.

First we want to look at the phase behavior that was observed in simulations so far. We found two works especially informative in this regard.

The first one published in 2001 by Koga et al [18] discusses the formation of ordered ice nanotubes inside carbon nanotubes. They investigate carbon nanotubes with diameters ranging from 11 Å to 14 Å and apply axial pressures of 500 bar to 5000 bar finding a

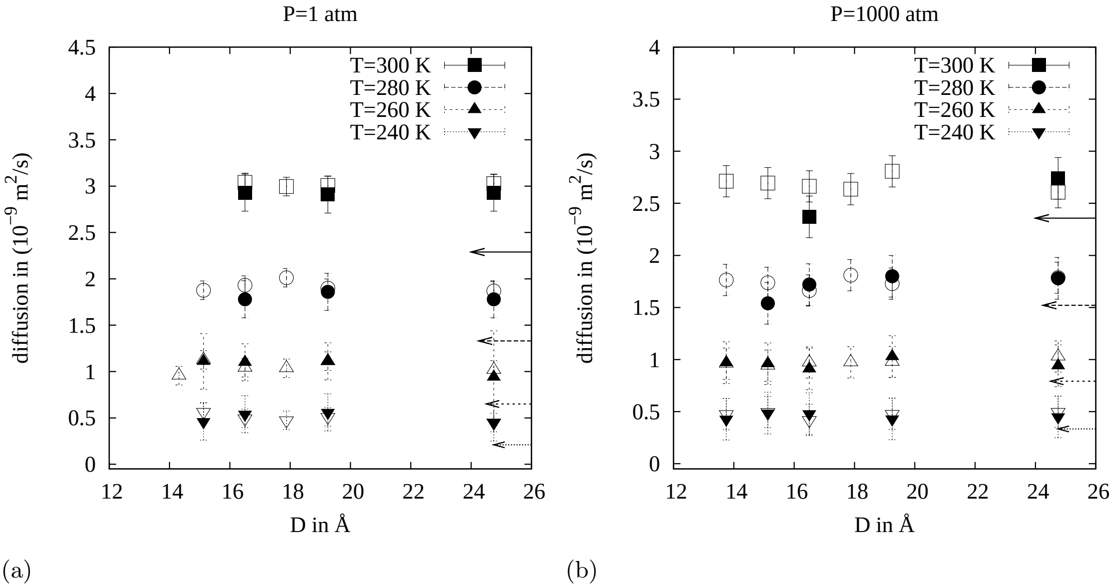

Figure 3.21.: The diffusion perpendicular to the tube axis $D^t_\perp$ (filled symbols) in dependence on the tube diameter D for different temperatures at 1 atm (a) and at 1000 atm (b). The open symbols show the parallel diffusion for comparison.

first-order freezing transition to hexagonal and heptagonal ice and a continuous phase transformation into solid-like square or pentagonal ice nanotubes.

They used molecular dynamics simulations of Tip4p water at constant temperature and axial pressure and simulated for long times of about 200 ns. The carbon tube was modeled by an integrated Lennard-Jones potential. They find a distinctive drop in the potential energy from higher to lower temperatures which is accompanied by a change in structure from unordered to ordered. While a hysteresis loop is observed for the bigger tubes of diameter 12.6 Å and 13.4 Å at a pressure of 500 bar, the transition seems to be continuous for the smaller tubes of diameter 11.1 Å and 11.9 Å. Koga et al argue that the difference in transition is connected to the symmetry change that occurs in the bigger tubes between the ice ring structure and the liquid structure, where molecules are also located in the center of the tube. In the small tubes there is not enough space even in the liquid state for molecules to be located outside the first layer of molecules adsorbed on the surface. Thus the ring structure is preserved.
On increasing the pressure they find that a weak hysteresis can be observed in the $D = 11.1$ Å tube at 2000 bar implying the possible existence of a solid-liquid critical point, which cannot occur in bulk systems. A structural analysis shows that the low-density phase is a square phase with a liquid-like disordered structure, whereas the high-density phase is a solid-like pentagonal-nanotube phase.

The second paper was written by Byl et al in 2006 [19]. They focus on an experimentally observed distinct OH stretching mode that they assign to the inter-ring hydrogen bonds in the stacked-ring structure. In order to identify structural, energetic, and vibrational properties of water in SWNTs they perform classical molecular simulations as well as quantum mechanical DFT calculations.

They find that water forms stacked ring structures in all of the nanotubes considered ((8,8) tube: 4-ring and 5-ring structure; (9,9) tube: 6-ring; (10,10) tube: 7-ring and 8-ring; (11,11) tube: 9-ring). They observe order-to-disorder structural transitions in the (10,10) and (11,11) SWNTs.

In our simulations we see stacked ring structures only in (8,8) and (9,9) SWNTs (see figures 3.22(a), (b) and (d) and a order-to-disorder transition in the (8,8) SWNT (see figure 3.22(b) to (c) and in the (9,9) SWNT (see figure 3.22(d) to (e)). While the melting transition from the hexagonal phase (d) to the liquid (e) is accompanied by a jump in density and potential energy, we observe only a moderate change for the transition from the square phase (b) to the liquid (c). Generally we find that the high density pentagonal phase (a) seems to transform to square ice (b) before melting (c).

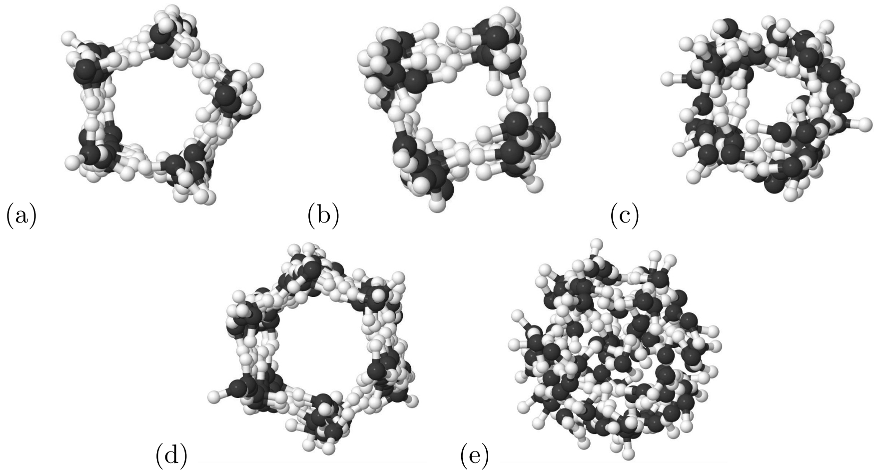

Figure 3.22.: Top views of different ring and liquid structures that are stable in the $D = 11.001$ Å ((a),(b),(c)) and $D = 12.376$ Å ((d),(e)) tubes (generated with jmol).

The structural order can also be seen in figures 3.23 and 3.24. For the $D = 11$ Å tube it is easy to differentiate between the two different ice forms in the radial density profile at $P = 2000$ atm (see 3.23(a)). The pair correlation function in z-direction shows the strong correlation signaling the ordered ice state (see 3.24(a)). The structure with the higher potential energy consists of stacked rings that are formed of 4 water molecules each (see figure 3.22(b)) and seems less ordered than the second structure that is formed out of stacked 5 molecule rings (see figure 3.22(a)).

For higher temperatures the 4-ring ice structure gets more and more disordered. Although there are still 4 molecules in each layer, they are no longer stacked exactly above each other (see figure 3.22(c)). As the radial density profile is not fundamentally changed by the melting transition in the 11.00 Å tube we only observe a slow broadening with temperature. Next we investigate tubes of diameter $D = 12.376$ Å . Here a transition occurs from a frozen ordered 6-stacked-ring structure with low diffusion constant, low potential energy and higher density at low temperatures and high pressures (see figure 3.22(d) to a liquid network structure with high diffusion constant, higher potential energy and lower density at higher temperatures and lower pressures (see figure 3.22(e)). The order-to-disorder transition can also clearly be seen in the density profile as well as in the z-pair correlation function (see figure 3.23(c) and 3.24(c)).

As mentioned before similar freezing transitions from 7 and 8 stacked rings to network structures were observed by Byl et al for tubes of diameter $D = 13.751$ Å [19, 18]. We do not find stacked-ring structures in the investigated temperature and pressure range for this tube size.

For wider tubes the structural changes with temperature and pressure are only weak, showing a general strengthening of the pair correlation with increasing pressure and decreasing temperature (see figure 3.23(b),(d) and 3.24(b),(d)). This is in agreement with earlier studies as no transitions have been observed for larger tubes in the literature.

More insight into the structural effect of confinement can be gained by comparison between the radial density profiles in a slit geometry with the same interaction parameters and at the same thermodynamical conditions (see figure 3.26). The slit has a large diameter of 50 Å in order to get density profiles similar to the ones near a single wall.
It is easy to see that the limited space inside the tubes puts strain on the water structure that gives rise to significant difference in peak height and position in the density profile.

Figures 3.27(a) and (b) depict the potential energy (only water-water interaction) for different temperatures at P=1 atm and P=1000 atm against the tube diameter. The bulk values are indicated by arrows as in earlier plots. In the liquid phase the potential energy rises with decreasing tube diameters with a similar slope for all temperatures. The energy drops on freezing. As mentioned earlier the points with the lower potential energy at 11 Å belong to the 5-ring structure, while the 4-ring structure has a higher potential energy.

The potential energy is also plotted in dependence on the temperature in figures 3.27(c) and (d). Here one can see, that while the potential energy in the larger tubes increases with temperature with a similar slope as for bulk water, there is a clear energy jump at $P = 1000$ atm on melting in the $D = 12.38$ Å tube. For the 4-ring structure in the $D = 11.00$ Å tube one can also see a clear increase in potential energy on melting. Energy values for a larger tube with diameter $D = 49.5$ Å are included to demonstrate the convergence to the bulk energies. Figure 3.28 shows the entropy per water molecule in dependence on the tube diamter, D.

Pressure

The diagonal components of the pressure tensor are shown in figure 3.29. With increasing tube diameter the pressure seems to converge to bulk pressure, althouth the convergence is slow. But as we have already established by looking at the density and the diffusion we are still far away from bulk behavior even for our widest tubes.

While the pressure in the liquid phase is independent of the tube length, L, this is not the case for the ice ring structures. Figure 3.30 shows the change in pressure with changing tube length for the 4-ring and 5-ring ice structures at $T = 240$ K and $P = 1$ atm. While the lateral pressure components are basically constant with L, P_{zz} changes strongly. One can observe a periodic behavior as L is increased enough, to allow another molecule layer to form. As the ice structure turns instable for very large negative pressures, we also performed μPT ensemble MC computations to fix the pressure in z direction to 1 or 1000 atm respectively. The resulting equilibrium lengths are also included in figure 3.30 and are in agreement with the μVT results.

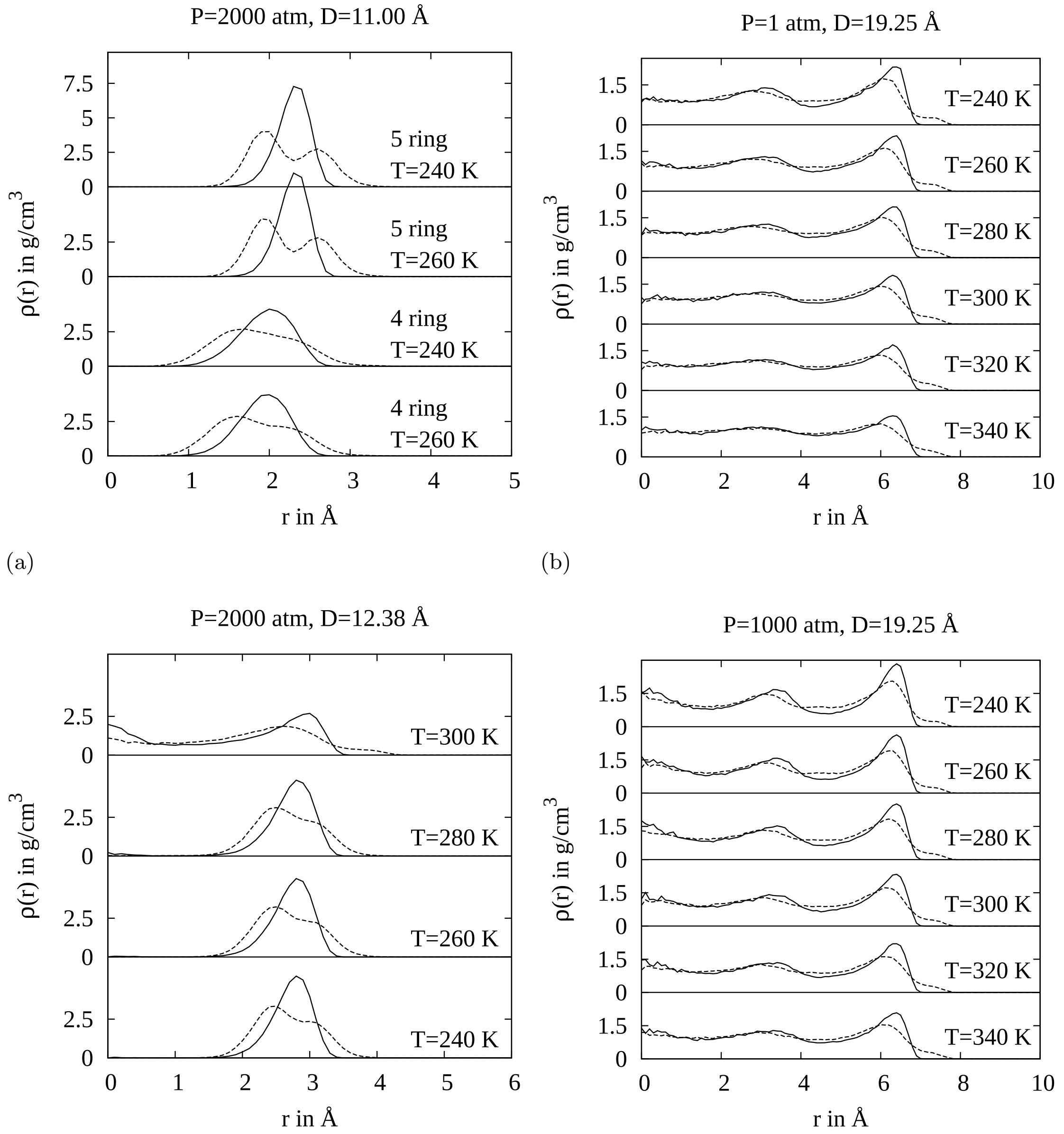

(a)

(b)

(c)

(d)

Figure 3.23.: The density profiles (solid line O atoms and dashed line H atoms) in lateral direction are shown for different temperatures at $P = 2000$ atm for tube diameters $D = 11.00$ Å (a) and $D = 12.38$ Å (c) as well as at $P = 1$ atm (b) and $P = 1000$ atm (d) for tube diameter $D = 19.25$ Å.

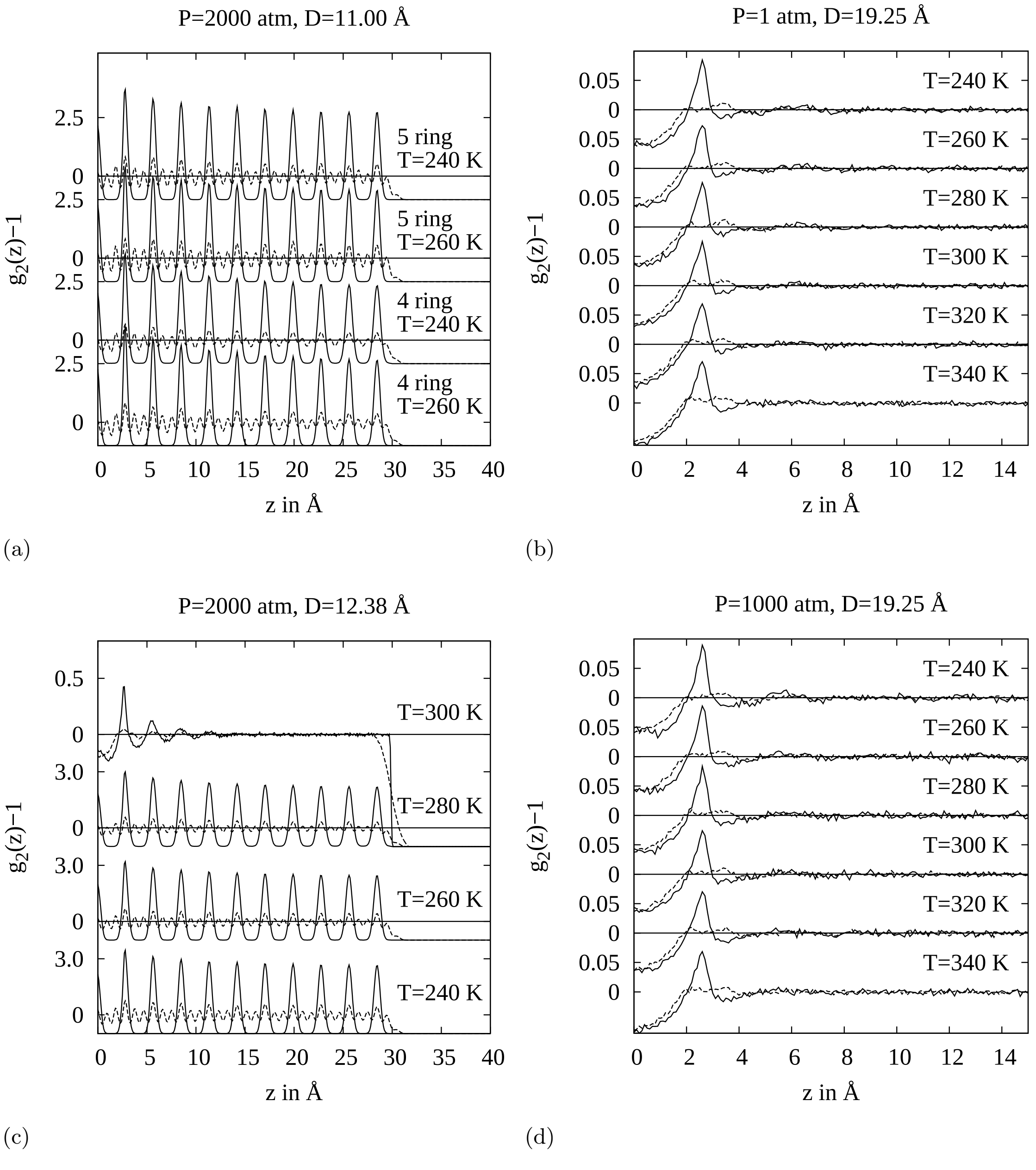

(a) (b)

(c) (d)

Figure 3.24.: The pair correlation functions in z direction (solid line O atoms and dashed line H atoms) is depicted for the same parameters as described in figure 3.23. ((a): $P = 2000$ atm, $D = 11.00$ Å; (b): $P = 1$ atm, $D = 19.25$ Å; (c): $P = 2000$ atm, $D = 12.38$ Å and (d): $P = 1000$ atm, $D = 19.25$ Å)

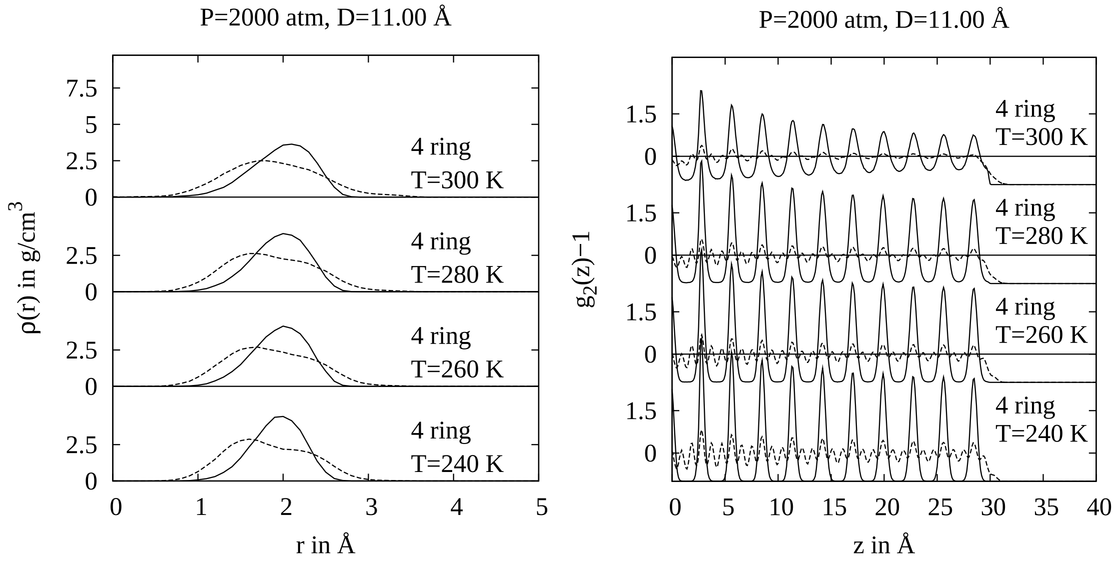

(a) (b)

Figure 3.25.: (a) The radial distribution function for the 4 ring structure at different temperatures (solid line O atoms and dashed line H atoms). (b) The pair correlation functions in z direction (solid line O atoms and dashed line H atoms) is depicted.

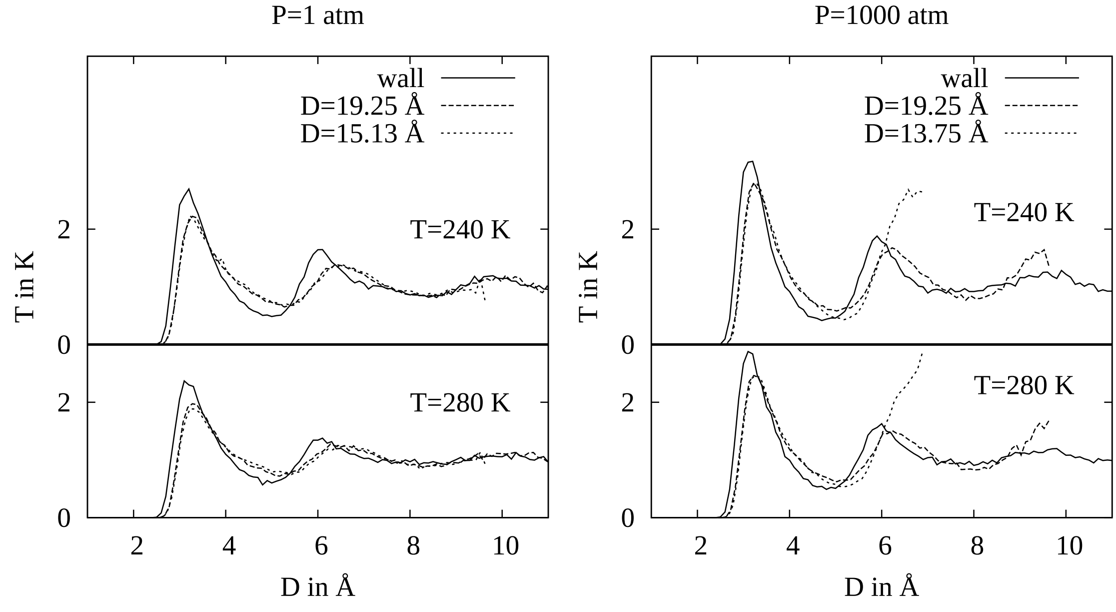

(a) (b)

Figure 3.26.: The radial density profile is shown for a slit geometry with width 50 Å and two tubes of diameters 19.25 Å and 15.13 Å for equal thermodynamical conditions.

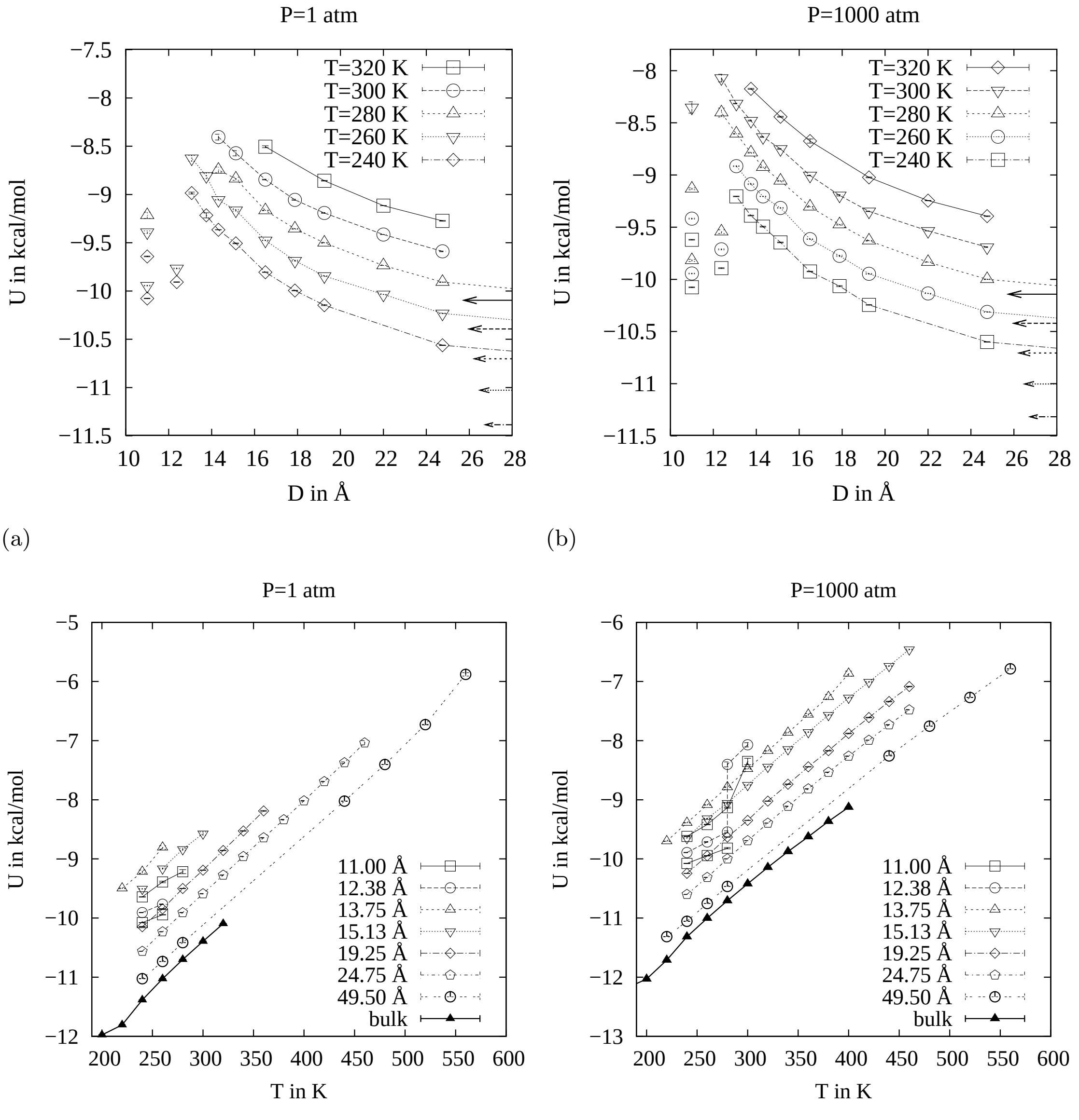

(a)

(b)

(c)

(d)

Figure 3.27.: The potential energy per water molecule without water-carbon interaction (polarization correction included) is depicted against the tube diameter D for different temperatures and pressures at 1 atm (a) and 1000 atm (b). The arrows indicate the bulk values. The potential energy is also plotted against the temperature T for different tube diameters at 1 atm (c) and 1000 atm (d).

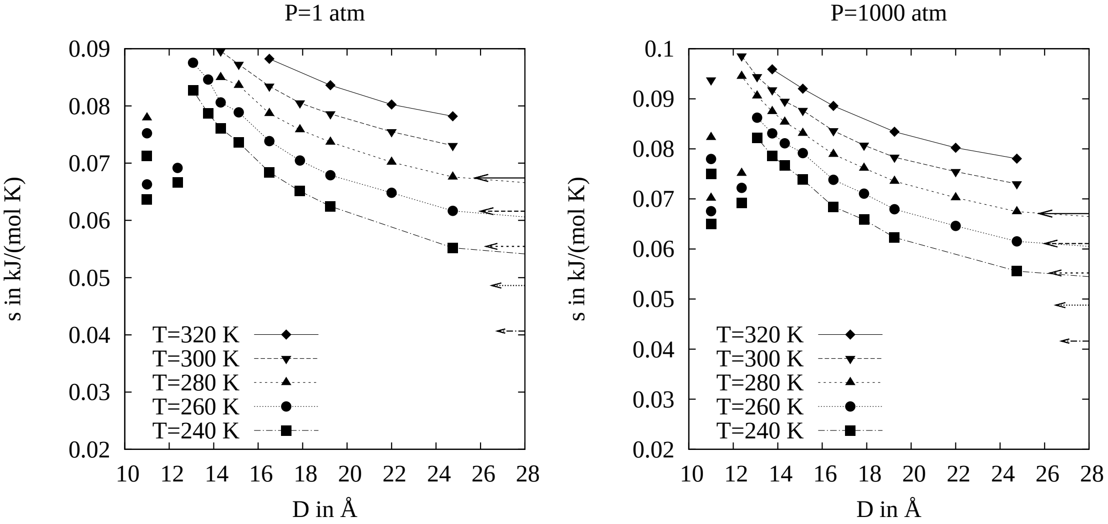

(a) (b)

Figure 3.28.: The entropy per water molecule is depicted against the tube diameter D for different temperatures and pressures at 1 atm (a) and 1000 atm (b).

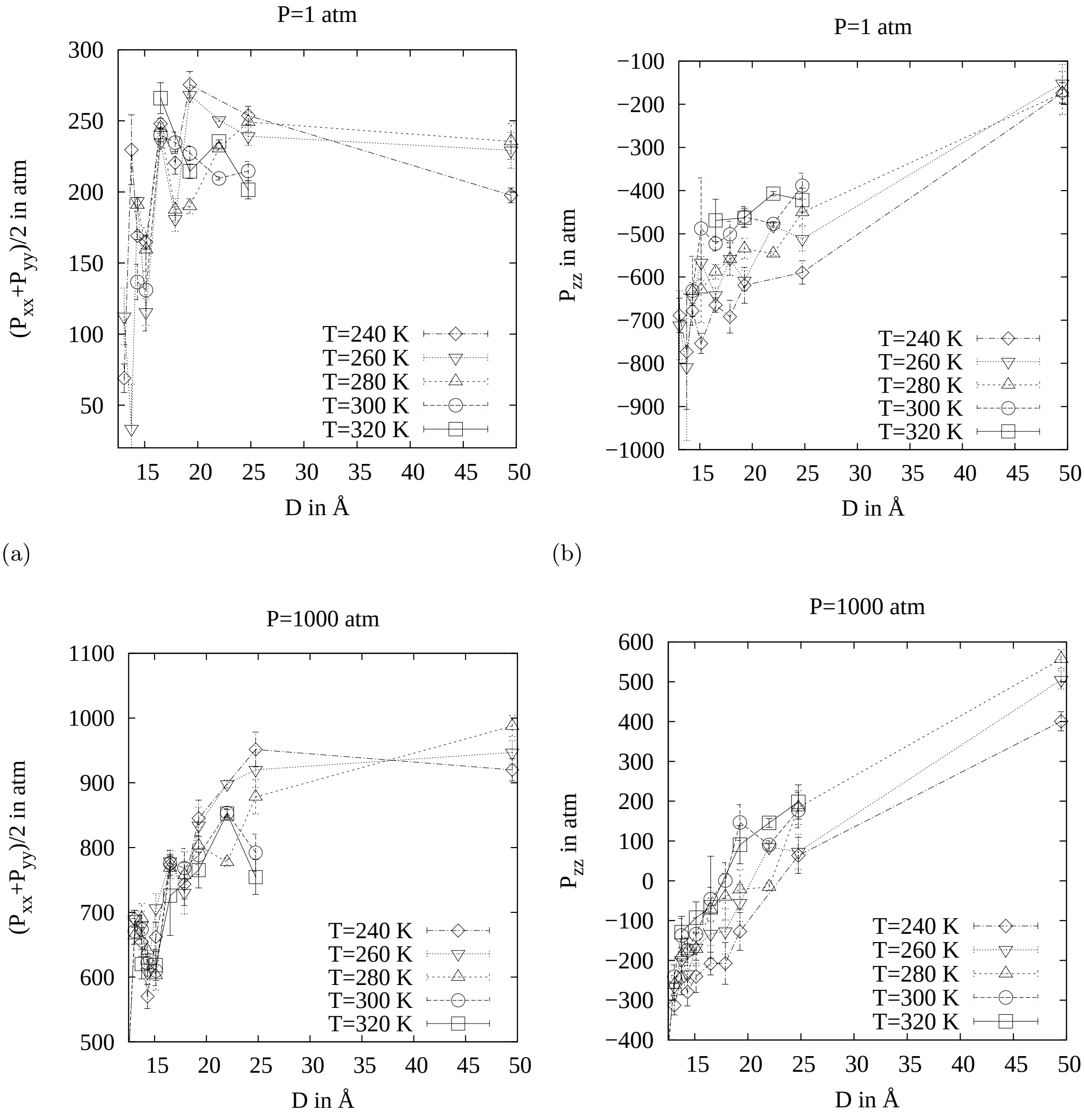

Figure 3.29.: The diagonal components of the pressure tensor against the tube diameter for different temperatures and two pressures 1 atm top and 1000 atm bottom.

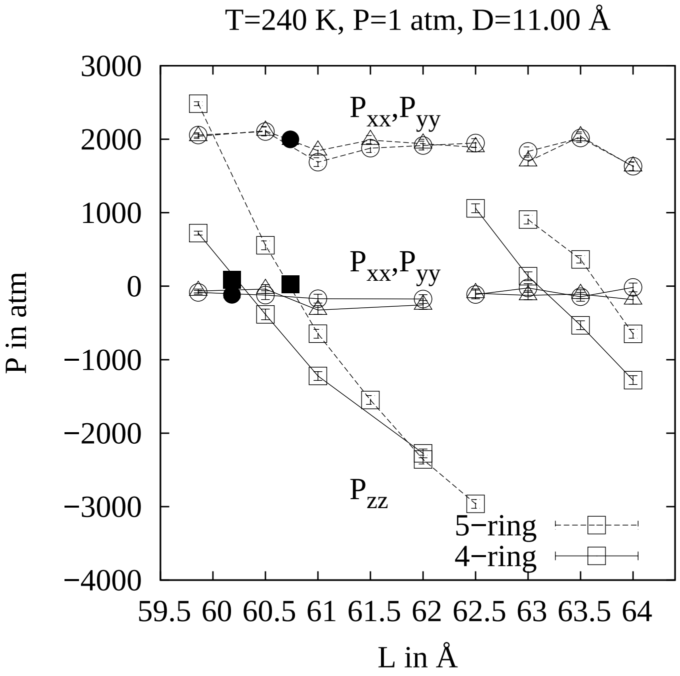

Figure 3.30.: The dependence of the pressure components on the tube length, L, for the 4-ring and 5-ring ice tubes (open symbols). Also shown are the equilibrium lengths from the constant pressure simulations (filled symbols).

Bibliography

[1] Striolo A, Chialvo A A, Gubbins K E, and Cummings P T. Water in carbon nanotubes: Adsorption isotherms and thermodynamic properties from molecular simulation. *J. Chem. Phys.* , 122:234712–14, 2005.

[2] Walton J P R B and Quirke N. Capillary condensation: A molecular simulation study. *Molecular Simulation*, 2(4):361–91, 1989.

[3] Hummer G, Rasaiah J C, and Noworyta J P. Water conduction through the hydrophobic channel of a carbon nanotube. *Nature*, 414(6860):188–90, 2001.

[4] Wang J, Zhu Y, Zhou J, and Lu X-H. Diameter and helicity effects on static properties of water molecules confined in carbon nanotubes. *Phys. Chem. Chem. Phys.*, 6(4):829–35, 2004.

[5] Kaneko K, Cracknell R F, and Nicholson D. Nitrogen adsorption in slit pores at ambient temperatures: Comparison of simulation and experiment. *Langmuir*, 10(12):4606–9, 1994.

[6] Ohba T and Kaneko K. Internal surface area evaluation of carbon nanotube with GCMC Simulation-Assisted n2 adsorption. *J. Phys. Chem. B*, 106(29):7171–6, 2002.

[7] Alexiadis A and Kassinos S. Self-diffusivity, hydrogen bonding and density of different water models in carbon nanotubes. *Molecular Simulation*, 34(7):671–84, 2008.

[8] Vega C, Abascal J L F, and Nezbeda I. Vapor-liquid equilibria from the triple point up to the critical point for the new generation of TIP4P-like models: TIP4P/Ew, TIP4P/2005, and TIP4P/ice. *J. Chem. Phys.* , 125:034503–9, 2006.

[9] Brovchenko I, Geiger A, and Oleinikova A. Water in nanopores. i. coexistence curves from gibbs ensemble monte carlo simulations. *J. Chem. Phys.* , 120:1958–72, 2004.

[10] Schoen M. *Computer simulation of condensed phases in complex geometries.* Springer-Verlag, 1993.

[11] Hall P L and Ross D K. Incoherent neutron scattering function for molecular diffusion in lamellar systems. *Molecular Physics*, 36(5):1549–54, 1978.

[12] Bródka A. Diffusion in restricted volume. *Molecular Physics*, 82(5):1075–78, 1994.

[13] Striolo A. The mechanism of water diffusion in narrow carbon nanotubes. *Nano. Lett.*, 6(4):633–9, 2006.

[14] Mukherjee B, Maiti P K, Dasgupta C, and Sood A K. Strong correlations and fickian water diffusion in narrow carbon nanotubes. *J. Chem. Phys.* , 126:124704, 2007.

[15] Alexiadis A and Kassinos S. Molecular simulation of water in carbon nanotubes. *Chem. Rev.*, 108(12):5014–34, 2008.

[16] Holt J K, Park H G, Wang Y, Stadermann M, Artyukhin A B, Grigoropoulos C P, Noy A, and Bakajin O. Fast mass transport through sub-2-nanometer carbon nanotubes. *Science*, 312(5776):1034–7, 2006.

[17] Brovchenko I, Geiger A, Oleinikova A, and Paschek D. Phase coexistence and dynamic properties of water in nanopores. *The European Physical Journal E*, 12(1):69–76, 2003.

[18] Koga K, Gao G T, Tanaka H, and Zeng X C. Formation of ordered ice nanotubes inside carbon nanotubes. *Nature*, 412(6849):802–5, 2001.

[19] Byl O, Liu J-C, Wang Y, Yim W-L, Johnson J K, and Yates J T. Unusual hydrogen bonding in Water-Filled carbon nanotubes. *J. Am. Chem. Soc.*, 128(37):12090–7, 2006.

4. Conclusion

Finally we want to summarize our results and discuss their relevance to the current research on water.

While unsurprisingly we were not able to solve the puzzle of water's complex behavior, we clarified some aspects of its nature.

In contrast to the early assumption that water's anomalies may be traced back to a mixture model, where two phases of different density develop with temperature, we did not observe any kind of large scale density fluctuations. Experimental evidence for such variations, namely the enhancement of the small angle X-ray scattering intensity, can be described by our model and is indeed also present in even simpler systems like the LJ fluid far away from any critical point and any noticeable inhomogeneities.

The structural information that can be gained from the X-ray scattering intensities regarding the quality of our simulation models is rather limited. This seems to be a general problem, as the reconstruction of meaningful and detailed structures from the experimental data is rather difficult. This is underlined by the fact that special methods like Empirical Potential Structure Refinement (EPSR) and Reverse Monte Carlo (RMC) are needed, whose results then differ considerably from ab initio and effective model computations [1]. In our case it seems that the best results regarding density, diffusion and intensity curves can be achieved with the TIP4P/2005 model, which shows the least change in the hydrogen bond network with temperature. Thus indicating that most models might overestimate structural development.

Some model characteristics like the phase behavior in the supercooled regime are not shared features of all successfully applied water models, some showing one, some multiple critical points [2]. Other features like the density minimum at about 210 K are common to all our investigated models.

This is of special interest as the density minimum was experimentally only found in heavy water confined in 1D cylindrical pores of mesoporous silica at 210 K [3].

Thus it becomes clear, that the predictive power of classical water models lies predominantly in their shared features and general trends.

Regarding the simulations of confined water, we found, that with our carbon-water interaction potential the condensation transition occurs above the saturation pressure for all contemplated slit widths, while evaporation happens below P_0 for larger slits. For a stronger carbon-water interaction evaporation and condensation are shifted to smaller pressures. In order to estimate the true interaction strength between carbon and water, experiments on substrates without active sites on the surface and a well defined pore size distribution would be mandatory.

Furthermore we learned, that the confinement of water in carbon nanotubes frustrates the hydrogen bond network even in tubes with a diameter of 26 Å enough to suppress the development of the density maximum, which in our simulations is only visible in the 49.5 Å tubes even though at a lower temperature.

In smaller tubes these constrictions lead to a varied phase behavior with the occurrence of several different ice nanotubes.

Nevertheless it is astounding how similar the diffusion characteristics of confined water are to that of bulk water. These results demonstrate, that while the structure of the hydrogen bond network is constricted its agility seems to be preserved. The fast water transport through carbon nanotubes that is found experimentally confirms this conclusion.

Therefore the determination of water's properties below the homogeneous nucleation line in larger sized nanopores seems feasible.

Bibliography

[1] Mantz Y A, Chen B, and Martyna G J. Temperature-dependent water structure: Ab initio and empirical model predictions. *Chem. Phys. Lett.*, 405(4-6):294–9, 2005.

[2] Brovchenko I, Geiger A, and Oleinikova A. Liquid-liquid phase transitions in supercooled water studied by computer simulations of various water models. *J. Chem. Phys.* , 123(4):44515–31, 2005.

[3] Liu D, Zhang Y, Chen C-C, Mou C-Y, Poole P H, and Chen S-H. Observation of the density minimum in deeply supercooled confined water. *Proc. Natl. Acad. Sci. USA*, 104(23):9570 –4, 2007.

4.1. Acknowledgment

I want to thank my supervising tutor, Professor Hentschke, for being not just a brilliant physicist but also a dedicated teacher, which is rare.

I am grateful to Professor Bomsdorf for his friendly collaboration, which brought me closer to experimental physics than expected.

Special thanks go to all the members of our research group, who helped me out with some tricky problems by their advise, especially Nils Hojdis, Sebastian Schreiber and Henning Hörstermann.

Finally I am deeply indebted to my family especially my father and to Heiko Braun and his family. They supported me patiently and braved all my occasional frustrations.

A. Appendix

A.1. Abbreviations

Abbreviation	Explanation
AIMD	ab initio Molecular Dynamics
ELC	Electrostatic Layer Correction
FFT	Fast Fourier Transformation
HDA	high-density amorphous ice
LDA	low-density amorphous ice
MC	Monte Carlo
MD	Molecular Dynamics
PME	Particle Mesh Ewald
PPPM	Particle-Particle Particle-Mesh
SPC	simple point charge
SWNTs	single wall nanotubes
TH	temperature of homogeneous nucleation
TIPnP	transferable intermolecular potential n point
TX	temperature of crystallisation
TMD	temperature of maximum density
VHDA	very high density amorphous ice
XAS	X-ray absorption experiments

A.2. Tables

A.2.1. Model parameters

	SPC[1]	TIP4P[2]	TIP4P/2005[3]	TIP5P-E[4]
ϵ (kcal/mol)	0.1554	0.1550	0.1851	0.178
σ (Å)	3.166	3.154	3.1589	3.097
θ_{HOH} (degrees)	109.47	104.52	104.52	104.52
r_{OH} (Å)	1.0	0.9572	0.9572	0.9572
r_{OM} (Å)	-	0.15	0.1546	0.70
θ_{MOM} (degrees)	-	-	-	109.47
Q_H (e)	0.41	0.52	0.5564	0.241

Table A.1.: Parameters for the non-polarizable models.

	SPC-FQ[5]	TIP4P-Pol2[6]	TIP4P-FQ[5]	TIP5P-FQ
ϵ (kcal/mol)	0.2941	0.1887	0.2862	0.2436
σ (Å)	3.176	2.6	3.159	3.18
b (Å/e)	-	0.5	-	-
θ_{HOH} (degrees)	109.47	104.52	104.52	104.52
r_{OH} (Å)	1.0	0.9572	0.9572	0.9572
r_{OM} (Å)	-	0.15	0.15	0.7
θ_{MOM} (degrees)	-	-	-	109.47
$\widetilde{\chi}_M - \widetilde{\chi}_H$ (kcal/(mol e))	73.33	68.49	68.49	65.69
J^0_{MM} (kcal/(mol e^2))	367.0	371.6	371.6	385.1
J^0_{HH} (kcal/(mol e^2))	392.2	353.0	353.0	391.9
$J_{MH}(r_{MH})$ (kcal/(mol e^2))	276.0	286.4	286.4	227.4
$J_{HH}(r_{HH})$ (kcal/(mol e^2))	196.0	203.6	203.6	208.5
$J_{MM}(r_{MM})$ (kcal/(mol e^2))	-	-	-	260.9

Table A.2.: Parameters for the polarizable models. Regarding the parameters dealing with the polarizability ($\widetilde{\chi}_M - \widetilde{\chi}_H$ to $J_{MM}(r_{MM})$) the M denotes the dummy site in case of the transferable models and the O site in case of the SPC-FQ model.

A.2.2. Chemical potential of the TIP4P/2005 model

	$P = 1$ bar	$P = 100$ bar	$P = 500$ bar	$P = 1000$ bar
$T = 100$ K	-49.7(2)	-49.5(2)	-48.8(2)	-47.8(2)
$T = 120$ K	-49.6(2)	-49.4(2)	-48.6(2)	-47.6(2)
$T = 140$ K	-49.6(1)	-49.4(1)	-48.6(1)	-47.7(2)
$T = 160$ K	-49.7(1)	-49.5(1)	-48.7(1)	-47.8(1)
$T = 180$ K	-49.93(7)	-49.74(8)	-48.98(8)	-48.07(7)
$T = 200$ K	-50.30(5)	-50.11(6)	-49.37(5)	-48.46(6)
$T = 220$ K	-50.84(4)	-50.65(4)	-49.92(4)	-49.03(4)
$T = 240$ K	-51.54(3)	-51.36(3)	-50.64(3)	-49.75(2)
$T = 260$ K	-52.45(2)	-52.27(2)	-51.55(2)	-50.68(2)
$T = 280$ K	-53.49(1)	-53.32(1)	-52.60(1)	-51.73(2)
$T = 300$ K	-54.67(1)	-54.50(1)	-53.78(1)	-52.92(1)
$T = 320$ K	-55.97(1)	-55.79(1)	-55.08(1)	-54.20(1)
$T = 340$ K	-57.37(1)	-57.19(1)	-56.47(19	-55.59(1)
$T = 360$ K	-58.70(1)	-58.54(1)	-57.96(1)	-57.07(1)
$T = 380$ K	-60.30(1)	-60.13(1)	-59.54(1)	-58.62(1)
$T = 400$ K	-61.99(1)	-61.80(1)	-61.19(1)	-60.25(1)

Table A.3.: Chemical potential of the TIP4P/2005 model in kJ/mol (polarization correction included).

Bibliography

[1] Berendsen H J C, Postma J P M, von Gunsteren W F, and Hermans I. *Intermolecular Forces*, page 331. edited by Pullman B (Reidel, Dordrecht), 1981.

[2] Jorgensen W L, Chandrasekhar J, Madura J D, Impey R W, and Klein M L. Comparison of simple potential functions for simulating liquid water. *J. Chem. Phys.* , 79(2):926–35, 1983.

[3] Abascal J L F and Vega C. A general purpose model for the condensed phases of water: TIP4P/2005. *J. Chem. Phys.* , 123:4505–17, 2005.

[4] Rick S W. A reoptimization of the five-site water potential (TIP5P) for use with ewald sums. *J. Chem. Phys.* , 120(13):6085–93, 2004.

[5] Rick S W, Stuart S J, and Berne B J. Dynamical fluctuating charge force fields: Application to liquid water. *J. Chem. Phys.* , 101(7):6141–56, 1994.

[6] Chen B, Xing J, and Siepmann J I. Development of polarizable water force fields for phase equilibrium calculations. *J. Phys. Chem. B*, 104:2391–2401, 2000.

B. Appendix

B.1. Computation of the gas phase energy per molecule E^{gp}

The potential energy of an isolated TIP5P-E water molecule is given by

$$\begin{aligned}\mathcal{U}^{\text{iso}} &= 2E_H(0) + 2E_M(0) + 2\tilde{\chi}_H^0 Q_H + 2\tilde{\chi}_M^0 Q_M + J_{HH}^0 Q_H^2 + J_{MM}^0 Q_M^2 + \\ &\quad J_{HH}(r_{HH})Q_H^2 + 2(J_{MH}(r_{MH}) + J_{MH}(r'_{MH}))Q_M Q_H + J_{MM}(r_{MM})Q_M^2 \\ &= 2E_H(0) + 2E_M(0) + 2(\tilde{\chi}_H^0 - \tilde{\chi}_M^0)Q_H + \\ &\quad (J_{HH}^0 + J_{MM}^0 + J_{HH}(r_{HH}) + J_{MM}(r_{MM}) - \\ &\quad 2(J_{MH}(r_{MH}) + J_{MH}(r'_{MH})))Q_H^2 \end{aligned} \tag{B.1}$$

So the charge on one hydrogen atom in the gas phase can be determined by mimimizing $\mathcal{U}^{\text{iso}}$ to

$$Q_H = -Q_M \tag{B.2}$$

$$= \frac{\tilde{\chi}_M^0 - \tilde{\chi}_H^0}{J_{HH}^0 + J_{MM}^0 + J_{HH}(r_{HH}) + J_{MM}(r_{MM}) - 2(J_{MH}(r_{MH}) + J_{MH}(r'_{MH}))}.$$

Inserting this into the equation for the enery and setting $E_H(0) = E_M(0) = 0$ one arrives at:

$$\mathcal{U}^{gp} = \frac{-(\tilde{\chi}_M^0 - \tilde{\chi}_H^0)^2}{J_{HH}^0 + J_{MM}^0 + J_{HH}(r_{HH}) + J_{MM}(r_{MM}) - 2(J_{MH}(r_{MH}) + J_{MH}(r'_{MH}))} \tag{B.3}$$

B.2. Potentials of carbon nanotubes and sheets

For the potential of a water molecule in distance z to a carbon sheet of carbon atom number density θ we have:

$$U = \theta \int_0^\infty \int_0^{2\pi} U(\tau, z; \epsilon; \sigma)\, d\phi\, \tau d\tau \tag{B.4}$$

$$= 2\pi 4\epsilon\theta \left[\sigma^{12} \int_0^\infty \frac{\tau}{(z^2+\tau^2)^6} d\tau - \sigma^6 \int_0^\infty \frac{\tau}{(z^2+\tau^2)^3} d\tau\right] \tag{B.5}$$

$$= 2\pi\epsilon\theta\sigma^2 \left[\frac{2}{5}\left(\frac{\sigma}{z}\right)^{10} - \left(\frac{\sigma}{z}\right)^4\right] \tag{B.6}$$

For the potential of a water molecule in a carbon nanotube of radius R we procede similar to above:

$$\begin{aligned}
U &= \theta R \int_{-\infty}^{\infty}\int_0^{2\pi} U(r,\phi,z;\epsilon,\sigma)\,d\phi\,dz && \text{(B.7)}\\
&= 4\epsilon\theta R \int_{-\infty}^{\infty}\int_0^{2\pi} \left[\sigma^{12}\frac{1}{(r^2+R^2-2rR\cos(\phi)+z^2)^6}\right.\\
&\qquad\qquad \left. -\,\sigma^6\frac{1}{(r^2+R^2-2rR\cos(\phi)+z^2)^3}\right] && \text{(B.8)}\\
&= 8\epsilon\theta R \int_0^{2\pi} \left[\sigma^{12}\frac{63\pi}{512}\frac{1}{\sqrt{r^2+R^2-2rR\cos(\phi)}^{11}} - \sigma^6\frac{3\pi}{16}\frac{1}{\sqrt{r^2+R^2-2rR\cos(\phi)}^{5}}\right] d\phi\\
&= 3\pi\epsilon\theta R\sigma^2 \int_0^{\pi} \left[\frac{21\sigma^{10}}{32}\frac{1}{\sqrt{r^2+R^2-2rR\cos(\phi)}^{11}} - \sigma^4\frac{1}{\sqrt{r^2+R^2-2rR\cos(\phi)}^{5}}\right] d\phi\\
&= 3\pi\theta\epsilon\sigma^2\left[\frac{21}{32}\left(\frac{\sigma}{R}\right)^{10} M_{11}(x) - \left(\frac{\sigma}{R}\right)^4 M_5(x)\right] && \text{(B.9)}
\end{aligned}$$

with

$$M_n(x) = \int_0^{\pi} d\phi\,\frac{1}{(1+x^2-2x\cos(\phi))^{n/2}} \qquad \text{(B.10)}$$

B.3. Structures of simulated carbon nanotubes

diameter in Å	conformation
9.62569	(7,7)
11.00079	(8,8)
12.37589	(9,9)
13.75099	(10,10)
15.12609	(11,11)
16.50118	(12,12)
17.87628	(13,13)
19.25138	(14,14)
20.62648	(15,15)
22.00158	(16,16)
23.37668	(17,17)
24.75178	(18,18)
26.12688	(19,19)

Table B.1.: Structures of the nanotubes.

B.4. Ewald summation

All our explanations in this section follow [1, 2]. The starting point is the identity

$$\sum_{\vec{a}} \frac{1}{|\vec{r}_{ij} + \vec{a}|} = \sum_{\vec{a}} \frac{2}{\sqrt{\pi}} \int_0^\infty ds \, \exp\left[-|\vec{r}_{ij} + \vec{a}|^2 s^2\right] \tag{B.11}$$

Now the integral is split into two parts

$$\int_0^\infty ds \, \cdots = \int_0^\kappa ds \, \cdots + \int_\kappa^\infty ds \, \ldots \tag{B.12}$$

The first part describes the interaction on a large scale and will be solved in Fourier space, while the second part describes it on a short scale and will be computed in real space.

We will first solve the first integral by Fourier transforming the integrand

$$\sum_{\vec{a}} \frac{2}{\sqrt{\pi}} \exp\left[-|\vec{r}_{ij} + \vec{a}|^2 s^2\right] = \sum_{\vec{g}} c_{\vec{g}} \exp\left[i \, \vec{g} \cdot \vec{r}_{ij}\right] \tag{B.13}$$

where

$$c_{\vec{g}} = \frac{2\pi}{V} \frac{1}{s^3} \exp\left(-\frac{g^2}{4s^2}\right) . \tag{B.14}$$

The remaining integral over s is given by

$$\frac{4\pi}{V} \sum_{\vec{g}} g^{-2} \exp\left[-\frac{g^2}{4\kappa^2}\right] \exp\left[i\vec{g} \cdot \vec{r}_{ij}\right] . \tag{B.15}$$

Now we have to look at the term for $\vec{g} = \vec{0}$

$$\frac{1}{g^2} \exp\left[-\frac{g^2}{3\kappa^2}\right] \cos\left[\vec{g} \cdot \vec{r}_{ij}\right] = \frac{1}{g^2} - \frac{1}{4\kappa^2} - \frac{1}{2} \left(\hat{g} \cdot \vec{r}_{ij}\right)^2 + O(g) . \tag{B.16}$$

The first two terms vanish because of charge neutrality $\sum_i q_i = 0$ and the remaining term can be rearranged to

$$-\frac{1}{2} \sum_{ij} q_i q_j \left(\hat{g} \cdot \vec{r}_{ij}\right)^2 = -\frac{1}{2} \sum_{ij} q_i q_j \vec{r}_{ij}^{\,2} \cos^2(\theta) = \frac{1}{3} (\sum_i q_i \vec{r}_i)^2 . \tag{B.17}$$

This polarization term

$$\mathcal{U}^{\mathrm{Pol}} = \frac{1}{4\pi\epsilon_0} \frac{2\pi}{3V} (\sum_i q_i \vec{r}_i)^2 \tag{B.18}$$

depends on the boundary conditions at infinity and incorporates the indeterminacy that is due to the conditional convergence of the sum. For arbitrary boundary conditions one obtains

$$\mathcal{U}^{\mathrm{Pol}} = \frac{1}{4\pi\epsilon_0} \frac{2\pi}{(1 + 2\epsilon')V} (\sum_i q_i \vec{r}_i)^2 . \tag{B.19}$$

The polarization term vanishes for metallic or tin-foil boundary conditions that will be used in this work.

The second integral is easier and can be solved directly

$$\sum_{\vec{a}} \frac{\operatorname{erfc}\left[\left|\vec{r}_{ij} + \vec{a}\right| \kappa\right]}{\left|\vec{r}_{ij} + \vec{a}\right|} \tag{B.20}$$

For $\vec{a} = \vec{0}$ and $|\vec{r}_{ij}| \to 0$ there is a divergent term. The first term is due to the interaction of a charge with itself and has to be substracted, while the second term remains and is often refered to as the self energy term.

$$\frac{1}{|\vec{r}_{ij}|} - \frac{\kappa}{\sqrt{\pi}} \tag{B.21}$$

Thus we finally arrive at

$$\sum_{\substack{\vec{a} \\ (i \neq j \text{ for } \vec{a} = \vec{0})}} \frac{\operatorname{erfc}\left[\kappa \left|\vec{r}_{ij} + \vec{a}\right|\right]}{\left|\vec{r}_{ij} + \vec{a}\right|} - \delta_{ij} \frac{\kappa}{\sqrt{\pi}}\,. \tag{B.22}$$

κ modulates the ratio between the part of the energy that is computed in real space against that in the reziprocal space. For a given cutoff in real space r_{cut} there exists an estimation for an ideal κ, that optimizes the accuracy of the computation [3]. Usually it is possible to choose κ big enough to apply the minimum image convention.

As can be seen in figure B.1 we computed the Madelung constant of TiO_2 and SiO_2 as a test. The results for TiO_2 for different cutoff radii are shown in dependence on κ. There is a clear plateau that is slightly shifted with r_{cut}. One observes that κ can be chosen in a wide range without altering the result.

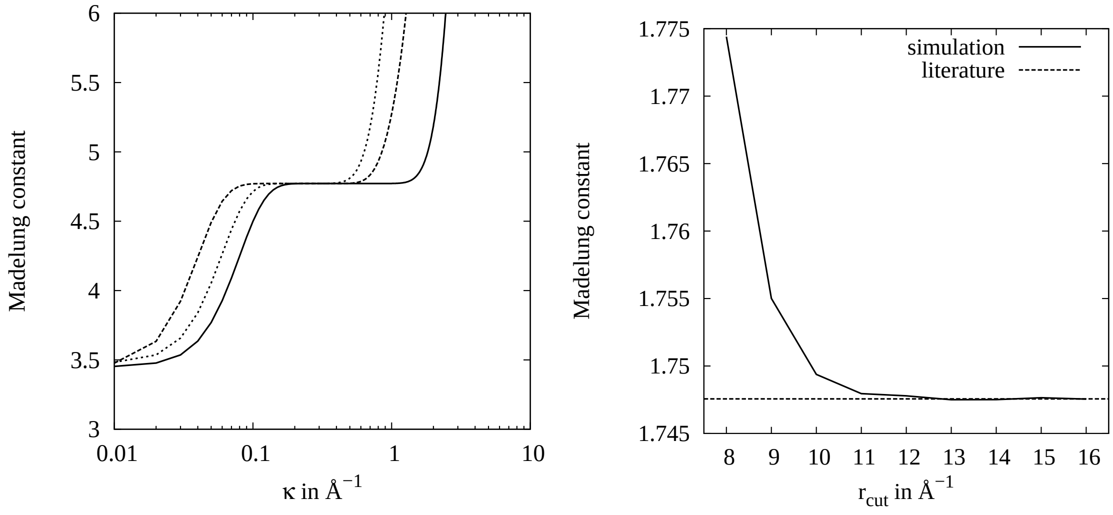

(a) (b)

Figure B.1.: (a) The Madelung constant of TiO_2 in dependence on κ for different cutoff radii. (b) The convergence of the Madelung constant of SiO_2 in dependence on r_{cut} when choosing the optimal κ according to [3]

Also plotted is the convergence of the Madelung constant for SiO_2 with the cutoff radius, while choosing κ to give optimal accuracy.

Now we can also compute the virial, which we need to get the pressure $P = P_{\text{ideal}} - \mathcal{V}/(3V) = (2/fE_{\text{kin}} - \mathcal{V}/3)/V$. As the Ewald sum is explicitly volume dependent one arrives at:

$$
\begin{aligned}
\mathcal{V}^{\text{real}} &= -\left\langle \frac{1}{2}\sum_{i,j}^{N} \vec{s}_{ij}\cdot\vec{\mathcal{F}}_{ij}^{\text{real}} \right\rangle && \text{(B.23)}\\
\mathcal{V}^{\text{rec}} &= -\left\langle \frac{1}{4\pi\varepsilon_0}\frac{4\pi}{V}\sum_{\vec{g}\neq\vec{0}} g^{-2}\exp\left[-\frac{g^2}{4\kappa^2}\right]\left[1-\frac{g^2}{2\kappa^2}\right]\right. && \text{(B.24)}\\
&\qquad \left. \frac{1}{2}\left\{\left[\sum_{i}^{N}\sum_{\alpha}^{M} q_\alpha \cos\left[\vec{g}\cdot\vec{r}_{i\alpha}\right]\right]^2 + \left[\sum_{i}^{N}\sum_{\alpha}^{M} q_\alpha \sin\left[\vec{g}\cdot\vec{r}_{i\alpha}\right]\right]^2\right\}\right\rangle && \text{(B.25)}\\
& && \text{(B.26)}
\end{aligned}
$$

B.5. PPPM

Our explanations in this section follow [1, 2]. In order to see where the FFT comes into play, we first have to rewrite expression 2.65. Using $\tilde{\rho}(\vec{g}) = \sum_j^N q_j e^{-i\vec{g}\vec{r}_j}$ it is possible to write

$$
\mathcal{U}^{\text{rec}} = \frac{1}{2}\frac{1}{4\pi\varepsilon_0}\frac{4\pi}{V}\sum_{\vec{g}\neq\vec{0}} g^{-2}\exp\left[-\frac{g^2}{4\kappa^2}\right]|\tilde{\rho}(\vec{g})|^2 \qquad \text{(B.27)}
$$

Denoting the Fourier transform of the Greensfunction by $\tilde{g}(\vec{g}) = 4\pi/g^2$ and $\tilde{\gamma}(\vec{g}) = \exp(-g^2/(4\kappa^2))$ one arrives at

$$
\mathcal{U}^{\text{rec}} = \frac{1}{4\pi\varepsilon_0}\frac{1}{2V}\sum_j q_j \sum_{\vec{g}\neq\vec{0}} \tilde{g}(\vec{g})\tilde{\gamma}(\vec{g})\tilde{\rho}(\vec{g})e^{i\vec{g}\vec{r}_j} \qquad \text{(B.28)}
$$

Now we introduce the so called influence function $\tilde{G} = \tilde{g}(\vec{g})\tilde{\gamma}(\vec{g})$ leading to

$$
\mathcal{U}^{\text{rec}} = \frac{1}{4\pi\varepsilon_0}\frac{1}{2V}\sum_j q_j \left[\overleftarrow{FT}\left[\overrightarrow{FT}\left[\rho\right]\tilde{G}\right]\right]. \qquad \text{(B.29)}
$$

Here $\overrightarrow{FT}$ denotes the Fourier transform and $\overleftarrow{FT}$ its inverse, which can be replaced by FFT after discretizing the charge density and the influence function on a mesh.

Now that we have introduced the right form for $\mathcal{U}^{\text{rec}}$, we can take a closer look at the charge discretization. We have to introduce a space mesh and to assign charges to it according to the distribution function $W(x_p - x)$, which are optimized to represent the actual charge distribution.

$$
\rho_M(x_p) = \frac{1}{h}\int_0^L dx\, W(x_p - x)\rho(x) \qquad \text{(B.30)}
$$

Here the index M stands for mesh with mesh size h, x_p denotes the mesh coordinates while x is the position of the actual charge. There are a number of charge distribution functions $W(x)$ in use.

The next step is to compute the Fourier transform of the mesh charge distribution. The Fourier transform of the discretized function, that can be done by FFT, is denoted by a hat.

$$\hat{\rho}(\vec{g}) := h^3 \sum_{\vec{r}_p \in M} \rho_M(\vec{r}_p) e^{-i\vec{g}\cdot\vec{r}_p} \,. \tag{B.31}$$

The influence function is not always the same as the simple Coulomb Greens function, but may be adjusted to minimize the error of the mesh calculation and to make it resemble the continuum solution more closely.

The main difference of the various Fast Fourier methods lies in the choice of the influence function in combination with the charge distribution function $W(x_p - x)$. The PME method uses the continuums coulomb Greens function and the Lagrangian charge distribution scheme, while in smooth PME an adapted influence function and the charge distribution scheme of Hockney and Eastwood are implemented. We use the PPPM scheme where the charge distribution of Hockney and Eastwood is combined with an optimized influence function.

$$\hat{G}_{opt}(\vec{g}) = \frac{\tilde{D}(\vec{g}) \cdot \sum_{m \in Z^3} \tilde{U}^2\left(\vec{g} + \frac{2\pi}{h}m\right) \tilde{R}\left(\vec{g} + \frac{2\pi}{h}m\right)}{\left|\tilde{D}(\vec{g})\right|^2 \left[\sum_{m \in Z^3} \tilde{U}^2\left(\vec{g} + \frac{2\pi}{h}m\right)\right]^2} \tag{B.32}$$

As the influence function does not depend on the particle coordinates it can be computed once at the beginning. Therefore its complexity does not lead to significant additional computational cost.

Now that we can compute the potential we need to differentiate it in order to get the accompanying forces. In case of the PME the differentiation is done in Fourier space by $\tilde{D}(\vec{g}) = i\vec{g}$ which guaranties momentum conservation. The smooth PME differentiates the distribution functions in real space, which saves additional Fourier transformations but does not conserve momentum, while the PPPM approach uses a discrete differentiation on the mesh in real space which conserves momentum.

Finally the charge distribution functions are applied again to assign the mesh forces to the actual particles.

We opted for the PPPM method as it allows an accurate error estimate [2].

B.6. ELC

The ELC method works in two steps as described in [4], which we will follow closely:

1. Use a three-dimensional summation method whose summation order is changed to slab-wise to compute to sum up the interactions in the 3D periodic slab-geometry.
2. Subtract the unwanted interactions with the image layers analytically, allowing full control of the errors.

The first step is already described in section 2.3.4, so we will now focus on the calculation of the electrostatic layer correction term. First we look at the formal definition of the Coulomb energy of the slab system,

$$E = \frac{1}{2} \sum_{S=0}^{\infty} \sum_{\substack{n \in \mathbb{Z}^2 \times \{0\} \\ n_x^2 + n_y^2 = S}} \sum_{i,j=1}^{N}{}' \frac{q_i q_j}{|r_i - r_j + \Lambda n|} \,. \tag{B.33}$$

Here $\Lambda = \mathrm{diag}(L, L, L_z)$ describes the shape of the box, while the vector $n = (n_x, n_y, n_z)$, where $n_z = 0$, denotes the images of the box. The prime on the inner summation indicates the omission of the self-interaction $i = j$ in the primary box $n = (0, 0, 0)$. Vacuum boundary conditions are assumed. The energy can now be rewritten as the sum of the standard three-dimensional Coulomb sum with spherical limit E_s, the correction term to change from spherical to slab-wise summation E_c and finally the layer correction term E_{lc}.

$$E = E_s + E_c + E_{lc} \tag{B.34}$$

$$E_{lc} = -\frac{1}{2} \sum_{\substack{T \in \mathbb{Z} \\ T > 0}} \sum_{n_z = \pm T} \sum_{S=0}^{\infty} \sum_{\substack{n \in \mathbb{Z}^2 \times \{n_z\} \\ n^2 = S}} \sum_{i,j=1}^{N} \frac{q_i q_j}{|r_i - r_j + \Lambda n|} \tag{B.35}$$

As shown in [4] E_{lc} can be rewritten as

$$E_{cl} = \sum_{i,j=1}^{N} q_i q_j \psi(r_i - r_j + \Lambda n) \tag{B.36}$$

where

$$\begin{aligned} \psi(x, y, z) = {} & \frac{4}{L} \sum_{k_x, k_y > 0} \frac{\cosh(2\pi k_{||} z_{ij}/L}{k_{||}(e^{2\pi k_{||} L_z/L} - 1)} \cos(2\pi k_x x_{ij}/L) \\ & \times \cos(2\pi k_y y_{ij}/L) \\ & + \frac{2}{L} \sum_{k_x > 0} \frac{\cosh(2\pi k_x z_{ij}/L) \cos(2\pi k_x x_{ij}/L)}{k_x(e^{2\pi k_x L_z/L} - 1)} \\ & + \frac{2}{L} \sum_{k_y > 0} \frac{\cosh(2\pi k_y z_{ij}/L) \cos(2\pi k_y y_{ij}/L)}{k_y(e^{2\pi k_y L_z/L} - 1)} \,, \end{aligned} \tag{B.37}$$

although, as might be guessed by the complexity of this term, this is non-trivial. The main advantage of this representation of E_{lc} is a linear computation time with respect to the number of particles N.

For details of the implementation of the layer correction for the standard Ewald (EW3DLC), that is used in this work, and the PPPM mesh Ewald (PPPMLC) methods see [5].

B.7. MMM1D

We follow [6] in the explanation of the MMM1D method. We start with a primary simulation box of dimensions $B_0 = (-\infty, \infty) \times (-\infty, \infty) \times (-\lambda_z/2, \lambda_z/2]$, where z is the periodic direction. If $r_{ij} = (x_{ij}, y_{ij}, z_{ij})$ is the distance vector between two charges i and j, we define $\rho_{ij} := \sqrt{x_{ij}^2 + y_{ij}^2}$. The base vector of the kth periodic image of the primary simulation box is denoted by

$$n_k = (0, 0, k\lambda_z), \tag{B.38}$$

and

$$r_k := |r + n_k| = \sqrt{\rho^2 + (z + k\lambda_z)^2}\,. \tag{B.39}$$

Finally the inverse peridicity length is denoted by

$$u_z = \frac{1}{\lambda_z}\,. \tag{B.40}$$

Thus we get for the Coulomb energy of the system

$$E = \frac{1}{2} \sum_{k=-\infty}^{\infty} \sum_{i,j}{}' \frac{q_i q_j}{|r_{ij} + n_k|}\,. \tag{B.41}$$

In contrast to fully periodic boundary conditions there is no shape-dependent term as the sum over k is absolutely convergent. This can be seen by adding $0 = 1/2 \sum_{ij}' q_i q_j / |n_k|$, which is zero by charge neutrality, to the energy.

$$\begin{aligned} E &= \frac{1}{2} \sum_{k=-\infty}^{\infty} \sum_{i,j}{}' q_i q_j \left(\frac{1}{|r_{ij} + n_k|} - \frac{1}{|n_k|} \right) \\ &\text{with} \\ \left| \frac{1}{|r_{ij} + n_k|} - \frac{1}{|n_k|} \right| &= \frac{||r_{ij} + n_k| - |n_k||}{|n_k||r_{ij} + n_k|} = O(|n_k|^{-2}) \end{aligned}$$

Now the Coulomb sum is modified by the application of a screening convergence factor $e^{-\beta r}$, and the limit $\beta \to 0$ taken after the lattice summation. Thus we arrive at

$$\tilde{E} = \frac{1}{2} \lim_{\beta \to 0} \sum_{k \in} \sum_{i,j=1}^{N}{}' \frac{q_i q_j e^{-\beta |r_{ij} + n_k|}}{|r_{ij} + n_k|} =: \frac{1}{2} \lim_{\beta \to 0} \sum_{i,j=1}^{N} q_i q_j \phi_\beta(r_{ij}) \tag{B.42}$$

where ϕ_β is given by

$$\phi_\beta(r) = \tilde{\phi}_\beta(r) + \begin{cases} \frac{e^{-\beta r}}{r}, & r \neq (0,0,0) \\ 0, & r = (0,0,0) \end{cases} \tag{B.43}$$

and

$$\tilde{\phi}_\beta(r) = \sum_{k \neq 0} \frac{e^{-\beta r_k}}{r_k}\,. \tag{B.44}$$

For a prove that $E = \tilde{E}$ see [6].

Far field formula For $\rho > 0$ and $\beta > 0$, we can Fourier transform $\phi_\beta(r)$ and sum over Bessel functions denoted by K_0. After cancelling out all singularities using charge neutrality one arrives at the far field formula:

$$\phi(\rho, z) = 4u_z \sum_{p>0} K_0(2\pi u_z p\rho) \cos(2\pi u_z p z) - 2u_z \log\left(\frac{\rho}{2\lambda_z}\right) - 2u_z\gamma \tag{B.45}$$

Near field formula As the far formula does not converge for $\rho = 0$ and only slowly for small ρ, a near formula is derived using the one-dimensional Lekner approach [7] that is valid for $\rho < (N_\phi - 1/2)\lambda_z$ and $(\rho, z) \neq 0$.

$$\begin{aligned}\phi(\rho, z) &= -u_z \sum_{n \geq 0} \begin{pmatrix} -\frac{1}{2} \\ n \end{pmatrix} \frac{(\psi^{(2n)}(N_\psi + u_z z) + \psi^{(2n)}(N_\psi - u_z z))}{(2n)!} (u_z \rho)^{2n} \\ &\quad -2u_z \gamma \left[\frac{1}{r_0} + \sum_{k=1}^{N_\psi - 1} \left(\frac{1}{r_k} + \frac{1}{r_{-k}} \right) \right] \qquad \text{(B.46)}\end{aligned}$$

Here γ is Euler's constant, and the polygamma functions are defined by

$$\begin{aligned}\psi(1+x) &= -\gamma + \sum_{k=1}^{\infty} \left(\frac{1}{k} - \frac{1}{k+x} \right), \text{ respectively,} \\ \psi^{(n)}(1+x) &= (-1)^{n+1} n! \sum_{k=1}^{\infty} \frac{1}{(k+x)^{n+1}}. \qquad \text{(B.47)}\end{aligned}$$

In the range $0 < \rho < (N_\psi - 1/2)\lambda_z$ the near as well as the far formula give the same result. This can be used to test the implementation and one can choose the formula that is faster to evaluate to increase performance. We fix a radius ρ_{min}, and for all $\rho < \rho_{min}$, the near formula is used, while for all other ρ the far formula is used. ρ_{min} is determined by fixing the desired accuracy of the computation using the error bounds described in [6] and then searching for a minimum in computation time.

B.8. Computation of the isosteric heat of adsorption

This derivation follows [8]. First we want to show that $< H >$ in the grand-canonical ensemble can be expressed as follows.

$$\begin{aligned}< H > &= \frac{1}{\Omega} \sum_{N>0}^{\infty} \frac{V^N}{N!} \frac{1}{\lambda_T^{3N}} \int d^{3N}\rho d^N\psi d^N\theta d^N\phi \left(\prod_{i=1}^{N} \frac{\sin\theta_i}{8\pi^2} \right) \\ &\quad [6N/2kT + U] \exp(-\beta(U - (\mu - \mu_{rot})N)) \qquad \text{(B.48)}\end{aligned}$$

Starting from the grand-canonical partition function, Ω we arrive at

$$\begin{aligned}\Omega &= \sum_{N=0}^{\infty} \frac{1}{N!} \int \frac{d^{3N}r d^{3N}p d^{3N}n d^{3N}p_n}{h^{3N} h^{3N}} e^{-\beta(H - \mu N)} \qquad \text{(B.49)} \\ &= \sum_{N=0}^{\infty} \frac{V^N}{N!} \frac{1}{\lambda_T^{3N}} \int d^{3N}\rho d^N\psi d^N\theta d^N\phi \left(\prod_{i=1}^{N} \frac{\sin\theta_i}{8\pi^2} \right) e^{-\beta(U - (\mu - \mu_{rot})N)} \qquad \text{(B.50)}\end{aligned}$$

with $\lambda_T = \sqrt{(h^2\beta)/(2\pi m)}$ and $q_{rot} = 4\pi^2/h^3\sqrt{I_1 I_2 I_3}\sqrt{2\pi/\beta}^3 = exp(-\beta\mu_{rot})$. As $\partial \ln(\Omega)/\partial(-\beta) =< H - \mu N >$ we can write

$$\begin{aligned}
< H > &= \frac{\partial \ln \Omega}{\partial(-\beta)} + < \mu N > && \text{(B.51)} \\
&= \frac{1}{\Omega}\sum_{N=0}^{\infty}\frac{V^N}{N!}\frac{1}{\lambda_T^{3N}}\int d^{3N}\rho d^N\psi d^N\theta d^N\phi\left(\prod_{i=1}^{N}\frac{\sin\theta_i}{8\pi^2}\right) \\
&\quad [3NkT + U - \mu N]\, e^{-\beta(U-(\mu-\mu_{rot})N)} + < \mu N > && \text{(B.52)} \\
&= \frac{1}{\Omega}\sum_{N>0}^{\infty}\frac{V^N}{N!}\frac{1}{\lambda_T^{3N}}\int d^{3N}\rho d^N\psi d^N\theta d^N\phi\left(\prod_{i=1}^{N}\frac{\sin\theta_i}{8\pi^2}\right) \\
&\quad [6N/2kT + U]\exp(-\beta(U - (\mu-\mu_{rot})N)) && \text{(B.53)}
\end{aligned}$$

As another ingredient we will derive the following equations

$$\begin{aligned}
\left(\frac{\partial < N >}{\partial \mu}\right)_{V,T} &= \beta\left[< N^2 > - < N >^2\right] = \beta\frac{\partial < N >}{\partial \ln\lambda} && \text{(B.54)} \\
\left(\frac{\partial < U >}{\partial \mu}\right)_{V,T} &= \beta\left[< UN > - < U >< N >\right] = \beta\frac{\partial < U >}{\partial \ln\lambda} && \text{(B.55)}
\end{aligned}$$

with $\lambda = \exp(\beta\mu)$.

$$\begin{aligned}
\left(\frac{\partial < N >}{\partial \mu}\right)_{V,T} &= \frac{1}{\beta}\frac{\partial}{\partial\mu}\left(\frac{\partial \ln\Omega}{\partial\mu}\right)_{V,T} && \text{(B.56)} \\
&= \frac{1}{\beta}\left(\frac{\partial}{\partial\mu}\frac{1}{\Omega}\right)_{V,T}\left(\frac{\partial\Omega}{\partial\mu}\right)_{V,T} + \left(\frac{1}{\beta}\frac{1}{\Omega}\frac{\partial^2\Omega}{\partial\mu^2}\right)_{V,T} && \text{(B.57)} \\
&= -\frac{1}{\beta}\frac{1}{\Omega^2}\left(\frac{\partial\Omega}{\partial\mu}\right)^2 + \frac{1}{\beta}\beta^2 < N >^2 && \text{(B.58)} \\
&= \beta\left[< N^2 > - < N >^2\right] && \text{(B.59)}
\end{aligned}$$

$$\begin{aligned}
\left(\frac{\partial < U >}{\partial \mu}\right)_{V,T} &= \left.\frac{\partial}{\partial\mu}\right|_{V,T}\frac{1}{\Omega}\sum_{N>0}^{\infty}\frac{V^N}{N!}\frac{1}{\lambda_T^{3N}}\int d^{3N}\rho d^N\psi d^N\theta d^N\phi\left(\prod_{i=1}^{N}\frac{\sin\theta_i}{8\pi^2}\right) \\
&\quad U\exp(-\beta(U - (\mu-\mu_{rot})N)) && \text{(B.60)} \\
&= \frac{\Omega\beta < NU > \Omega - < U > \Omega\beta < N > \Omega}{\Omega^2} && \text{(B.61)} \\
&= \beta\left[< NU > - < N >< U >\right] && \text{(B.62)}
\end{aligned}$$

The isosteric heat of adsorption, q_{st} is given by

$$\begin{aligned}
q_{st} &= \left(\frac{\partial Q}{\partial N^\Sigma}\right)_{P,T} = T\left(\frac{\partial S}{\partial N^\Sigma}\right) && \text{(B.63)} \\
&= \left(\frac{\partial H^G}{\partial N^G}\right)_{P,T} - \left(\frac{\partial H^\Sigma}{\partial N^\Sigma}\right)_{P,T} + PV^G - PV^A\,, && \text{(B.64)}
\end{aligned}$$

because of $dN^{\Sigma} = -dN^{G}$. The excess of M is defined as $M^{\Sigma} = M - \tilde{M}^{G}$ and V^{G} and V^{A} are the partial molar volumes of the gas phase and of the adsorbed phase. We start with the term

$$\begin{aligned} q_u^{\Sigma} &= \left(\frac{\partial U^{\Sigma}}{\partial N^{\Sigma}}\right)_{P,T} && \text{(B.65)} \\ &= \left(\frac{\partial U^{\Sigma}}{\partial \lambda}\right)_{P,T} \left(\frac{\partial \lambda}{\partial N^{\Sigma}}\right)_{P,T} && \text{(B.66)} \\ &= \frac{1}{\lambda}\left(\frac{\partial U^{\Sigma}}{\partial \ln \lambda}\right)_{P,T} \left[\frac{1}{\lambda}\left(\frac{\partial N^{\Sigma}}{\partial \ln \lambda}\right)_{P,T}\right]^{-1}, && \text{(B.67)} \end{aligned}$$

to which we can apply equations (B.54) and (B.55).

$$\begin{aligned} \left(\frac{\partial N^{\Sigma}}{\partial \ln \lambda}\right)_{P,T} &= \frac{\partial}{\partial \ln \lambda}(N - \tilde{N}^{G}) && \text{(B.68)} \\ &= < N^2 > - < N >^2 - \frac{\partial \tilde{N}^{G}}{\partial \ln \lambda} && \text{(B.69)} \end{aligned}$$

$$\begin{aligned} \left(\frac{\partial U^{\Sigma}}{\partial \ln \lambda}\right)_{P,T} &= \frac{\partial}{\partial \ln \lambda}(U - \tilde{U}^{G}) && \text{(B.70)} \\ &= < UN > - < U >< N > - \frac{\partial \tilde{U}^{G}}{\partial \ln \lambda} && \text{(B.71)} \end{aligned}$$

In addition we have

$$q_k^{\Sigma} = \left(\frac{\partial K^{\Sigma}}{\partial N^{\Sigma}}\right)_{P,T} = 3kT\,, \tag{B.72}$$

da $< K >= 6/2kT < N >$. Thus we arrive at q_{st}

$$\begin{aligned} q_{st} &= \left(\frac{\partial H^{G}}{\partial N^{G}}\right)_{P,T} - \left(\frac{\partial H^{\Sigma}}{\partial N^{\Sigma}}\right)_{P,T} + PV^{G} - PV^{A} && \text{(B.73)} \\ &= \left(\frac{\partial U^{G}}{\partial N^{G}}\right)_{P,T} - \frac{< UN > - < U >< N > - \frac{\partial \tilde{U}^{G}}{\partial \ln \lambda}}{< N^2 > - < N >^2 - \frac{\partial \tilde{N}^{G}}{\partial \ln \lambda}} - 3kT \\ &\quad + PV^{G} - PV^{A} && \text{(B.74)} \end{aligned}$$

For the pressures used in this work we can assume that the gas phase is ideal, so that $(\partial U^{G}/\partial N^{G}) = 3kT$, $\partial U/\partial \mu = 0$, $PV^{G} = kT$ and $(\partial \tilde{N}^{G}/\partial \lambda) = \tilde{N}^{G}$. This leaves us with

$$q_{st} = -\frac{< UN > - < U >< N >}{< N^2 > - < N >^2 - \tilde{N}^{G}} + kT - PV^{A} \tag{B.75}$$

Assume PV^{A} to be small against kT we arrive at the final equation.

$$q_{st} = -\frac{< UN > - < U >< N >}{< N^2 > - < N >^2 - \tilde{N}^{G}} + kT \tag{B.76}$$

Bibliography

[1] Deserno M and Holm C. How to mesh up ewald sums. I. a theoretical and numerical comparison of various particle mesh routines. *J. Chem. Phys.* , 109:7678–93, 1998.

[2] Deserno M and Holm C. How to mesh up ewald sums. II. an accurate error estimate for the particle-particle-particle-mesh algorithm. *J. Chem. Phys.* , 109:7694–702, 1998.

[3] Kolafa J and Perram J W. Cutoff errors in the ewald summation formulae for point charge systems. *Molecular Simulation*, 9(5):351–70, 1992.

[4] Arnold A, De Joannis J, and Holm C. Electrostatics in periodic slab geometries. I. *J. Chem. Phys.* , 117:2496–502, 2002.

[5] De Joannis J, Arnold A, and Holm C. Electrostatics in periodic slab geometries. II. *J. Chem. Phys.* , 117:2503–12, 2002.

[6] Arnold A and Holm C. MMM1D: A method for calculating electrostatic interactions in one-dimensional periodic geometries. *J. Chem. Phys.* , 123:144103–8, 2005.

[7] Bródka A. Comment on MMM1D: A method for calculating electrostatic interactions in one-dimensional periodic geometries[J. Chem. Phys.[bold 123], 144103 (2005)]. *J. Chem. Phys.* , 125:107103–2, 2006.

[8] David Nicholson and Neville George Parsonage. *Computer simulation and the statistical mechanics of adsorption.* Academic Press, December 1982.

Index